

AFIT/GE/ENG/91D-41

AD--A243 742



DTIC
SELECT
DEC 27 1991
S C D

INCORPORATION OF DIFFERENTIAL GLOBAL
POSITIONING SYSTEM MEASUREMENTS
USING AN EXTENDED KALMAN FILTER
FOR IMPROVED REFERENCE
SYSTEM PERFORMANCE

THESIS

William Joseph Nestor
Captain, US-7

AFIT/GE/ENG/91D-41

Approved for public release; distribution unlimited

91-18999



20000901037

91 12 24 019

REPORT DOCUMENTATION PAGE

1 AGENCY USE ONLY

December 1991

Master's Thesis

4 TITLE AND SUBTITLE

INCORPORATION OF DIFFERENTIAL GLOBAL POSITIONING
SYSTEM MEASUREMENTS USING AN EXTENDED KALMAN
FILTER FOR IMPROVED REFERENCE SYSTEM PERFORMANCE

5 AUTHOR

William Joseph Negast, Captain, USAF

Air Force Institute of Technology
WPAFB OH 45433-6383

AFIT/GE/ENG/91D-41

6585th Test Group / GDAN
Holloman AFB, NM 88330-5000

Approved for public release; distribution unlimited

To quantify the performance abilities of existing or proposed navigation systems, the U.S. Air Force has, for the last several years, compared the performance of the system under test to the performance of a *baseline* navigation system known as the Completely Integrated Reference Instrumentation System (CIRIS). CIRIS obtains a highly accurate navigation solution by combining information from three major subsystems: inertial navigation system (INS) information, barometric altitude information, and range and range-rate information from ground transponders which have been precisely surveyed. Although the navigation solution produced by CIRIS is highly accurate, it will soon be inadequate as the standard against which future navigation systems can be tested. This research proposes an alternative to CIRIS - a hybrid Enhanced Navigation Reference System (ENRS) which is designed to take advantage of a newer INS (the LN-93), certain features of the current CIRIS, and certain features of differential corrections to Global Positioning System (DGPS) measurements. Analysis is conducted using a Kalman filter development package known as the Multimode Simulation for Optimal Filter Evaluation (MSOFE). Both a large order *truth* model for the ENRS (in which a full 24 satellite constellation is modeled) and full- and reduced-order Kalman filters are developed. Results suggest that the proposed ENRS (with DGPS aiding) provides a navigation solution one order of magnitude better than CIRIS.

Enhanced Navigation Reference System (ENRS), Differential Global Positioning System (DGPS), Inertial Navigation System (INS), Completely Integrated Reference Instrumentation System (CIRIS), Kalman Filtering

213

Unclassified

Unclassified

Unclassified

UL

AFIT/GE/ENG/91D-41

INCORPORATION OF DIFFERENTIAL GLOBAL
POSITIONING SYSTEM MEASUREMENTS
USING AN EXTENDED KALMAN FILTER
FOR IMPROVED REFERENCE
SYSTEM PERFORMANCE



Accession For	
NTIS Gnal	<input checked="" type="checkbox"/>
DTIC Tab	<input type="checkbox"/>
Unannounced	<input type="checkbox"/>
Justification	
By	
Distribution/	
Availability Codes	
Dist	Avail and/or Special
A-1	

THESIS

Presented to the Faculty of the School of Engineering
of the Air Force Institute of Technology
Air University

In Partial Fulfillment of the
Requirements for the Degree of
Master of Science in Electrical Engineering

William Joseph Negast, B.S. Electrical Engineering, B.S. Physics, B.S. Chemistry
Captain, USAF

December, 1991

Approved for public release: distribution unlimited

Preface

This thesis is the fourth in a series devoted to increasing the accuracy of the Completely Integrated Reference Instrumentation System (CIRIS) used by the Central Inertial Guidance Test Facility (CIGTF), Holloman AFB, NM to validate the accuracy of inertial navigation systems (INSs). However, the material contained within these pages is not limited only to this application. The incorporation of Global Positioning System (GPS) and Differential GPS (DGPS) measurements extends to any INS in production or development through the use of Kalman filtering. As GPS usage expands throughout the military and civilian communities, I hope this thesis provides a small contribution in this area.

As the fourth in a series of theses, I would be delinquent if I did not mention the people responsible for the excellent work which proceeded this thesis. Captains Solomon, Snodgrass, and Stacey all deserve more thanks than I can give them in this format, so I will just say "well done". Their previous theses provided the backbone from which my DGPS work grew, and I would not have completed one-fourth of the work I accomplished were it not for their legacy.

I would also like to thank Mr Darwin Abbey and Mr Scott Dance of Intermetrics for taking time out of their busy schedule to explain DGPS to an apprentice. The DGPS filters within this thesis can largely be attributed to their recommendations, and I hope performance is up to their expectations. I can honestly say I am looking forward to working with these gentlemen when I get to CIGTF to further refine the basic filters contained in this thesis.

Next, a few kind words to the gentlemen on my thesis committee are in order. Captain Randall Paschall, my advisor, kept me "on course" throughout this work and his guidance allowed me to complete as much work as I did. Thanks, Randy, for showing me the light at the end of the tunnel. Dr Peter Maybeck, a visionary in

the field of stochastic estimation, gave me the clear insights on filter order reduction and tuning used throughout this thesis. Without his advice, this thesis would not be worth the paper it is printed on. Lt Col David Meer and Maj Robert Riggins provided their time and enthusiasm over my work when it was needed, and I thank them for their efforts.

A special word of thanks must go to Mr Dan Zambon, a man greatly responsible for my success in completing this thesis. Dan gave me the opportunity to utilize six different computer systems and over 300 mega-bytes of storage space for all my simulations and results. Were it not for his dedicated efforts keeping the computer systems working at high efficiency, I would never have completed the first Monte Carlo simulation or tuned the first filter let alone the *three thousand* Monte Carlo runs this thesis encompasses.

Also, my parents must also be recognized for instilling in me the need for higher education. Their support throughout the years made it possible for me to complete this thesis and earn yet another degree. I am only now beginning to realize how much their guidance throughout my life has contributed to my current success.

Finally, a word to my wonderful wife Annette. I will never be able to repay you for the many months you were neglected so that I could complete this thesis. Your endless encouragement is the driving force making all my successes possible. I thank God for giving me someone as special as you to spend the rest of my life with.

William Joseph Negast

Table of Contents

	Page
Preface	ii
Table of Contents	iv
List of Figures	ix
List of Tables	xv
List of Symbols	xvii
Abstract	xix
I. Introduction	1-1
1.1 Background	1-1
1.2 Problem Definition	1-2
1.2.1 Summary of Effort.	1-2
1.3 Summary of Previous Research	1-3
1.4 Research Objectives	1-4
1.5 Research Approach	1-6
1.6 Assumptions	1-9
1.7 Overview of Thesis	1-9
II. Extended Kalman Filtering	2-1
2.1 Overview	2-1
2.2 The Extended Kalman Filter	2-1
2.3 Filter Order Reduction	2-5
2.4 Tuning Kalman Filters	2-7
2.5 Summary	2-10

	Page
III. The Navigation Reference System (NRS)	3-1
3.1 Overview	3-1
3.2 The 93-State LN-93 Error Model	3-1
3.3 Stacey's 128-State NRS Model	3-3
3.3.1 The 72-State LN-93 Error Model.	3-3
3.3.2 The 26-State RRS Error Model.	3-4
3.3.3 The 30-State GPS Error Model.	3-9
3.4 Reduction to a 41-State LN-93 Error Model	3-17
3.5 The 97-State NRS Error Model	3-18
3.6 The 69-State NRS Filter Model	3-18
3.7 Summary	3-20
IV. The Enhanced Navigation Reference System (ENRS)	4-1
4.1 Overview	4-1
4.2 Differential Corrections to GPS Measurements	4-1
4.2.1 The 22-State DGPS Model.	4-3
4.2.2 DGPS Pseudorange Measurement Equation.	4-5
4.3 The 89-State ENRS Error Model	4-7
4.4 The 48-State ENRS Filter (Position Measurements Only)	4-7
4.5 DGPS Delta-Range Measurements	4-8
4.5.1 DGPS Delta-Range Calculation From INS Data	4-9
4.5.2 The 22-State DGPS Filter (No RRS).	4-12
4.6 Transponder Range-Rate Measurements	4-12
4.6.1 RRS Range-Rate Calculation From INS Data.	4-13
4.6.2 The 46-State CIRIS Filter (No DGPS).	4-15
4.7 The 48-State ENRS Filter (Position and Velocity Measurements)	4-16
4.8 Summary	4-16

	Page
V. Results of Filter Implementations	5-1
5.1 Overview	5-1
5.1.1 The Double Precision Factor.	5-1
5.2 The NRS Filters	5-3
5.2.1 Stacey's 128-State NRS Filter.	5-4
5.2.2 The 97-State NRS Filter.	5-5
5.2.3 The 69-State NRS Filter.	5-6
5.3 The ENRS Filters	5-7
5.3.1 The 89-State NRS Filter (Position Measurements Only).	5-8
5.3.2 The 48-State ENRS Filter (Position Measure- ments Only).	5-9
5.4 Velocity-Aiding Filters	5-10
5.4.1 The 22-State DGPS Filter.	5-11
5.4.2 The 46-State CIRIS Filter.	5-12
5.5 The Complete 48-State ENRS Filter	5-14
5.6 Filter Tuning Parameters	5-15
5.7 Summary	5-18
VI. Conclusions and Recommendations	6-1
6.1 Conclusions	6-1
6.1.1 The NRS Filters.	6-1
6.1.2 The ENRS Filters.	6-2
6.2 Recommendations	6-3
6.2.1 Velocity-Aiding Measurements Require Further Study.	6-3
6.2.2 Return to a 93-State INS Truth Model.	6-4
6.2.3 Use of Real Measurements.	6-4
6.2.4 Reduction of the RRS error-states in the Filter.	6-5

	Page
Appendix A. Error Model State Definitions	A-1
A.1 Litton LN-93 Error-States	A-1
A.2 RRS Transponder Error States	A-1
A.3 GPS Error States	A-1
A.4 Reduced Order INS Truth Model States	A-1
A.5 DGPS Error States	A-2
Appendix B. Litton LN-93 Error-State Model Dynamics Matrix	B-1
B.1 Elements of the Process Noise Matrix	B-6
Appendix C. Comparison of 93-state and 41-State INS Models	C-1
Appendix D. Stacey's 128-State NRS Filter Performance Plots	D-1
D.1 Stacey's 128-State NRS Filter Performance Plots	D-2
Appendix E. 97-State NRS Filter Performance Plots	E-1
Appendix F. 69-State NRS Filter Performance Plots	F-1
Appendix G. 89-State ENRS Filter Performance Plots	G-1
Appendix H. 48-State ENRS Filter Performance Plots	H-1
Appendix I. 22-State DGPS Filter Performance Plots	I-1
I.1 2-Hour Fighter Flight Profile	I-2
I.2 2-Hour Straight Flight Profile	I-8
Appendix J. 46-State CIRIE Filter Performance Plots	J-1
J.1 2-Hour Fighter Flight Profile	J-2
J.2 2-Hour Racetrack Flight Profile	J-9
Appendix K. 48-State ENRS Filter Performance Plots	K-1

	Page
Bibliography	BIB-1
Vita	VITA-1

List of Figures

Figure	Page
3.1. 93 vs 41 State INS Models (a) Latitude (b) East Velocity and (c) East Tilt Errors.	3-19
4.1. GPS Data Analysis/Reference Station	4-3
5.1. Typical GPS Clock Bias Error State for Two Hour Flight Profile	5-2
C.1. 2-Hour Fighter Flight Profile (a) Latitude (b) Longitude and (c) Altitude	C-2
C.2. 93 vs 41 State INS Models (a) Latitude (b) Longitude and (c) Altitude Errors.	C-3
C.3. 93 vs 41 State INS Models (a) East Velocity (b) North Velocity and (c) Vertical Velocity Errors.	C-4
C.4. 93 vs 41 State INS Models (a) East Tilt (b) North Tilt and (c) Azimuth Errors.	C-5
D.1. 2-Hour Fighter Flight Profile (a) Latitude (b) Longitude and (c) Altitude	D-3
D.2. 128-State NRS Filter (a) Latitude (b) Longitude and (c) Altitude Errors.	D-4
D.3. 128-State NRS Filter (a) East Velocity (b) North Velocity and (c) Vertical Velocity Errors.	D-5
D.4. 128-State NRS Filter (a) East Tilt (b) North Tilt and (c) Azimuth Errors.	D-6
D.5. 128-State NRS Filter (a) Lagged Altitude (b) Del S3 and (c) Baro-Altimeter Errors.	D-7
D.6. 128-State NRS Filter (a) RRS Range Bias (b) RRS Vel Bias and (c) T1 Atmosphere Errors.	D-8

Figure	Page
D.7. 128-State NRS Filter (a) T1 X Position (b) T1 Y Position and (c) T1 Z Position Errors.	D-9
D.8. 128-State NRS Filter (a) User Clock Bias (b) User Clock Drift and (c) SV1 Code Loop Errors.	D-10
D.9. 128-State NRS Filter (a) SV1 Troposphere (b) SV1 Ionosphere and (c) SV1 Clock Errors.	D-11
D.10. 128-State NRS Filter (a) SV1 X Position (b) SV1 Y Position and (c) SV1 Z Position Errors.	D-12
E.1. 2-Hour Fighter Flight Profile (a) Latitude (b) Longitude and (c) Altitude	E-2
E.2. 97-State NRS Filter (a) Latitude (b) Longitude and (c) Altitude Errors.	E-3
E.3. 97 State NRS Filter (a) East Velocity (b) North Velocity and (c) Vertical Velocity Errors.	E-4
E.4. 97-State NRS Filter (a) East Tilt (b) North Tilt and (c) Azimuth Errors.	E-5
E.5. 97-State NRS Filter (a) Lagged Altitude (b) Del S3 and (c) Baro-Altimeter Errors.	E-6
E.6. 97-State NRS Filter (a) RRS Range Bias (b) RRS Vel Bias and (c) T1 Atmosphere Errors.	E-7
E.7. 97-State NRS Filter (a) T1 X Position (b) T1 Y Position and (c) T1 Z Position Errors.	E-8
E.8. 97-State NRS Filter (a) User Clock Bias (b) User Clock Drift and (c) SV1 Code Loop Errors.	E-9
E.9. 97-State NRS Filter (a) SV1 Troposphere (b) SV1 Ionosphere and (c) SV1 Clock Errors.	E-10
E.10. 97-State NRS Filter (a) SV1 X Position (b) SV1 Y Position and (c) SV1 Z Position Errors.	E-11
F.1. 2-Hour Fighter Flight Profile (a) Latitude (b) Longitude and (c) Altitude	F-2

Figure	Page
F.2. 69-State NRS Filter (a) Latitude (b) Longitude and (c) Altitude Errors.	F-3
F.3. 69-State NRS Filter (a) East Velocity (b) North Velocity and (c) Vertical Velocity Errors.	F-4
F.4. 69-State NRS Filter (a) East Tilt (b) North Tilt and (c) Azimuth Errors.	F-5
F.5. 69-State NRS Filter (a) Lagged Altitude (b) Del S3 and (c) Baro-Altitude Errors.	F-6
F.6. 69-State NRS Filter (a) RRS Range Bias (b) RRS Vel Bias and (c) T1 Atmosphere Errors.	F-7
F.7. 69-State NRS Filter (a) T1 X Position (b) T1 Y Position and (c) T1 Z Position Errors.	F-8
F.8. 69-State NRS Filter (a) User Clock Bias and (b) User Clock Drift Errors.	F-9
G.1. 2-Hour Fighter Flight Profile (a) Latitude (b) Longitude and (c) Altitude	G-2
G.2. 89-State ENRS Filter (a) Latitude (b) Longitude and (c) Altitude Errors.	G-3
G.3. 89-State ENRS Filter (a) East Velocity (b) North Velocity and (c) Vertical Velocity Errors.	G-4
G.4. 89-State ENRS Filter (a) East Tilt (b) North Tilt and (c) Azimuth Errors.	G-5
G.5. 89-State ENRS Filter (a) Lagged Altitude (b) Del S3 and (c) Baro-Altitude Errors.	G-6
G.6. 89-State ENRS Filter (a) RRS Range Bias (b) RRS Vel Bias and (c) T1 Atmosphere Errors.	G-7
G.7. 89-State ENRS Filter (a) T1 X Position (b) T1 Y Position and (c) T1 Z Position Errors.	G-8
G.8. 89-State ENRS Filter (a) User Clock Bias and (b) User Clock Drift Errors.	G-9

Figure	Page
G.9. 89-State ENRS Filter (a) SV1 Troposphere and (b) SV1 Ionosphere Errors.	G-10
G.10.89-State ENRS Filter (a) SV1 X Position (b) SV1 Y Position and (c) SV1 Z Position Errors.	G-11
H.1. 2-Hour Fighter Flight Profile (a) Latitude (b) Longitude and (c) Altitude	H-2
H.2. 48-State ENRS Filter (a) Latitude (b) Longitude and (c) Altitude Errors.	H-3
H.3. 48-State ENRS Filter (a) East Velocity (b) North Velocity and (c) Vertical Velocity Errors.	H-4
H.4. 48-State ENRS Filter (a) East Tilt (b) North Tilt and (c) Azimuth Errors.	H-5
H.5. 48-State ENRS Filter (a) Lagged Altitude (b) Del S3 and (c) Baro-Altimeter Errors.	H-6
H.6. 48-State ENRS Filter (a) RRS Range Bias (b) RRS Vel Bias and (c) T1 Atmosphere Errors.	H-7
H.7. 48-State ENRS Filter (a) T1 X Position (b) T1 Y Position and (c) T1 Z Position Errors.	H-8
H.8. 48-State ENRS Filter (a) User Clock Bias and (b) User Clock Drift Errors.	H-9
I.1. 2-Hour Fighter Flight Profile (a) Latitude (b) Longitude and (c) Altitude	I-2
I.2. 22-State DGPS Filter, Fighter Flight Profile (a) Latitude (b) Longitude and (c) Altitude Errors.	I-3
I.3. 22-State DGPS Filter, Fighter Flight Profile (a) East Velocity (b) North Velocity and (c) Vertical Velocity Errors.	I-4
I.4. 22-State DGPS Filter, Fighter Flight Profile (a) East Tilt (b) North Tilt and (c) Azimuth Errors.	I-5
I.5. 22-State DGPS Filter, Fighter Flight Profile (a) Lagged Altitude (b) Del S3 and (c) Baro-Altimeter Errors.	I-6

Figure	Page
I.6. 22-State DGPS Filter, Fighter Flight Profile (a) User Clock Bias and (b) User Clock Drift Errors.	I-7
I.7. 2-Hour Straight Flight Profile (a) Latitude (b) Longitude and (c) Altitude	I-8
I.8. 22-State DGPS Filter, Straight Flight Profile (a) Latitude (b) Longitude and (c) Altitude Errors.	I-9
I.9. 22-State DGPS Filter, Straight Flight Profile (a) East Velocity (b) North Velocity and (c) Vertical Velocity Errors.	I-10
I.10. 22-State DGPS Filter, Straight Flight Profile (a) East Tilt (b) North Tilt, and (c) Azimuth Errors.	I-11
I.11. 22-State DGPS Filter, Straight Flight Profile (a) Lagged Altitude (b) Del S3 and (c) Baro-Altimeter Errors.	I-12
I.12. 22-State DGPS Filter, Straight Flight Profile (a) User Clock Bias and (b) User Clock Drift Errors.	I-13
J.1. 2-Hour Fighter Flight Profile (a) Latitude (b) Longitude and (c) Altitude	J-2
J.2. 46-State CIRIS Filter, Fighter Flight Profile (a) Latitude (b) Longitude and (c) Altitude Errors.	J-3
J.3. 46-State CIRIS Filter, Fighter Flight Profile Filter (a) East Velocity (b) North Velocity, and (c) Vertical Velocity Errors.	J-4
J.4. 46-State CIRIS Filter, Fighter Flight Profile Filter (a) East Tilt (b) North Tilt and (c) Azimuth Errors.	J-5
J.5. 46-State CIRIS Filter, Fighter Flight Profile Filter (a) Lagged Altitude (b) Del S3 and (c) Baro-Altimeter Errors.	J-6
J.6. 46-State CIRIS Filter, Fighter Flight Profile Filter (a) RRS Range Bias (b) RRS Vel Bias and (c) T1 Atmosphere Errors.	J-7
J.7. 46-State CIRIS Filter, Fighter Flight Profile Filter (a) T1 X Position (b) T1 Y Position and (c) T1 Z Position Errors.	J-8
J.8. 2-Hour Racetrack Flight Profile (a) Latitude (b) Longitude and (c) Altitude	J-9

Figure	Page
J.9. 46-State CIRIS Filter, Racetrack Flight Profile (a) Latitude (b) Longitude and (c) Altitude Errors.	J-10
J.10. 46-State CIRIS Filter, Racetrack Flight Profile Filter (a) East Velocity (b) North Velocity and (c) Vertical Velocity Errors.	J-11
J.11. 46-State CIRIS Filter, Racetrack Flight Profile Filter (a) East Tilt (b) North Tilt and (c) Azimuth Errors.	J-12
J.12. 46-State CIRIS Filter, Racetrack Flight Profile Filter (a) Lagged Altitude (b) Del S3 and (c) Baro-Altitude Errors.	J-13
J.13. 46-State CIRIS Filter, Racetrack Flight Profile Filter (a) RRS Range Bias (b) RRS Vel Bias and (c) T1 Atmosphere Errors.	J-14
J.14. 46-State CIRIS Filter, Racetrack Flight Profile Filter (a) T1 X Position (b) T1 Y Position and (c) T1 Z Position Errors.	J-15
K.1. 2-Hour Fighter Flight Profile (a) Latitude (b) Longitude and (c) Altitude	K-2
K.2. 48-State ENRS Filter (a) Latitude (b) Longitude and (c) Altitude Errors.	K-3
K.3. 48-State ENRS Filter (a) East Velocity (b) North Velocity and (c) Vertical Velocity Errors.	K-4
K.4. 48-State ENRS Filter (a) East Tilt (b) North Tilt and (c) Azimuth Errors.	K-5
K.5. 48-State ENRS Filter (a) Lagged Altitude (b) Del S3 and (c) Baro-Altitude Errors.	K-6
K.6. 48-State ENRS Filter (a) RRS Range Bias (b) RRS Vel Bias and (c) T1 Atmosphere Errors.	K-7
K.7. 48-State ENRS Filter (a) T1 X Position (b) T1 Y Position and (c) T1 Z Position Errors.	K-8
K.8. 48-State ENRS Filter (a) User Clock Bias and (b) User Clock Drift Errors.	K-9

List of Tables

Table	Page
5.1. Temporal Average of the Ensemble Average of True Errors for Stacey's 128 Error-State Filter	5-4
5.2. Temporal Average of the Ensemble Average of True Errors for 128- and 97-State NRS Filters	5-5
5.3. Temporal Average of the Ensemble Average of True Errors for NRS Filters	5-6
5.4. Temporal Average of the Ensemble Average of True Errors for NRS and 89-State ENRS Filters	5-8
5.5. Temporal Average of the Ensemble Average of True Errors for NRS, 89-State ENRS, and 48-State ENRS Filters	5-10
5.6. Temporal Average of the Ensemble Average of True Errors for Previous and 22-State DGPS (Velocity Aiding) Filters	5-11
5.7. Temporal Average of the Ensemble Average of True Errors for Previous and 46-State CIRIS (Velocity Aiding) Filters	5-13
5.8. Temporal Average of the Ensemble Average of True Errors for All Filters	5-14
5.9. INS States Tuning Parameters $Q(t)$	5-15
5.10. RRS States Tuning Parameters $Q(t)$	5-16
5.11. GPS States Tuning Parameters $Q(t)$	5-17
5.12. DGPS States Tuning Parameters $Q(t)$	5-17
5.13. GPS/DGPS Measurement Noise Variance Tuning Parameters $R(t_i)$	5-18
A.1. INS System Model: INS States 1 \rightarrow 29	A-3
A.2. INS System Model: INS States 30 \rightarrow 47	A-4
A.3. INS System Model: INS States 48 \rightarrow 69	A-5
A.4. INS System Model: INS States 70 \rightarrow 93	A-6

Table	Page
A.5. RRS Error States	A-7
A.6. GPS Error States	A-8
A.7. Reduced-Order INS System Model: INS States 1 → 20	A-9
A.8. Reduced-Order INS System Model: INS States 21 → 41	A-10
A.9. DGPS Error States	A-11
B.1. Elements of the Dynamics Submatrix F_{11}	B-2
B.2. Elements of the Dynamics Submatrix F_{12}	B-3
B.3. Elements of the Dynamics Submatrix F_{13}	B-3
B.4. Elements of the Dynamics Submatrix F_{14}	B-4
B.5. Elements of the Dynamics Submatrix F_{15}	B-4
B.6. Elements of the Dynamics Submatrix F_{16}	B-5
B.7. Elements of the Dynamics Submatrix F_{22}	B-5
B.8. Elements of the Dynamics Submatrix F_{55}	B-5
B.9. Non-zero Elements of Process Noise Submatrix Q_{11}	B-6
B.10. Non-zero Elements of Process Noise Submatrix Q_{22}	B-6

List of Symbols

Symbol	Page
$f[\mathbf{x}(t), t]$	2-1
$\mathbf{x}(t)$	2-1
t	2-1
$\mathbf{G}(t)$	2-1
\mathbf{I}	2-1
$\mathbf{w}(t)$	2-1
$\mathbf{Q}(t)$	2-2
$\mathbf{z}(t_i)$	2-2
$\mathbf{v}(t_i)$	2-2
$\mathbf{x}_n(t)$	2-2
$f[\mathbf{x}_n(t), t]$	2-2
$\delta\mathbf{x}(t)$	2-3
$\mathbf{F}[t; \mathbf{x}_n(t)]$	2-3
$f[\mathbf{x}(t), t]$	2-3
$\mathbf{x}_n(t)$	2-3
$\mathbf{R}(t_i)$	2-8
$\delta\mathbf{x}_1$	3-2
$\delta\mathbf{x}_2$	3-2
$\delta\mathbf{x}_3$	3-2
$\delta\mathbf{x}_4$	3-2
$\delta\mathbf{x}_5$	3-2
$\delta\mathbf{x}_6$	3-2
$\mathbf{F}(t)$	3-3
S_{INS}	3-4

Symbol	Page
x_{br}	3-5
x_{bv}	3-5
i	3-6
τ	3-6
R^3	3-8
x_{Uclk_b}	3-11
x_{Uclk_d}	3-11
R_p	3-13
c	3-13
t_e	3-13
X_s	3-15
x_{Uclk_b}	4-4
x_{Uclk_d}	4-4
\dot{R}_{DGPS}	4-9
\dot{R}_t	4-9
\dot{R}_{RRS}	4-13
\dot{R}_t	4-13

Abstract

To quantify the performance abilities of existing or proposed navigation systems, the U.S. Air Force has, for the last several years, compared the performance of the system under test to the performance of a *baseline* navigation system known as the Completely Integrated Reference Instrumentation System (CIRIS). CIRIS obtains a highly accurate navigation solution by combining information from three major subsystems: inertial navigation system (INS) information, barometric altitude information, and range and range-rate information from ground transponders which have been precisely surveyed. Although the navigation solution produced by CIRIS is highly accurate, it will soon be inadequate as the standard against which future navigation systems can be tested. This research proposes an alternative to CIRIS - a hybrid Enhanced Navigation Reference System (ENRS) which is designed to take advantage of a newer INS (the LN-93), certain features of the current CIRIS, and certain features of differential corrections to Global Positioning System (DGPS) measurements. Analysis is conducted using a Kalman filter development package known as the Multimode Simulation for Optimal Filter Evaluation (MSOFE). Both a large order *truth* model for the ENRS (in which a full 24 satellite constellation is modeled) and full- and reduced-order Kalman filters are developed. Results suggest that the proposed ENRS (with DGPS aiding) provides a navigation solution one order of magnitude better than CIRIS.

INCORPORATION OF DIFFERENTIAL GLOBAL
POSITIONING SYSTEM MEASUREMENTS
USING AN EXTENDED KALMAN FILTER
FOR IMPROVED REFERENCE
SYSTEM PERFORMANCE

I. Introduction

The Completely Integrated Reference Instrumentation System (CIRIS) is a transponder aided Inertial Navigation System (INS) test reference currently used by the Air Force for the development and testing of new aircraft navigation systems (20:1-1). The Office of Primary Responsibility (OPR) for the CIRIS system is the Central Inertial Guidance Test Facility (CIGTF), 6585th Test Group, Air Force Systems Command (AFSC), Holloman AFB, NM. The operation of CIRIS involves flying the INS to be tested, referred to as the test article, and CIRIS through an aircraft trajectory of interest across a CIRIS transponder range. The data from each system is recorded during the flight and compared to analyze how well the test article performed. Up to this point in time, CIRIS was considered more accurate than the test articles and formed the baseline for determining the performance of aircraft INSs.

1.1 Background

CIRIS determines the aircraft's latitude and longitude with a 1σ accuracy of 13 feet(ft) horizontal and 40 ft vertical; the north and west velocity to 0.1 ft/sec (fps) 1σ ; and the vertical velocity to 0.4 fps 1σ (20:1-1). This accuracy is due to the

Range/Range-Rate System (RRS) transponder aiding (8, 9). Recently, there have been a few state-of-the-art aircraft INSs developed (and many more in the design stage) approaching the accuracy of CIRIS. Interestingly, many of these new INSs use the Global Positioning System (GPS) to increase their accuracy. In order to use CIRIS as a baseline against these new INSs, CIRIS must be enhanced to provide an order of magnitude more accurate navigation solution.

1.2 Problem Definition

By using Differential Global Positioning System (DGPS) measurements to augment the navigation solution of CIRIS, it should be possible to increase the accuracy of CIRIS to produce an order of magnitude better estimate of the navigation solution. *Specifically, this thesis concentrates on developing a post-processing Extended Kalman Filter (EKF) of 70 states or less to augment the CIRIS navigation solution with DGPS pseudorange and delta-range measurements.* An EKF is developed instead of a smoother due to the limited computer storage capacity available. The EKF is limited to 70 states or less to ensure 24 hour turn-around time for post-processing real measurements during INS testing at CIGTF. Pseudorange and delta-range measurements are explained in detail in the DGPS sections of Chapter IV.

1.2.1 Summary of Effort. The Navigation Reference System (NRS) filter Stacey designed (22) is tuned by Monte Carlo analysis and its performance relative to CIRIS is analyzed. A 41 error-state reduced-order INS filter model is developed based on the recommendations of Lewantowicz and Keen (10). 97- and 69-state NRS filter models are evaluated and compared to Stacey's NRS filter and CIRIS. A DGPS error model is developed and augmented to the INS and RRS error models to form the 89-state Enhanced Navigation Reference System (ENRS) truth and filter models. Finally, a reduced-order ENRS filter of 48 error-states incorporating delta-range and range-rate measurements is designed, developed, and compared to the NRS and CIRIS.

1.3 Summary of Previous Research

Previous research at AFIT by Captains Joe Solomon (GE-89M), Britt Snodgrass (GE-90M), and Richard Stacey (GE-91M) focused on improving CIRIS performance (20, 21, 19, 22). Solomon modified the CIRIS error model, produced an extended Kalman filter designed to enhance CIRIS performance (20), and performed preliminary work on the GPS error-state model (21). Snodgrass evaluated and modified Solomon's filter design (19). Stacey augmented the LN-93 baro-altimeter model, implemented a reduced-order INS error model, designed high order CIRIS/GPS truth and filter models, and developed a Kalman filter to integrate GPS pseudorange measurements into CIRIS (22).

Capt Solomon concentrated his effort on designing an improved Kalman filter for CIRIS (20). He used an 85-state truth model for the LN-39 INS and 42 states to model 10 RRS transponders for a total of 127 states in his full-state truth model. He designed a 127-state Kalman filter using this design and verified its performance using actual CIRIS flight data. He then developed a reduced-order 70-state Kalman filter which performed as well as the full-order filter but required much less computational time to implement. In a special study, Solomon designed a 28-state error model for the GPS system assuming stationary satellites (21). Solomon never developed an integrated CIRIS/GPS filter.

Capt Snodgrass continued the development of Solomon's 70-state reduced-order filter (19). He improved the filter software by modifying the structure of the source code, making it easier to change filter parameters, thus increasing its efficiency and capabilities. He then tuned various filter parameters which improved filter performance. Finally, he designed a fixed-interval smoothing algorithm to use as a post-processor to generate the optimal reference trajectory. Snodgrass was never able to evaluate his smoother due to limitations in time and computer memory.

Capt Stacey returned to a 93-state truth model for the INS in his thesis when he incorporated the error-model for a Litton LN-93 INS (11) instead of the LN-39

INS used by Solomon and Snodgrass (20, 19, 22). He increased this to a 96-state model through improvement of the baro-altimeter model by using a four-state model instead of a one-state model. He then designed a 72-state reduced-order INS model and filter to reduce computational times. He augmented this reduced-order model with 26 RRS transponder error-states and 30 GPS error-states for a 128-state truth and filter model. He completed one simulation run with this model, referred to as the Navigation Reference System. It is important to note Stacey never implemented GPS delta-range or RRS range-rate measurement equations in his research.

1.4 Research Objectives

This research finishes developing the NRS filter started by Stacey. The full-order Kalman filter is analyzed and the performance increase over CIRIS is characterized. Then both the truth and filter models are reduced by decreasing the 72-state INS model to 41 states, thus decreasing the full-order truth and filter models to 97 states from Stacey's 128 states. This decrease is necessary for a timely completion of this thesis and matches the results of the higher order truth and filter models developed by Stacey (22).

An Enhanced Navigation Reference System (ENRS) is then developed. The ENRS augments standard CIRIS with DGPS *pseudorange* and *delta-range* measurements. The ENRS is evaluated against the NRS as well as CIRIS to show the performance increase available from augmenting CIRIS with DGPS measurements. By increasing accuracy using the ENRS, the position and velocity estimates are more accurate than the current CIRIS's navigation solution.

The following objectives are based on the statement of the problem as presented in the previous sections.

1. Perform 10-run Monte Carlo analysis on the 128-state NRS filter designed by Stacey (22). Compare these results to CIRIS performance and show the increment in

performance possible with the NRS. This analysis completes the work Stacy started on this full-order filter and completes all of the stated objectives in his thesis.

2. Decrease both the truth and filter models of the INS down to 41 states from the 72 states Stacey implemented. Show this reduced state truth model calculates position, velocity, and attitude error-states with no discernible difference from the 93 error-state INS model (one baro-state) but reduces computational times greatly.

3. Develop a new full-order NRS EKF incorporating the above reduced-state INS truth model. This 97-error-state filter's performance is compared to CIRIS as well as Stacey's 128-error-state NRS filter. This proves that the navigation solution accuracy of CIRIS can be improved with the incorporation of GPS pseudorange measurements. A 69-error-state reduced-order NRS filter is implemented and its performance compared to CIRIS, Stacey's NRS filter, and the 97-state full-order NRS filter.

4. Develop a DGPS error-state truth model. This model is similar to the GPS truth model but produces less variance in the position estimates due to removal of most of the atmospheric and ephemeris errors and elimination of the space vehicle (SV) clock errors (1, 5, 18).

5. Design and implement an ENRS EKF using the above DGPS truth model and the CIRIS truth model which has been previously developed (20, 19, 22). This 89-state full-order filter differs from the 97-state NRS filter only by a change in the GPS states due to implementation of a DGPS model. The performance of the ENRS filter is compared to CIRIS and to the NRS filters to show the position accuracy improvement possible with the incorporation of DGPS pseudorange measurements. Then a 48-error-state reduced-order ENRS filter is developed to reduce computational times

while maintaining accuracy. Its performance is compared to CIRIS, Stacey's NRS filter, and the 97- and 69-error-state NRS filters described above.

6. Design and implement DGPS *delta-range* and RRS *range-rate* measurements into the 89-state ENRS truth model and the 48-state ENRS filter to improve the velocity error estimation. Show the velocity estimates with this filter are more accurate than CIRIS and the 48-state filter above having no velocity measurements.

7. Compare the accuracy of the 48-state ENRS filter to all previous filters. This comparison shows the reduced-order ENRS filter with delta-range and range-rate measurements outperforms all the NRS filters and has an order of magnitude increase in position-error accuracy and an increase in velocity-error accuracy over the CIRIS navigation solution.

1.5 Research Approach

Before any filter analysis can be accomplished, the Multimode Simulation for Optimal Filter Evaluation (MSOFE) software package must be thoroughly understood (3). MSOFE, as used in this thesis, propagates and updates the EKF and also propagates the truth model of the system. As in Stacey's thesis, a two-hour fighter flight profile is used to generate the truth model for each analysis (22). Once MSOFE is mastered, filter evaluation and tuning is accomplished. Chapter II contains an overview of the EKF and also describes filter order reduction and tuning. The remainder of this section gives a brief overview of the approach to completing each of the research objectives outlined in the previous section.

1. Stacey's truth and filter model is evaluated using 10-run Monte-Carlo analysis and the NRS filter performance is compared to CIRIS to show the increase in

navigation solution accuracy possible by incorporating GPS pseudorange measurements into CIRIS. Stacey's NRS truth and filter models are described in Chapter III and the results are analyzed in Chapter V.

2. Stacey's truth and filter models are based on 128 error-states. It presently takes over 18 hours for a single MSOFE one-run analysis to be completed for a 2-hour simulated fighter flight trajectory. A 10-run Monte Carlo analysis is considered the minimum which should be completed before any reasonable estimate of filter performance can be evaluated. Decreasing the INS truth model from 72 states to 41 states allows a 10-run analysis to be completed in only 4 days. However, for the 41-state INS model to be considered adequate, it must provide a true navigation solution as accurate as the full LN-93 93-state INS truth model. Using MSOFE and the recommendations of Lewantowicz and Keen, the 41-state INS truth model is evaluated against the 93-state INS truth model showing almost identical performance (10). The reduction of INS states is explained in Chapter III with results in Chapter V.

3. Once the INS truth model is reduced, new full-order 97 error-state NRS truth and filter models are developed. A 10-run Monte Carlo analysis is performed on the filter and the results are compared to CIRIS and Stacey's NRS filter. Since four days is still a long time to wait for results and the objective of this thesis is to develop a filter of less than 70 states, a 69-state reduced-order filter is implemented by eliminating all but two GPS error-states (the receiver clock states). This filter completes a 10-run Monte-Carlo analysis in 36 hours, but with proper tuning (see Chapter II) produces a navigation solution just as accurate as Stacey's NRS filter or the 97-state NRS filter described above. The work in this section provides a baseline to analyze how well the DGPS model performs. The filter reduction is explained in detail in Chapter III with the analysis of filter performance presented in Chapter V.

4. The DGPS model is very similar to the GPS model developed by Stacey. The differences lie in the fact that the SV's clock error is totally eliminated while the atmospheric and SV ephemeris errors are greatly reduced. A complete discussion of DGPS as well as a detailed analysis of the 22 error-states which make up the DGPS error model are given in Chapter IV.

5. The 89-state truth and filter models in the full-order ENRS are only different from the 97-state NRS models discussed above by the change in the number of GPS error-states when using DGPS. A 10-run Monte Carlo analysis is performed and the results discussed in Chapter IV. Then, in order to meet the 70-filter-state requirement and reduce the 10-run time to less than one day, a 48-state filter model is implemented by again eliminating all but two of the DGPS error-states (the two clock states) and 21 more INS states according to the recommendation of Lewantowicz and Keen (10). This 48-state filter is discussed in Chapter IV with the filter results presented in Chapter V.

6. DGPS delta-range and RRS range-rate measurements are both needed if the velocity error estimates of the ENRS filter are to be more accurate than CIRIS which uses range-rate measurements alone for velocity aiding. The theory presented behind delta-range and range-rate measurements is given in Chapter IV. A DGPS-INS filter of 22 error-states (no RRS) and RRS-INS filter of 46 error-states (no DGPS) are used to tune the velocity aiding measurements separately for optimal performance using a 10-run Monte Carlo analysis. The results of these two filters are presented in Chapter V.

7. Finally, delta-range and range-rate measurements are incorporated into the 48-state ENRS filter to complete the ENRS. A 25-run Monte Carlo analysis is performed

for a final comparison against all previously discussed filters. The results of this comparison are presented in Chapter V.

1.6 Assumptions

Because of the lack of performance of Stacey's 4-state baro-altimeter model, the Litton 93-state error model using one baro-altimeter state is considered the true error model of the INS subsystem of CIRIS. The 41-state error model implemented as truth in this thesis is shown to be a very close approximation to the 93-state LN-93 error model. Snodgrass's RRS error model is used as the truth model for the RRS subsystem as it was implemented in Stacey's thesis (19, 22). Finally, Stacey's GPS error model derived from articles by Cox (4), Martin (12), and Milliken and Zoller (17) is considered adequate to use as a starting point for the DGPS subsystem for the ENRS.

1.7 Overview of Thesis

Chapter II provides a brief description of the EKF theory used in this thesis. Filter order reduction and tuning are also presented. Chapter III overviews the NRS developed by Stacey. An explanation of the procedure used in reducing the INS error-state model from 72 to 41 states is given. The 97-state NRS truth and filter models and the 69-state reduced-order filter model are explained. Chapter IV begins with an explanation of the ENRS. DGPS principles and error-states are presented. Detailed analysis of the DGPS full-state truth and filter models are shown along with the development of the reduced-order ENRS EKF and the delta-range and range-rate measurement equations. Chapter V discusses the results of all the Monte Carlo analyses of the above EKFs. Chapter VI contains the conclusions drawn from the work presented in this thesis. A summation of the overall performance of the NRS and ENRS filters is given. Recommendations for further research in this area are also addressed.

II. *Extended Kalman Filtering*

2.1 *Overview*

This chapter refamiliarizes the informed reader with the extended Kalman filter (EKF) dynamics, measurement, propagation and update equations as they pertain to this thesis, and discusses filter state reduction and tuning. The reader who is not familiar with Kalman filtering is directed to Maybeck's textbooks on stochastic control in which robust derivations of the EKF equations and discussions of state reduction and filter tuning are presented (14, 15, 16).

2.2 *The Extended Kalman Filter*

When both the dynamics and measurement equations of a system of interest are constructed using a *linear* combination of the states modeled, a linear Kalman filter can be developed. However, the error-state model for this research is not a linear function of the error-states in either the dynamics or measurement equations. Because of this, a linearized Kalman filter of some form must be used. The linearized Kalman filter implemented here is the *extended* Kalman filter, which allows relinearization at each measurement update time. The equations describing the EKF used in this research are derived from a nonlinear continuous-time dynamics equation (14):

$$\dot{\mathbf{x}}(t) = \mathbf{f}[\mathbf{x}(t), t] + \mathbf{G}(t)\mathbf{w}(t) \quad (2.1)$$

In this case, the state dynamics matrix $\mathbf{f}[\mathbf{x}(t), t]$ is a nonlinear function of the state vector $\mathbf{x}(t)$ and time t . For this thesis, $\mathbf{G}(t) = \mathbf{I}$ and the white Gaussian noise $\mathbf{w}(t)$ is defined with mean:

$$\mathbf{m}_{\mathbf{w}} = E\{\mathbf{w}(t)\} = \mathbf{0} \quad (2.2)$$

and noise strength $Q(t)$ of:

$$E \{ \mathbf{w}(t) \mathbf{w}^T(t + \tau) \} = \mathbf{Q}(t) \delta(\tau) \quad (2.3)$$

In addition, the discrete-time measurement equations $\mathbf{z}(t_i)$ are also a nonlinear function of the state vector and time (15):

$$\mathbf{z}(t_i) = \mathbf{h}[\mathbf{x}(t_i), t_i] + \mathbf{v}(t_i) \quad (2.4)$$

The discrete-time noise vector $\mathbf{v}(t_i)$ is also *zero-mean* and its covariance is described by:

$$E \{ \mathbf{v}(t_i) \mathbf{v}^T(t_j) \} = \begin{cases} \mathbf{R}(t_i) & \text{for } t_i = t_j \\ \mathbf{0} & \text{for } t_i \neq t_j \end{cases} \quad (2.5)$$

A system must be linear in order for the Kalman filter to yield the "optimal" state estimates, so the nonlinear Equations (2.1) and (2.4) are linearized by the method given in Mayock's Volume II (15). A nominal state trajectory, $\mathbf{x}_n(t)$ is generated satisfying $\mathbf{x}_n(t_0) = \mathbf{x}_{n_0}$ and

$$\dot{\mathbf{x}}_n(t) = \mathbf{f}[\mathbf{x}_n(t), t] \quad (2.6)$$

where $\mathbf{f}[\mathbf{x}_n(t), t]$ is specified in Equation (2.1). The nominal measurements are defined as:

$$\mathbf{z}_n(t_i) = \mathbf{h}[\mathbf{x}_n(t_i), t_i] \quad (2.7)$$

The "perturbation" of the states are obtained by subtracting the nominal trajectory (Equation (2.6)) from the original nonlinear dynamics equation (Equation (2.1)):

$$[\dot{\mathbf{x}}(t) - \dot{\mathbf{x}}_n(t)] = \mathbf{f}[\mathbf{x}(t), t] - \mathbf{f}[\mathbf{x}_n(t), t] + \mathbf{G}(t)\mathbf{w}(t) \quad (2.8)$$

The equation above is approximated to first order by a Taylor series expansion:

$$\delta \dot{\mathbf{x}}_n(t) = \mathbf{F}[t; \mathbf{x}_n(t)] + \mathbf{G}(t)\mathbf{w}(t) \quad (2.9)$$

where $\delta\mathbf{x}(t)$ represents a first-order approximation of the process $[\mathbf{x}(t) - \mathbf{x}_n(t)]$, and $\mathbf{F}[t; \mathbf{x}_n(t)]$ is a matrix of partial derivatives of $\mathbf{f}[\mathbf{x}(t), t]$ with respect to $\mathbf{x}(t)$ evaluated along the nominal trajectory $\mathbf{x}_n(t)$ (15):

$$\mathbf{F}[t; \mathbf{x}_n(t)] = \left. \frac{\partial \mathbf{f}[\mathbf{x}(t), t]}{\partial \mathbf{x}} \right|_{\mathbf{x}=\mathbf{x}_n(t)} \quad (2.10)$$

The perturbed discrete-time measurement equation is derived in like fashion and is expressed as (15):

$$\delta z_n(t_i) = \mathbf{H}[t_i; \mathbf{x}_n(t_i)] + \mathbf{v}(t_i) \quad (2.11)$$

where

$$\mathbf{H}[t_i; \mathbf{x}_n(t_i)] = \left. \frac{\partial \mathbf{h}[\mathbf{x}(t_i), t_i]}{\partial \mathbf{x}} \right|_{\mathbf{x}=\mathbf{x}_n(t_i)} \quad (2.12)$$

The nonlinear continuous-time dynamics and discrete-time measurement equations have now been successfully converted to linearized "error-state" equations. Estimates of the whole-valued quantities of interest are calculated from (15):

$$\hat{\mathbf{x}}(t) = \mathbf{x}_n(t) + \delta \hat{\mathbf{x}}(t) \quad (2.13)$$

The expression above for the linearized Kalman filter is useful provided that the linearization assumption is not violated. However, if the nominal and "true" trajectories differ by too large an amount, unacceptable errors may result (15). It is for this reason that extended Kalman filtering is useful in many cases where perturbation techniques alone do not suffice. Extended Kalman filtering allows for *relinearizing* about newly declared nominals at each sample time, to enhance the adequacy of the linearization process, and thus of the resulting filter performance as well. (22)

Discrete-time measurements are incorporated into the EKF by the following state equations (15):

$$\mathbf{K}(t_i) = \mathbf{P}(t_i^-) \mathbf{H}^T[(t_i); \hat{\mathbf{x}}(t_i^-)] \left\{ \mathbf{H}[(t_i); \hat{\mathbf{x}}(t_i^-)] \mathbf{P}(t_i^-) \mathbf{H}^T[(t_i); \hat{\mathbf{x}}(t_i^-)] + \mathbf{R}(t_i) \right\}^{-1} \quad (2.14)$$

$$\hat{\mathbf{x}}(t_i^+) = \hat{\mathbf{x}}(t_i^-) + \mathbf{K}(t_i) \{ \mathbf{z}_i - \mathbf{h}[\hat{\mathbf{x}}(t_i^-); (t_i)] \} \quad (2.15)$$

$$\mathbf{P}(t_i^+) = \mathbf{P}(t_i^-) - \mathbf{K}(t_i) \mathbf{H}[(t_i); \hat{\mathbf{x}}(t_i^-)] \mathbf{P}(t_i^-) \quad (2.16)$$

where

$$\mathbf{H}[(t_i); \hat{\mathbf{x}}(t_i^-)] = \left. \frac{\partial \mathbf{h}[\mathbf{x}(t_i), t_i]}{\partial \mathbf{x}} \right|_{\mathbf{x}=\hat{\mathbf{x}}(t_i^-)} \quad (2.17)$$

The state estimate and covariance are propagated from t_i to t_{i+1} by integrating the following equations (15):

$$\dot{\hat{\mathbf{x}}}(t/t_i) = \mathbf{f}[\hat{\mathbf{x}}(t/t_i), t] \quad (2.18)$$

$$\dot{\mathbf{P}}(t/t_i) = \mathbf{F}[t; \hat{\mathbf{x}}(t/t_i)] \mathbf{P}(t/t_i) + \mathbf{P}(t/t_i) \mathbf{F}^T[t; \hat{\mathbf{x}}(t/t_i)] + \mathbf{G}(t) \mathbf{Q}(t) \mathbf{G}^T(t) \quad (2.19)$$

where

$$\mathbf{F}[t; \hat{\mathbf{x}}(t/t_i)] = \left. \frac{\partial \mathbf{f}[\mathbf{x}(t), t]}{\partial \mathbf{x}} \right|_{\mathbf{x}=\hat{\mathbf{x}}(t/t_i)} \quad (2.20)$$

and the initial conditions are:

$$\hat{\mathbf{x}}(t_i/t_i) = \hat{\mathbf{x}}(t_i^+) \quad (2.21)$$

$$\mathbf{P}(t_i/t_i) = \mathbf{P}(t_i^+) \quad (2.22)$$

The EKF equations given are programmed in MSOFE for optimal error-state determination. It is important to point out MSOFE uses the U-D Factored form of the update and propagation equations (3). A complete development of linear and linearized/extended Kalman filters is given by Maybeck's Volumes 1 and 2, respectively (14, 15). An extensive explanation of Kalman filtering as it pertains to this research is given in Chapter II of Stacey's thesis, and the information presented in this section is paraphrased from it (22).

2.3 Filter Order Reduction

When an engineer is faced with the task of designing a Kalman filter for a system with a large state vector, it sometimes becomes desirable or necessary to decrease the number of states modeled in the filter, often referred to as "filter order reduction." How and why the filter is to be utilized are important considerations in setting the final number of states modeled. As an example, a filter which is implemented off-line on a large mainframe or supercomputer can include a larger number of filter states than a filter implemented on an 8-bit aircraft navigation computer operating real-time to estimate INS position and velocity errors. Even in the case of this thesis, where a post-processing filter is developed to run off-line on a Hewlett-Packard minicomputer, time considerations limit the filter to less than 70 states (a 10-run Monte Carlo analysis of a 2-hour flight trajectory must be completed in 24 hours or less). Proper choice of states from the truth model is critical to ensure accurate position and velocity error estimates. The next few paragraphs offer some general recommendations for filter order reduction with a bias toward the work performed in this thesis.

A good starting point for filter order reduction is determining which states *cannot* be eliminated. For example: the position, velocity, attitude, and baro-altimeter states are the 10 states of interest for an INS and cannot be considered for elimination (assuming they are observable) (14). Those readers familiar with aircraft Kalman filters notes that these states compose the bulk of the states used in aircraft navigation filters. However, the other 83 states which compose the full-order LN-93 INS error model are states which are not directly of interest, but contribute to the position, velocity, and attitude errors (see the discussion of Stacey's INS model in Chapter III). Which of the 83 states can be eliminated? A smart engineer starts by conducting a literature search on the type of model he is implementing and analyzes the work previously accomplished with good results. The paper by Lewantowicz and Keen (10) is a good example for this thesis. It presents four different reduced-order

filters for the INS ranging from 41 states down to 17 states, all performing reasonably well. This paper forms the basis for both the truth and filter state reductions executed in this thesis.

What happens when there is no literature on the subject? The engineer must then analyze the states mathematically or use software tools such as MSOFE (3). Normally, the time and frequency response of the states are determined. Then, states with negligible magnitudes can be eliminated, or they can be combined with those of larger magnitudes and similar frequency responses. Note that filter "tuning" is often necessary when states are combined or eliminated, and this subject is covered in the next section. The engineer must be extremely careful when performing state reduction to ensure that accurate state estimates of the quantities of interest are maintained.

A filter analysis tool such as MSOFE also helps the engineer in other ways than those expressed above (3). When a full-order filter's state estimates are compared to the truth model of the system, sometimes even a well-tuned filter provides estimates of states that do not adequately follow the true states dynamics. Normally, this lack of filter performance in estimating states can be attributed to a lack of observability of the states (14). Maybeck states that it is improper to include unobservable truth model states in the filter design model (13). Examples of this phenomena in this thesis are the GPS space vehicle (SV) position errors (see Appendices D, E, and G). The filter's covariance values for these states show an adequately tuned filter. However, the filter's state estimates never follow the true error states due to a lack of observability of the states. MSOFE allows the engineer to perform Monte Carlo or covariance analysis on the filter and accurately assess its state estimation performance under a wide range of conditions. Maybeck recommends using covariance analysis on linear or linearized Kalman filters because only one simulation run is required to determine the true states covariance (14). However, this one simulation run takes a much longer time to complete when large dimension filters are implemented

and is not as useful for an EKF implementation, both satisfied in this thesis. Monte Carlo analysis provides quicker results if many-run analysis is not used, though not it is not as accurate as the covariance analysis. Often filter designers use 1- to 5-run Monte Carlo analysis at first to get quickly "in the ballpark" and then use covariance analysis to determine true filter performance. Only Monte Carlo analysis is used in this thesis due to time constraints and the implementation of an EKF.

A brief discussion of filter order reduction has been given. The general procedure used to eliminate filter states successfully in this thesis has been outlined. This procedure is by no means all inclusive, but should give the inexperienced engineer a foundation for performing filter order reduction.

2.4 Tuning Kalman Filters

When the truth model of a system of interest is composed of linear dynamics and measurement equations, a linear Kalman filter based upon this system proves to be the "optimal" estimator by almost any criteria (14). When a full-order filter of the truth model is implemented, the dynamics and measurement noises used to construct the filter (similar to the noises used in the nonlinear filter derivation given previously) would normally match the truth model noises. However, when filter order reduction is performed on this linear filter, the noise strengths may have to be adjusted to compensate for the missing/combined states. Along similar lines, when a linearized/extended full-order Kalman filter is implemented to simulate a nonlinear system, the noise strengths again may have to be adjusted in both the full-order and reduced-order filters to compensate for the approximations used in implementing linearized equations to model a nonlinear system and for the reduction/combination of states. This filter noise strength adjustment, or "tuning", is overviewed in the next few paragraphs as it applies to this thesis.

The dynamics and measurement equations used in this research have been shown previously (Section 2.2). The closer the full-order filter approximates the

truth model, the less the noise strength $Q(t)$ and covariance $R(t_i)$ are adjusted (normally increased) to compensate for nonlinearities in the true dynamics. For the full-order filters implemented in this research, there are three main reasons why the dynamics noise strength $Q(t)$ on some of the states needed increasing.

The first reason occurs when states which have noise (or have no noise) associated with them in the truth model need increased noise (or some noise) in the filter model to track the dynamics of the true state adequately. Adding noise increases the uncertainty of the filter-assumed state's dynamics to compensate for nonlinear behavior or to keep the Kalman filter gains in that channel from going to zero. Usually the states in the filter needing this type of noise adjustment are the states which are not part of the measurement equation. In this thesis, some of the INS states not part of a measurement equation need a small amount of added noise to compensate for nonlinear dynamics. If the states are not directly part of the measurement equation, and the dynamics equations do not totally describe the true states behavior, the EKF has difficulty estimating these states. The noise increase/addition is not large, just enough to increase the uncertainty in the dynamics equation to account for using a linearized/extended Kalman filter (14).

The second reason that dynamics noise needs to be added into a filter model occurs when the filter variance of a state goes negative. Maybeck states that this numerical difficulty is a normal occurrence when the range of numbers the filter estimates is large as in this filter when some of the INS states are on the order of $1.0e-6$ and the GPS clock bias state is often $1.0e10$ (14). The problem of negative variances arises due to the limited numerical precision of computers which must multiply high order matrices together. True state variances which showed this tendency often have a value of 0.0 in the truth model, and the filter does a good job of estimating the state, but the variance often goes negative. A small amount of added noise in the filter keeps the variance of the state positive and does not degrade the filter's state estimate.

The third and final reason why dynamics noise is added involves filter order reduction. States are eliminated in the INS model: states which do not show up directly in the measurement equations, but which impact the states which are part of the measurement equations. To compensate for the eliminated states, the noise in the states they affect is increased. The noise increase is small, since the eliminated states all have small magnitudes, but is necessary to ensure a well-tuned filter. In this thesis, the first two INS states in the reduced-order filters relating to latitude and longitude need a small amount of noise added into the filter to compensate for the elimination of INS states.

There are two reasons why the measurement noise covariance $\mathbf{R}(t_i)$ is adjusted in the filters. The first reason is the same as why the dynamics equation noise is adjusted upward in the full-order filters, to increase the uncertainty in the measurement equations due to using linearized equations to model nonlinear systems. Remember, the EKF only has access to measurements which are a combination of states, not to the states themselves.

The second reason for increasing the measurement noise $\mathbf{R}(t_i)$, and the most important and time consuming reason for increasing noise in these filter models, is due to filter order reduction. When states are eliminated in the filter model which are part of the measurement equation, it is necessary to increase $\mathbf{R}(t_i)$. This increase in noise is often not small, as some eliminated states have large covariance values. A good starting point for this noise increase is to add the variance of the eliminated states from the full-order model to the original variance of the measurement noise (13). If this is done progressively for each eliminated state, the resulting $\mathbf{R}(t_i)$ is often very close to what is needed for a well-tuned filter.

An overview of how and why filter tuning is performed in this thesis is given. Once again, these procedures are not universal to all Kalman filter tuning. They are basic reasons why Kalman filters need to be tuned, and any engineer involved in Kalman filter tuning needs to be familiar with them.

2.5 Summary

This chapter gives a summary of the Kalman filter techniques utilized in this thesis. The general EKF equations, filter order reduction, and filter tuning are examined, with a bias toward how they were accomplished in this thesis. A more detailed derivation of the EKF equations as they pertain to this research can be found in Stacey's thesis (22). Now that the basic theory is covered, the NRS truth and filter models are described in the next chapter.

III. The Navigation Reference System (NRS)

3.1 Overview

This chapter overviews the Litton LN-93 error model and the NRS developed by Stacey (22) along with the 97- and 69-state NRS models implemented in this thesis. First, the original Litton LN-93 error-state model is overviewed. Second, Stacey's INS, RRS, and GPS models are briefly described since they form the basis for all the other models and filters in this thesis. Third, the steps used to reduce the 93-state INS error-model to 41 states while maintaining the accuracy of the full 93-state model are explained. Fourth, a 97-state NRS model incorporating the new 41-state INS truth model is described. Finally, a 69-state reduced-order NRS filter is described. For a detailed explanation of Stacey's NRS, refer to Chapters 3, 4, and 5 of his thesis (22).

3.2 The 93-State LN-93 Error Model

This section overviews the original 93-state Litton INS error model (11). Six categories of errors are associated with this error model. The first category represents the "general" error-states, states which are combinations of several other states in the error model. Position, velocity, platform tilt, and vertical channel errors are in this category. The second category of errors consists of states described by first-order Markov processes. Both the gyros and accelerometers have exponentially time-correlated errors, and the baro-altimeter state is also included in this group. The third and fourth categories of error states are the gyro and accelerometer bias errors, respectively. These states are modeled as random constants in the truth model. The fifth category of error states are again first-order Markov processes modeling the gyro and accelerometer thermal transients. Finally, the last category of error states are gyro compliance errors modeled as random constants. The following equation

describes the overall 93-state error model using the six categories of states (22):

$$\delta \mathbf{x} = [\delta \mathbf{x}_1^T \quad \delta \mathbf{x}_2^T \quad \delta \mathbf{x}_3^T \quad \delta \mathbf{x}_4^T \quad \delta \mathbf{x}_5^T \quad \delta \mathbf{x}_6^T]^T \quad (3.1)$$

where $\delta \mathbf{x}$ is a 93×1 column vector and:

$\delta \mathbf{x}_1$ represents the "general" error vector containing 13 position, velocity, attitude, and vertical channel errors.

$\delta \mathbf{x}_2$ consists of 16 gyro, accelerometer, and baro-altimeter exponentially time-correlated errors, and "trend" states. These states are modeled as first order Markov processes in both the truth (system) model and in the Kalman filter.

$\delta \mathbf{x}_3$ represents gyro bias errors. These 18 states are modeled as random constants in the truth model and are modeled as random walks (with small magnitude pseudo-noises) in the Kalman filter.

$\delta \mathbf{x}_4$ is composed of the accelerometer bias error states. These 22 states are modeled in exactly the same manner as the gyro bias states.

$\delta \mathbf{x}_5$ depicts accelerometer and gyro initial thermal transients. The 6 thermal transient states are first order Markov processes in the system and Kalman filter.

$\delta \mathbf{x}_6$ models the gyro compliance errors. These 18 error states are modeled as biases in the system model and as random walks in the Kalman filter.

The truth model system state space differential equation is of the form:

$$\begin{Bmatrix} \delta \dot{\mathbf{x}}_1 \\ \delta \dot{\mathbf{x}}_2 \\ \delta \dot{\mathbf{x}}_3 \\ \delta \dot{\mathbf{x}}_4 \\ \delta \dot{\mathbf{x}}_5 \\ \delta \dot{\mathbf{x}}_6 \end{Bmatrix} = \begin{bmatrix} \mathbf{F}_{11} & \mathbf{F}_{12} & \mathbf{F}_{13} & \mathbf{F}_{14} & \mathbf{F}_{15} & \mathbf{F}_{16} \\ \mathbf{0} & \mathbf{F}_{22} & \mathbf{0} & \mathbf{0} & \mathbf{0} & \mathbf{0} \\ \mathbf{0} & \mathbf{0} & \mathbf{0} & \mathbf{0} & \mathbf{0} & \mathbf{0} \\ \mathbf{0} & \mathbf{0} & \mathbf{0} & \mathbf{0} & \mathbf{0} & \mathbf{0} \\ \mathbf{0} & \mathbf{0} & \mathbf{0} & \mathbf{0} & \mathbf{F}_{55} & \mathbf{0} \\ \mathbf{0} & \mathbf{0} & \mathbf{0} & \mathbf{0} & \mathbf{0} & \mathbf{0} \end{bmatrix} \begin{Bmatrix} \delta \mathbf{x}_1 \\ \delta \mathbf{x}_2 \\ \delta \mathbf{x}_3 \\ \delta \mathbf{x}_4 \\ \delta \mathbf{x}_5 \\ \delta \mathbf{x}_6 \end{Bmatrix} + \begin{Bmatrix} \mathbf{w}_1 \\ \mathbf{w}_2 \\ \mathbf{0} \\ \mathbf{0} \\ \mathbf{0} \\ \mathbf{0} \end{Bmatrix} \quad (3.2)$$

Appendix A, Tables A.1 through A.4, contains a full listing of the 93 INS error states as well as the RRS (Table A.5) and GPS (Table A.6) states which are explained in later sections of this chapter. Appendix B, Tables B.1 through B.10 contain the non-zero entries of the LN-93 error-state dynamics matrix $F(t)$ and the the dynamics equation noise strength matrix $Q(t)$. Stacey's thesis describes the LN-93 error states in more detail including the mathematical models of first order Markov processes, random constants and random walks used in all the truth models and filters (22).

3.3 Stacey's 128-State NRS Model

This section overviews the NRS model Stacey developed in his thesis (22). Stacey only performed a single Monte Carlo run on this filter, and its performance was inconclusive. This thesis analyzes Stacey's 128-state filter using 10-run Monte Carlo analysis. The results of this analysis can be found in Chapter V with plots of filter performance in Appendix D.

3.3.1 The 72-State LN-93 Error Model. Stacey used the Litton LN-93 error state model as the basis for the work performed in his thesis (22). However, Stacey recognized the inadequacy of the a baro-altimeter state in this model and designed a 4-state baro-altimeter error model (22) to implement as the truth and filter models in his thesis. This increased the INS error model to 96 total error states. Unfortunately, Stacey's four-state baro-altimeter model never performed up to expectations, and the ENRS designed in this thesis returns to a single baro-altimeter state (22). Tables A.1 through A.4 in Appendix A list the 93 INS error states.

When Stacey merged his 96 state INS model with the 26 state RRS model and the 30 state GPS model, he found the VAX III workstations he was using did not contain enough memory to compile and link the 152-state Fortran code. He knew Solomon had successfully executed code with 127 states, so he reduced the

INS model by 24 states, maintaining the 93-state error performance, bringing the total error model to 128 states (20, 22). Stacey eliminated the last 24 states in the INS model and then ran simulations to prove the position, velocity, and attitude errors were essentially the same as in the full 96-state error model. At this point, Stacey declared this 72-state INS model to be the truth and filter models in his analysis (22).

3.3.2 The 26-State RRS Error Model. The Range/Range-Rate System (RRS) is a navigation aiding system which comprises a significant part of CIRIS. Consequently, the RRS is used in both the NRS and ENRS. Navigation information is obtained by "interrogating" ground transponders and subsequently processing the electromagnetic (EM) signals which the transponders emit. The information obtained allows high quality range and range-rate measurements to be calculated by the RRS interrogating hardware (19). Using these range and range-rate measurements, updates to the NRS position (and ENRS position and velocity estimates) are then possible.

Solomon, Snodgrass, and Stacey each have given detailed explanations of the RRS error-states and the range measurement equation (20, 19, 22). This section reviews these topics to acquaint the reader to the dynamics and measurement equations. The range-rate measurement is explained in the next chapter when the ENRS is developed. The following sections have been excerpted from Chapter 4 of Stacey's thesis, and the reader should review his thesis if a detailed explanation of the Range/Range-Rate System (RRS) is needed.

3.3.2.1 RRS Model Equations. The RRS error state vector is composed of 26 elements (shown in Table A.5, Appendix A). The RRS states occupy numbers $S_{INS}+1$ through $S_{INS}+26$ in the complete error state model, where S_{INS} represents the total number of states used to model the INS subsystem in the truth model. The first two RRS states are simple random constant (bias) states which model

the effects of user hardware (RRS interrogator) range and range-rate calibration errors, respectively. Coupling of these states into the RRS measurement equation is presented in the next subsection. The error state model equation for these states is (19):

$$\begin{Bmatrix} \dot{x}_{br} \\ \dot{x}_{bv} \end{Bmatrix} = \begin{bmatrix} 0 & 0 \\ 0 & 0 \end{bmatrix} \begin{Bmatrix} x_{br} \\ x_{bv} \end{Bmatrix} \quad (3.3)$$

where

$$\begin{aligned} x_{br} &= \text{range equivalent of interrogator bias} \\ x_{bv} &= \text{velocity equivalent of interrogator bias} \end{aligned}$$

The initial state estimates and covariances for these states are (19):

$$\begin{Bmatrix} \hat{x}_{br}(t_0) \\ \hat{x}_{bv}(t_0) \end{Bmatrix} = \begin{bmatrix} 0 \\ 0 \end{bmatrix} \quad (3.4)$$

and

$$P_{br,bv}(t_0) = \begin{bmatrix} 1ft^2 & 0 \\ 0 & 10^{-4}ft^2/sec^2 \end{bmatrix} \quad (3.5)$$

While the two states discussed above are common to all RRS measurements, there exist two sources of errors which are unique to each individual transponder. First is the error due to transponder surveyed position uncertainty (x, y, z components in earth-centered earth fixed (ECEF) frame (2)), and second is the error due to atmospheric propagation delays between the user and each individual transponder. The three position error sources are well modeled by random bias states and the atmospheric error states are represented by first order Markov processes. Then for

each transponder, four states are used to define error sources (19):

$$\begin{Bmatrix} \dot{x}_i \\ \dot{y}_i \\ \dot{z}_i \\ \delta R_{atm_i} \end{Bmatrix} = \begin{bmatrix} 0 & 0 & 0 & 0 \\ 0 & 0 & 0 & 0 \\ 0 & 0 & 0 & 0 \\ 0 & 0 & 0 & -\frac{1}{\tau} \end{bmatrix} \begin{Bmatrix} x_i \\ y_i \\ z_i \\ \delta R_{atm_i} \end{Bmatrix} + \begin{Bmatrix} w_{x_i} \\ w_{y_i} \\ w_{z_i} \\ w_{atm_i} \end{Bmatrix} \quad (3.6)$$

The subscript i in the equation above denotes the i^{th} transponder and $\tau = 300 \text{ sec}$ is the transponder atmospheric error state time constant. The initial conditions for these states are (19):

$$\hat{\mathbf{x}}_{x,y,z,atm}(t_0) = \mathbf{0} \quad (3.7)$$

$$\mathbf{P}_{x,y,z,atm}(t_0) = \begin{bmatrix} 25ft^2 & 0 & 0 & 0 \\ 0 & 25ft^2 & 0 & 0 \\ 0 & 0 & 25ft^2 & 0 \\ 0 & 0 & 0 & 100(PPM)^2 \end{bmatrix} \quad (3.8)$$

and

$$E\{\mathbf{w}_{x,y,z,atm}\} = \mathbf{0} \quad (3.9)$$

$$E\{\mathbf{w}_{x,y,z,atm}(t)\mathbf{w}_{x,y,z,atm}(t+\tau)\} = \begin{bmatrix} 0 & 0 & 0 & 0 \\ 0 & 0 & 0 & 0 \\ 0 & 0 & 0 & 0 \\ 0 & 0 & 0 & \frac{2\sigma_{atm}^2}{300} \end{bmatrix} \delta(\tau) \quad (3.10)$$

with $\sigma_{atm}^2 = 10^{-10}ft^2$. Equations (3.3) through (3.10) were developed by the Cubic Corporation, designers of the RRS system for CIGTF, and are based on real static and dynamic measurement analysis of the RRS (20). Once again, the set of equations above (Equations (3.6) through (3.10)) apply to a single transponder. There are six such sets of equations for RRS transponders which are used in this thesis. The complete RRS error vector is specified in Appendix A.

3.3.2.2 RRS Range Measurement Equation. In CIRIS, RRS range measurements aid in estimating position errors of the reference INS. The RRS range measurement is derived from the time delay detected between the time at which the reference hardware (CIRIS or NRS) sends an interrogation signal and the time at which a reply from the transponder is received. This temporal difference is multiplied by the speed of light (and divided by two, to account for the "round trip" of the EM signal) to obtain an uncorrected range measurement. Correction factors are then applied in order to compensate for delays introduced by the propagation of EM signals through the atmosphere and to correct for errors introduced by equipment calibration biases (19). The uncorrected range measurement as *obtained from RRS* is modeled as:

$$R_{RRS} = R_t + \delta R_{atm} + \delta R_{br} + v \quad (3.11)$$

where

R_{RRS}	=	RRS range measurement, from transponder to user
R_t	=	true range, from transponder to user
δR_{atm}	=	range error due to atmospheric delay
δR_{br}	=	range error due to equipment calibration
v	=	zero-mean white Gaussian measurement noise

Equation (3.11) is a model for the range as determined by the RRS truth model. It includes the true range (which is never precisely known) along with terms which reflect the sources of error discussed in the previous subsection.

3.3.2.3 Range Calculation From INS Data. In order to formulate a *difference* measurement as shown in Chapter II, two sources of range information must be obtained. The first is the RRS range *measurement* which is *modeled* by Equation (3.11). Another range indication is computed from the INS *indicated* position

and RRS (surveyed) positions. (Both the indicated INS position and transponder surveyed position contain uncertainties which must be considered.) In this approach, the user (INS) indicated position is represented by an R^3 vector expressed in the Litton ECEF coordinates as:

$$\mathbf{X}_U = \begin{Bmatrix} x_U \\ y_U \\ z_U \end{Bmatrix}^e \quad (3.12)$$

while the true RRS transponder position is represented in the Litton ECEF frame by:

$$\mathbf{X}_T = \begin{Bmatrix} x_T \\ y_T \\ z_T \end{Bmatrix}^e \quad (3.13)$$

Then the calculated range from the user (INS) to the transponder is given by:

$$R_{INS} = \left| \mathbf{X}_U - \mathbf{X}_T \right| = \left\| \begin{Bmatrix} x_U \\ y_U \\ z_U \end{Bmatrix}^e - \begin{Bmatrix} x_T \\ y_T \\ z_T \end{Bmatrix}^e \right\| \quad (3.14)$$

Equation (3.14) may be rewritten as:

$$R_{INS} = \sqrt{(x_U - x_T)^2 + (y_U - y_T)^2 + (z_U - z_T)^2} \quad (3.15)$$

If the nonlinear equation above is "perturbed" to reflect uncertainties in user and transponder positions, then a first-order Taylor series may be written to approximate the range (2, 14). The truncated first-order series is of the form (20):

$$R_{INS} = R_t + \left. \frac{\partial R_{INS}(\mathbf{X}_T, \mathbf{X}_U)}{\partial \mathbf{X}_T} \right|_{(\mathbf{X}_T, \mathbf{X}_U)_{nom}} \cdot \delta \mathbf{X}_T + \left. \frac{\partial R_{INS}(\mathbf{X}_T, \mathbf{X}_U)}{\partial \mathbf{X}_U} \right|_{(\mathbf{X}_T, \mathbf{X}_U)_{nom}} \cdot \delta \mathbf{X}_U \quad (3.16)$$

After substituting Equation (3.15) into Equation (3.16) and evaluating the partial derivatives, the INS-derived range approximation becomes (19, 20):

$$\begin{aligned}
 R_{INS} = R_t & - \left[\frac{x_T - x_U}{|R_{INS}|} \right] \cdot \delta x_U - \left[\frac{y_T - y_U}{|R_{INS}|} \right] \cdot \delta y_U - \left[\frac{z_T - z_U}{|R_{INS}|} \right] \cdot \delta z_U \\
 & + \left[\frac{x_T - x_U}{|R_{INS}|} \right] \cdot \delta x_T + \left[\frac{y_T - y_U}{|R_{INS}|} \right] \cdot \delta y_T + \left[\frac{z_T - z_U}{|R_{INS}|} \right] \cdot \delta z_T \quad (3.17)
 \end{aligned}$$

At this point, the *difference* measurement may be formed as:

$$\begin{aligned}
 \delta z & = R_{INS} - R_{RRS} \\
 & = - \left[\frac{x_T - x_U}{|R_{INS}|} \right] \cdot \delta x_U - \left[\frac{y_T - y_U}{|R_{INS}|} \right] \cdot \delta y_U - \left[\frac{z_T - z_U}{|R_{INS}|} \right] \cdot \delta z_U \\
 & \quad + \left[\frac{x_T - x_U}{|R_{INS}|} \right] \cdot \delta x_T + \left[\frac{y_T - y_U}{|R_{INS}|} \right] \cdot \delta y_T + \left[\frac{z_T - z_U}{|R_{INS}|} \right] \cdot \delta z_T \\
 & \quad - [1] \delta R_{atm} - [1] \delta R_{br} - v \quad (3.18)
 \end{aligned}$$

The range measurement noise v has been determined to have a variance of 4 ft^2 in the truth model when RRS range measurements occur at 6 second intervals (20, 19). Note that the true whole-valued range (R_t) formerly present in both individual range measurements is cancelled in the differencing operation (2, 14). Also note that the bracketed coefficients in the equation above appear in the \mathbf{H} matrix presented in the EKF update equations overviewed in Chapter II. Also note that the measurement equations must be implemented in a single coordinate frame, the Litton ECEF frame being the frame of choice in this thesis (11). Although not presented in this thesis, Capt Stacey does an outstanding job of deriving the necessary coordinate frame transformations to implement all the measurement equations in his thesis (22).

3.3.3 The 30-State GPS Error Model. GPS is designed to be a highly accurate, stand-alone navigation system. However, for this research, GPS is used as a subsystem to improve the navigation solution of the LN-93 based NRS. In a manner

somewhat reminiscent of the RRS transponder system discussed in the previous section, GPS navigation information is obtained from EM signal propagation through the media (space and atmosphere) between the user (NRS) and each of the space vehicles (SVs) which the user "locks" into a reception channel of the GPS receiver. In a stand-alone GPS receiver, navigation information is obtained by receiving GPS SV ephemeris data which are broadcast continuously from each active ("locked-on") SV, correlating the phase of the signal with a matching signal in the GPS receiver, and correcting for known error sources to produce a highly accurate *range* estimate between the user and each SV which is monitored. In this thesis, uncorrected range measurements (known as *pseudorange* measurements) are channeled to a Kalman filter which provides estimates of the error sources. Although not used by the NRS, range-rate information may be obtained from GPS ephemeris in a similar manner. As in the RRS, GPS range measurements make refinements to the NRS navigation solution possible.

A basic dynamic *error* model for the GPS system was developed by Solomon (20) and revised in (6). However, *substantial changes* to the basic GPS model have been made by Stacey (22). In the references cited (6, 20), a simplified GPS model was assumed. It consisted of four *stationary* space vehicles (SVs) and did not perform geometry optimization calculations. In Stacey's model, a 24-SV "optimal" constellation based on a paper by Green (7) is modeled. Stacey's model includes orbital calculations for all SVs, and *simulates GPS receiver operation* as well. These enhancements are discussed in detail in Chapter V of Stacey's thesis (22). The *measurement* model equations for the GPS system follow a parallel development to that of the RRS measurement model shown previously.

3.3.3.1 GPS Error-Model Equations. The GPS error state vector is composed of 30 elements (shown in Table A.6, Appendix A). The GPS states occupy the thirty "uppermost" states in the NRS error state model. The first two GPS states model the user set (receiver) clock bias and drift errors, respectively.

The error state model equation for these states is (6, 20):

$$\begin{Bmatrix} \dot{x}_{Uclk_b} \\ \dot{x}_{Uclk_{dr}} \end{Bmatrix} = \begin{bmatrix} 0 & 1 \\ 0 & 0 \end{bmatrix} \begin{Bmatrix} x_{Uclk_b} \\ x_{Uclk_{dr}} \end{Bmatrix} \quad (3.19)$$

where

$$\begin{aligned} x_{Uclk_b} &= \text{range equivalent of user set clock bias} \\ x_{Uclk_{dr}} &= \text{velocity equivalent of user set clock drift} \end{aligned}$$

The initial state estimates and covariances for these states are (19):

$$\begin{Bmatrix} \hat{x}_{Uclk_b}(t_0) \\ \hat{x}_{Uclk_{dr}}(t_0) \end{Bmatrix} = \begin{bmatrix} 0 \\ 0 \end{bmatrix} \quad (3.20)$$

and

$$\mathbf{P}_{Uclk_b, Uclk_{dr}}(t_0) = \begin{bmatrix} 9.0 \times 10^{14} \text{ft}^2 & 0 \\ 0 & 9.0 \times 10^{10} \text{ft}^2/\text{sec}^2 \end{bmatrix} \quad (3.21)$$

Note the large uncertainties associated with the user clock states. These values are representative of the normal receiver clock bias and drifts associated with GPS receivers used in military and civilian airborne applications. Until the user clock error is determined, it is the single largest source of error in GPS range measurements. While the two states discussed above are common to all GPS measurements, there exist five sources of errors which are unique to each individual SV.

One error source specific to each SV is code range quantization error. At the heart of any GPS receiver exists a pair of interacting tracking loops (12). One of these loops, the "code tracking loop" is the source of pseudorange error which is modeled as a first order Markov process (12) with an exponential autocorrelation function. Other significant error sources include the tropospheric and ionospheric propagation delays. Both of these error sources are modeled and corrected to a large

degree by the GPS receiver. However the uncompensated error contribution of these error sources is still significant. Both of these are also modeled as first order Markov processes (with different time constants). Still other sources of error which must be included in the GPS model are SV clock error and SV position error, which are treated as random bias states. The reader should note the strong possibility for observability problems in a model such as this. In this case, three position error states are used, but the measurements provide new information *only along the line-of-sight vector* between the user and SV. All error sources discussed above which are unique to each SV are included in an error state vector shown below:

$$\begin{Bmatrix} \delta R_{cl} \\ \delta R_{trop} \\ \delta R_{ion} \\ \delta R_{Sclk} \\ \delta x_{s_i} \\ \delta y_{s_i} \\ \delta z_{s_i} \end{Bmatrix} = \begin{bmatrix} -1 & 0 & 0 & 0 & 0 & 0 & 0 \\ 0 & -\frac{1}{500} & 0 & 0 & 0 & 0 & 0 \\ 0 & 0 & -\frac{1}{1500} & 0 & 0 & 0 & 0 \\ 0 & 0 & 0 & 0 & 0 & 0 & 0 \\ 0 & 0 & 0 & 0 & 0 & 0 & 0 \\ 0 & 0 & 0 & 0 & 0 & 0 & 0 \\ 0 & 0 & 0 & 0 & 0 & 0 & 0 \end{bmatrix} \begin{Bmatrix} \delta R_{cl} \\ \delta R_{trop} \\ \delta R_{ion} \\ \delta R_{Sclk} \\ \delta x_{s_i} \\ \delta y_{s_i} \\ \delta z_{s_i} \end{Bmatrix} + \begin{Bmatrix} w_{cl} \\ w_{trop} \\ w_{ion} \\ 0 \\ 0 \\ 0 \\ 0 \end{Bmatrix} \quad (3.22)$$

$$\mathbf{P}_{GPS}(t_0) = \begin{bmatrix} 0.25ft^2 & 0 & 0 & 0 & 0 & 0 & 0 \\ 0 & 1.0ft^2 & 0 & 0 & 0 & 0 & 0 \\ 0 & 0 & 1.0ft^2 & 0 & 0 & 0 & 0 \\ 0 & 0 & 0 & 25ft^2 & 0 & 0 & 0 \\ 0 & 0 & 0 & 0 & 25ft^2 & 0 & 0 \\ 0 & 0 & 0 & 0 & 0 & 25ft^2 & 0 \\ 0 & 0 & 0 & 0 & 0 & 0 & 25ft^2 \end{bmatrix} \quad (3.23)$$

and

$$E\{\mathbf{w}_{GPS}(t)\} = \mathbf{0} \quad (3.24)$$

$$E \{ \mathbf{w}_{GPS}(t) \mathbf{w}_{GPS}(t + \tau) \} = \begin{bmatrix} 0.5 & 0 & 0 & 0 & 0 & 0 & 0 \\ 0 & 0.004 & 0 & 0 & 0 & 0 & 0 \\ 0 & 0 & 0.004 & 0 & 0 & 0 & 0 \\ 0 & 0 & 0 & 0 & 0 & 0 & 0 \\ 0 & 0 & 0 & 0 & 0 & 0 & 0 \\ 0 & 0 & 0 & 0 & 0 & 0 & 0 \\ 0 & 0 & 0 & 0 & 0 & 0 & 0 \end{bmatrix} ft^2/sec \cdot \delta(\tau) \quad (3.25)$$

The GPS model depicted by Equations (3.19) through (3.25) is representative of a military 5-channel GPS receiver operating on P-code. Once again, the set of equations above apply to each SV. There are four such sets of matrix equations for GPS SV errors modeled in this thesis since it is assumed 4 SVs are required for receiver operation. The error-state vector is completely specified in Appendix A.

3.3.3.2 GPS Pseudorange Measurement Equation. GPS range measurements aid in estimating position errors of the reference system. The GPS range measurement is derived by decoding ephemeris data which are broadcast continuously by each active SV. The user's GPS receiver (considered to be a subsystem in NRS and ENRS) processes signals received from the GPS SVs to determine pseudorange between the user and the SV. The range measurement thus obtained is corrupted by several error sources which must be estimated and compensated.

In its simplest form, a range measurement between a single GPS SV and the user (in this case, NRS) may be determined as the product of propagation speed of the EM signal and elapsed time during such propagation. Stated mathematically, the pseudorange is given by:

$$R_p = c \cdot t_e \quad (3.26)$$

where R_p is pseudorange, c is the speed of light in vacuum, and t_e represents the time for transit of the EM signal.

However, two major problems exist in using this simple definition for range. First, the EM signal is not propagated entirely in vacuum. The signal originates in space (where the assumption of vacuum is acceptable), but must subsequently propagate some distance through the earth's atmosphere as well. Naturally, the *signal delay* introduced by atmospheric propagation must be taken into account. Second, in order to preserve any hope of accurately determining range, it is *critical* to determine the EM signal transit time with an extremely high degree of accuracy. Recalling that light (or any EM signal) propagates on the order of $3 \times 10^8 m/s$, it is readily apparent that even a very small error in determining the EM signal propagation time can wreak havoc on attempts to use uncorrected pseudorange information to improve the navigation system solution in the NRS (or any other such system).

As a consequence of the concerns above, it is imperative to develop a much higher fidelity model for range estimation. A typical model for the pseudorange measurement between the user and space vehicles is given by the following equation (20):

$$R_{GPS} = R_t + \delta R_{cl} + \delta R_{trop} + \delta R_{ion} + \delta R_{sclk} + \delta R_{uclk} + v \quad (3.27)$$

where

R_{GPS}	=	GPS pseudorange measurement, from SV to user
R_t	=	true range, from SV to user
δR_{cl}	=	range error due to code loop error
δR_{trop}	=	range error due to tropospheric delay
δR_{ion}	=	range error due to ionospheric delay
δR_{sclk}	=	range error due to SV clock error
δR_{uclk}	=	range error due to User clock error
v	=	zero-mean white Gaussian measurement noise

As in the comparable equation for RRS, the GPS pseudorange equation above includes the true range (which can never be known exactly) along with terms which reflect sources of error and uncertainty inherent to GPS range measurements.

3.3.3.3 GPS Pseudorange Calculation From INS Data. As in the RRS subsystem, it is desirable to formulate a *difference* measurement in the GPS model as well. Once again, two sources of range information must be obtained. Like the RRS case, the first source is the range *measurement* which comes from the GPS subsystem and which is *modeled* by Equation (3.27). The second range estimate is constructed by differencing INS-indicated position and SV (broadcast) positions to calculate the range. (Note that the indicated INS position and SV position contain uncertainties which must be considered.) The user (INS) position is represented by an R^3 vector expressed in the Litton ECEF which is repeated below for convenience. SV position, \mathbf{X}_s , is represented in like fashion.

$$\mathbf{X}_u = \begin{Bmatrix} x_u \\ y_u \\ z_u \end{Bmatrix}, \quad \mathbf{X}_s = \begin{Bmatrix} x_s \\ y_s \\ z_s \end{Bmatrix} \quad (3.28)$$

Then user-to-SV pseudorange may be *calculated* as:

$$R_{INS} = |\mathbf{X}_u - \mathbf{X}_s| = \left| \begin{Bmatrix} x_u \\ y_u \\ z_u \end{Bmatrix} - \begin{Bmatrix} x_s \\ y_s \\ z_s \end{Bmatrix} \right| \quad (3.29)$$

Equation (3.29) may also be written in the equivalent form:

$$R_{INS} = \sqrt{(x_u - x_s)^2 + (y_u - y_s)^2 + (z_u - z_s)^2} \quad (3.30)$$

Invoking perturbation theory (2, 14), the nonlinear equation above is written as a first-order Taylor series to approximate the (INS derived) calculation of user to SV range. The truncated (to first-order) series is expressed as:

$$\begin{aligned}
R_{INS} = R_t &+ \left. \frac{\partial R_{INS}(X_S, X_U)}{\partial X_S} \right|_{(X_S, X_U)_{nom}} \cdot \delta X_S \\
&+ \left. \frac{\partial R_{INS}(X_S, X_U)}{\partial X_U} \right|_{(X_S, X_U)_{nom}} \cdot \delta X_U \quad (3.31)
\end{aligned}$$

When Equation (3.30) is substituted into Equation (3.31) and the partial derivatives evaluated, the INS-derived pseudorange approximation becomes:

$$\begin{aligned}
R_{INS} = R_t &- \left[\frac{x_S - x_U}{|R_{INS}|} \right] \cdot \delta x_U - \left[\frac{y_S - y_U}{|R_{INS}|} \right] \cdot \delta y_U - \left[\frac{z_S - z_U}{|R_{INS}|} \right] \cdot \delta z_U \\
&+ \left[\frac{x_S - x_U}{|R_{INS}|} \right] \cdot \delta x_S + \left[\frac{y_S - y_U}{|R_{INS}|} \right] \cdot \delta y_S + \left[\frac{z_S - z_U}{|R_{INS}|} \right] \cdot \delta z_S \quad (3.32)
\end{aligned}$$

Now the GPS pseudorange *difference* measurement is formed as:

$$\begin{aligned}
\delta z &= R_{INS} - R_S \\
&= - \left[\frac{x_S - x_U}{|R_{INS}|} \right] \cdot \delta x_U - \left[\frac{y_S - y_U}{|R_{INS}|} \right] \cdot \delta y_U - \left[\frac{z_S - z_U}{|R_{INS}|} \right] \cdot \delta z_U \\
&+ \left[\frac{x_S - x_U}{|R_{INS}|} \right] \cdot \delta x_S + \left[\frac{y_S - y_U}{|R_{INS}|} \right] \cdot \delta y_S + \left[\frac{z_S - z_U}{|R_{INS}|} \right] \cdot \delta z_S \\
&- [1] \delta R_{cl} - [1] \delta R_{trop} - [1] \delta R_{ion} \\
&- [1] \delta R_{Sclk} - [1] \delta R_{Uclk} - v \quad (3.33)
\end{aligned}$$

The pseudorange measurement noise v Stacey used has a variance of 2 ft^2 when GPS pseudorange measurements occur every 10 seconds. It should also be noted that the 97-state NRS truth model also has slightly higher noise modeled in its GPS pseudorange measurement equation. Stacey had implemented a measurement noise variance of only 2 ft^2 , while further research reveals the actual noise variance to be

9 ft^2 for this type of GPS model (12). Of course, the filter measurement noise was correspondingly increased. As noted in the RRS case, the true whole-valued range (R_t) formerly present in the individual pseudorange representations (R_{INS} and R_{GPS}) is cancelled in the differencing operation. The bracketed coefficients in the equation above are used in the \mathbf{H} matrix appear in the EKF update equations shown in Chapter II.

3.4 Reduction to a 41-State LN-33 Error Model

The NRS developed by Stacey contains 68 states in both its truth and filter models (22). A one-run Monte Carlo analysis of a 2-hour flight trajectory of Stacey's NRS using MSOFE on a 3 MIP VAX workstation takes over 18 hours to complete. In order to reduce the computational burden, the INS truth and filter model in the ENRS is further reduced from the 72 states Stacey used down to the 41 states following the recommendations of Lewantowicz and Keen (10). This 31 state reduction significantly decreases the computational time needed for analysis of the NRS and ENRS filters, but does not significantly affect the estimation accuracy of the errors of interest (position, velocity, and attitude). Tables A.7 and A.8 in Appendix A list the 41 states used in this new INS truth model.

It is necessary to confirm Lewantowicz and Keens' claim that a 41-state error model gives essentially the same solutions for position, velocity, and attitude error as the full-order truth model (10). Their methodology for arriving at 41 states, based on their 68-state truth model for the INS which had already eliminated states 69 through 93 from the 93-state truth model, was to eliminate 15 states which contributed one or more orders of magnitude less error contribution to the attitude and velocity error estimates than the states that were retained. They also combined 12 other states with errors which exhibited similar behavior, but were more dominant (10). This thesis takes a slightly different approach, by simply eliminating all the states they recommend, including the 12 states they combined with other states.

This one deviation from their recommendations doesn't appear to affect the results adversely. Tables A.7 and A.8 in Appendix A contain lists of the 41-state INS error model. Appendix C gives a 10-run Monte Carlo comparison between the 93-state LN-93 truth model and the 41-state truth model discussed above. As shown by Figure 3.1 (and Appendix C), the 41-state model does give position, velocity, and attitude error-states almost exactly matching the 93-state model over the two-hour fighter flight profile. At this point, the 41 error-state INS model is considered the truth model for this thesis.

3.5 The 97-State NRS Error Model

By merging the 41-state INS model, the 26-state RRS model, and the 30-state GPS model, a new 97-state NRS model is formed. This NRS model performs as well as Stacey's 128 state model did, but does so 3 times faster due to the elimination of 31 INS states. Chapter V discusses the performance of Stacey's NRS model and the 97-state NRS model and compares their performance to each other and various other filters which are described in this and the following chapter. Appendix E contains the results of a 10-run Monte Carlo analysis performed on the 97-state NRS filter.

3.6 The 69-State NRS Filter Model

Once the 97-state NRS truth and full-order filter models are developed, filter order reduction is performed. The state dimension for the ENRS post-processing filter is limited to 70 states, this number was set as the target for a NRS reduced-order filter. Recognize that only the number of filter states is to be reduced; the truth model remains at 97 states.

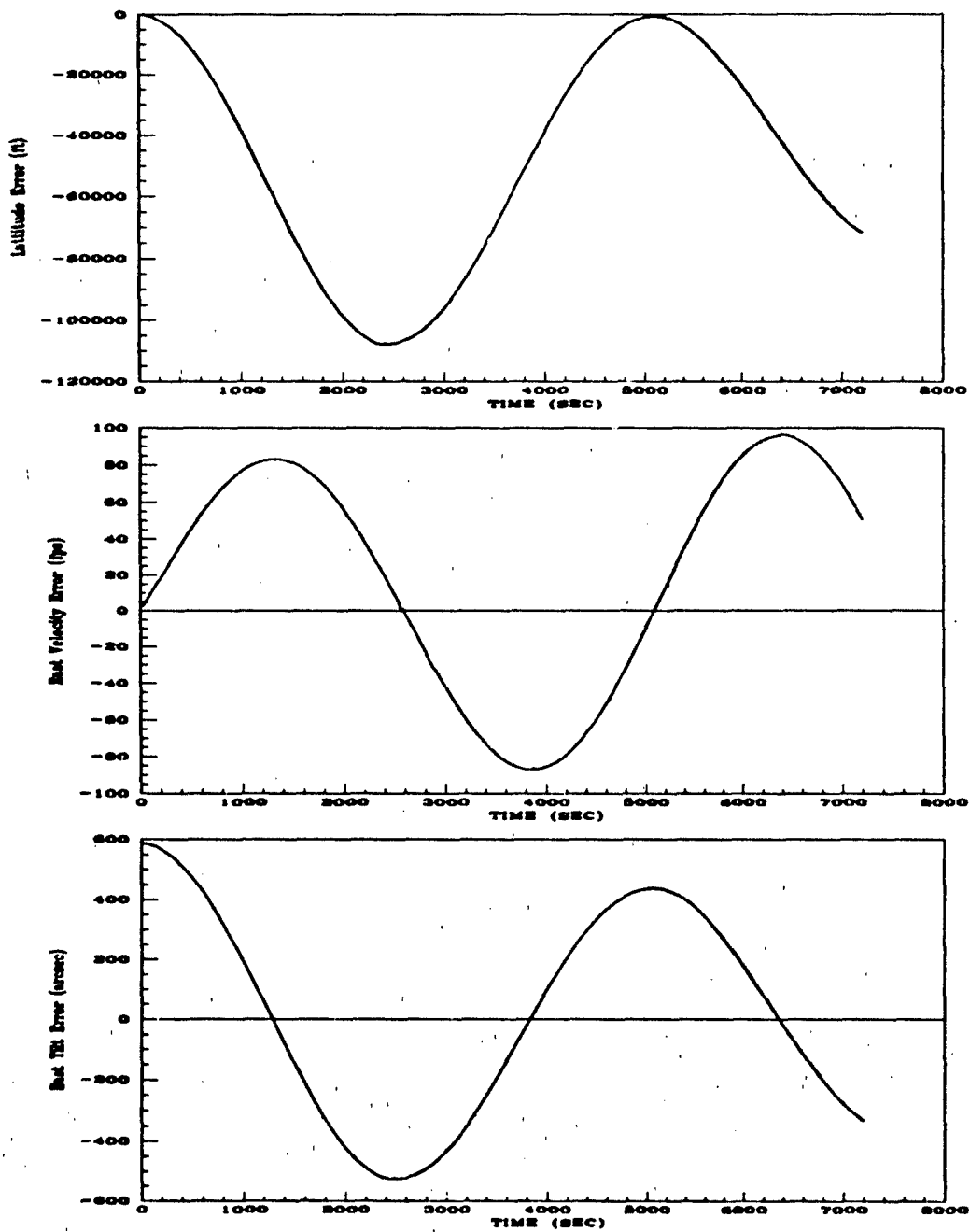


Figure 3.1. 93 vs 41 State INS Models (a) Latitude (b) East Velocity and (c) East Tilt Errors.

—	93-State INS Model
.....	41-State INS Model

Using research accomplished before as a basis (12, 5), the Kalman filter's GPS error-model was reduced from 30 states to only 2 states (10, 12). The two remaining states are the receiver clock bias and drift states (see Appendix A or GPS error-state discussion), leaving a 69-state NRS filter. Looking at the plots of the 97-state NRS filter in Appendix E, note that the two GPS receiver clock error-states are many orders of magnitude larger than the eliminated code drift, atmosphere, SV clock, and SV position error-states. This huge magnitude difference gives an indication as to why these states can be eliminated while retaining the two dominating states (see Chapter II's filter order reduction section). However, these states cannot simply be dropped with the expectation of adequate filter performance. The filter tuning techniques of Chapter II are exploited, noting each of the eliminated states is part of the pseudorange measurement equation. Thus, the measurement equation noise (see Equation (3.33)) is increased to compensate for the eliminated states.

As stated previously, the truth model measurement noise variance was $9 ft^2$. Chapter II recommends adding the filter covariance values of the eliminated states to the measurement noise variance to compute a new value for the measurement noise variance. Performing this operation gives a new value of approximately $225 ft^2$ ($9 ft^2$ original noise + $.09 ft^2$ code loop + $6.3 ft^2$ atmosphere + $16 ft^2$ SV clock + $64.3 ft^2$ SV position). Remember, this new value of the measurement noise is only a first best guess, further tuning may be needed for optimum filter performance. Chapter 5 discusses and compares the 69-state NRS filter performance to the other filters analyzed in this thesis. Appendix F contains the plots of the 69-state reduced-order NRS filters performance against the 97-state truth model.

3.7 Summary

This chapter reviewed the LN-93 and Stacey's NRS error-state models, and then developed 97-state and 69-state error models by eliminating 31 INS and 28 GPS states, respectively. These three NRS filters form a baseline to which the

ENRS filters developed in the next chapter are compared. Comparisons of filter performance can be found in Chapter V while the state variable plots are located in Appendices D, E, and F.

IV. The Enhanced Navigation Reference System (ENRS)

4.1 Overview

This chapter gives a complete description of the ENRS. First, an explanation of DGPS and how it is implemented at CIGTF is given. Second, a DGPS error model is developed. Third, the DGPS error model is combined with the 41-state INS and 26-state RRS models from Chapter III to form an 89-state ENRS model using only DGPS and RRS range measurements to update the filter. Fourth, a 48-state reduced-order ENRS filter is developed. Fifth, the DGPS delta-range measurement equation is derived and merged into a 22-state reduced-order DGPS filter (no RRS) to speed the tuning of delta-range measurements. Sixth, the RRS range-rate measurement equation is overviewed and merged into a 46-state CIRIS filter (no DGPS) to speed tuning of the range-rate measurements. Finally, DGPS delta-range and RRS range-rate measurements are merged into the 48-state reduced-order ENRS filter to complete the development of a post processing ENRS filter of less than 70 states.

4.2 Differential Corrections to GPS Measurements

This section discusses the theory behind DGPS as it is being implemented at CIGTF. Intermetrics, Inc. is the government sponsored contractor responsible for the DGPS reference station at CIGTF (1, 5). Personal interviews were conducted with Mr Darwin Abbey and Mr Scott Dance of Intermetrics to determine how differential corrections to GPS are implemented at CIGTF. The following discussion of DGPS comes directly from these interviews and the DGPS error model created in the next section is a combination of Intermetric's description and a course given by Navtech Seminars on DGPS error models (1, 5, 18).

In order to apply differential corrections to GPS measurements, a ground based reference receiver (GBR) is needed as well as the airborne GPS receiver (ABR) used

in the NRS. Figure 4.1 shows the basic DGPS system as it is being implemented at CIGTF. The ground based receiver must be capable of tracking all SVs in view, possibly as many as eleven when the full GPS constellation is placed in orbit. The GBR's antenna position has been permanently fixed and surveyed to within centimeter accuracy. A high accuracy rubidium clock is used in place of the GBR's normal clock, greatly decreasing the large clock errors common to the ABR as discussed in Section 3.3.3.1. Using the transmitted SV ephemeris data, the GBR computes its position (different from the surveyed position) known as the *ground truth*. The data (pseudorange measurements, SV transmitted corrections, GBR applied corrections, ground truth, clock errors, etc...) is fed to a 30386 personal computer which then estimates the SV position errors, SV clock errors, and atmospheric delays with great precision. Because the GBR's true position is accurately known and its clock errors are much smaller than the ABR's, the SV position and clock errors and atmospheric delays are highly observable. This is unlike the NRS GPS model where the large ABR's clock errors and dynamics cause these states to be largely unobservable. These errors, now called differential corrections, are time tagged and stored on magnetic tape or disc. Note that the differential corrections could be immediately transmitted via a data link for real-time differential corrections if the need ever arises (1, 5).

Remembering that the NRS is a post-processing filter, the ~~raw~~ airborne pseudorange measurements (which are also stored magnetically and time tagged) now have the differential corrections applied before they are analyzed in the post-processing filter. Of course, this assumes the GBR is tracking the same four SVs the ABR was tracking (a good assumption if the ABR is within the CIRIS test range). Using differential corrections in this manner, the SV clock error is eliminated from each pseudorange measurement and the SV position errors are nearly eliminated. Depending on the distance between the ABR and the GBR during the flight profile, the atmospheric propagation errors can be almost totally eliminated for close

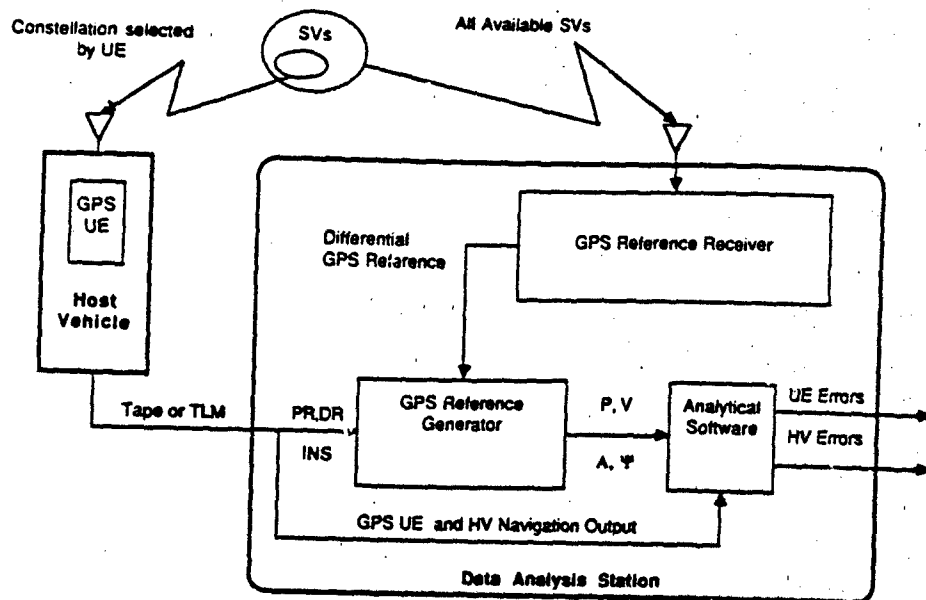


Figure 4.1. GPS Data Analysis/Reference Station

trajectories or greatly reduced for flights within 200 miles of the GBR. Even with long-range DGPS (flights which extend more than 200 miles from the GBR), the post-processing in the 30386 personal computer eliminates some of the atmospheric propagation errors. The largest remaining errors in the pseudorange measurement are the ABR clock errors (see Section 4.2.2). With this basic knowledge of DGPS, a new DGPS error model is now developed assuming that *differential corrections have previously been applied to the raw pseudorange measurements from the ABR* (1, 5, 18).

4.2.1 The 22-State DGPS Model. The DGPS error-model is composed of 22 states (shown in Table A.9, Appendix A). Note the DGPS states are almost identical to the GPS states except for elimination of the SV clock error through differential corrections, and removal of the SV code loop error. Dance states that compensation for the code loop error (truth and filter models) is provided by the measurement noise variance in the pseudorange measurement as implemented in this thesis (5). While the names of the states are the same, only the receiver clock error states are

modeled exactly as in the NRS. These two error-states are again modeled by (22):

$$\begin{Bmatrix} \dot{x}_{Uclk_b} \\ \dot{x}_{Uclk_{dr}} \end{Bmatrix} = \begin{bmatrix} 0 & 1 \\ 0 & 0 \end{bmatrix} \begin{Bmatrix} x_{Uclk_b} \\ x_{Uclk_{dr}} \end{Bmatrix} \quad (4.1)$$

where

$$\begin{aligned} x_{Uclk_b} &= \text{range equivalent of ABR clock bias} \\ x_{Uclk_{dr}} &= \text{velocity equivalent of ABR clock drift} \end{aligned}$$

Again the initial state estimates and covariances for these states are (22):

$$\begin{Bmatrix} \hat{x}_{Uclk_b}(t_0) \\ \hat{x}_{Uclk_{dr}}(t_0) \end{Bmatrix} = \begin{bmatrix} 0 \\ 0 \end{bmatrix} \quad (4.2)$$

and

$$P_{Uclk_b, Uclk_{dr}}(t_0) = \begin{bmatrix} 9.0 \times 10^{14} ft^2 & 0 \\ 0 & 9.0 \times 10^{10} ft^2/sec^2 \end{bmatrix} \quad (4.3)$$

As noted previously, until the ABR clock error is determined, it is the single largest source of error in DGPS range measurements. While the two states discussed above apply to all DGPS measurements, The troposphere, ionosphere and SV position errors are unique to each SV. Note that these errors have a much smaller contribution after differential corrections than in the GPS model (see Section 3.3.3.1) (18):

$$\begin{Bmatrix} \delta R_{trop} \\ \delta R_{ion} \\ \delta x_{s_i} \\ \delta y_{s_i} \\ \delta z_{s_i} \end{Bmatrix} = \begin{bmatrix} -\frac{1}{500} & 0 & 0 & 0 & 0 \\ 0 & -\frac{1}{1500} & 0 & 0 & 0 \\ 0 & 0 & 0 & 0 & 0 \\ 0 & 0 & 0 & 0 & 0 \\ 0 & 0 & 0 & 0 & 0 \end{bmatrix} \begin{Bmatrix} \delta R_{trop} \\ \delta R_{ion} \\ \delta x_{s_i} \\ \delta y_{s_i} \\ \delta z_{s_i} \end{Bmatrix} + \begin{Bmatrix} w_{trop} \\ w_{ion} \\ 0 \\ 0 \\ 0 \end{Bmatrix} \quad (4.4)$$

$$\mathbf{P}_{DGPS}(t_0) = \begin{bmatrix} 1.0ft^2 & 0 & 0 & 0 & 0 \\ 0 & 1.0ft^2 & 0 & 0 & 0 \\ 0 & 0 & .35ft^2 & 0 & 0 \\ 0 & 0 & 0 & .35ft^2 & 0 \\ 0 & 0 & 0 & 0 & .35ft^2 \end{bmatrix} \quad (4.5)$$

and

$$E \{ \mathbf{w}_{DGPS}(t) \} = \mathbf{0} \quad (4.6)$$

$$E \{ \mathbf{w}_{DGPS}(t) \mathbf{w}_{DGPS}(t + \tau) \} = \begin{bmatrix} 0.001 & 0 & 0 & 0 & 0 \\ 0 & 0.0004 & 0 & 0 & 0 \\ 0 & 0 & 0 & 0 & 0 \\ 0 & 0 & 0 & 0 & 0 \\ 0 & 0 & 0 & 0 & 0 \end{bmatrix} (ft^2/sec) \cdot \delta(\tau) \quad (4.7)$$

Once again, the set of equations above apply to a single SV. The initial covariance values in Equation (4.5) and atmospheric error dynamics noise variances in Equation (4.7) were obtained from (18) and are modeled slightly larger than Abbey and Dance (1, 5) recommend since a conservative filter is developed. There are four such sets of matrix equations for DGPS SV errors modeled in this thesis. The error-state vector is completely specified in Appendix A.

4.2.2 DGPS Pseudorange Measurement Equation. The DGPS pseudorange measurement equation is developed identically to the GPS pseudorange measurement equation of Section 3.3.3.2. After applying differential corrections, the measurement equation is modeled as:

$$R_{DGPS} = R_t + \delta R_{trop} + \delta R_{ion} + \delta R_{clk} + v \quad (4.8)$$

where

R_{DGPS}	=	DGPS pseudorange measurement, from SV to user
R_t	=	true range, from SV to user
δR_{trop}	=	range error due to tropospheric delay
δR_{ion}	=	range error due to ionospheric delay
δR_{Uclk}	=	range error due to ABR clock error
v	=	zero-mean white Gaussian measurement noise

As in the comparable equation for GPS (Equation (3.27)), the DGPS pseudorange equation above includes the true range (which can never be known exactly) along with terms which reflect sources of error and uncertainty inherent to DGPS range measurements.

4.2.2.1 DGPS Pseudorange Calculation From INS Data. As in the NRS subsystem, it is desirable to formulate a *difference* measurement in the DGPS model as well. Once again, two sources of range information must be obtained. Like the NRS case, the first source is the range *measurement* coming from the DGPS reference station and *modeled* by Equation (4.8). The second range estimate is constructed by differencing INS-indicated position and SV (broadcast) positions to calculate the range. Following the same derivation as in Section 3.3.3.3, the DGPS difference measurement is formed as:

$$\begin{aligned}
 \delta z &= R_{INS} - R_{DGPS} \\
 &= - \left[\frac{x_s - x_u}{|R_{INS}|} \right] \cdot \delta x_u - \left[\frac{y_s - y_u}{|R_{INS}|} \right] \cdot \delta y_u - \left[\frac{z_s - z_u}{|R_{INS}|} \right] \cdot \delta z_u \\
 &\quad + \left[\frac{x_s - x_u}{|R_{INS}|} \right] \cdot \delta x_s + \left[\frac{y_s - y_u}{|R_{INS}|} \right] \cdot \delta y_s + \left[\frac{z_s - z_u}{|R_{INS}|} \right] \cdot \delta z_s \\
 &\quad - [1] \delta R_{trop} - [1] \delta R_{ion} - [1] \delta R_{Uclk} - v
 \end{aligned} \tag{4.9}$$

The pseudorange measurement noise variance is 9 ft^2 when DGPS pseudorange measurements occur every 10 seconds. As noted in the NRS case, the true whole-valued range (R_t) formerly present in the individual pseudorange representations (R_{INS} and

R_{DGPS}) is cancelled in the differencing operation. The bracketed coefficients in the equation above appear in the \mathbf{H} matrix used in the EKF update equations shown in Section 2.2.

4.3 *The 89-State ENRS Error Model*

The 22-state DGPS error-model developed is now merged with the 41-state INS model and 26-state RRS model to form an 89-error-state ENRS model. At this point, only DGPS pseudorange and RRS range measurements are available to the filter for position updating. A 10-run Monte Carlo analysis is performed and the plots of filter performance are located in Appendix G. This filter serves as a baseline for DGPS measurements, and a discussion of its performance relative to the NRS filters is given in Chapter V.

4.4 *The 48-State ENRS Filter (Position Measurements Only)*

Now that a full-order filter has been discussed, a reduced-order filter of 70 states or less is developed. The first step in filter-order reduction uses the method discussed in Sections 2.3 and 2.4. Since all the DGPS error-states are small except for the ABR's clock errors, they are eliminated. All 20 states eliminated are part of the pseudorange equation, so again the measurement noise v is increased to compensate for the eliminated states. The original measurement noise variance is $9ft^2$, and the modified noise variance is calculated to be approximately $25ft^2$. Once again, this is only a first best guess and additional filter tuning may be necessary (see Chapter V).

At this point the 89-state model has been reduced to 69 states by the elimination of 20 DGPS states. However, DGPS delta-range and RRS range-rate measurement equations are to be implemented and the additional computation time required to implement 4 DGPS delta-range and 6 RRS range-rate measurements slows the Monte Carlo analysis down by 50 percent over the NRS 69-state filter using only

position aiding measurements. Further order reduction is necessary to ensure the post-processing filter can complete its analysis of a 2-hour flight trajectory within 24 hours. For this reason, an additional 21 INS states are eliminated to reduce the ENRS filter to 48 error-states. Once again the recommendations of Lewantowicz and Keen are followed for this INS state reduction (10). The new 20-state INS filter is formed by elimination of states 21 through 41 of the 41-state INS model, and this model is shown in Tables A.7 of Appendix A. Zero-mean white-gaussian noise ($10^{-16} \text{rad}^2/\text{sec}$) is added to dynamics equations of the first two INS states (related to position errors) to compensate for this filter order reduction (see Section 2.4). The plots of filter performance for the 48 error-state ENRS filter (no velocity aiding) are found in Appendix H with a discussion of filter performance relative to the previously designed filters in this thesis found in Chapter V.

4.5 DGPS Delta-Range Measurements

In a manner similar to the GPS and DGPS pseudorange measurement equations development in Sections 3.3.3.2 and 4.2.2, the delta-range measurement equation can also be developed. Typically, the velocity between the user and SV is not directly measured in a GPS receiver. Rather, the number of carrier-cycles for a period of time is counted, which calculates the change in pseudorange over a time interval, not the time rate of change of pseudorange (12). For this thesis, since error-states are modeled and not the true receiver operation, the previous pseudorange measurement (see Equation (4.8)) is subtracted from the current pseudorange measurement and divided by the time interval between measurements to yield:

$$\dot{R}_{DGPS} = \dot{R}_t + \delta \dot{R}_{v,ub} + v \quad (4.10)$$

where

\dot{R}_{DGPS}	=	DGPS delta-range measurement, from SV to user
\dot{R}_t	=	true delta-range, from SV to user
$\delta\dot{R}_{Uclk}$	=	delta-range error due to ABR clock drift error
v	=	zero-mean white Gaussian measurement noise

Note that the atmospheric errors in Equation (4.8), once subtracted, are small and are ignored. The delta-range equation above includes true delta-range (which is never known) along with an ABR clock drift error term.

4.5.1 DGPS Delta-Range Calculation From INS Data. As in the GPS subsystem, it is desirable to formulate a *difference* measurement in the DGPS delta-range model as well. Once again, two sources of delta-range information must be obtained. Like the pseudorange case, the first source is the delta-range *measurement* which comes from the DGPS subsystem and which is *modeled* by Equation (4.10). The second delta-range estimate is constructed by taking the time derivative of Equation (3.30). As a reminder, Equation (3.30) defined R_{INS} as:

$$R_{INS} = [(x_U - x_S)^2 + (y_U - y_S)^2 + (z_U - z_S)^2]^{1/2} \quad (4.11)$$

and taking its time derivative yields:

$$\dot{R}_{INS} = S_{INS} / R_{INS} \quad (4.12)$$

where:

$$S_{INS} = [(x_U - x_S)(\dot{x}_U - \dot{x}_S) + (y_U - y_S)(\dot{y}_U - \dot{y}_S) + (z_U - z_S)(\dot{z}_U - \dot{z}_S)] \quad (4.13)$$

Remember from Section 3.3.3.3 that:

$$\mathbf{X}_U = [x_U \ y_U \ z_U]^T \quad (4.14)$$

$$\mathbf{X}_S = [x_S \ y_S \ z_S]^T \quad (4.15)$$

so that:

$$\dot{\mathbf{X}}_U = [\dot{x}_U \ \dot{y}_U \ \dot{z}_U]^T \quad (4.16)$$

$$\dot{\mathbf{X}}_S = [\dot{x}_S \ \dot{y}_S \ \dot{z}_S]^T \quad (4.17)$$

Invoking perturbation theory (2, 14), Equation (4.12) is written as a first-order Taylor series to approximate the (INS derived) calculation of user to SV delta-range.

The truncated (to first-order) series is expressed as:

$$\begin{aligned} \dot{R}_{INS} = \dot{R}_t &+ \left. \frac{\partial \dot{R}_{INS}(\mathbf{X}_S, \mathbf{X}_U, \dot{\mathbf{X}}_S, \dot{\mathbf{X}}_U)}{\partial \mathbf{X}_S} \right|_{(\mathbf{X}_S, \mathbf{X}_U, \dot{\mathbf{X}}_S, \dot{\mathbf{X}}_U)_{nom}} \cdot \delta \mathbf{X}_S \\ &+ \left. \frac{\partial \dot{R}_{INS}(\mathbf{X}_S, \mathbf{X}_U, \dot{\mathbf{X}}_S, \dot{\mathbf{X}}_U)}{\partial \dot{\mathbf{X}}_S} \right|_{(\mathbf{X}_S, \mathbf{X}_U, \dot{\mathbf{X}}_S, \dot{\mathbf{X}}_U)_{nom}} \cdot \delta \dot{\mathbf{X}}_S \\ &+ \left. \frac{\partial \dot{R}_{INS}(\mathbf{X}_S, \mathbf{X}_U, \dot{\mathbf{X}}_S, \dot{\mathbf{X}}_U)}{\partial \mathbf{X}_U} \right|_{(\mathbf{X}_S, \mathbf{X}_U, \dot{\mathbf{X}}_S, \dot{\mathbf{X}}_U)_{nom}} \cdot \delta \mathbf{X}_U \\ &+ \left. \frac{\partial \dot{R}_{INS}(\mathbf{X}_S, \mathbf{X}_U, \dot{\mathbf{X}}_S, \dot{\mathbf{X}}_U)}{\partial \dot{\mathbf{X}}_U} \right|_{(\mathbf{X}_S, \mathbf{X}_U, \dot{\mathbf{X}}_S, \dot{\mathbf{X}}_U)_{nom}} \cdot \delta \dot{\mathbf{X}}_U \end{aligned} \quad (4.18)$$

Because the SV position errors are modeled as bias (constant) terms, their time derivative is zero, so that $\delta \dot{\mathbf{X}}_S = 0$. When Equation (4.12) is substituted into Equation (4.18) and the partial derivatives evaluated, the INS-derived delta-range approximation becomes:

$$\begin{aligned} \dot{R}_{INS} = \dot{R}_t &+ [(R_{INS}^{-1})(\dot{x}_U - \dot{x}_S) - (R_{INS}^{-3/2})(S_{INS})(x_U - x_S)]\delta x_U \\ &+ [(R_{INS}^{-1})(\dot{y}_U - \dot{y}_S) - (R_{INS}^{-3/2})(S_{INS})(y_U - y_S)]\delta y_U \\ &+ [(R_{INS}^{-1})(\dot{z}_U - \dot{z}_S) - (R_{INS}^{-3/2})(S_{INS})(z_U - z_S)]\delta z_U \end{aligned}$$

$$\begin{aligned}
& + [(R_{INS}^{-1})(x_U - x_S)]\delta\dot{x}_U \\
& + [(R_{INS}^{-1})(y_U - y_S)]\delta\dot{y}_U \\
& + [(R_{INS}^{-1})(z_U - z_S)]\delta\dot{z}_U \\
& - [(R_{INS}^{-1})(\dot{x}_U - \dot{x}_S) - (R_{INS}^{-3/2})(S_{INS})(x_U - x_S)]\delta x_S \\
& - [(R_{INS}^{-1})(\dot{y}_U - \dot{y}_S) - (R_{INS}^{-3/2})(S_{INS})(y_U - y_S)]\delta y_S \\
& - [(R_{INS}^{-1})(\dot{z}_U - \dot{z}_S) - (R_{INS}^{-3/2})(S_{INS})(z_U - z_S)]\delta z_S
\end{aligned} \tag{4.19}$$

Now the delta-range *difference* measurement is formed by subtracting Equation (4.10) from (4.19):

$$\begin{aligned}
\delta z & = \dot{R}_{INS} - \dot{R}_{DGPS} \\
& = [(R_{INS}^{-1})(\dot{x}_U - \dot{x}_S) - (R_{INS}^{-3/2})(S_{INS})(x_U - x_S)]\delta x_U \\
& + [(R_{INS}^{-1})(\dot{y}_U - \dot{y}_S) - (R_{INS}^{-3/2})(S_{INS})(y_U - y_S)]\delta y_U \\
& + [(R_{INS}^{-1})(\dot{z}_U - \dot{z}_S) - (R_{INS}^{-3/2})(S_{INS})(z_U - z_S)]\delta z_U \\
& + [(R_{INS}^{-1})(x_U - x_S)]\delta\dot{x}_U \\
& + [(R_{INS}^{-1})(y_U - y_S)]\delta\dot{y}_U \\
& + [(R_{INS}^{-1})(z_U - z_S)]\delta\dot{z}_U \\
& - [(R_{INS}^{-1})(\dot{x}_U - \dot{x}_S) - (R_{INS}^{-3/2})(S_{INS})(x_U - x_S)]\delta x_S \\
& - [(R_{INS}^{-1})(\dot{y}_U - \dot{y}_S) - (R_{INS}^{-3/2})(S_{INS})(y_U - y_S)]\delta y_S \\
& - [(R_{INS}^{-1})(\dot{z}_U - \dot{z}_S) - (R_{INS}^{-3/2})(S_{INS})(z_U - z_S)]\delta z_S \\
& - [1]\delta\dot{R}_{Udh} - v
\end{aligned} \tag{4.20}$$

The variance of the delta-range measurement noise v used is 0.16 ft^2 when delta-range measurements occur every 10 seconds (12). The true whole-valued range-rate (\dot{R}_t) formerly present in the individual delta-range representations (\dot{R}_{INS} and \dot{R}_{DGPS}) is cancelled in the differencing operation. The bracketed coefficients in the equation above appear in the \mathbf{H} matrix of the EKF update equations shown in Section 2.2.

4.5.2 The 22-State DGPS Filter (No RRS). Now that the DGPS delta-range model has been derived, it is necessary to implement this algorithm into MSOFE to analyze its performance. To speed up the process of implementation, a 22-state reduced-order filter is modeled. This filter contains the 20 INS states discussed in the 48-state ENRS filter and 2 DGPS clock states. No RRS states are included in the filter or truth model, so the full-order truth model for this system is 63 states (41 INS and 22 DGPS). A 10-run Monte Carlo analysis using the 2 hour fighter flight profile on this filter is completed in 5 hours, allowing two or three analyses per day until the algorithm is properly implemented and the filter well-tuned. The filter performance plots from the fighter flight profile are located in Section I.1 of Appendix I. For a robustness check, the filter was then analyzed using a 10-run Monte Carlo analysis of a 2-hour straight flight profile. These filter performance plots are located in Section I.2 of Appendix I. A discussion of the results of this filter implementation can be found in Chapter V.

4.6 Transponder Range-Rate Measurements

In a manner similar to the DGPS delta-range measurement equation development in Section 4.5, the RRS range-rate measurement equation can also be developed. From Equation (3.11), the RRS range-rate equation is modeled by:

$$\dot{R}_{RRS} = \dot{R}_t + \delta \dot{R}_{BV} + v \quad (4.21)$$

where

$$\begin{aligned}
 \dot{R}_{RRS} &= \text{RRS range-rate measurement, from transponder to user} \\
 \dot{R}_t &= \text{true range-rate, from transponder to user} \\
 \delta \dot{R}_{BV} &= \text{range-rate error due to calibration bias error} \\
 v &= \text{zero-mean white Gaussian measurement noise}
 \end{aligned}$$

Again the atmospheric error is small and can be neglected. The delta-range equation above includes true range-rate (which is never known) along with an equipment calibration velocity error term.

4.6.1 RRS Range-Rate Calculation From INS Data. As in the DGPS subsystem, it is desirable to formulate a *difference* measurement in the RRS range-rate model as well. Once again, two sources of range-rate information must be obtained. Like the delta-range case, the first source is the range-rate *measurement* which comes from the RRS subsystem and which is *modeled* by Equation (4.21). The second delta-range estimate is constructed by taking the time derivative of Equation (3.15). As a reminder, Equation (3.15) defined R_{INS} as:

$$R_{INS} = [(x_U - x_T)^2 + (y_U - y_T)^2 + (z_U - z_T)^2]^{1/2} \quad (4.22)$$

and taking its time derivative yields:

$$\dot{R}_{INS} = T_{INS} / R_{INS} \quad (4.23)$$

where:

$$T_{INS} = [(x_U - x_T)(\dot{x}_U) + (y_U - y_T)(\dot{y}_U) + (z_U - z_T)(\dot{z}_U)] \quad (4.24)$$

Remember from Section 3.3.2.3 that:

$$\mathbf{X}_U = [x_U \ y_U \ z_U]^T \quad (4.25)$$

$$\mathbf{X}_T = [x_T \ y_T \ z_T]^T \quad (4.26)$$

and again $\dot{\mathbf{X}}_U$ is defined:

$$\dot{\mathbf{X}}_U = [\dot{x}_U \ \dot{y}_U \ \dot{z}_U]^T \quad (4.27)$$

The transponders do not move, so the velocity term $\dot{\mathbf{X}}_T = 0$. Invoking perturbation theory (2, 14), Equation (4.23) is written as a first-order Taylor series to approximate the (INS derived) calculation of user to transponder velocity. The truncated (to first-order) series is expressed as:

$$\begin{aligned} \dot{R}_{INS} = \dot{R}_t + & \left. \frac{\partial \dot{R}_{INS}(\mathbf{X}_T, \mathbf{X}_U, \dot{\mathbf{X}}_U)}{\partial \mathbf{X}_T} \right|_{(\mathbf{X}_T, \mathbf{X}_U, \dot{\mathbf{X}}_U)_{nom}} \cdot \delta \mathbf{X}_T \\ & + \left. \frac{\partial \dot{R}_{INS}(\mathbf{X}_T, \mathbf{X}_U, \dot{\mathbf{X}}_U)}{\partial \mathbf{X}_U} \right|_{(\mathbf{X}_T, \mathbf{X}_U, \dot{\mathbf{X}}_U)_{nom}} \cdot \delta \mathbf{X}_U \\ & + \left. \frac{\partial \dot{R}_{INS}(\mathbf{X}_T, \mathbf{X}_U, \dot{\mathbf{X}}_U)}{\partial \dot{\mathbf{X}}_U} \right|_{(\mathbf{X}_T, \mathbf{X}_U, \dot{\mathbf{X}}_U)_{nom}} \cdot \delta \dot{\mathbf{X}}_U \end{aligned} \quad (4.28)$$

When Equation (4.23) is substituted into Equation (4.28) and the partial derivatives evaluated, the INS-derived range-rate approximation becomes:

$$\begin{aligned} \dot{R}_{INS} = \dot{R}_t + & [(R_{INS}^{-1})(\dot{x}_U) - (R_{INS}^{-3/2})(T_{INS})(x_U - x_T)]\delta x_U \\ & + [(R_{INS}^{-1})(\dot{y}_U) - (R_{INS}^{-3/2})(T_{INS})(y_U - y_T)]\delta y_U \\ & + [(R_{INS}^{-1})(\dot{z}_U) - (R_{INS}^{-3/2})(T_{INS})(z_U - z_T)]\delta z_U \\ & + [(R_{INS}^{-1})(x_U - x_T)]\delta \dot{x}_U \\ & + [(R_{INS}^{-1})(y_U - y_T)]\delta \dot{y}_U \\ & + [(R_{INS}^{-1})(z_U - z_T)]\delta \dot{z}_U \\ & - [(R_{INS}^{-1})(\dot{x}_U) - (R_{INS}^{-3/2})(T_{INS})(x_U - x_T)]\delta x_T \\ & - [(R_{INS}^{-1})(\dot{y}_U) - (R_{INS}^{-3/2})(T_{INS})(y_U - y_T)]\delta y_T \\ & - [(R_{INS}^{-1})(\dot{z}_U) - (R_{INS}^{-3/2})(T_{INS})(z_U - z_T)]\delta z_T \end{aligned}$$

(4.29)

Now the range-rate *difference* measurement is formed by subtracting Equation (4.21) from (4.29):

$$\begin{aligned}
\delta z &= \dot{R}_{INS} - \dot{R}_{RRS} \\
&= [(R_{INS}^{-1})(\dot{x}_U) - (R_{INS}^{-3/2})(T_{INS})(x_U - x_T)]\delta x_U \\
&\quad + [(R_{INS}^{-1})(\dot{y}_U) - (R_{INS}^{-3/2})(T_{INS})(y_U - y_T)]\delta y_U \\
&\quad + [(R_{INS}^{-1})(\dot{z}_U) - (R_{INS}^{-3/2})(T_{INS})(z_U - z_T)]\delta z_U \\
&\quad + [(R_{INS}^{-1})(x_U - x_T)]\delta \dot{x}_U \\
&\quad + [(R_{INS}^{-1})(y_U - y_T)]\delta \dot{y}_U \\
&\quad + [(R_{INS}^{-1})(z_U - z_T)]\delta \dot{z}_U \\
&\quad - [(R_{INS}^{-1})(\dot{x}_U) - (R_{INS}^{-3/2})(T_{INS})(x_U - x_T)]\delta x_T \\
&\quad - [(R_{INS}^{-1})(\dot{y}_U) - (R_{INS}^{-3/2})(T_{INS})(y_U - y_T)]\delta y_T \\
&\quad - [(R_{INS}^{-1})(\dot{z}_U) - (R_{INS}^{-3/2})(T_{INS})(z_U - z_T)]\delta z_T \\
&\quad - [1]\delta \dot{R}_{BV} - v
\end{aligned} \tag{4.30}$$

The variance of the range-rate measurement noise v is 0.09 ft^2 when range-rate measurements occur every 6 seconds (19). The true whole-valued range (\dot{R}_t) formerly present in the individual delta-range representations (\dot{R}_{INS} and \dot{R}_{RRS}) is cancelled in the differencing operation. The bracketed coefficients in the equation above appear in the \mathbf{H} matrix of the EKF update equations shown in Section 2.2.

4.6.2 The 46-State CIRIS Filter (No DGPS). In a manner similar to the 22-error-state DGPS filter, a 46-error-state CIRIS filter is developed to implement the

RRS range-rate measurement algorithm. The filter model consists of the 20-state INS model and 26-state RRS model. A 10-run Monte Carlo analysis using the 2-hour fighter flight profile is again used to tune the filter, and the filter performance plots are located in Section J.1 of Appendix J. As a robustness check, another 10-run Monte Carlo analysis using a 2-hour racetrack flight profile is performed. The filter performance plots of this analysis are located in Section J.2 of Appendix J. A discussion of this filter's performance is found in Chapter V.

4.7 The 48-State ENRS Filter (Position and Velocity Measurements)

The culmination of the work in many other theses is finally reached when the 20-error-state INS model, the 26-state RRS model with range and range-rate measurements, and a 2-state DGPS model with pseudorange and delta-range measurements are assembled into the 48-error-state ENRS filter. This filter is tuned using a 10-run Monte Carlo analysis using the fighter flight profile, and a final 25-run Monte Carlo analysis is performed to demonstrate this filter's performance relative to all the other filters analyzed in this thesis. The filter performance plots are found in Appendix K while a complete discussion of the final results is located in Chapter 5.

4.8 Summary

This chapter steps through the development leading to the 48-error-state ENRS filter. Differential corrections to GPS measurements are first discussed, followed by development of a DGPS model. Then full- and reduced-order models and delta-range and range-rate measurement equations are developed. Finally, all this data is merged into a 48-state post-processing ENRS filter designed to determine the position and velocity of the test article accurately so its performance can be evaluated. Remember, the truth model throughout this chapter is composed of 41 INS error-states, 26 RRS error-states, and 22 DGPS error-states. All NRS and ENRS filters' performance is discussed in detail in the next chapter.

V. Results of Filter Implementations

5.1 Overview

This chapter evaluates the performance of all the filters implemented in this thesis. Reduced-order filters are compared to their full-order counterparts, GPS filters are compared to DGPS filters, and all the filters are analyzed relative to the current CIRIS system. As a final presentation of results, a section is given containing tables of the filter tuning parameters $Q(t)$ and $R(t_i)$ if different from their truth model values for all the filters implemented in this thesis. Before any analysis of filter performance can begin, an important assumption pertaining to three of the truth/filter models in this thesis must be explained to the reader.

5.1.1 The Double Precision Factor. The truth/filter models implemented previously by Solomon, Snodgrass, and Stacey utilized Fortran on VAX mainframe and workstation computers (20, 19, 22). Their computer code was normally compiled, linked, and executed using "single precision" (the 7 most significant numbers are stored). For Solomon and Snodgrass, whose work dealt mainly with implementing an updated CIRIS filter without GPS, this method was more than adequate. However, when Stacey implemented his GPS subsystem and brought in pseudorange measurements, all his filters utilizing GPS diverged and could not be tuned properly. As seen in Figure 5.1, the typical truth model GPS clock bias error state attains values requiring much more than 7 significant figures to estimate the state adequately. As Stacey had mentioned in his thesis, "double precision" (14 most significant figures) is required for optimal filter performance.

Because the clock bias grows to such a large number, executing in single precision mode denies the filter the 1- or 2-foot clock bias state estimation accuracy required for accurate pseudorange measurements. However, simply switching to double precision is not as easy as it seems. When Stacey's 128-state model algorithms were

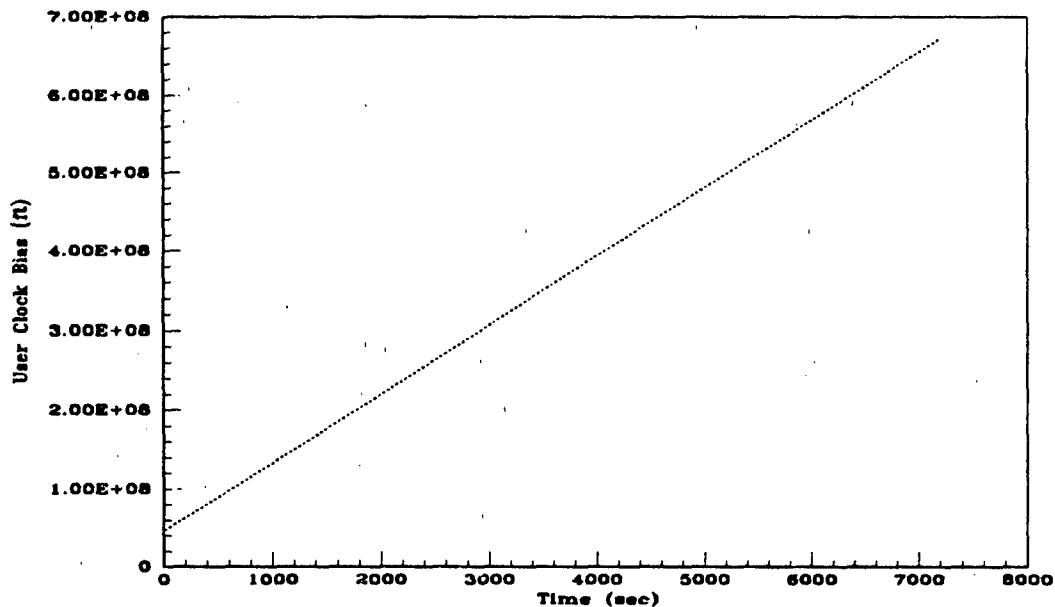


Figure 5.1. Typical GPS Clock Bias Error State for Two Hour Flight Profile

modified to double precision, neither the VAX mainframe nor workstation computers had enough memory available to link the code. The same problem arises with the 97-State NRS and 89-State ENRS full-order filter models. However, all the reduced-order filters in this thesis are compiled, linked, and executed in double precision mode.

At this point an assumption is made so that the full-order filters can be analyzed, and the reduced-order filters have benchmark filters for comparison purposes. *All the full-order filters truth models have their 2 GPS clock states' initial covariance values reduced four orders of magnitude (see Section 3.3.3 or 4.2.1).* By reducing their magnitudes, the filters are able to estimate the clock bias error-state adequately in single precision mode, and these 2 clock states still maintain errors several orders of magnitude larger than any other error states. Notice in Figures D.8, E.8, and G.8, that at the very end of the two-hour flight profiles the clock bias state approaches the limit of single precision and once again starts to diverge slightly, causing the clock

drift state to diverge also. However, overall, these full-order filters are tuned well enough to produce accurate navigation solutions. Note that, if these clock states were not so much larger in magnitude than the other error states, this approach would not be valid and the results could not be accepted without serious reservations. Also note that the CIRIS filter without the GPS subsystem does not need double precision, and it is not implemented in this filter.

In summary, the 128- and 97-state NRS and the 89-state ENRS truth and full-order filter models were run in single precision mode with the GPS clock error truth states' initial covariance values reduced 4 orders of magnitude. This modification in no way affects the reliability of these filters when used as benchmarks, as the 2 GPS clock error-states are much larger than any other error states, and the GPS clock bias state continues to be the largest source of errors in the pseudorange measurement by several orders of magnitude. The 46-state CIRIS filter is also run in single precision, but it does not model GPS states, so double precision is not needed. All of the reduced-order NRS, DGPS, and ENRS filters (evaluated against 97-state NRS, 63-state DGPS, and 89-state ENRS full-order double precision truth models) are programmed in double precision so the performance of these filters is in no way compromised.

5.2 The NRS Filters

This section evaluates the performance of the 3 NRS filters analyzed in this thesis. Remember that the NRS models the error states of a LN-93 INS with baro-altimeter, RRS transponders with range measurements, and GPS receiver with pseudorange measurements. Stacey's 128-State NRS filter is examined first. After some preliminary tuning runs, its performance is outstanding. Then the 97-State NRS filter is analyzed. It too produces a navigation solution one order of magnitude better than CIRIS. Finally, a 69-state reduced-order NRS filter is examined. Although

not as impressive as the first two NRS filters, its performance is well above that of CIRIS.

5.2.1 *Stacey's 128-State NRS Filter.* As the largest truth/filter model in this thesis, taking over 8 days to complete a 10-run Monte Carlo simulation, this filter also had the least amount of tuning performed on it for optimal state estimation. Appendix D contains the plots of the filters performance on the main states of interest. While some of the GPS states require further tuning, overall, this filter performs well, with the possibility of a significant increase in precision over CIRIS as it is implemented today. Remembering this filter was implemented in single precision, Table 5.1 contains the temporal average of the ensemble average of true filter estimation errors (1σ) for the position, velocity, and attitude errors over the two-hour fighter flight profile. *Ensemble* average is the average of the error-states for the number of Monte Carlo runs performed in the analysis over the 2-hour trajectories. This *vector* is the σ_{true} in the filter performance plots in Appendices D through K. The *scalar* temporal average is simply the average of the ensemble average for the 2-hour trajectories. As a reminder from Chapter 1, CIRIS specified accuracy is also included in this and all tables in this chapter for comparison purposes. Attitude is included in this and future tables simply to round out the navigation solution and show how INS state reduction affects these error states. Remember, no attitude measurements are present in any of the filters implemented in this thesis.

Table 5.1. Temporal Average of the Ensemble Average of True Errors for Stacey's 128 Error-State Filter

Filter	Latitude (ft)	Longitude (ft)	Altitude (ft)	East Vel (fps)	North Vel (fps)	Up Vel (fps)	East Tilt (arcs)	North Tilt (arcs)	Azi- muth (arcs)
CIRIS	14.00	14.00	40.00	0.100	0.100	0.400			
128-NRS	1.59	2.35	5.58	0.015	0.011	0.045	1.65	2.02	12.83

Stacey never resolved the precision problem for this filter due to time constraints and was only able to perform a one-run Monte Carlo simulation. The tuning performed in this thesis on his filter involved only the random bias states in the RRS and GPS subsystems. RRS range bias and transponder position error states and the GPS SV clock and SV position error states have a dynamics noise strength $Q(t)$ addition of approximately $10^{-3} ft^2/sec$ for the performance seen in Appendix D. Although not yet optimal, the filter's performance at this point speaks for itself. Using only RRS range and GPS pseudorange measurements, and once adequately tuned, Stacey's filter will produce a navigation solution *one order of magnitude more accurate than CIRIS*.

5.2.2 The 97-State NRS Filter. This filter is only different from Stacey's filter by use of the 41-state INS model instead of Stacey's 72-state model in the truth and filter models. Since the 41-state model provides true error states which almost match those for the 93-state LN-93 error model (see Appendix C), this filter's performance should also be very close to that of Stacey's 128-state filter. This simulation was also implemented in single precision, with the 2 GPS clock error states' initial covariance values decreased 4 orders of magnitude. Table 5.2 compares the 128- and 97-state NRS filters to each other and to CIRIS.

Table 5.2. Temporal Average of the Ensemble Average of True Errors for 128- and 97-State NRS Filters

Filter	Latitude (ft)	Longitude (ft)	Altitude (ft)	East Vel (fps)	North Vel (fps)	Up Vel (fps)	East Tilt (arcs)	North Tilt (arcs)	Azi- muth (arcs)
CIRIS	14.00	14.00	40.00	0.100	0.100	0.400			
128-NRS	1.59	2.35	5.58	0.015	0.011	0.045	1.65	2.02	12.83
97-NRS	1.35	2.71	5.28	0.014	0.010	0.045	1.07	1.29	9.74

As surmised, the performance of these two filters is almost identical, with a large increase in performance over the CIRIS system. Any discrepancy between

Stacey's 128-state NRS filter's performance and the 97-state NRS filter's performance is attributed to the fact that more time was spent tuning the 97-state NRS filter than the 128-state filter. Again, the only filter states requiring tuning were the random bias RRS and GPS states mentioned in the previous section, and these states have increased dynamics equation noise similar to the 128-state filter. Appendix E contains the filter performance plots of the main states of interest. Once again, the 97-State NRS filter provides a navigation solution one order of magnitude more accurate than the current CIRIS system while using only RRS range and GPS pseudorange measurements.

5.2.3 The 69-State NRS Filter. This first attempt at a reduced-order filter shows less optimal results than the previous two NRS full-order filters. As a reminder, the 69 error-states implemented in this filter were a combination of 41 INS error-states, 26 RRS error-states, and the 2 GPS clock error-states. Also, the 97-state truth and 69-state reduced-order filter models in this analysis were coded and executed in double precision, so the GPS clock error states' initial covariance values are at their true magnitude. The filter performance plots are found in Appendix F while Table 5.3 compares this filter with the other NRS filters and CIRIS.

Table 5.3. Temporal Average of the Ensemble Average of True Errors for NRS Filters

Filter	Latitude (ft)	Longitude (ft)	Altitude (ft)	East Vel (fps)	North Vel (fps)	Up Vel (fps)	East Tilt (arcs)	North Tilt (arcs)	Azimuth (arcs)
CIRIS	14.00	14.00	40.00	0.100	0.100	0.400			
128-NRS	1.59	2.35	5.58	0.015	0.011	0.045	1.65	2.02	12.83
97-NRS	1.35	2.71	5.28	0.014	0.010	0.045	1.07	1.29	9.74
69-NRS	3.28	4.21	9.04	0.033	0.026	0.070	1.37	2.11	18.42

As discussed in Section 3.6, the pseudorange measurement noise variance of this filter is adjusted upward to compensate for the eliminated GPS error-states

(which are all part of the pseudorange measurement equation). The first best guess was 225 ft^2 , while the currently implemented value of 300 ft^2 is still not enough to ensure adequate performance using conservative filter tuning methods (see the latitude state in Figure F.2). Even when taking into account the filter's nonoptimal tuning, it appears the navigation solution from this filter is not as accurate as the two full-order filters. However, when comparing to CIRIS performance, this filter is at least 3 times more accurate in position and velocity estimates. This is a substantial increase, considering only RRS range and GPS pseudorange equations are used to update the filter's state estimates. It can be deduced from this filter implementation that the eliminated GPS states, even though they have relatively small magnitudes, do affect the navigation solution accuracy even when the filter is optimally tuned. It is with this thought in mind that one is led into implementing differential corrections to GPS measurements to achieve higher accuracy in the navigation solution when implementing reduced-order filters.

5.3 The ENRS Filters

Various NRS filters have been implemented and analyzed with impressive results compared to CIRIS. The incorporation of differential corrections to GPS pseudorange measurements takes this accuracy a step further with the ENRS. The 89-State ENRS filter is analyzed first. Using only DGPS pseudorange measurements, this full-order filter's performance in horizontal position error standard deviation is on the order of 1 ft. Then a 48-state reduced-order filter is examined. Forty-one states are eliminated with only a slight decrease in velocity and attitude error estimation performance. Then two filters are examined which implement DGPS delta-range and RRS range-rate measurements for velocity aiding. Finally, delta-range and range-rate measurements are combined into the 48-state ENRS reduced-order filter as the conclusion to the work performed in this thesis.

It is also important to bring out at this time that when an ENRS filter is actually implemented at CIGTF, the differential corrections should ensure that this filter performs almost as well in real life as it does in simulation. Because the atmospheric, SV clock, and SV position GPS error sources are computed very accurately at the GPS Reference Station, the post-processing filter can estimate the true position errors with higher accuracy than can a filter utilizing normal GPS measurements. The added error sources of real world GPS measurements will likely decrease the accuracy of the NRS filter somewhat, while having much less affect on the ENRS filter due to the large reduction in magnitude of the error sources through differential corrections to the pseudorange measurement.

5.3.1 The 89-State NRS Filter (Position Measurements Only). This filter is very similar to the 97-state NRS filter, except for the assumption that differential corrections have been applied to the raw pseudorange measurements before filter processing. It includes the 41-state INS model and the 26-state RRS model with the GPS clock states' initial covariances decreased so the filter executes accurately in single precision mode. As shown by Table 5.4, the inclusion of differential corrections improves filter performance by almost 50 percent in position error estimation accuracy over the 97-state NRS filter.

Table 5.4. Temporal Average of the Ensemble Average of True Errors for NRS and 89-State ENRS Filters

Filter	Latitude (ft)	Longitude (ft)	Altitude (ft)	East Vel (fps)	North Vel (fps)	Up Vel (fps)	East Tilt (arcs)	North Tilt (arcs)	Azimuth (arcs)
CIRIS	14.00	14.00	40.00	0.100	0.100	0.400			
128-NRS	1.59	2.35	5.58	0.015	0.011	0.045	1.65	2.02	12.83
97-NRS	1.35	2.71	5.28	0.014	0.010	0.045	1.07	1.29	9.74
69-NRS	3.28	4.21	9.04	0.033	0.026	0.070	1.37	2.11	18.42
89-ENRS	0.84	1.04	3.80	0.013	0.010	0.042	0.94	1.29	6.46

The filter performance plots are located in Appendix G, and the reader will note how well the filter is tuned. The only unusual behavior in any of the plots stems from the fact that the GPS clock bias state approaches the limit of accuracy of single precision near the end of the run and both GPS clock states diverge slightly due to this fact. Other than this small anomaly, this filter performs better than any filter examined so far.

5.3.2 The 48-State ENRS Filter (Position Measurements Only). Since the full-order ENRS filter performs so well, it is now time to analyze the reduced-order filter designed to fulfill the "less than 70 state" requirement as stated in Section 1.2. To remind the reader, 48 states were chosen over the 69 states of the NRS filter because the addition of DGPS delta-range and RRS range-rate measurements increases the time required to update the states in the EKF by 50 percent, causing the Monte Carlo analysis to take almost 50 percent longer. Because of this time increase, 21 additional INS states relating to velocity and attitude errors were eliminated along with the 20 upper DGPS error states as discussed in Section 4.4. Table 5.5 once again compares the performance of this 48-state reduced-order ENRS filter to all previous filters and CIRIS. As can be seen, the position states suffer almost no degradation due to the order reduction, while the velocity and attitude states degrade significantly from the eliminated INS states. However, the addition of velocity aiding measurements should increase the velocity states' accuracy and approach the full-order filters' performance.

Appendix H contains the 10-run Monte Carlo analysis plots for the 2-hour fighter flight profile. Once again, using the techniques of Section 2.4, this filter has been conservatively tuned for optimum performance. As mentioned in Section 4.4, the variance of the pseudorange measurement equation noise $v(t_i)$ was increased from its full-order value of $9ft^2$ to $30ft^2$ to compensate for the eliminated DGPS states. Also, a dynamics equation noise of $10^{-16}rad^2/sec$ is added to the first two INS states to compensate for the 21 eliminated states. It is of interest to note

Table 5.5. Temporal Average of the Ensemble Average of True Errors for NRS, 89-State ENRS, and 48-State ENRS Filters

Filter	Latitude (ft)	Longitude (ft)	Altitude (ft)	East Vel (fps)	North Vel (fps)	Up Vel (fps)	East Tilt (arcs)	North Tilt (arcs)	Azimuth (arcs)
CIRIS	14.00	14.00	40.00	0.100	0.100	0.400			
128-NRS	1.59	2.35	5.58	0.015	0.011	0.045	1.65	2.02	12.83
97-NRS	1.35	2.71	5.28	0.014	0.010	0.045	1.07	1.29	9.74
69-NRS	3.28	4.21	9.04	0.033	0.026	0.070	1.37	2.11	18.42
89-ENRS	0.84	1.04	3.80	0.013	0.010	0.042	0.94	1.29	6.46
48-ENRS-P	0.90	1.32	3.05	0.027	0.020	0.044	3.83	4.09	19.23

that the 21 eliminated INS states actually feed into the velocity and attitude error states, but these states need no increase in noise, while the position-related states do need noise added for acceptable tuning. Once again, this 48-state reduced-order ENRS filter with DGPS pseudorange and RRS range measurements increases the navigation solution accuracy in position by better than one order of magnitude compared to CIRIS. Now the velocity aiding filters are explored to analyze how velocity measurements can increase INS velocity error-state estimation accuracy.

5.4 Velocity-Aiding Filters

The filters analyzed in this section implement velocity-aiding measurements into the DGPS and RRS subsystems. By implementing the DGPS delta-range and RRS range-rate equations separately in this way, each measurement is separately tuned for optimal performance before they are merged together into the final 48-state ENRS filter. Also, separating the DGPS and RRS error models allows faster execution of the simulations so that more tuning runs can be performed in a shorter period of time. All of these simulations operate in double precision mode using a 10-run Monte Carlo analysis.

5.4.1 *The 22-State DGPS Filter.* This section analyzes the results of the 22-state DGPS filter used for DGPS delta-range measurement equation implementation. Table 5.6 contains three entries for the 22-state DGPS filter. The first entry "22-DGPS-P" displays the average errors for the 22-state filter using only pseudorange measurements during a 10-run Monte Carlo fighter flight profile analysis. No plots are included in the appendixes for this filter; it is evaluated simply to establish a baseline to show what the true navigation solution errors are without delta-range measurements. The second entry for this filter, "22-DGPS-1", is a 10-run Monte Carlo fighter profile analysis incorporating DGPS delta-range measurements. The third entry, "22-DGPS-2" utilizes a straight flight profile in its 10-run analysis.

Table 5.6. Temporal Average of the Ensemble Average of True Errors for Previous and 22-State DGPS (Velocity Aiding) Filters

Filter	Latitude (ft)	Longitude (ft)	Altitude (ft)	East Vel (fps)	North Vel (fps)	Up Vel (fps)	East Tilt (arcs)	North Tilt (arcs)	Azi- muth (arcs)
CIRIS	14.00	14.00	40.00	0.100	0.100	0.400			
128-NRS	1.59	2.35	5.58	0.015	0.011	0.045	1.65	2.02	12.83
97-NRS	1.35	2.71	5.28	0.014	0.010	0.045	1.07	1.29	9.74
69-NRS	3.28	4.21	9.04	0.033	0.026	0.070	1.37	2.11	18.42
89-ENRS	0.84	1.04	3.80	0.013	0.010	0.042	0.94	1.29	6.46
48-ENRS-P	0.90	1.32	3.05	0.027	0.020	0.044	3.83	4.09	19.23
22-DGPS-P	1.95	1.84	3.14	0.037	0.044	0.052	5.28	3.94	29.85
22-DGPS-1	2.10	1.96	3.25	0.043	0.051	0.063	5.46	4.33	45.02
22-DGPS-2	2.20	2.14	3.33	0.044	0.049	0.060	5.56	4.09	63.24

The filter performance plots for the delta-range DGPS filters are located in Appendix I (22-DGPS-1 and -2). As seen from the plots and the values in Table 5.6, the DGPS delta-range measurement is corrupting the position and velocity error-state estimation in these filters a small amount (remember position errors are part of the delta-range measurement). This degradation in filter performance is likely to be caused by cross-correlations of the position and velocity measurements which are

not modeled in this thesis, and it is currently being investigated to solve this problem. However, even with this anomaly, this reduced-order filter performs as well or better than the 69-state reduced-order NRS filter (a reduced-order DGPS only filter versus a reduced-order GPS/RRS filter issue). Assuming the anomaly with the DGPS delta-range measurement equation is remedied, this 22-state DGPS filter is expected to produce position and velocity error estimates 50 percent more accurate than the 69-state NRS filter and on par with the other full-order filters discussed previously. The DGPS delta-range measurement is implemented exactly as discussed in Section 4.5.1, with no changes required in state dynamics noise or measurement noise from the truth model values. This is not unusual since no measurement states have been eliminated, essentially a "full-order" measurement equation. Since the DGPS delta-range and RRS range-rate measurements are very similar, it is no surprise if the 46-state CIRIS filter analyzed in the next section suffers from the same anomaly as the 22-state DGPS filter.

5.4.2 The 46-State CIRIS Filter. Again, this filter is implemented to evaluate RRS range-rate measurements optimally before they are incorporated with DGPS delta-range measurements in the 48-state ENRS filter. Table 5.7 contains values for three CIRIS filters similar to the DGPS filters discussed in the previous section. The first filter, "46-CIRIS-P", is a 46-state filter incorporating only RRS range measurements. It is used as a baseline to evaluate the performance of the range-rate measurement equations. No plots are contained in appendices for this 10-run Monte Carlo fighter profile analysis since filters utilizing only RRS range measurements have been thoroughly covered in previous thesis (20, 19, 22). The results of the second CIRIS filter, "46-CIRIS-1", are derived from a 10-run Monte Carlo fighter profile analysis using RRS range and range-rate measurements. The third filter, "46-CIRIS-2", was analyzed with 10-run analysis using a racetrack flight profile and also incorporates RRS range and range-rate measurements.

Table 5.7. Temporal Average of the Ensemble Average of True Errors for Previous and 46-State CIRIS (Velocity Aiding) Filters

Filter	Latitude (ft)	Longitude (ft)	Altitude (ft)	East Vel (fps)	North Vel (fps)	Up Vel (fps)	East Tilt (arcs)	North Tilt (arcs)	Azimuth (arcs)
CIRIS	14.00	14.00	40.00	0.100	0.100	0.400			
128-NRS	1.59	2.35	5.58	0.015	0.011	0.045	1.65	2.02	12.83
97-NRS	1.35	2.71	5.28	0.014	0.010	0.045	1.07	1.29	9.74
69-NRS	3.28	4.21	9.04	0.033	0.026	0.070	1.37	2.11	18.42
89-ENRS	0.84	1.04	3.80	0.013	0.010	0.042	0.94	1.29	6.46
48-ENRS-P	0.90	1.32	3.05	0.027	0.020	0.044	3.83	4.09	19.23
22-DGPS-P	1.95	1.84	3.14	0.037	0.044	0.052	5.28	3.94	29.85
22-DGPS-1	2.10	1.96	3.25	0.043	0.051	0.063	5.46	4.33	45.02
22-DGPS-2	2.20	2.14	3.33	0.044	0.049	0.060	5.56	4.09	63.24
46-CIRIS-P	3.12	6.84	18.09	0.046	0.026	0.100	4.01	4.39	47.48
46-CIRIS-1	2.80	6.40	11.87	0.042	0.024	0.046	4.01	4.34	45.53
46-CIRIS-2	3.91	6.20	8.94	0.039	0.026	0.044	4.08	4.13	12.92

Appendix J contains the filter performance plots for the filters utilizing range and range-rate measurements (46-CIRIS-1 and -2). In this filter, the range-rate measurements are not corrupting the position states, but they do not improve the velocity states' estimation except possibly in the vertical channel. In this filter, the velocity measurement anomaly does not have a pronounced effect as in the DGPS filter, possibly because the transponders are stationary and the GPS satellites circle the earth. In any case, this anomaly still hinders the evaluation of how much velocity aiding will enhance the navigation solution. The RRS range-rate measurement is implemented exactly as discussed in Section 4.6.1, with no changes required in state dynamics noise or measurement noise from the truth model values. Again, this is not unusual since no measurements states have been eliminated, essentially producing a "full-order" measurement equation. For completeness and in the hopes the anomaly is eventually corrected, both DGPS delta-range and RRS range-rate measurement equations are merged into the 48-state ENRS filter in the next section.

5.5 The Complete 48-State ENRS Filter

Because the velocity aiding measurements do not cause the DGPS or CIRIS filters to diverge or become unstable, a decision is made to proceed with incorporating DGPS delta-range and RRS range-rate measurements into the 48-state ENRS filter. This way, when the anomaly is discovered, the Fortran code can be quickly fixed and filter analysis preformed. Table 5.8 contains the true errors for the navigation solution for all filters discussed and implemented in this thesis. Notice that even with velocity measurement corruption, the 48-state ENRS filter performs much better than CIRIS or even the 69-state NRS filter. In fact, its position error-state estimation is one of the best, even with the anomaly present.

Table 5.8. Temporal Average of the Ensemble Average of True Errors for All Filters

Filter	Latitude (ft)	Longitude (ft)	Altitude (ft)	East Vel (fps)	North Vel (fps)	Up Vel (fps)	East Tilt (arcs)	North Tilt (arcs)	Azimuth (arcs)
CIRIS	14.00	14.00	40.00	0.100	0.100	0.400			
128-NRS	1.59	2.35	5.58	0.015	0.011	0.045	1.65	2.02	12.83
97-NRS	1.35	2.71	5.28	0.014	0.010	0.045	1.07	1.29	9.74
69-NRS	3.28	4.21	9.04	0.033	0.026	0.070	1.37	2.11	18.42
89-ENRS	0.84	1.04	3.80	0.013	0.010	0.042	0.94	1.29	6.46
48-ENRS-P	0.90	1.32	3.05	0.027	0.020	0.044	3.83	4.09	19.23
22-DGPS-P	1.95	1.84	3.14	0.037	0.044	0.052	5.28	3.94	29.85
22-DGPS-1	2.10	1.96	3.25	0.043	0.051	0.063	5.46	4.33	45.02
22-DGPS-2	2.20	2.14	3.33	0.044	0.049	0.060	5.56	4.09	63.24
46-CIRIS-P	3.12	6.84	18.09	0.046	0.026	0.100	4.01	4.39	47.48
46-CIRIS-1	2.80	6.40	11.87	0.042	0.024	0.046	4.01	4.34	45.53
46-CIRIS-2	3.91	6.20	8.94	0.039	0.026	0.044	4.08	4.13	12.92
48-ENRS	1.19	1.80	5.46	0.040	0.029	0.087	5.14	4.92	31.21

Plots of this filter's state estimation performance can be found in Appendix K. These plots represent a 25-run Monte-Carlo analysis of the fighter flight profile. No changes were made to the dynamics equation or measurement noises other than those discussed in previous sections. It appears that when the velocity measurement

equations anomaly is remedied, this 48-state ENRS filter will produce navigation solutions one order of magnitude more accurate than current CIRIS system, and will rival any of the full-order filters implemented or analyzed in this thesis.

5.6 Filter Tuning Parameters

This section contains tables of the filter tuning parameter's ($Q(t)$ and $R(t_i)$) final values for the filters implemented in this thesis when the values were different from the truth model values. Table 5.9 lists the $Q(t)$ values from among the first 20 INS error-states. The listed states were the only states requiring tuning when a 20-state INS filter model was implemented, and the tuning values were the same for all the filters. For a definition of the listed states, consult Table A.7 in Appendix A.

Table 5.9. INS States Tuning Parameters $Q(t)$

State Number	State Symbol	Truth Model Value	Filter Value
1	$\delta\theta_x$	0.0	$10^{-16} \text{rad}^2/\text{sec}$
2	$\delta\theta_y$	0.0	$10^{-16} \text{rad}^2/\text{sec}$
12	δS_3	0.0	$10^{-8} \text{ft}^2/\text{sec}^3$
13	δS_4	0.0	$10^{-5} \text{ft}^2/\text{sec}$
14	∇_{x_c}	0.0	$10^{-18} \text{rad}^2/\text{sec}$
15	∇_{y_c}	0.0	$10^{-18} \text{rad}^2/\text{sec}$
16	∇_{z_c}	0.0	$10^{-18} \text{rad}^2/\text{sec}$
17	δg_x	0.0	$10^{-12} \text{ug}^2/\text{sec}$
18	δg_y	0.0	$10^{-12} \text{ug}^2/\text{sec}$
19	δg_z	0.0	$10^{-12} \text{ug}^2/\text{sec}$

Table 5.10 lists the 26 RRS error-state's tuning parameters. All of the RRS error-states required tuning and are listed. Remember that there are range and velocity bias states along with four error states (3 position errors and 1 atmospheric error) for each of six transponders in the truth and filter models throughout this

thesis. Table A.5 in Appendix A contains the definition for each of the states now listed.

Table 5.10. RRS States Tuning Parameters $Q(t)$

State Number	State Symbol	Truth Model Value	Filter Value
1	δR_b	0.0	$10^{-5} ft^2/sec$
2	δv_b	0.0	$10^{-8} ft^2/sec^3$
3, 7,11,15,19,23	$\delta P_{T_{i_x}}$	0.0	$2 \cdot 10^{-3} ft^2/sec$
4, 8,12,16,20,24	$\delta P_{T_{i_y}}$	0.0	$2 \cdot 10^{-3} ft^2/sec$
5, 9,13,17,21,25	$\delta P_{T_{i_z}}$	0.0	$2 \cdot 10^{-3} ft^2/sec$
6,10,14,18,22,26	$\delta R_{T_{i_a}}$	$6.66 \cdot 10^{-13} ft^2/sec$	$6.66 \cdot 10^{-6} ft^2/sec$

Table 5.11 lists the 30 GPS error-state's tuning parameters. Most of the GPS error-states required tuning, so they are all listed. Listed are receiver clock bias and drift error-states along with seven error-states (1 code-loop, 2 atmosphere, 1 SV clock, and 3 position errors) for each of 4 SVs in the full-order filter models throughout this thesis. The reduced-order GPS filters only include the two clock error-states but are still tuned with the values shown below for these two states. Table A.6 in Appendix A contains the definition for each of the states now listed.

Table 5.12 lists the 22 DGPS error-state's tuning parameters. All of the DGPS error-states required tuning, so they are all listed. Listed are receiver clock bias and drift error-states along with five error-states (2 atmosphere and 3 position errors) for each of 4 SVs in the full-order filter models throughout this thesis. The reduced-order DGPS filters only include the two clock error-states but are still tuned with the values shown below for these two states. Table A.9 in Appendix A contains the definition for each of the states now listed.

Table 5.11. GPS States Tuning Parameters $Q(t)$

State Number	State Symbol	Truth Model Value	Filter Value
1	δR_{clk_u}	0.0	$10^{-2} ft^2/sec$
2	δD_{clk_u}	0.0	$10^{-6} ft^2/sec$
3,10,17,24	δR_{loop_i}	$0.5 ft^2/sec$	$0.5 ft^2/sec$
4,11,18,25	δR_{trop_i}	$4 \cdot 10^{-3} ft^2/sec$	$4 \cdot 10^{-3} ft^2/sec$
5,12,19,26	δR_{ion_i}	$4 \cdot 10^{-3} ft^2/sec$	$4 \cdot 10^{-3} ft^2/sec$
6,13,20,27	$\delta R_{clk_{sv_i}}$	0.0	$10^{-8} ft^2/sec$
7,14,21,28	δx_{sv_i}	0.0	$10^{-2} ft^2/sec$
8,15,22,29	δy_{sv_i}	0.0	$10^{-2} ft^2/sec$
9,16,23,30	δz_{sv_i}	0.0	$10^{-2} ft^2/sec$

Table 5.12. DGPS States Tuning Parameters $Q(t)$

State Number	State Symbol	Truth Model Value	Filter Value
1	δR_{Uclk_u}	0.0	$10^{-2} ft^2/sec$
2	δD_{Uclk_u}	0.0	$10^{-6} ft^2/sec$
3, 8,13,18	δR_{trop_i}	$1 \cdot 10^{-3} ft^2/sec$	$5 \cdot 10^{-4} ft^2/sec$
4, 9,14,19	δR_{ion_i}	$4 \cdot 10^{-4} ft^2/sec$	$15 \cdot 10^{-4} ft^2/sec$
5,10,15,20	δx_{sv_i}	0.0	$1 \cdot 10^{-4} ft^2/sec$
6,11,16,21	δy_{sv_i}	0.0	$1 \cdot 10^{-4} ft^2/sec$
7,12,17,22	δz_{sv_i}	0.0	$1 \cdot 10^{-4} ft^2/sec$

The last table in this section lists the final $R(t_i)$ value for the GPS/DGPS pseudorange measurement for the reduced-order filters implemented in this thesis. The full-order GPS/DGPS filters measurement noise variance is always $9 ft^2$. The RRS range measurement noise variance is always $4 ft^2$. Only the 69-state NRS, 48-state ENRS, and 22-state DGPS reduced-order filters need adjustment of their pseudorange measurement noise variance, so only values for these filters are listed.

Table 5.13. GPS/DGPS Measurement Noise Variance Tuning Parameters $R(t_i)$

Filter	Truth Model Value	Filter Value
69-State NRS	$9ft^2$	$300ft^2$
48-State ENRS	$9ft^2$	$30ft^2$
22-State DGPS	$9ft^2$	$30ft^2$

5.7 Summary

This chapter discusses the results of all the filters designed, implemented, and analyzed in this thesis. As expected, the full-order filters perform better than the reduced order filters, while the filters utilizing DGPS measurements outperform filters with only GPS measurements. Again as a reminder, the truth model for the INS is 41 states (except for Stacey's 72-state model), the RRS truth model is 26 states, the GPS truth model 30 states, and the DGPS truth model is 22 states. The anomaly in the velocity-aiding measurement equations hindered the analysis of the filters implementing this type of measurement. However, every filter in this thesis significantly outperforms CIRIS and shows the benefit of augmenting the RRS transponder measurements with GPS and DGPS measurements.

VI. *Conclusions and Recommendations*

6.1 *Conclusions*

6.1.1 *The NRS Filters.* All three NRS filters performed well and greatly increased the accuracy of the navigation solution over CIRIS as it is implemented today. The following sections contain specific conclusions drawn from the NRS filters' performance while recommendations derived from their implementation are found later in this chapter.

6.1.1.1 *41-State INS Model.* The 41-state INS error model proves to be an adequate substitute for the 93-state LN-93 INS error model in both the truth and filters models were it was utilized. As shown in Appendix C, the 41-state error model followed the 93-state error model to within one percent over the entire fighter flight trajectory with respect to position, velocity, and attitude errors. The reader must recognize that the eliminated states from the 93-state model feed into the first ten states in the INS error model, so the remaining INS states (states 11 through 41 in Tables A.7 and A.8 in Appendix A) do not vary from the 93-state error model and plots from these states are not included in Appendix C. This reduction in states in both truth and filter models greatly decreased the time required for filter performance analysis.

6.1.1.2 *Single versus Double Precision.* As stated in Section 5.1.1, double precision is necessary to faithfully model GPS/DGPS measurements in VAX Fortran. Recognizing that every computer system implements precision differently, the reader is warned that 12-bit accuracy is the minimum accuracy required for a 2-hour simulation with receiver clock errors modeled as in this thesis. However, also recognize that the single precision assumption used in the full-order filters implemented in this thesis only affects the initial filter acquisition (estimation) of the receiver

clock errors, and the size of these two clock errors makes the decreased magnitude assumption a viable alternative to double precision simulation analysis.

6.1.1.3 NRS Filter Performance. As stated in Chapter V, the full-order 128- and 97-state NRS filters perform so much alike that any discrepancy in performance shown in the tables is a tuning issue and not a performance issue. However, the 69-state NRS filter performance degrades significantly when compared to the two full-order filters mentioned above. Even though the 69-state filter is not optimally tuned, it is a safe assumption that its position and velocity error estimation accuracy will be worse than the full-order filters. Recognize, though, that the 69-state filter is at least 3 times *more accurate* than the current CIRIS system. This increase in performance can be attributed to the incorporation of GPS pseudorange measurements to augment transponder aiding and more filter states used for the analysis (69 in the NRS versus 11 in CIRIS). How much each of these attributes individually increases performance is not in the scope of this thesis; however, an educated guess would be that increased filter states give the most increase in performance in evaluating the 69-state NRS filter's performance increase over CIRIS.

6.1.2 The ENRS Filters. Like the NRS filters, the ENRS filters all show a great increase in performance over CIRIS. The full-order 89-state ENRS filter outperforms any other filter implemented in this thesis by producing a navigation solution one order of magnitude more accurate than CIRIS. The 48-state reduced-order filter is also very accurate, and produces position error estimates one order of magnitude better than CIRIS along with velocity error estimates 5 times better (using only DGPS pseudorange and RRS range measurements). As stated in Chapter V, the 48-state ENRS filter using position- and velocity-aiding measurements has not been adequately modeled and the corruption of the navigation solution by an anomaly eliminates any meaningful conclusions which can be drawn from this filter.

However, the following section contains a conclusion which can be drawn from the ENRS filters successfully implemented in this thesis.

6.1.2.1 Utility of DGPS. The one main conclusion which can be drawn from the work performed in this thesis, and one which cannot be emphasized enough, is that **incorporation of DGPS pseudorange measurements greatly increases the navigation solution accuracy of CIRIS.** When either the 89-state full-order filter or the 48-state reduced-order filter is analyzed, it is readily apparent that *DGPS provides the increase in navigation solution accuracy required for CIRIS to be used as a test reference against the GPS-aided INSs CIGTF is likely to be testing in the next decade.* This one conclusion is the culmination of the work performed in this thesis and the 3 other theses which preceded it (20, 19, 22).

6.2 Recommendations

There are many recommendations which could be derived from the work performed in this thesis. The following sections contain a few of the most important as determined by the author and the thesis committee.

6.2.1 Velocity-Aiding Measurements Require Further Study. When velocity-aiding measurements (DGPS delta-range and RRS range-rate) were implemented into the 48-state ENRS filter, corruption of both position and velocity error-state estimation precluded performance analysis of the filter. At first, an error in the algorithm implementation was suspected; however, careful analysis proves this not to be the case. Then, the coordinate transformation from the navigation frame (NWU) to Litton ECEF became suspect. When a different transformation was implemented (results not shown in this thesis), the corruption of position and velocity states continued. Finally, during the thesis defense, the correlation between position and velocity measurements in the DGPS subsystem as it is modeled in this thesis (and is performed by the ABR in real life) was brought to the surface. *Since there is a*

definite correlation between position and velocity measurements in the truth and filter models of this thesis, it is necessary to model them as being correlated. This requires further analysis on the part of CIGTF to determine to true correlation values so they can be implemented accurately in the EKF. The measurement noise covariance matrix $\mathbf{R}(t_i)$ is modified to include off-diagonal terms describing the correlation between the position and velocity measurements. Note that when utilizing MSOFE as the EKF evaluation tool, *scaler* measurements are assumed ($\mathbf{R}(t_i)$ is a diagonal matrix) so that for correlated measurements (off-diagonal terms), this matrix must be *diagonalized* before implementation. Unfortunately, Maybeck has stated this lack of correlation between measurements used in this thesis still does not account for the corruption of the navigation solution, since the truth model implements uncorrelated measurements as well (13). This anomaly, which has plagued the three previous theses also (20, 19, 22), remains undefined and a subject for further research.

6.2.2 Return to a 93-State INS Truth Model. The NRS and ENRS truth and filter models developed or analyzed in this thesis assume that either a 72-state INS model (Stacey's NRS) or 41-state INS model (all other models in this thesis) perform close enough to the true 93-state LN-93 error model so that any real difference can be ignored. However, before real measurements are used to test any of the filters, the 93-state INS model should be included in the truth model and filter performance against a full-order truth model analyzed in case further tuning is required.

6.2.3 Use of Real Measurements. Once the velocity-aiding measurements' anomaly has been identified and corrected and the filter analyzed against the true 93-state INS model, actual DGPS and RRS measurements should be used to test the 48-state ENRS filter for robustness. It is a foregone conclusion that the filter will need further tuning for optimal performance, and this tuning can only be accomplished using real measurements.

6.2.4 *Reduction of the RRS error-states in the Filter.* Another worthwhile effort could be the reduction of the 26-state RRS model in the filter to a 2-state model. The RRS range and velocity bias states would be retained (see Table A.5 in Appendix A) with increased variance of the RRS range measurement noise to compensate for the eliminated states. Recognize this reduction does not affect the RRS range-rate measurement since the eliminated states don't appear in this measurement. Also, since DGPS measurements alone provide an accurate navigation solution, only a minimal degradation of the navigation solution should be realized. Preliminary work using this technique has begun utilizing only position-aiding measurements (not included in this thesis), and the results look very encouraging. Note that reduction of the RRS states from 26 to 2 reduces the 48-state ENRS filter to 24 states. This allows for inclusion of the 21 previously eliminated INS states (see Table A.8 in Appendix A) definitely increasing the filter's ability to estimate attitude and velocity error-states while staying under the 70-state post-processing filter limit. This newly proposed filter would in theory have 41 INS error-states, 2 RRS error-states, and 2 DGPS error-states for a total of 45 error-states to be compared to the 89-state ENRS truth model developed in Chapter IV.

Appendix A. *Error Model State Definitions*

This appendix contains a tabular listing of the 93 Litton INS, 26 RRS, 30 GPS, 41 reduced INS truth model, and the 22 DGPS error-states.

A.1 Litton LN-93 Error-States

Tables A.1 through A.4 list the LN-93 error model (93 states) as defined in the Litton CDRL (11). Note that this document contains several errors, which have been corrected in these tables (22).

A.2 RRS Transponder Error States

Table A.5 lists the RRS transponder error states as they are modeled in the NRS. These states are defined in and extracted from (19). A total of 26 states are included to model the error characteristics of six ground transponders plus interrogator error sources (22).

A.3 GPS Error States

Table A.6 lists the GPS error states as they are modeled in the NRS. These states are defined in and extracted from (6). The definitions are believed to be ultimately traceable to the paper by D.B. Cox (4). A total of 30 states are included to model the error characteristics of 4 space vehicles plus user equipment error sources. (22)

A.4 Reduced Order INS Truth Model States

Tables A.7 and A.8 list the 41 INS states used in all the full-order models in this thesis except for Stacey's 128-state model. These states are based on the the recommendations of Lewantowicz and Keen (10).

A.5 DGPS Error States

Table A.9 lists the DGPS error states as they are modeled in the ENRS. A total of 22 states are included to model the error characteristics of 4 space vehicles plus user equipment error sources.

Table A.1. INS System Model: INS States 1 → 29

State Number	State Symbol	Definition
1	$\delta\theta_x$	X-component of vector angle from true to computer frame
2	$\delta\theta_y$	Y-component of vector angle from true to computer frame
3	$\delta\theta_z$	Z-component of vector angle from true to computer frame
4	ϕ_x	X-component of vector angle from true to platform frame
5	ϕ_y	Y-component of vector angle from true to platform frame
6	ϕ_z	Z-component of vector angle from true to platform frame
7	δV_x	X-component of error in computed velocity
8	δV_y	Y-component of error in computed velocity
9	δV_z	Z-component of error in computed velocity
10	δh	Error in vehicle altitude above reference ellipsoid
11	δh_L	Error in lagged inertial altitude
12	δS_3	Error in vertical channel aiding state
13	δS_4	Error in vertical channel aiding state
14	b_{x_c}	X-component of gyro correlated drift rate
15	b_{y_c}	Y-component of gyro correlated drift rate
16	b_{z_c}	Z-component of gyro correlated drift rate
17	∇_{x_c}	X-component of accelerometer and velocity quantizer correlated noise
18	∇_{y_c}	Y-component of accelerometer and velocity quantizer correlated noise
19	∇_{z_c}	Z-component of accelerometer and velocity quantizer correlated noise
20	δg_x	X-component of gravity vector errors
21	δg_y	Y-component of gravity vector errors
22	δg_z	Z-component of gravity vector errors
23	δh_B	Total baro-altimeter correlated error
24	b_{x_t}	X-component of gyro trend
25	b_{y_t}	Y-component of gyro trend
26	b_{z_t}	Z-component of gyro trend
27	∇_{x_t}	X-component of accelerometer trend
28	∇_{y_t}	Y-component of accelerometer trend
29	∇_{z_t}	Z-component of accelerometer trend

Table A.2. INS System Model: INS States 30 → 47

State Number	State Symbol	Definition
30	b_x	X-component of gyro drift rate repeatability
31	b_y	Y-component of gyro drift rate repeatability
32	b_z	Z-component of gyro drift rate repeatability
33	S_{g_x}	X-component of gyro scale factor error
34	S_{g_y}	Y-component of gyro scale factor error
35	S_{g_z}	Z-component of gyro scale factor error
36	χ_1	X gyro misalignment about Y-axis
37	χ_2	Y gyro misalignment about X-axis
38	χ_3	Z gyro misalignment about X-axis
39	ν_1	X gyro misalignment about Z-axis
40	ν_2	Y gyro misalignment about Z-axis
41	ν_3	Z gyro misalignment about Y-axis
42	D_{xxx}	X gyro scale factor non-linearity
43	D_{yyy}	Y gyro scale factor non-linearity
44	D_{zzz}	Z gyro scale factor non-linearity
45	S_{Qb_x}	X gyro scale factor asymmetry error
46	S_{Qb_y}	Y gyro scale factor asymmetry error
47	S_{Qb_z}	Z gyro scale factor asymmetry error

Table A.3. INS System Model: INS States 48 → 69

State Number	State Symbol	Definition
48	∇_{b_x}	X-component of accelerometer bias repeatability
49	∇_{b_y}	Y-component of accelerometer bias repeatability
50	∇_{b_z}	Z-component of accelerometer bias repeatability
51	S_{A_x}	X-component of accelerometer and velocity quantizer scale factor error
52	S_{A_y}	Y-component of accelerometer and velocity quantizer scale factor error
53	S_{A_z}	Z-component of accelerometer and velocity quantizer scale factor error
54	S_{QA_x}	X-component of accelerometer and velocity quantizer scale factor asymmetry
55	S_{QA_y}	Y-component of accelerometer and velocity quantizer scale factor asymmetry
56	S_{QA_z}	Z-component of accelerometer and velocity quantizer scale factor asymmetry
57	f_{xx}	Coefficient of error proportional to square of measured acceleration
58	f_{yy}	Coefficient of error proportional to square of measured acceleration
59	f_{zz}	Coefficient of error proportional to square of measured acceleration
60	f_{xy}	Coefficient of error proportional to products of acceleration along and orthogonal to accelerometer sensitive axis
61	f_{xz}	Coefficient of error proportional to products of acceleration along and orthogonal to accelerometer sensitive axis
62	f_{yx}	Coefficient of error proportional to products of acceleration along and orthogonal to accelerometer sensitive axis
63	f_{yz}	Coefficient of error proportional to products of acceleration along and orthogonal to accelerometer sensitive axis
64	f_{zx}	Coefficient of error proportional to products of acceleration along and orthogonal to accelerometer sensitive axis
65	f_{zy}	Coefficient of error proportional to products of acceleration along and orthogonal to accelerometer sensitive axis
66	μ_1	X accelerometer misalignment about Z-axis
67	μ_2	Y accelerometer misalignment about Z-axis
68	μ_3	Z accelerometer misalignment about Y-axis
69	σ_3	Z-accelerometer misalignment about X-axis

Table A.4. INS System Model: INS States 70 → 93

State Number	State Symbol	Definition
70	∇_{xq}	X-component of accelerometer bias thermal transient
71	∇_{yq}	Y-component of accelerometer bias thermal transient
72	∇_{zq}	Z-component of accelerometer bias thermal transient
73	b_{xq}	X-component of initial gyro drift rate bias thermal transient
74	b_{yq}	Y-component of initial gyro drift rate bias thermal transient
75	b_{zq}	Z-component of initial gyro drift rate bias thermal transient
76	F_{xyz}	X gyro compliance term
77	F_{xyy}	X gyro compliance term
78	F_{xyx}	X gyro compliance term
79	F_{xzy}	X gyro compliance term
80	F_{xzz}	X gyro compliance term
81	F_{xxz}	X gyro compliance term
82	F_{yzz}	Y gyro compliance term
83	F_{yzz}	Y gyro compliance term
84	F_{yzy}	Y gyro compliance term
85	F_{yzz}	Y gyro compliance term
86	F_{yzz}	Y gyro compliance term
87	F_{yzy}	Y gyro compliance term
88	F_{zzy}	Z gyro compliance term
89	F_{zxx}	Z gyro compliance term
90	F_{zxx}	Z gyro compliance term
91	F_{zyx}	Z gyro compliance term
92	F_{zyy}	Z gyro compliance term
93	F_{zyz}	Z gyro compliance term

Table A.5. RRS Error States

State Number	State Symbol	Definition [NOTE: S_{INS} = Total INS States]
$S_{INS} + 1$	δR_b	Range error due to equipment bias
$S_{INS} + 2$	δv_b	Velocity error due to equipment bias
$S_{INS} + 3$	δP_{T1_x}	Transponder 1 x-component of position error
$S_{INS} + 4$	δP_{T1_y}	Transponder 1 y-component of position error
$S_{INS} + 5$	δP_{T1_z}	Transponder 1 z-component of position error
$S_{INS} + 6$	δR_{T1_o}	Transponder 1 range error due to atm propagation
$S_{INS} + 7$	δP_{T2_x}	Transponder 2 x-component of position error
$S_{INS} + 8$	δP_{T2_y}	Transponder 2 y-component of position error
$S_{INS} + 9$	δP_{T2_z}	Transponder 2 z-component of position error
$S_{INS} + 10$	δR_{T2_o}	Transponder 2 range error due to atm propagation
$S_{INS} + 11$	δP_{T3_x}	Transponder 3 x-component of position error
$S_{INS} + 12$	δP_{T3_y}	Transponder 3 y-component of position error
$S_{INS} + 13$	δP_{T3_z}	Transponder 3 z-component of position error
$S_{INS} + 14$	δR_{T3_o}	Transponder 3 range error due to atm propagation
$S_{INS} + 15$	δP_{T4_x}	Transponder 4 x-component of position error
$S_{INS} + 16$	δP_{T4_y}	Transponder 4 y-component of position error
$S_{INS} + 17$	δP_{T4_z}	Transponder 4 z-component of position error
$S_{INS} + 18$	δR_{T4_o}	Transponder 4 range error due to atm propagation
$S_{INS} + 19$	δP_{T5_x}	Transponder 5 x-component of position error
$S_{INS} + 20$	δP_{T5_y}	Transponder 5 y-component of position error
$S_{INS} + 21$	δP_{T5_z}	Transponder 5 z-component of position error
$S_{INS} + 22$	δR_{T5_o}	Transponder 5 range error due to atm propagation
$S_{INS} + 23$	δP_{T6_x}	Transponder 6 x-component of position error
$S_{INS} + 24$	δP_{T6_y}	Transponder 6 y-component of position error
$S_{INS} + 25$	δP_{T6_z}	Transponder 6 z-component of position error
$S_{INS} + 26$	δR_{T6_o}	Transponder 6 range error due to atm propagation

Table A.6. GPS Error States

State Number	State Symbol	Definition [NOTE: S_{RRS} = Total RRS States]
$S_{INS} + S_{RRS} + 1$	δR_{clk_u}	User clock bias
$S_{INS} + S_{RRS} + 2$	δD_{clk_u}	User clock drift
$S_{INS} + S_{RRS} + 3$	δR_{cloop_1}	SV 1 code loop error
$S_{INS} + S_{RRS} + 4$	δR_{trop_1}	SV 1 tropospheric error
$S_{INS} + S_{RRS} + 5$	δR_{ion_1}	SV 1 ionospheric error
$S_{INS} + S_{RRS} + 6$	$\delta R_{clk_{sv_1}}$	SV 1 clock error
$S_{INS} + S_{RRS} + 7$	δx_{sv_1}	SV 1 x-component of position error
$S_{INS} + S_{RRS} + 8$	δy_{sv_1}	SV 1 y-component of position error
$S_{INS} + S_{RRS} + 9$	δz_{sv_1}	SV 1 z-component of position error
$S_{INS} + S_{RRS} + 10$	δR_{cloop_2}	SV 2 code loop error
$S_{INS} + S_{RRS} + 11$	δR_{trop_2}	SV 2 tropospheric error
$S_{INS} + S_{RRS} + 12$	δR_{ion_2}	SV 2 ionospheric error
$S_{INS} + S_{RRS} + 13$	$\delta R_{clk_{sv_2}}$	SV 2 clock error
$S_{INS} + S_{RRS} + 14$	δx_{sv_2}	SV 2 x-component of position error
$S_{INS} + S_{RRS} + 15$	δy_{sv_2}	SV 2 y-component of position error
$S_{INS} + S_{RRS} + 16$	δz_{sv_2}	SV 2 z-component of position error
$S_{INS} + S_{RRS} + 17$	δR_{cloop_3}	SV 3 code loop error
$S_{INS} + S_{RRS} + 18$	δR_{trop_3}	SV 3 tropospheric error
$S_{INS} + S_{RRS} + 19$	δR_{ion_3}	SV 3 ionospheric error
$S_{INS} + S_{RRS} + 20$	$\delta R_{clk_{sv_3}}$	SV 3 clock error
$S_{INS} + S_{RRS} + 21$	δx_{sv_3}	SV 3 x-component of position error
$S_{INS} + S_{RRS} + 22$	δy_{sv_3}	SV 3 y-component of position error
$S_{INS} + S_{RRS} + 23$	δz_{sv_3}	SV 3 z-component of position error
$S_{INS} + S_{RRS} + 24$	δR_{cloop_4}	SV 4 code loop error
$S_{INS} + S_{RRS} + 25$	δR_{trop_4}	SV 4 tropospheric error
$S_{INS} + S_{RRS} + 26$	δR_{ion_4}	SV 4 ionospheric error
$S_{INS} + S_{RRS} + 27$	$\delta R_{clk_{sv_4}}$	SV 4 clock error
$S_{INS} + S_{RRS} + 28$	δx_{sv_4}	SV 4 x-component of position error
$S_{INS} + S_{RRS} + 29$	δy_{sv_4}	SV 4 y-component of position error
$S_{INS} + S_{RRS} + 30$	δz_{sv_4}	SV 4 z-component of position error

Table A.7. Reduced-Order INS System Model: INS States 1 → 20

State Number	State Symbol	Definition
1	$\delta\theta_x$	X-component of vector angle from true to computer frame
2	$\delta\theta_y$	Y-component of vector angle from true to computer frame
3	$\delta\theta_z$	Z-component of vector angle from true to computer frame
4	ϕ_x	X-component of vector angle from true to platform frame
5	ϕ_y	Y-component of vector angle from true to platform frame
6	ϕ_z	Z-component of vector angle from true to platform frame
7	δV_x	X-component of error in computed velocity
8	δV_y	Y-component of error in computed velocity
9	δV_z	Z-component of error in computed velocity
10	δh	Error in vehicle altitude above reference ellipsoid
11	δh_L	Error in lagged inertial altitude
12	δS_3	Error in vertical channel aiding state
13	δS_4	Error in vertical channel aiding state
14	∇_{x_c}	X-component of accelerometer and velocity quantizer correlated noise
15	∇_{y_c}	Y-component of accelerometer and velocity quantizer correlated noise
16	∇_{z_c}	Z-component of accelerometer and velocity quantizer correlated noise
17	δg_x	X-component of gravity vector errors
18	δg_y	Y-component of gravity vector errors
19	δg_z	Z-component of gravity vector errors
20	δh_s	Total baro-altimeter correlated error

Table A.8. Reduced-Order INS System Model: INS States 21 → 41

State Number	State Symbol	Definition
21	b_x	X-component of gyro drift rate repeatability
22	b_y	Y-component of gyro drift rate repeatability
23	b_z	Z-component of gyro drift rate repeatability
24	S_{g_x}	X-component of gyro scale factor error
25	S_{g_y}	Y-component of gyro scale factor error
26	S_{g_z}	Z-component of gyro scale factor error
27	∇_{b_x}	X-component of accelerometer bias repeatability
28	∇_{b_y}	Y-component of accelerometer bias repeatability
29	∇_{b_z}	Z-component of accelerometer bias repeatability
30	S_{A_x}	X-component of accelerometer and velocity quantizer scale factor error
31	S_{A_y}	Y-component of accelerometer and velocity quantizer scale factor error
32	S_{A_z}	Z-component of accelerometer and velocity quantizer scale factor error
33	S_{QA_x}	X-component of accelerometer and velocity quantizer scale factor asymmetry
34	S_{QA_y}	Y-component of accelerometer and velocity quantizer scale factor asymmetry
35	S_{QA_z}	Z-component of accelerometer and velocity quantizer scale factor asymmetry
36	μ_1	X accelerometer misalignment about Z-axis
37	μ_2	Y accelerometer misalignment about Z-axis
38	μ_3	Z accelerometer misalignment about Y-axis
39	σ_1	X-accelerometer misalignment about Y-axis
40	σ_2	Y-accelerometer misalignment about X-axis
41	σ_3	Z-accelerometer misalignment about X-axis

Table A.9. DGPS Error States

State Number	State Symbol	Definition [NOTE: S_{RRS} = Total RRS States]
$S_{INS} + S_{RRS} + 1$	δR_{Uclk_u}	ABR clock bias
$S_{INS} + S_{RRS} + 2$	δD_{Uclk_u}	ABR clock drift
$S_{INS} + S_{RRS} + 3$	δR_{trop1}	SV 1 tropospheric error
$S_{INS} + S_{RRS} + 4$	δR_{ion1}	SV 1 ionospheric error
$S_{INS} + S_{RRS} + 5$	δx_{sv1}	SV 1 x-component of position error
$S_{INS} + S_{RRS} + 6$	δy_{sv1}	SV 1 y-component of position error
$S_{INS} + S_{RRS} + 7$	δz_{sv1}	SV 1 z-component of position error
$S_{INS} + S_{RRS} + 8$	δR_{trop2}	SV 2 tropospheric error
$S_{INS} + S_{RRS} + 9$	δR_{ion2}	SV 2 ionospheric error
$S_{INS} + S_{RRS} + 10$	δx_{sv2}	SV 2 x-component of position error
$S_{INS} + S_{RRS} + 11$	δy_{sv2}	SV 2 y-component of position error
$S_{INS} + S_{RRS} + 12$	δz_{sv2}	SV 2 z-component of position error
$S_{INS} + S_{RRS} + 13$	δR_{trop3}	SV 3 tropospheric error
$S_{INS} + S_{RRS} + 14$	δR_{ion3}	SV 3 ionospheric error
$S_{INS} + S_{RRS} + 15$	δx_{sv3}	SV 3 x-component of position error
$S_{INS} + S_{RRS} + 16$	δy_{sv3}	SV 3 y-component of position error
$S_{INS} + S_{RRS} + 17$	δz_{sv3}	SV 3 z-component of position error
$S_{INS} + S_{RRS} + 18$	δR_{trop4}	SV 4 tropospheric error
$S_{INS} + S_{RRS} + 19$	δR_{ion4}	SV 4 ionospheric error
$S_{INS} + S_{RRS} + 20$	δx_{sv4}	SV 4 x-component of position error
$S_{INS} + S_{RRS} + 21$	δy_{sv4}	SV 4 y-component of position error
$S_{INS} + S_{RRS} + 32$	δz_{sv4}	SV 4 z-component of position error

Appendix B. *Litton LN-93 Error-State Model Dynamics Matrix*

(22)

The LN-93 error-state dynamics matrix (F) as provided by Litton is a 93-by-93 array that contains a large number of elements that are identically zero. Litton partitions the F matrix into thirty-six subarrays (11) reflecting the logical divisions of error sources discussed in Chapter III.

The reader should note that only the NON-ZERO elements are included in the tables which follow, and should further note that the revised baro-altimeter model states are NOT included in this set of ORIGINAL F matrix elements extracted from the Litton document (11).

A notational convention (22) is to label elements of the C_s^t , sensor-to-true, matrix as C_{ij} where i is the row and j is the column in the transformation matrix.

Table B.1. Elements of the Dynamics Submatrix F_{11} (22)

Element	Term	Element	Term
(1,3)	$-\rho_y$	(1,8)	$-C_{RY}$
(2,3)	ρ_x	(2,7)	C_{RX}
(3,1)	ρ_y	(3,2)	$-\rho_x$
(4,2)	$-\Omega_z$	(4,3)	Ω_y
(4,5)	ω_{it_x}	(4,6)	$-\omega_{it_y}$
(4,8)	$-C_{RY}$	(5,1)	Ω_x
(5,3)	$-\Omega_x$	(5,4)	$-\omega_{it_x}$
(5,6)	ω_{it_x}	(5,7)	C_{RX}
(6,1)	$-\Omega_y$	(6,2)	Ω_x
(6,4)	ω_{it_y}	(6,5)	$-\omega_{it_x}$
(7,1)	$-2V_y\Omega_y - 2V_z\Omega_z$	(7,2)	$2V_y\Omega_x$
(7,3)	$2V_z\Omega_y$	(7,5)	$-A_z$
(7,6)	A_y	(7,7)	$-V_zC_{RX}$
(7,8)	$2\Omega_z$	(7,9)	$-\rho_y - 2\Omega_y$
(8,1)	$2V_x\Omega_y$	(8,2)	$-2V_x\Omega_x - 2V_z\Omega_z$
(8,3)	$2v_z\Omega_y$	(8,4)	A_z
(8,6)	$-A_x$	(8,7)	$-2\Omega_z$
(8,8)	$-V_zC_{RY}$	(8,9)	$\rho_x + 2\Omega_x$
(9,1)	$2V_x\Omega_z$	(9,2)	$2V_y\Omega_z$
(9,3)	$-2V_y\Omega_y - 2V_z\Omega_x$	(9,4)	$-A_y$
(9,5)	A_x	(9,7)	$\rho_y + 2\Omega_y + V_xC_{RX}$
(9,8)	$-\rho_x - 2\Omega_x + V_yC_{RY}$	(9,10)	$2g_o/a$
(9,11)	$-k_2$	(9,12)	-1
(9,13)	k_2	(10,9)	1
(10,11)	$-k_1$	(10,13)	$k_1 - 1$
(11,10)	1	(11,11)	-1
(12,11)	k_3	(12,13)	$-k_3$
(13,10)	k_4	(13,11)	$-k_4$
(13,13)	$k_4 - 1$		

Table B.2. Elements of the Dynamics Submatrix F_{12} (22)

Element	Term	Element	Term	Element	Term
(4,14)	C_{11}	(4,15)	C_{12}	(4,16)	C_{13}
(4,24)	C_{11t}	(4,25)	C_{12t}	(4,26)	C_{13t}
(5,14)	C_{21}	(5,15)	C_{22}	(5,16)	C_{23}
(5,24)	C_{21t}	(5,25)	C_{22t}	(5,26)	C_{23t}
(6,14)	C_{31}	(6,15)	C_{32}	(6,16)	C_{33}
(6,24)	C_{31t}	(6,25)	C_{32t}	(6,26)	C_{33t}
(7,17)	C_{11}	(7,18)	C_{12}	(7,19)	C_{13}
(7,20)	1	(7,27)	C_{11t}	(7,28)	C_{12t}
(7,29)	C_{13t}	(8,17)	C_{21}	(8,18)	C_{22}
(8,19)	C_{23}	(8,21)	1	(8,27)	C_{21t}
(8,28)	C_{22t}	(8,29)	C_{23t}	(9,17)	C_{31}
(9,18)	C_{32}	(9,19)	C_{33}	(9,22)	1
(9,23)	k_2	(9,27)	C_{31t}	(9,28)	C_{32t}
(9,29)	C_{33t}	(10,23)	k_1	(12,23)	$-k_3$
(13,23)	$k_4/600$				

Table B.3. Elements of the Dynamics Submatrix F_{13} (22)

Element	Term	Element	Term	Element	Term
(4,30)	C_{11}	(4,31)	C_{12}	(4,32)	C_{13}
(4,33)	$C_{11}\omega_{ib_z}$	(4,34)	$C_{12}\omega_{ib_y}$	(4,35)	$C_{13}\omega_{ib_x}$
(4,36)	$C_{11}\omega_{ib_x}$	(4,37)	$-C_{12}\omega_{ib_x}$	(4,38)	$C_{13}\omega_{ib_y}$
(4,39)	$-C_{11}\omega_{ib_y}$	(4,40)	$C_{12}\omega_{ib_z}$	(4,41)	$-C_{13}\omega_{ib_z}$
(4,42)	$C_{11}\omega_{ib_z}^2$	(4,43)	$C_{12}\omega_{ib_y}^2$	(4,44)	$C_{13}\omega_{ib_x}^2$
(4,45)	$0.5C_{11} \omega_{ib_x} $	(4,46)	$0.5C_{12} \omega_{ib_y} $	(4,47)	$0.5C_{13} \omega_{ib_z} $
(5,30)	C_{21}	(5,31)	C_{22}	(5,32)	C_{23}
(5,33)	$C_{21}\omega_{ib_z}$	(5,34)	$C_{22}\omega_{ib_y}$	(5,35)	$C_{23}\omega_{ib_x}$
(5,36)	$C_{21}\omega_{ib_x}$	(5,37)	$-C_{22}\omega_{ib_x}$	(5,38)	$C_{23}\omega_{ib_y}$
(5,39)	$-C_{21}\omega_{ib_y}$	(5,40)	$C_{22}\omega_{ib_z}$	(5,41)	$-C_{23}\omega_{ib_z}$
(5,42)	$C_{21}\omega_{ib_z}^2$	(5,43)	$C_{22}\omega_{ib_y}^2$	(5,44)	$C_{23}\omega_{ib_x}^2$
(5,45)	$0.5C_{21} \omega_{ib_x} $	(5,46)	$0.5C_{22} \omega_{ib_y} $	(5,47)	$0.5C_{23} \omega_{ib_z} $
(6,30)	C_{31}	(6,31)	C_{32}	(6,32)	C_{33}
(6,33)	$C_{31}\omega_{ib_z}$	(6,34)	$C_{32}\omega_{ib_y}$	(6,35)	$C_{33}\omega_{ib_x}$
(6,36)	$C_{31}\omega_{ib_x}$	(6,37)	$-C_{32}\omega_{ib_x}$	(6,38)	$C_{33}\omega_{ib_y}$
(6,39)	$-C_{31}\omega_{ib_y}$	(6,40)	$C_{32}\omega_{ib_z}$	(6,41)	$-C_{33}\omega_{ib_z}$
(6,42)	$C_{31}\omega_{ib_z}^2$	(6,43)	$C_{32}\omega_{ib_y}^2$	(6,44)	$C_{33}\omega_{ib_x}^2$
(6,45)	$0.5C_{31} \omega_{ib_x} $	(6,46)	$0.5C_{32} \omega_{ib_y} $	(6,47)	$0.5C_{33} \omega_{ib_z} $

Table B.4. Elements of the Dynamics Submatrix F_{14} (22)

Element	Term	Element	Term	Element	Term
(7,48)	C_{11}	(7,49)	C_{12}	(7,50)	C_{13}
(7,51)	$C_{11}A_x^B$	(7,52)	$C_{12}A_y^B$	(7,53)	$C_{13}A_z^{B'}$
(7,54)	$C_{11} A_x^B $	(7,55)	$C_{12} A_y^B $	(7,56)	$C_{13} A_z^{B'} $
(7,57)	$C_{11}A_x^{B^2}$	(7,58)	$C_{12}A_y^{B^2}$	(7,59)	$C_{13}A_z^{B'^2}$
(7,60)	$C_{11}A_x^B A_y^B$	(7,61)	$C_{11}A_x^B A_z^B$	(7,62)	$C_{12}A_y^B A_x^B$
(7,63)	$C_{12}A_y^B A_z^B$	(7,64)	$C_{13}A_x^B A_z^B$	(7,65)	$C_{13}A_y^B A_x^B$
(7,66)	$C_{11}A_y^B$	(7,67)	$-C_{12}A_x^B$	(7,68)	$C_{13}A_y^B$
(7,69)	$C_{13}A_x^B$	(8,48)	C_{21}	(8,49)	C_{22}
(8,50)	C_{23}	(8,51)	$C_{21}A_x^B$	(8,52)	$C_{22}A_y^B$
(8,53)	$C_{23}A_z^{B'}$	(8,54)	$C_{21} A_x^B $	(8,55)	$C_{22} A_y^B $
(8,56)	$C_{23} A_z^{B'} $	(8,57)	$C_{21}A_x^{B^2}$	(8,58)	$C_{22}A_y^{B^2}$
(8,59)	$C_{23}A_z^{B'^2}$	(8,60)	$C_{21}A_x^B A_y^B$	(8,61)	$C_{21}A_x^B A_z^B$
(8,62)	$C_{22}A_y^B A_x^B$	(8,63)	$C_{22}A_y^B A_z^B$	(8,64)	$C_{23}A_x^B A_z^B$
(8,65)	$C_{23}A_y^B A_z^B$	(8,66)	$C_{21}A_y^B$	(8,67)	$-C_{22}A_x^B$
(8,68)	$C_{23}A_x^B$	(8,69)	$C_{23}A_x^B$	(9,48)	C_{31}
(9,49)	C_{32}	(9,50)	C_{33}	(9,51)	$C_{31}A_x^B$
(9,52)	$C_{32}A_y^B$	(9,53)	$C_{33}A_z^{B'}$	(9,54)	$C_{31} A_x^B $
(9,55)	$C_{32} A_y^B $	(9,56)	$C_{33} A_z^{B'} $	(9,55)	$C_{31}A_x^{B^2}$
(9,58)	$C_{32}A_y^{B^2}$	(9,59)	$C_{33}A_z^{B'^2}$	(9,60)	$C_{31}A_x^B A_y^B$
(9,61)	$C_{31}A_x^B A_z^B$	(9,62)	$C_{32}A_y^B A_x^B$	(9,63)	$C_{32}A_y^B A_z^B$
(9,64)	$C_{33}A_x^B A_z^B$	(9,65)	$C_{33}A_y^B A_z^B$	(9,66)	$C_{31}A_y^B$
(9,67)	$-C_{32}A_x^B$	(9,68)	$C_{33}A_y^B$	(9,69)	$C_{33}A_x^B$

Table B.5. Elements of the Dynamics Submatrix F_{15} (22)

Element	Term	Element	Term	Element	Term
(4,73)	C_{11}	(4,74)	C_{12}	(4,75)	C_{13}
(5,73)	C_{21}	(5,74)	C_{22}	(5,75)	C_{23}
(6,73)	C_{31}	(6,74)	C_{32}	(6,75)	C_{33}
(7,70)	C_{11}	(7,71)	C_{12}	(7,72)	C_{13}
(8,70)	C_{21}	(8,71)	C_{22}	(8,72)	C_{23}
(9,70)	C_{31}	(9,71)	C_{32}	(9,72)	C_{33}

Table B.6. Elements of the Dynamics Submatrix F_{16} (22)

Element	Term	Element	Term	Element	Term
(4,76)	$C_{11}A_y^B \omega_{ib_x}$	(4,77)	$C_{11}A_y^B \omega_{ib_y}$	(4,78)	$C_{11}A_y^B \omega_{ib_z}$
(4,79)	$C_{11}A_z^B \omega_{ib_y}$	(4,80)	$C_{11}A_z^B \omega_{ib_z}$	(4,81)	$C_{11}A_z^B \omega_{ib_x}$
(4,82)	$C_{12}A_z^B \omega_{ib_x}$	(4,83)	$C_{12}A_z^B \omega_{ib_z}$	(4,84)	$C_{12}A_z^B \omega_{ib_y}$
(4,85)	$C_{12}A_x^B \omega_{ib_x}$	(4,86)	$C_{12}A_x^B \omega_{ib_z}$	(4,87)	$C_{12}A_x^B \omega_{ib_y}$
(4,88)	$C_{13}A_x^B \omega_{ib_y}$	(4,89)	$C_{13}A_x^B \omega_{ib_z}$	(4,90)	$C_{13}A_x^B \omega_{ib_x}$
(4,91)	$C_{13}A_y^B \omega_{ib_x}$	(4,92)	$C_{13}A_y^B \omega_{ib_y}$	(4,93)	$C_{13}A_y^B \omega_{ib_z}$
(5,76)	$C_{21}A_y^B \omega_{ib_x}$	(5,77)	$C_{21}A_y^B \omega_{ib_y}$	(5,78)	$C_{21}A_y^B \omega_{ib_z}$
(5,79)	$C_{21}A_z^B \omega_{ib_y}$	(5,80)	$C_{21}A_z^B \omega_{ib_z}$	(5,81)	$C_{21}A_z^B \omega_{ib_x}$
(5,82)	$C_{22}A_z^B \omega_{ib_x}$	(5,83)	$C_{22}A_z^B \omega_{ib_z}$	(5,84)	$C_{22}A_z^B \omega_{ib_y}$
(5,85)	$C_{22}A_x^B \omega_{ib_x}$	(5,86)	$C_{22}A_x^B \omega_{ib_z}$	(5,87)	$C_{22}A_x^B \omega_{ib_y}$
(5,88)	$C_{23}A_x^B \omega_{ib_y}$	(5,89)	$C_{23}A_x^B \omega_{ib_z}$	(5,90)	$C_{23}A_x^B \omega_{ib_x}$
(5,91)	$C_{23}A_y^B \omega_{ib_x}$	(5,92)	$C_{23}A_y^B \omega_{ib_y}$	(5,93)	$C_{23}A_y^B \omega_{ib_z}$
(6,76)	$C_{31}A_y^B \omega_{ib_x}$	(6,77)	$C_{31}A_y^B \omega_{ib_y}$	(6,78)	$C_{31}A_y^B \omega_{ib_z}$
(6,79)	$C_{31}A_z^B \omega_{ib_y}$	(6,80)	$C_{31}A_z^B \omega_{ib_z}$	(6,81)	$C_{31}A_z^B \omega_{ib_x}$
(6,82)	$C_{32}A_z^B \omega_{ib_x}$	(6,83)	$C_{32}A_z^B \omega_{ib_z}$	(6,84)	$C_{32}A_z^B \omega_{ib_y}$
(6,85)	$C_{32}A_x^B \omega_{ib_x}$	(6,86)	$C_{32}A_x^B \omega_{ib_z}$	(6,87)	$C_{32}A_x^B \omega_{ib_y}$
(6,88)	$C_{33}A_x^B \omega_{ib_y}$	(6,89)	$C_{33}A_x^B \omega_{ib_z}$	(6,90)	$C_{33}A_x^B \omega_{ib_x}$
(6,91)	$C_{33}A_y^B \omega_{ib_x}$	(6,92)	$C_{33}A_y^B \omega_{ib_y}$	(6,93)	$C_{33}A_y^B \omega_{ib_z}$

Table B.7. Elements of the Dynamics Submatrix F_{22} (22)

Element	Term	Element	Term	Element	Term
(14,14)	$-\beta_{b_{z_c}}$	(15,15)	$-\beta_{b_{y_c}}$	(16,16)	$-\beta_{b_{x_c}}$
(17,17)	$-\beta_{\nabla_{z_c}}$	(18,18)	$-\beta_{\nabla_{y_c}}$	(19,19)	$-\beta_{\nabla_{x_c}}$
(20,20)	$-\beta_{\delta_{g_x}}$	(21,21)	$-\beta_{\delta_{g_y}}$	(22,22)	$-\beta_{\delta_{g_z}}$
(23,23)	$-\beta_{\delta_{h_c}}$				

Table B.8. Elements of the Dynamics Submatrix F_{55} (22)

Element	Term	Element	Term	Element	Term
(70,70)	$-\beta_{\nabla_{x_g}}$	(71,71)	$-\beta_{\nabla_{y_g}}$	(72,72)	$-\beta_{\nabla_{z_g}}$
(73,73)	$-\beta_{b_{x_g}}$	(74,74)	$-\beta_{b_{y_g}}$	(75,75)	$-\beta_{b_{z_g}}$

B.1 Elements of the Process Noise Matrix

The Litton document (11) includes a 93-by-93 process noise matrix (**Q**) for the LN-93 error model. Like the **F** matrix, the **Q** matrix is partitioned into subarrays which correspond to the error-state subvectors discussed in Chapter III. The vast majority of the elements in **Q** are identically zero. Only the non-zero elements of **Q** are shown below.

Table B.9. Non-zero Elements of Process Noise Submatrix **Q₁₁** (22)

Element	Term	Element	Term
(4,4)	$\sigma_{\eta_{b_x}}^2$	(5,5)	$\sigma_{\eta_{b_y}}^2$
(6,6)	$\sigma_{\eta_{b_z}}^2$	(7,7)	$\sigma_{\eta_{A_x}}^2$
(8,8)	$\sigma_{\eta_{A_y}}^2$	(9,9)	$\sigma_{\eta_{A_z}}^2$

Table B.10. Non-zero Elements of Process Noise Submatrix **Q₂₂** (22)

Element	Term	Element	Term
(14,14)	$2\beta_{b_{x_c}} \sigma_{b_{x_c}}^2$	(15,15)	$2\beta_{b_{y_c}} \sigma_{b_{y_c}}^2$
(16,16)	$2\beta_{b_{z_c}} \sigma_{b_{z_c}}^2$	(17,17)	$2\beta_{\nabla_{x_c}} \sigma_{\nabla_{x_c}}^2$
(18,18)	$2\beta_{\nabla_{y_c}} \sigma_{\nabla_{y_c}}^2$	(18,18)	$2\beta_{\nabla_{z_c}} \sigma_{\nabla_{z_c}}^2$
(20,20)	$2\beta_{\delta_{R_x}} \sigma_{\delta_{R_x}}^2$	(21,21)	$2\beta_{\delta_{R_y}} \sigma_{\delta_{R_y}}^2$
(22,22)	$2\beta_{\delta_{R_z}} \sigma_{\delta_{R_z}}^2$	(23,23)	$2\beta_{\delta_{h_c}} \sigma_{\delta_{h_c}}^2$

Appendix C. *Comparison of 93-state and 41-State INS Models*

This appendix contains plots of position, velocity, and attitude errors of the 93-state and 41-state Litton Ln-93 INS truth models during a 10-run Monte Carlo 2-hour flight profile (11). No alignment was performed previous to the start of the flight, causing the large magnitudes in all the errors. These plots show that the 41-state truth model almost exactly matches the 93-state truth model, and it is suitable for use as the truth model for all the filters developed in this thesis.

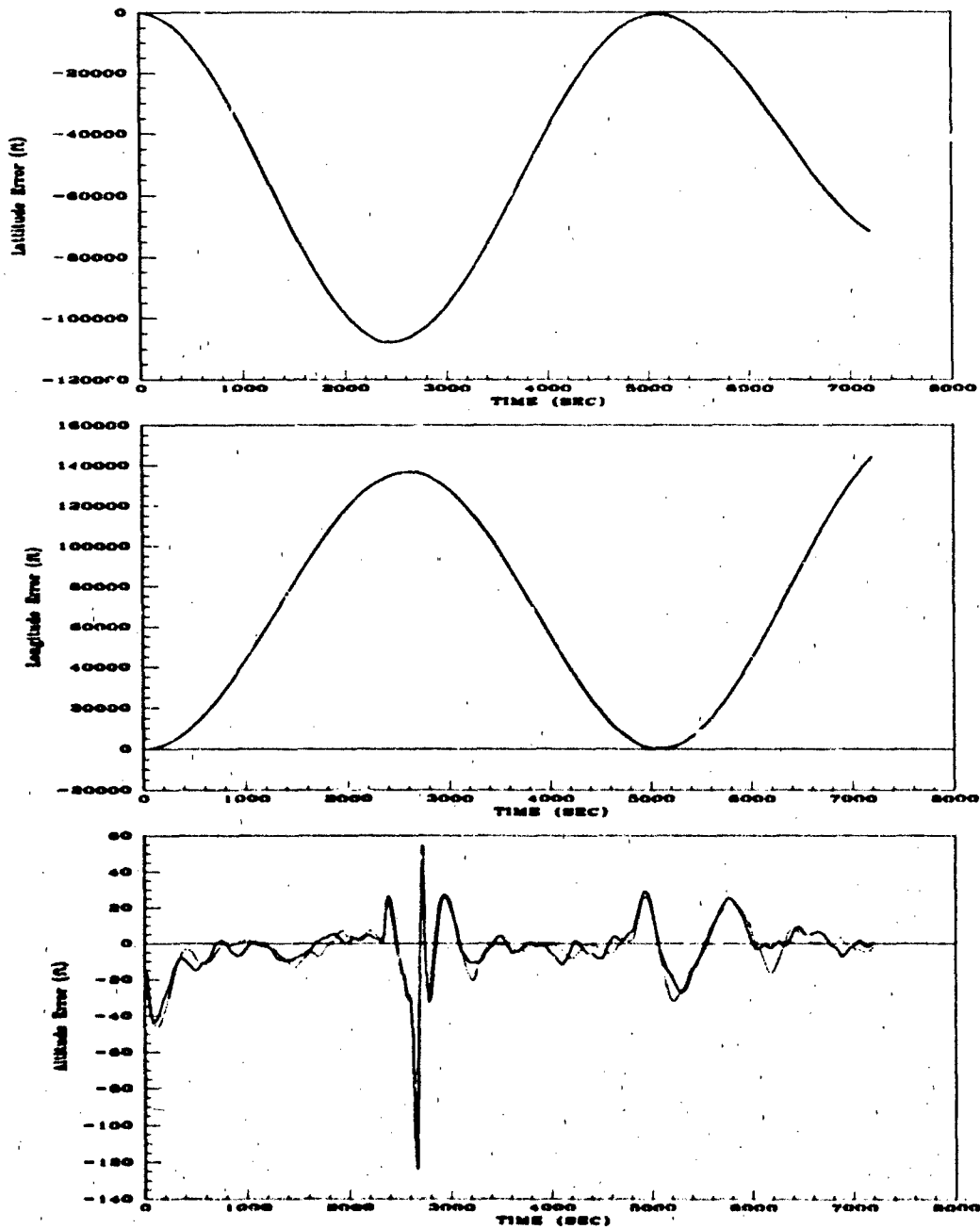


Figure C.2. 93 vs 41 State INS Models (a) Latitude (b) Longitude and (c) Altitude Errors.

---	93-State INS Model
....	41-State INS Model

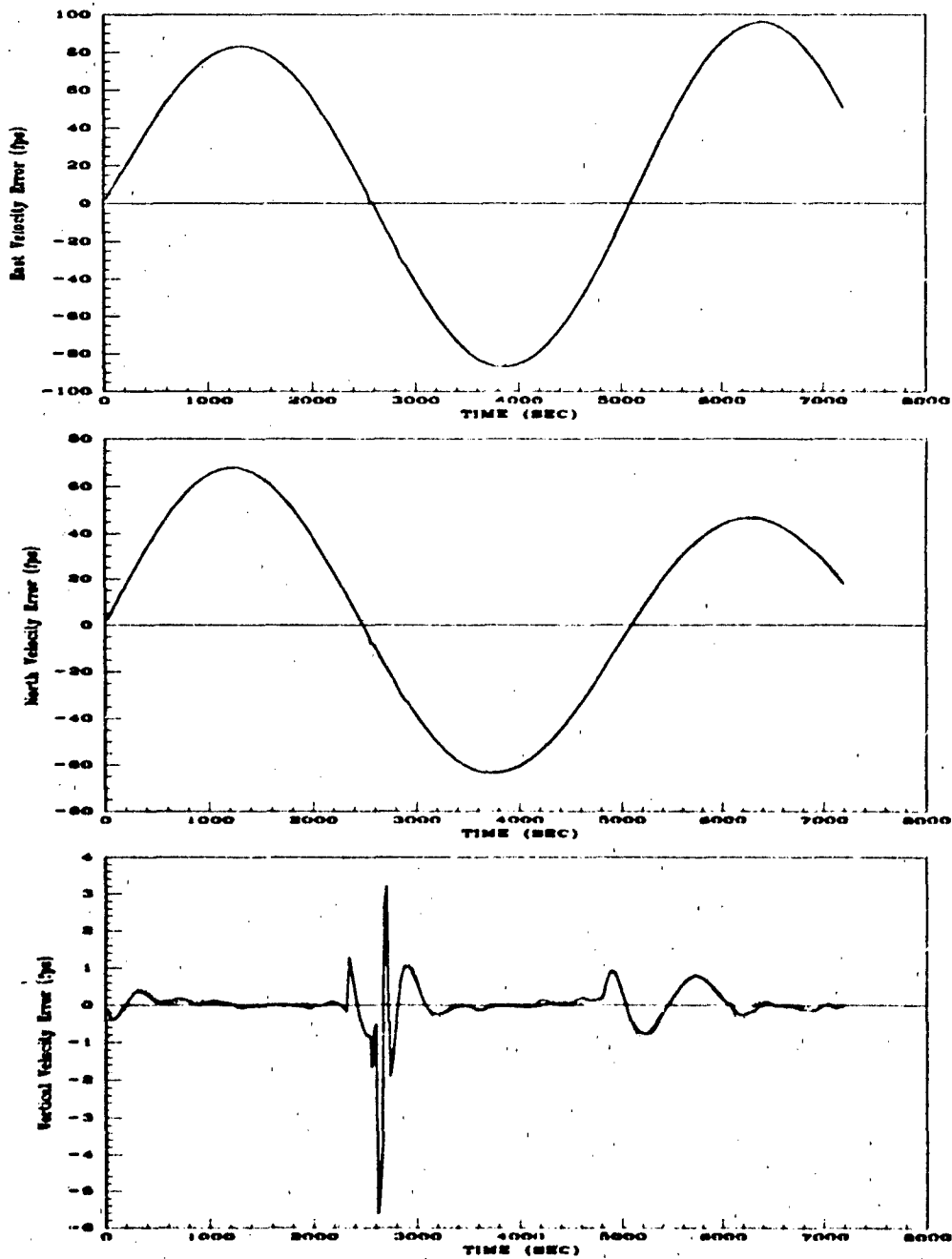


Figure C.3. 93 vs 41 State INS Models (a) East Velocity (b) North Velocity and (c) Vertical Velocity Errors.

—	93-State INS Model
- - - -	41-State INS Model

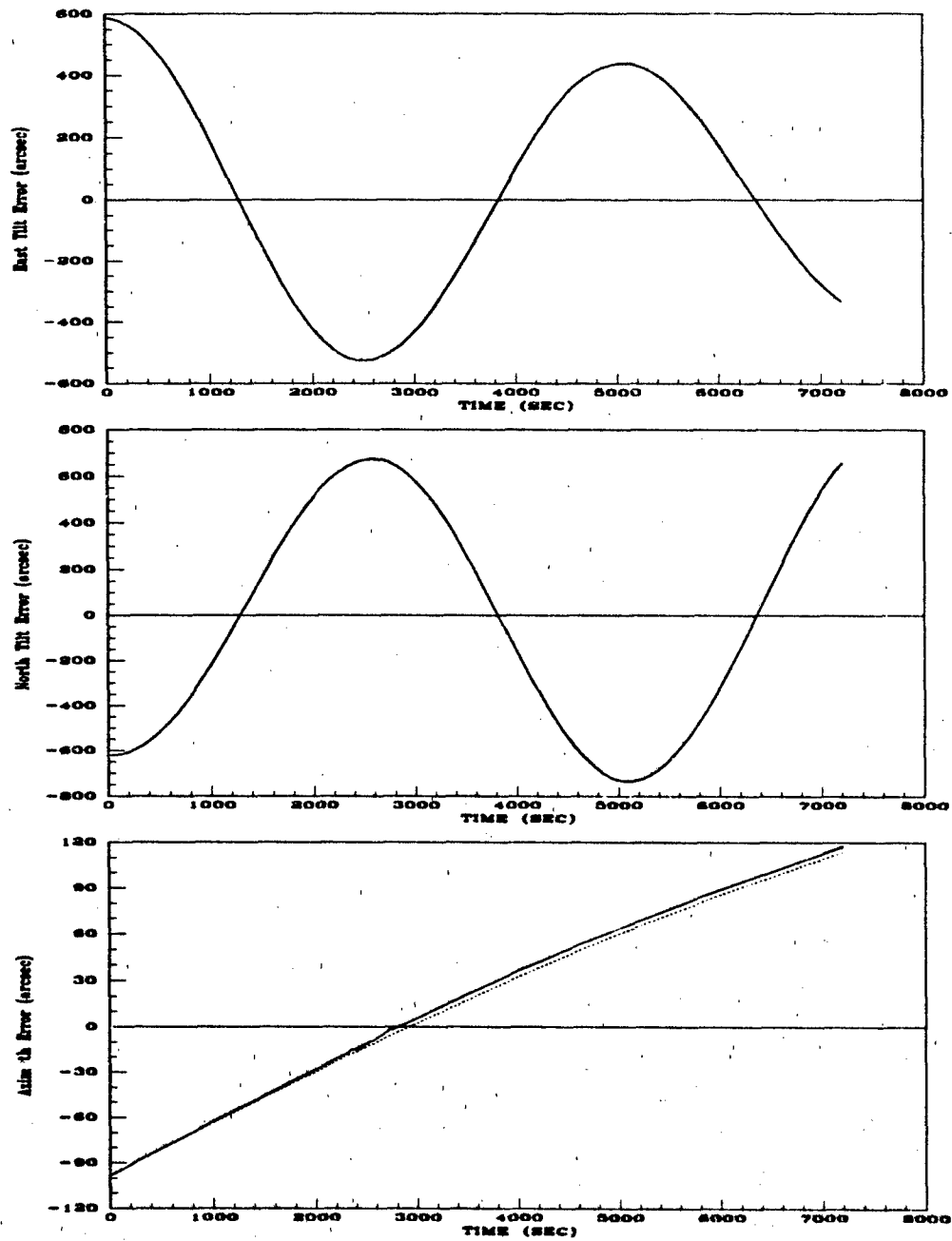


Figure C.4. 93 vs 41 State INS Models (a) East Tilt (b) North Tilt and (c) Azimuth Errors.

—	93-State INS Model
...	41-State INS Model

Appendix D. *Stacey's 128-State NRS Filter Performance Plots*

All plots contained in this and subsequent appendices are discussed in Chapter V (Results). All plots contained in this *and subsequent* appendices contain five traces. The innermost trace (---) on each data plot is the *mean error* time history for the applicable state. Mean Error is defined as being the difference between the filter's estimate of the state and the true state averaged over the number of Monte Carlo runs performed. The equation describing this relationship is defined by (14, 22):

$$\widehat{M}_e(t_i) = \frac{1}{N} \sum_{j=1}^N e_j(t_i) = \frac{1}{N} \sum_{j=1}^N \{ \widehat{x}_j(t_i) - x_{true,j}(t_i) \} \quad (D.1)$$

where $\widehat{x}_j(t_i)$ is the filter-computed estimate of variable j and $x_{true,j}(t_i)$ is the *truth* model value of the same variable, at time t_i , for sample j , and N is the number of time histories in the simulation (10 in this thesis).

In addition to the center trace, two more *pairs* of traces are plotted. The first pair (represented by ...) is symmetrically displaced about the mean and as a result follows the "undulations" of the $\widehat{M}_e(t_i)$. The locus of these traces is calculated from (15, 22) $\widehat{M}_e(t_i) \pm \sqrt{P_e(t_i)}$, where $P_e(t_i)$ is the *true* error covariance at time t_i . The true standard deviation is calculated from (14, 22):

$$\sigma_{true}(t_i) = \sqrt{P_e(t_i)} = \sqrt{\frac{1}{N-1} \sum_{j=1}^N e_j^2(t_i) - \frac{1}{N} \widehat{M}_e^2(t_i)} \quad (D.2)$$

where N is the number of runs in the Monte Carlo simulation (10 in this thesis), and $\widehat{M}_e^2(t_i)$ is the mean-squared value of the variable at each time of interest (such as measurement times).

The last pair of traces (—) represents the filter computed $\pm \sigma_{filter}$ values for the same variables of interest and are symmetrically displaced about zero because the filter "believes" that it is producing zero-mean errors (16, 22). These quantities

are propagated and updated in the MSOFE (3, 22) software using the covariance propagation equation shown in Chapter II. These traces represent the filter's estimate of its own error.

D.1 Stacey's 128-State NRS Filter Performance Plots

The plots in this section represent results of a 10-run Monte Carlo 2-hour fighter flight profile simulation. In these runs the GPS receiver clock states initial covariance values have been decreased 4 orders of magnitude, as discussed in Chapter V, so that single precision could be used in the MSOFE simulation. This filter incorporates both RRS range and GPS pseudorange measurements.

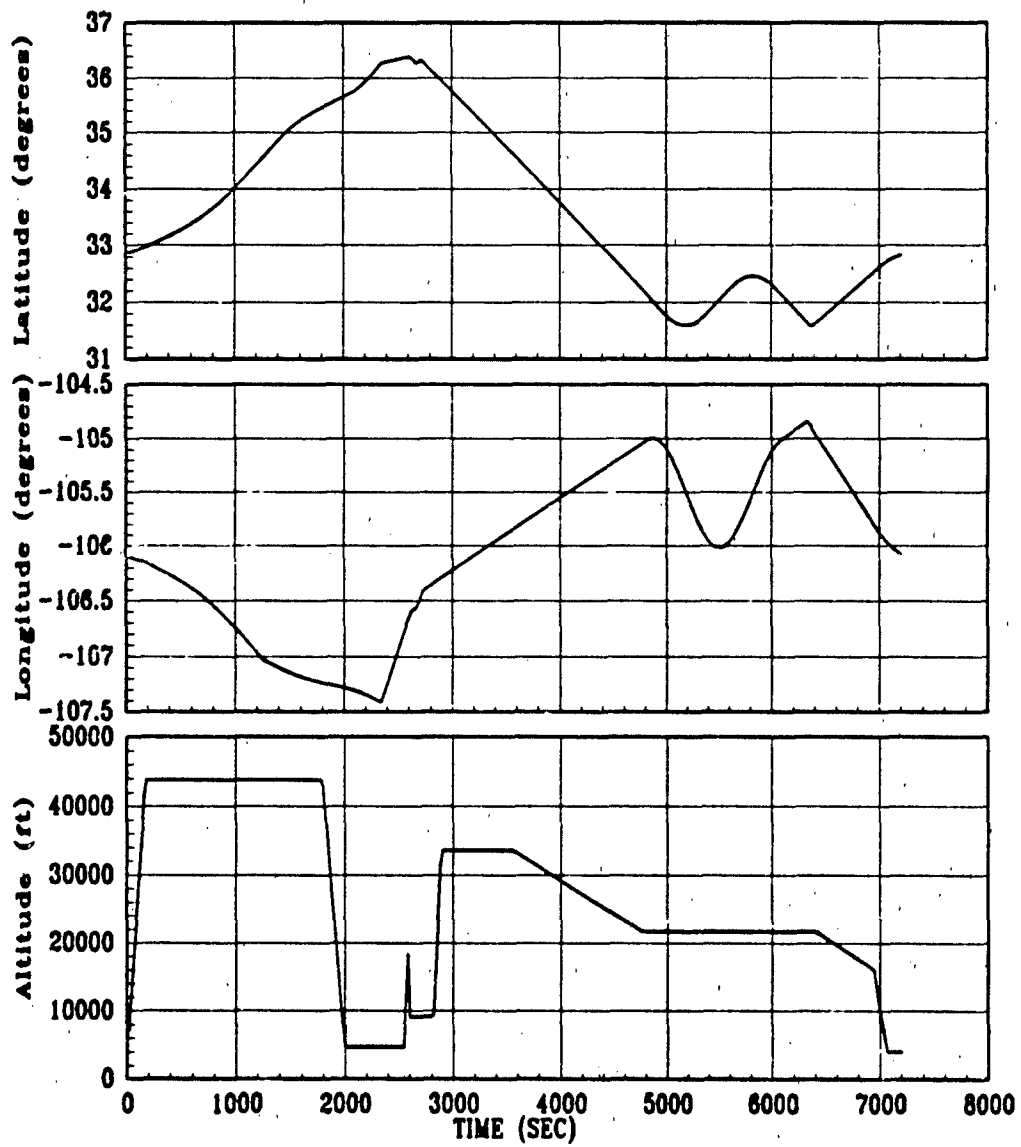


Figure D.1. 2-Hour Fighter Flight Profile (a) Latitude (b) Longitude and (c) Altitude

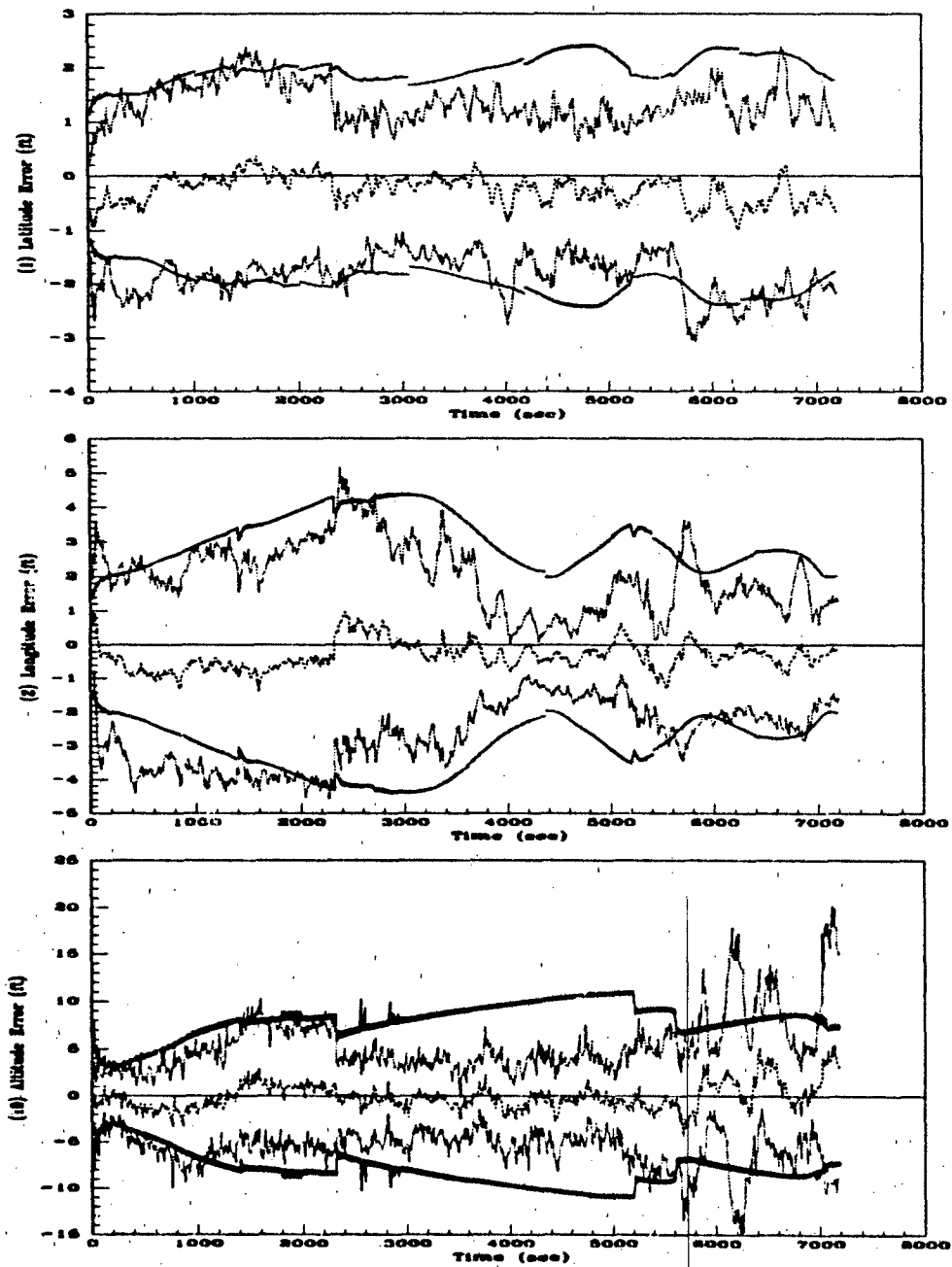


Figure D.2. 128-State NRS Filter (a) Latitude (b) Longitude and (c) Altitude Errors.

-----	Mean Error = $\bar{M}_x - (M_x)_{true}$
.....	Mean Error $\pm \sigma_{true}$
—	$0 \pm \sigma_{filter}$

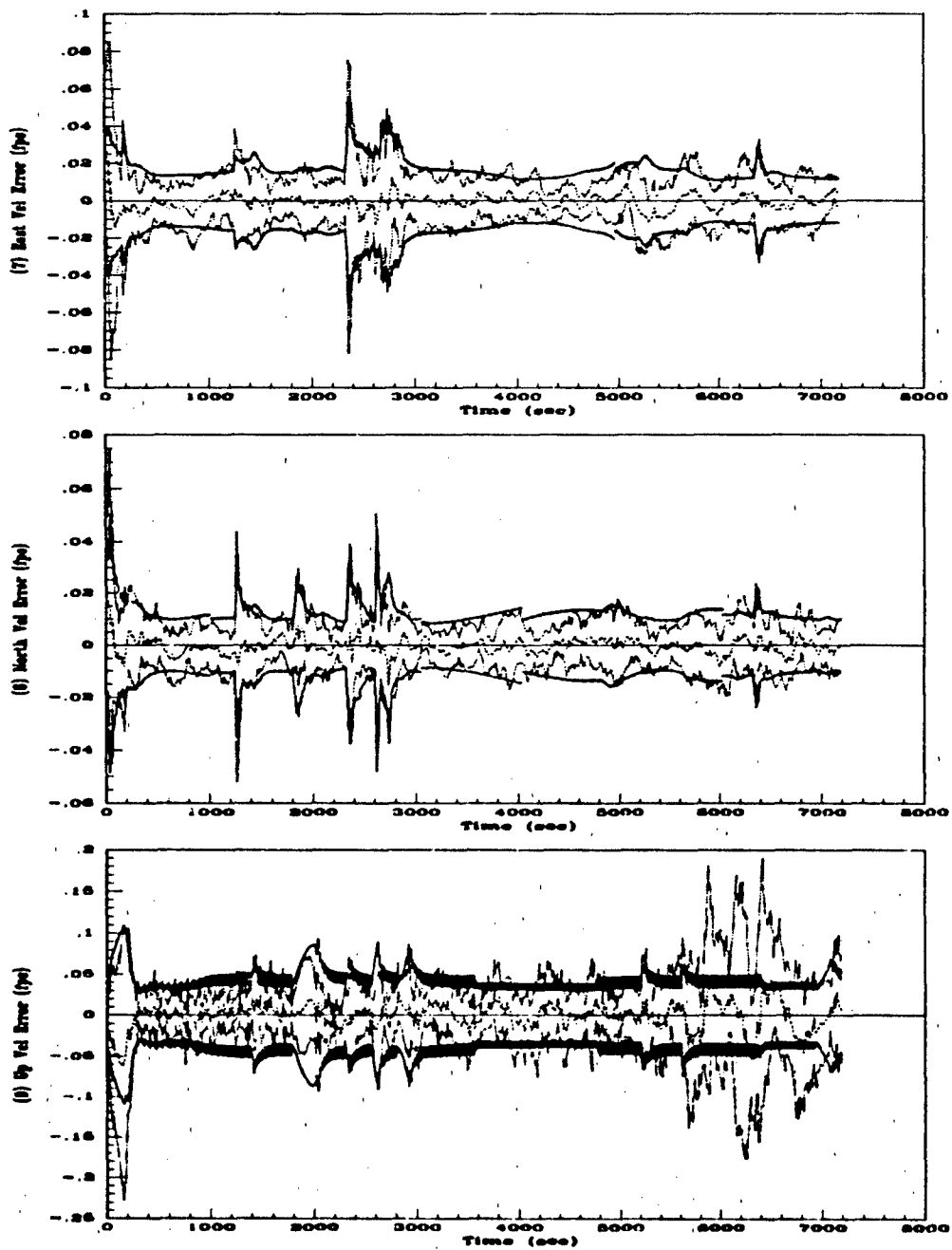


Figure D.3. 128-State NRS Filter (a) East Velocity (b) North Velocity and (c) Vertical Velocity Errors.

.....	Mean Error = $\bar{M}_x - (M_x)_{true}$
.....	Mean Error $\pm \sigma_{true}$
—	$0 \pm \sigma_{filter}$

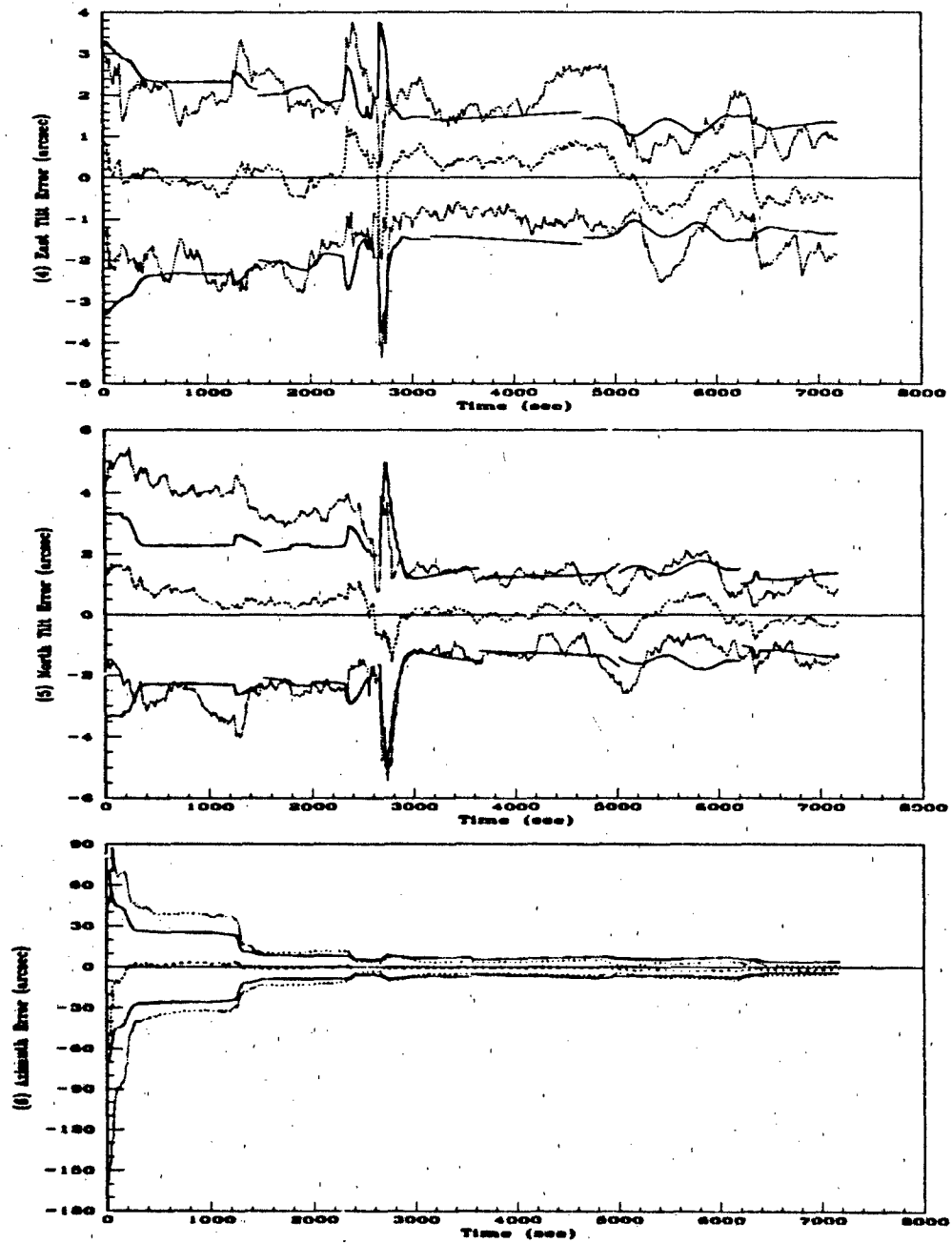


Figure D.4. 128-State NRS Filter (a) East Tilt (b) North Tilt and (c) Azimuth Errors.

-----	Mean Error = $\bar{M}_x - (M_x)_{true}$
.....	Mean Error $\pm \sigma_{true}$
————	$0 \pm \sigma_{filter}$

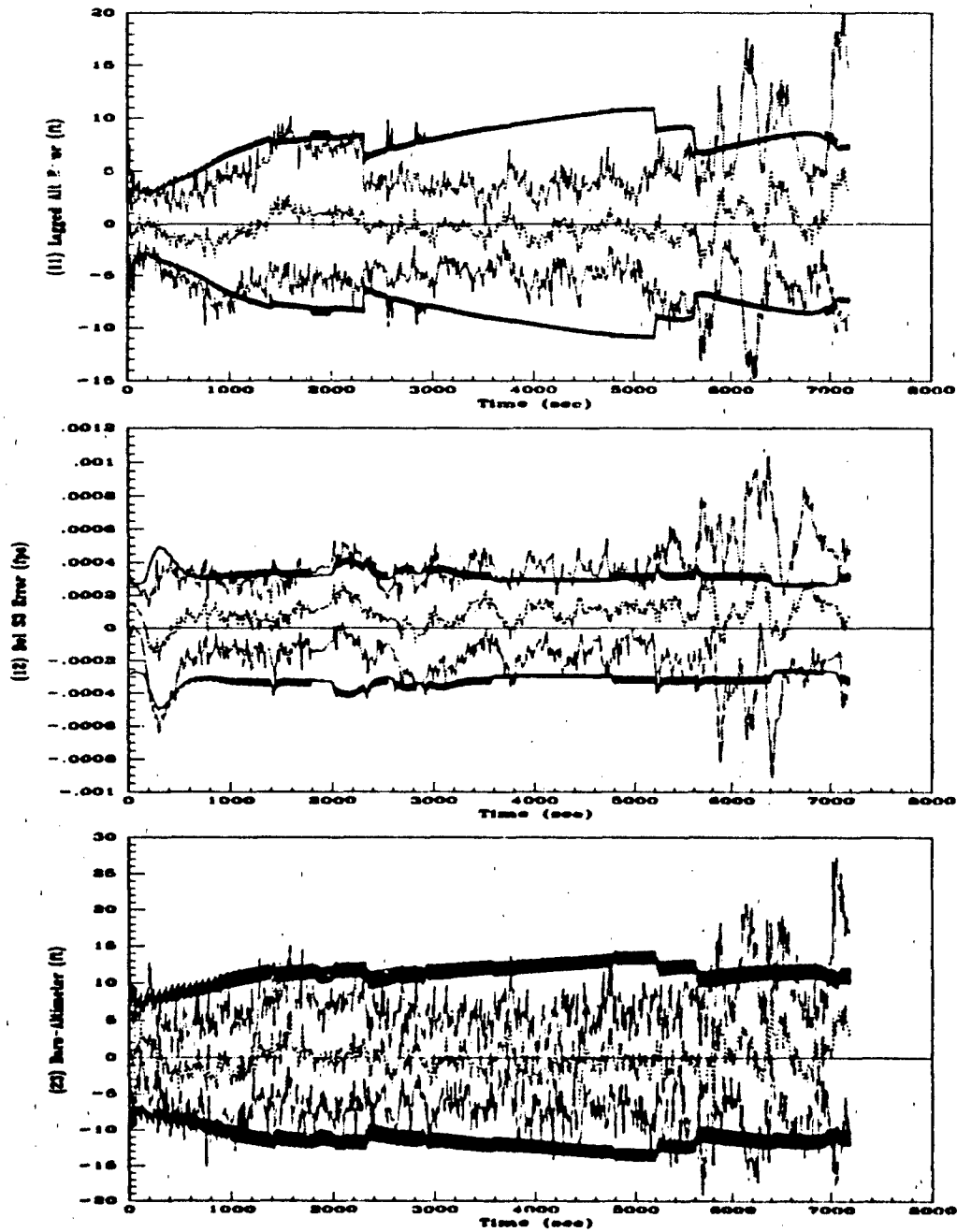


Figure D.5. 128-State NRS Filter (a) Lagged Altitude (b) Del S3 and (c) Baro-Altimeter Errors.

----	Mean Error = $\bar{M}_x - (M_x)_{true}$
.....	Mean Error $\pm \sigma_{true}$
—	$0 \pm \sigma_{filter}$

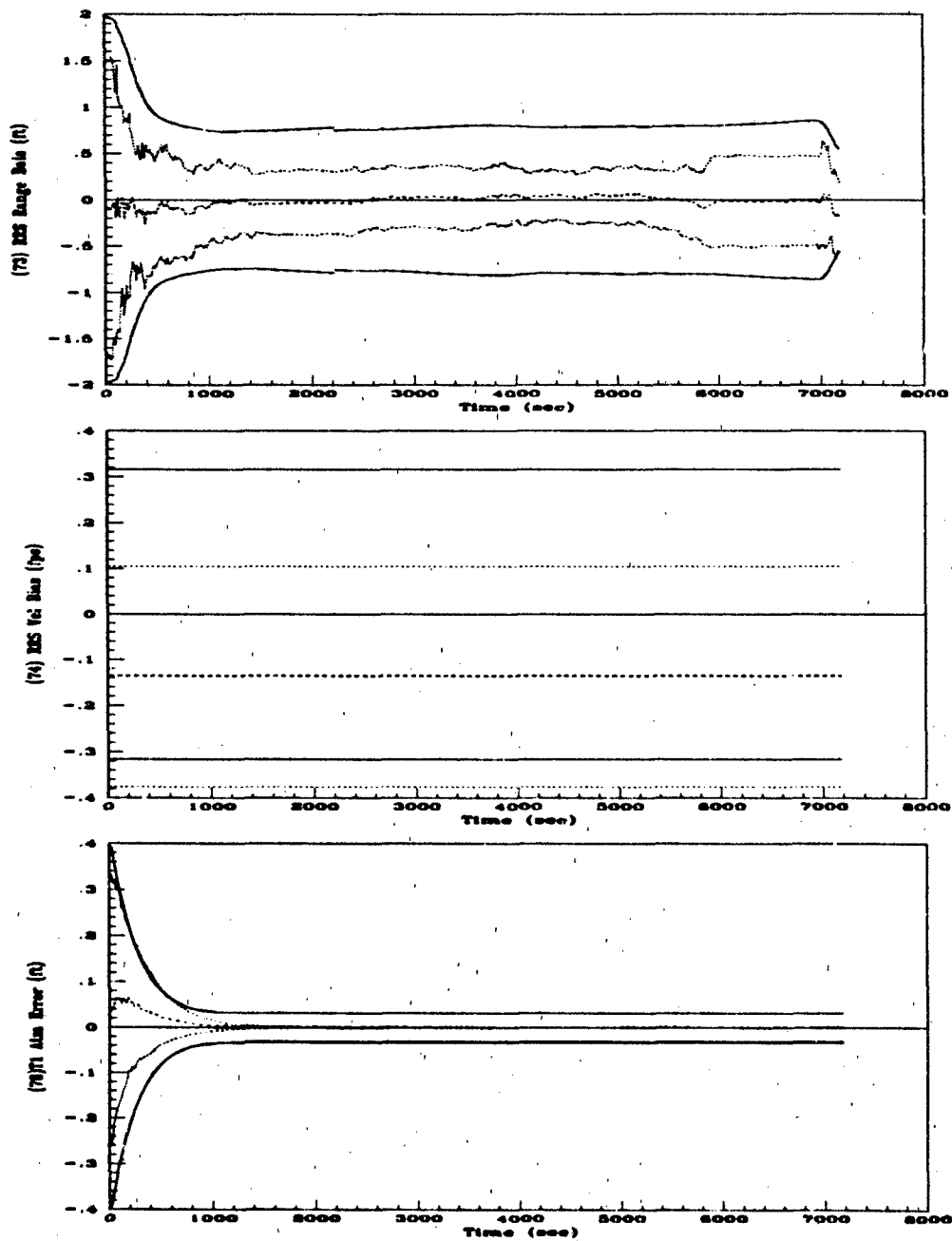


Figure D.6. 128-State NRS Filter (a) RRS Range Bias (b) RRS Vel Bias and (c) T1 Atmosphere Errors.

- - - -	Mean Error = $\bar{M}_x - (M_x)_{true}$
.....	Mean Error $\pm \sigma_{true}$
—	$0 \pm \sigma_{filter}$

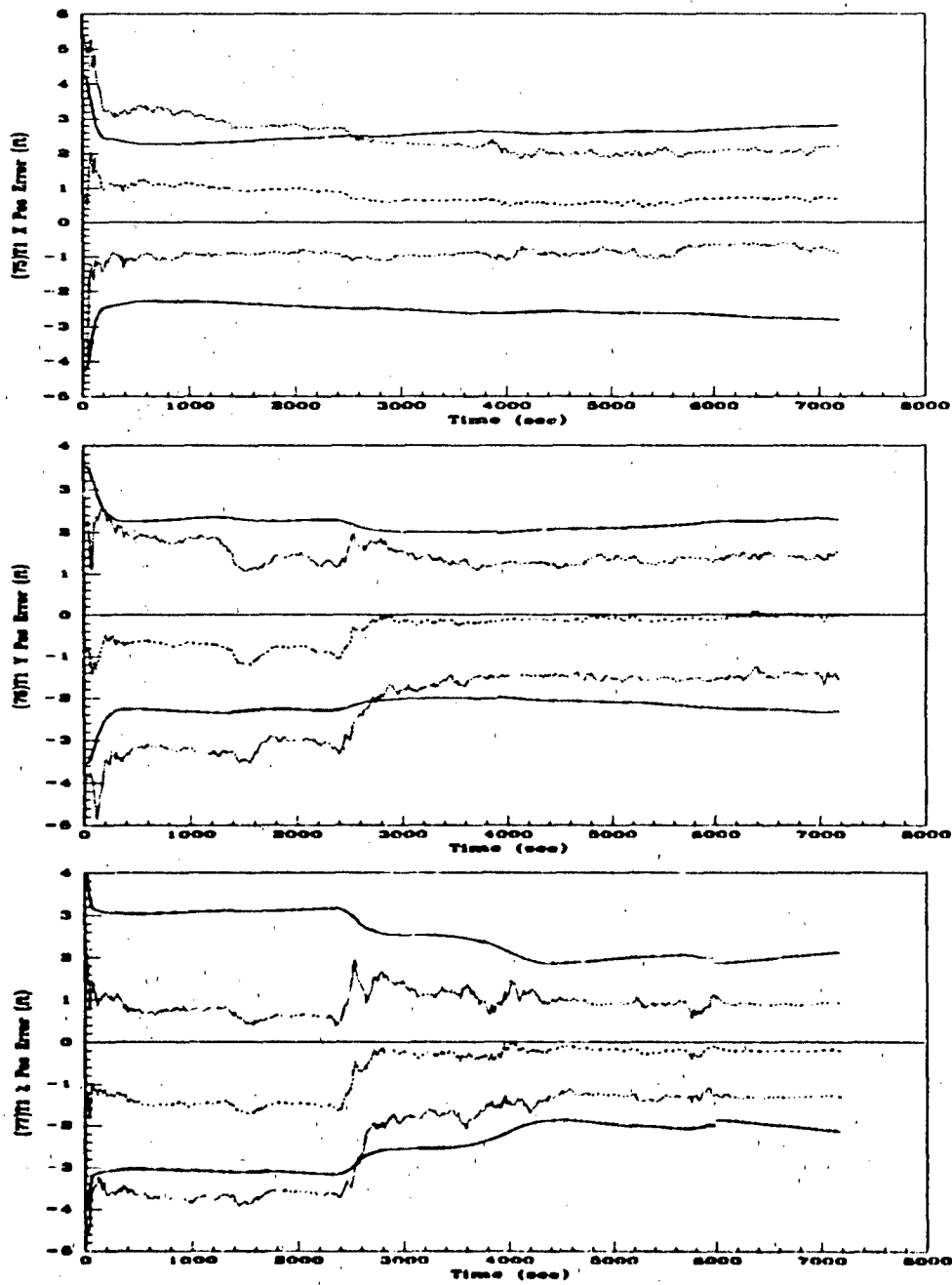


Figure D.7. 128-State NRS Filter (a) T1 X Position (b) T1 Y Position and (c) T1 Z Position Errors.

.....	Mean Error = $M_x - (M_x)_{true}$
.....	Mean Error $\pm \sigma_{true}$
----	$0 \pm \sigma_{filter}$

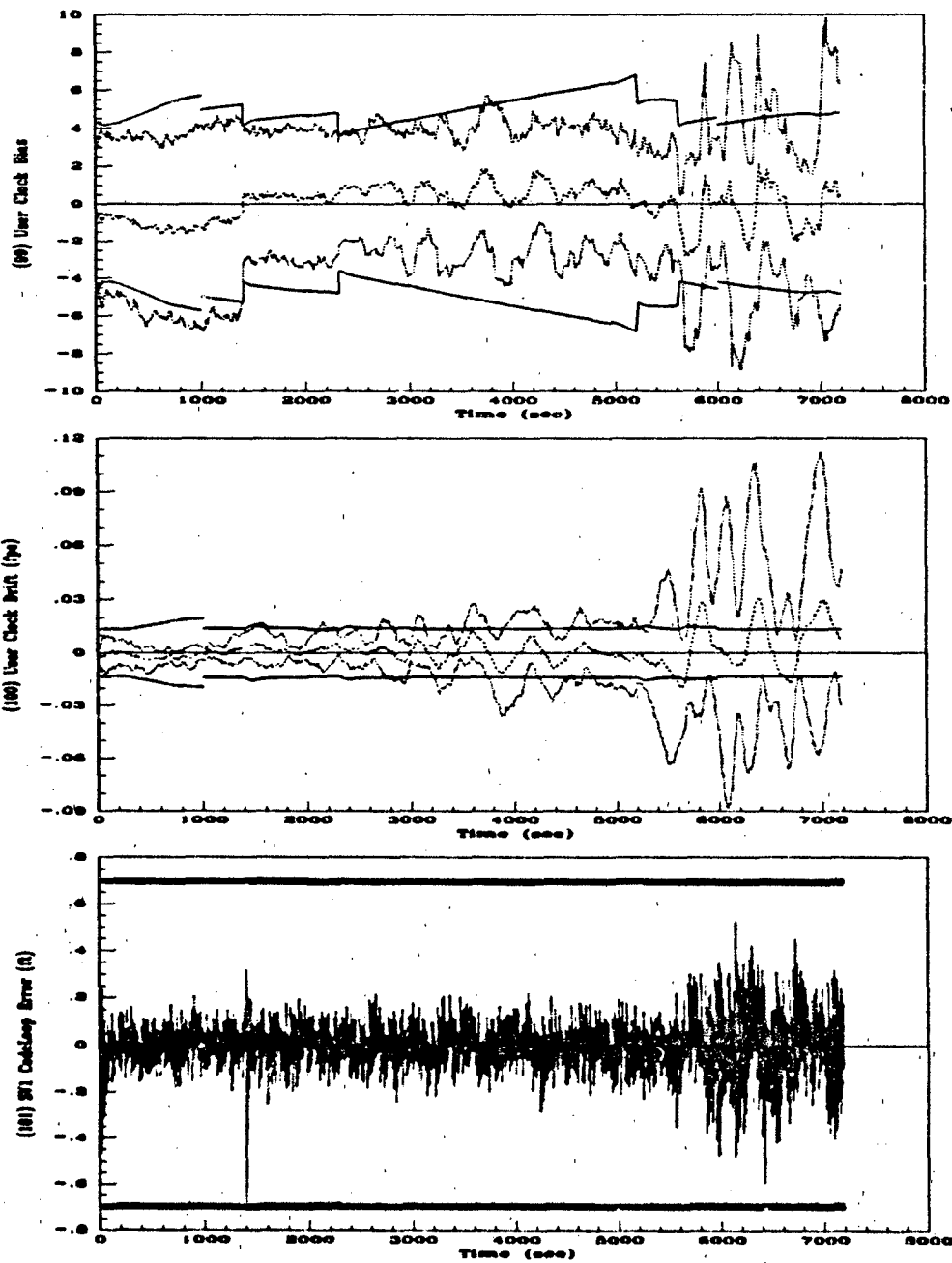


Figure D.8. 128-State NRS Filter (a) User Clock Bias (b) User Clock Drift and (c) SV1 Code Loop Errors.

.....	Mean Error = $\bar{M}_x - (M_x)_{true}$
.....	Mean Error $\pm \sigma_{true}$
—	$0 \pm \sigma_{filter}$

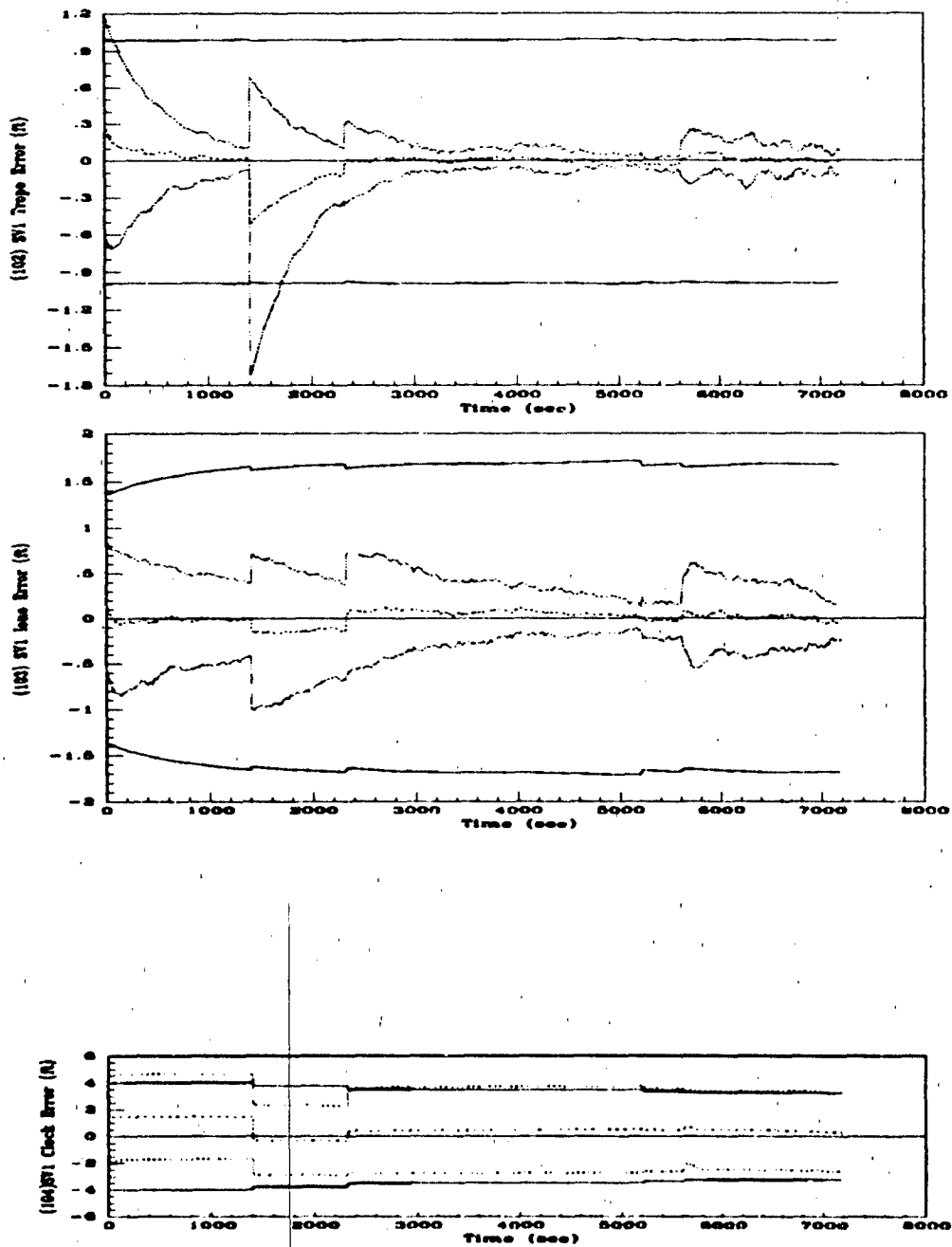


Figure D.9. 128-State NRS Filter (a) SV1 Troposphere (b) SV1 Ionosphere and (c) SV1 Clock Errors.

---	Mean Error = $\bar{M}_r - (M_r)_{true}$
.....	Mean Error $\pm \sigma_{true}$
—	$0 \pm \sigma_{filter}$

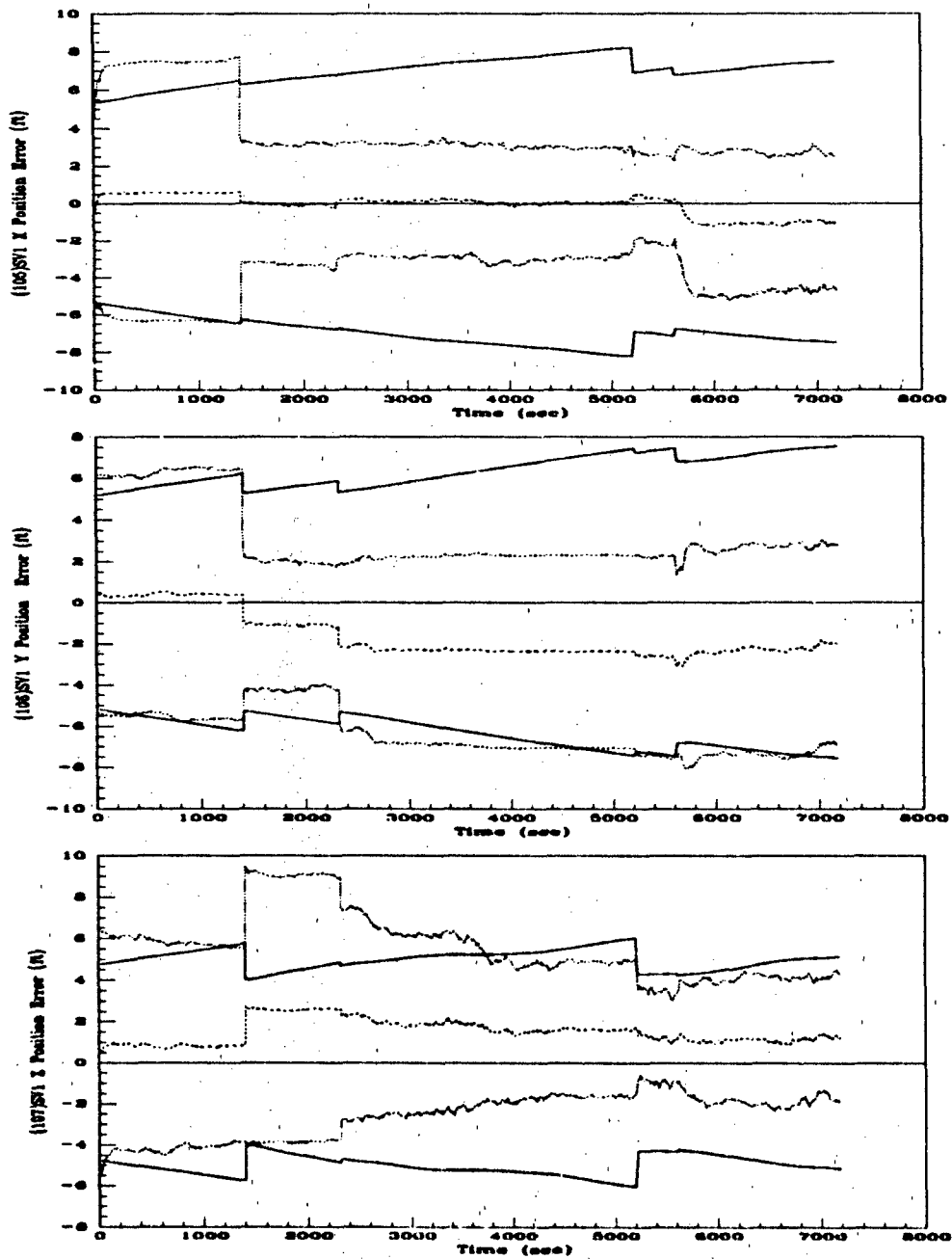


Figure D.10. 128-State NRS Filter (a) SV1 X Position (b) SV1 Y Position and (c) SV1 Z Position Errors.

.....	Mean Error = $M_x - (M_x)_{true}$
.....	Mean Error $\pm \sigma_{true}$
—	$0 \pm \sigma_{filter}$

Appendix E. *97-State NRS Filter Performance Plots*

The plots in this section represent results of a 10-run Monte Carlo 2-hour fighter flight profile simulation. In these runs the GPS receiver clock states initial covariance values have been decreased 4 orders of magnitude, as discussed in Chapter V, so that single precision could be used in the MSOFE simulation. This filter incorporates both RRS range and GPS pseudorange measurements.

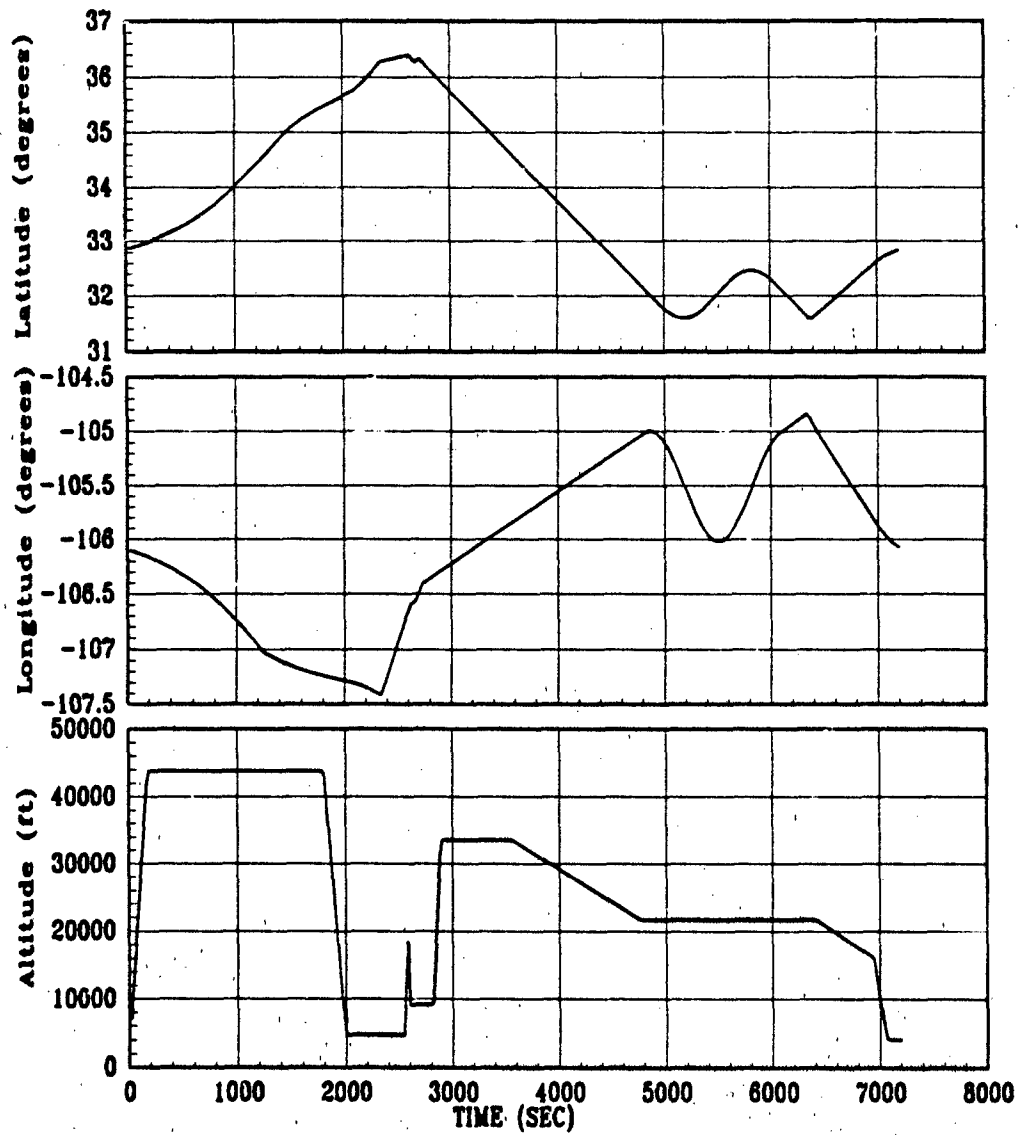


Figure E.1. 2-Hour Fighter Flight Profile (a) Latitude (b) Longitude and (c) Altitude

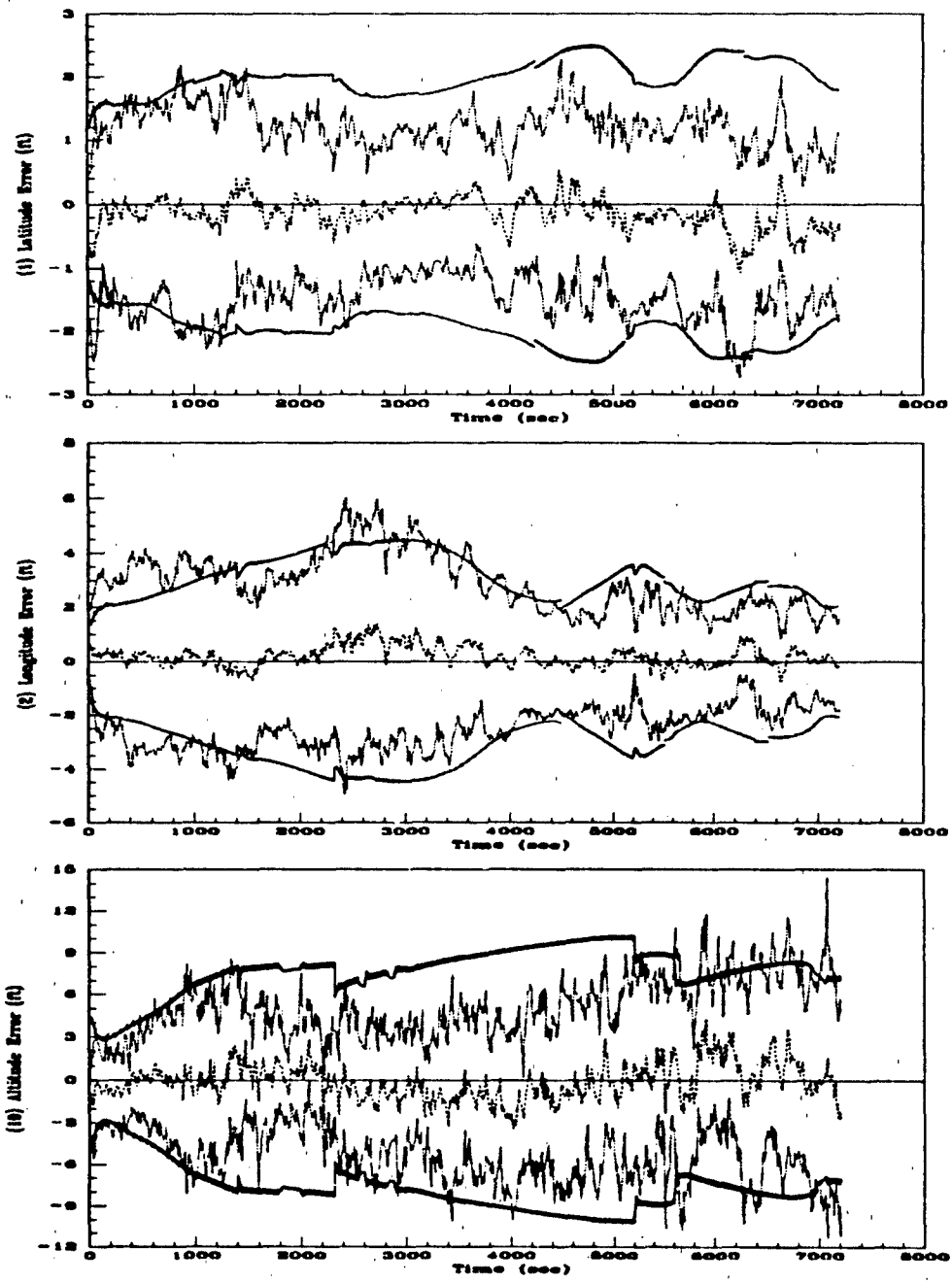


Figure E.2. 97-State NRS Filter (a) Latitude (b) Longitude and (c) Altitude Errors.

-----	Mean Error = $M_x - (M_x)_{true}$
.....	Mean Error $\pm \sigma_{true}$
—	$0 \pm \sigma_{filter}$

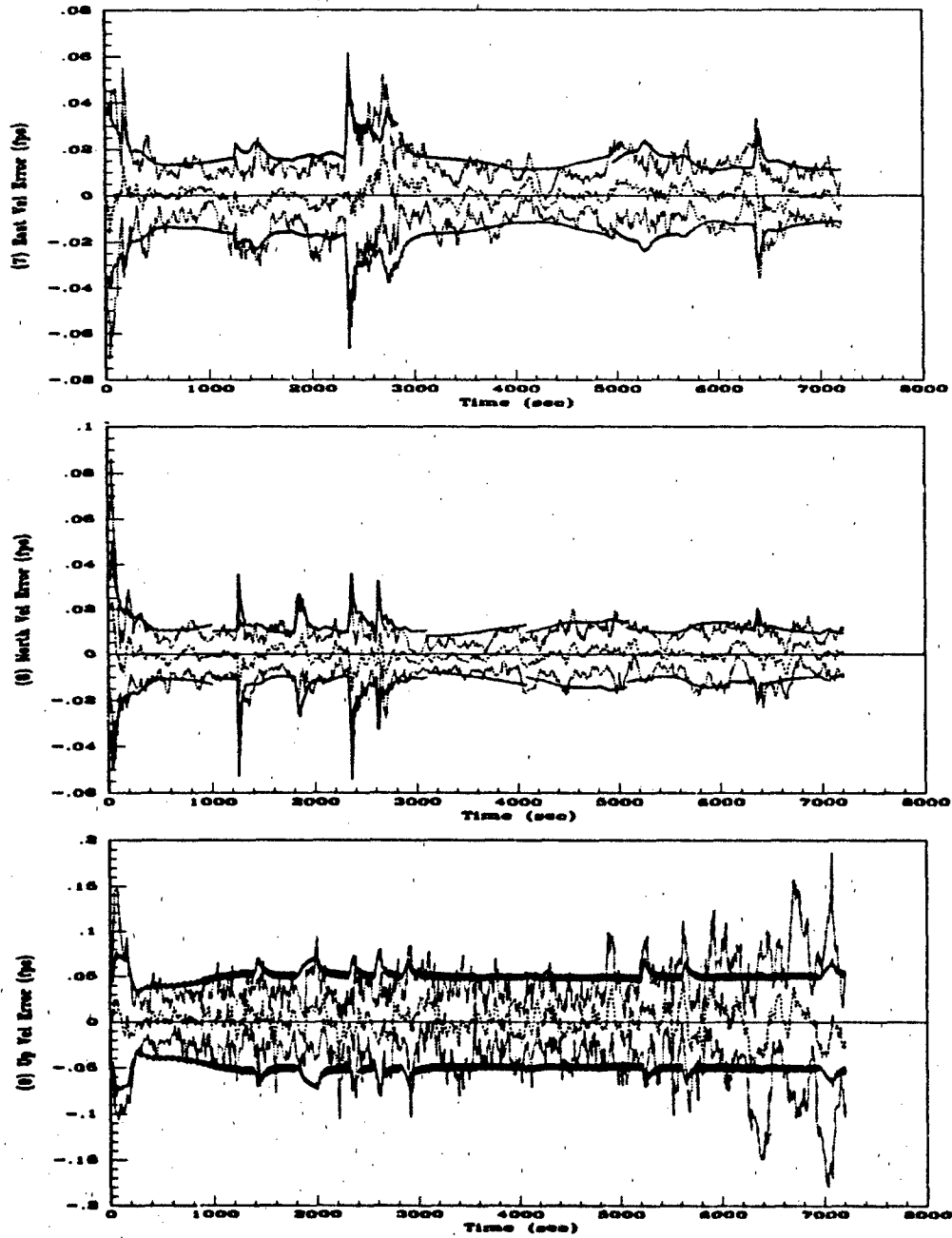


Figure E.3. 97-State NRS Filter (a) East Velocity (b) North Velocity and (c) Vertical Velocity Errors.

- - - -	Mean Error = $\bar{M}_x - (M_x)_{true}$
.....	Mean Error $\pm \sigma_{true}$
————	$0 \pm \sigma_{filter}$

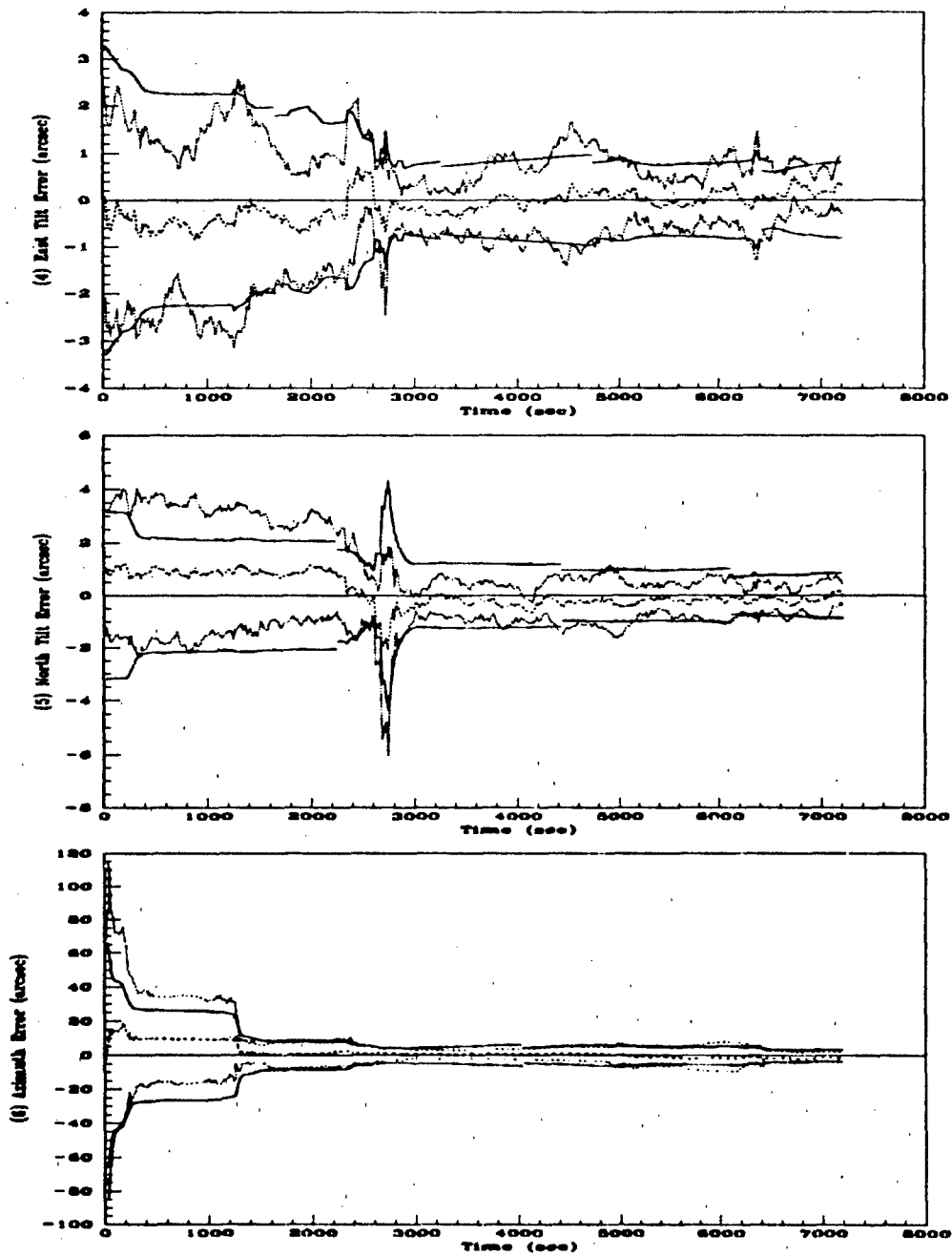


Figure E.4. 97-State NRS Filter (a) East Tilt (b) North Tilt and (c) Azimuth Errors.

----	Mean Error = $\bar{M}_x - (M_x)_{true}$
.....	Mean Error $\pm \sigma_{true}$
—	$0 \pm \sigma_{filter}$

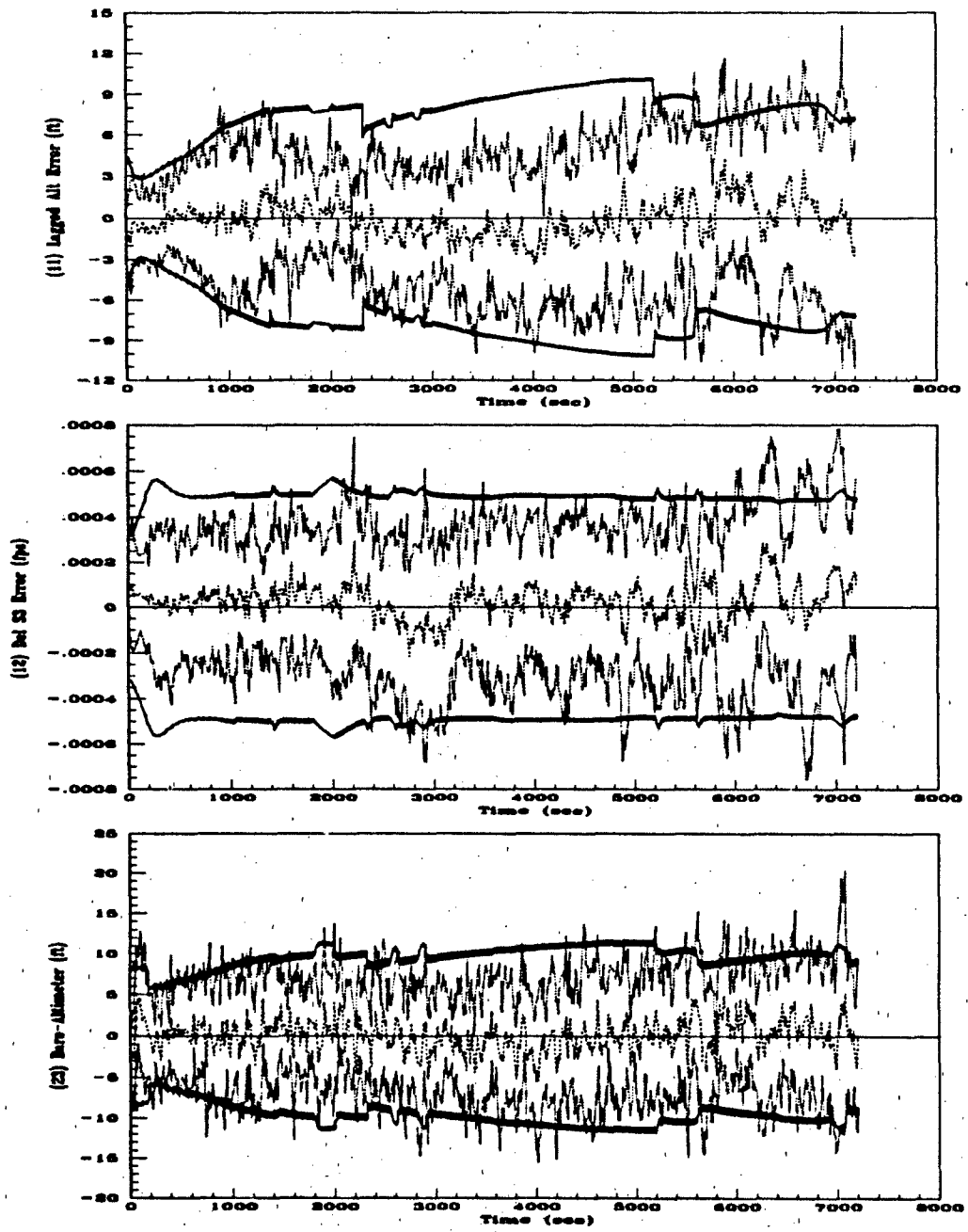


Figure E.5. 97-State NRS Filter (a) Lagged Altitude (b) Del S3 and (c) Baro-Altimeter Errors.

----	Mean Error = $\bar{M}_x - (M_x)_{true}$
.....	Mean Error $\pm \sigma_{true}$
—	$0 \pm \sigma_{filter}$

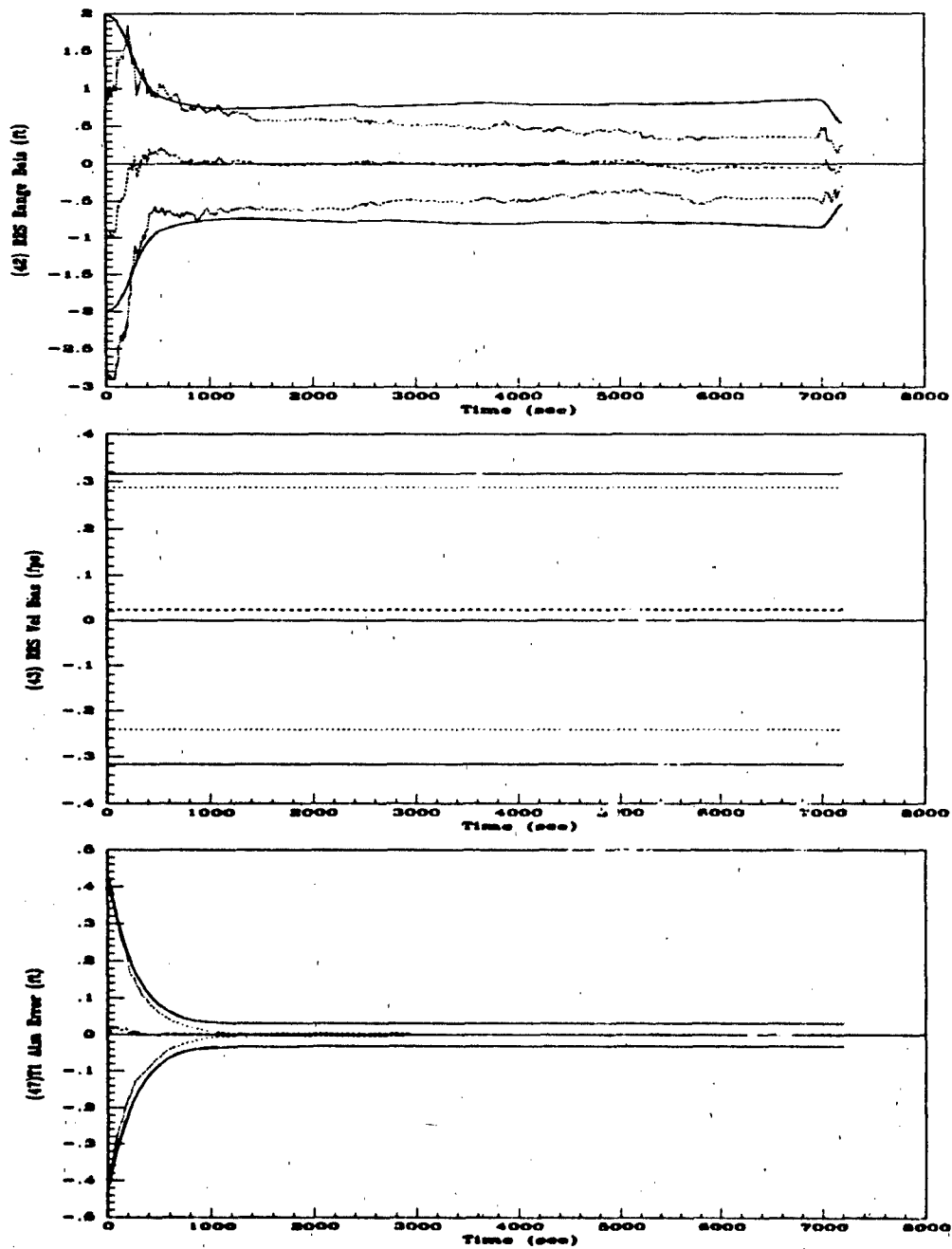


Figure E.6. 97-State NRS Filter (a) RRS Range Bias (b) RRS Vel Bias and (c) T1 Atmosphere Errors.

-----	Mean Error = $\bar{M}_x - (M_x)_{true}$
.....	Mean Error $\pm \sigma_{true}$
—	$0 \pm \sigma_{filter}$

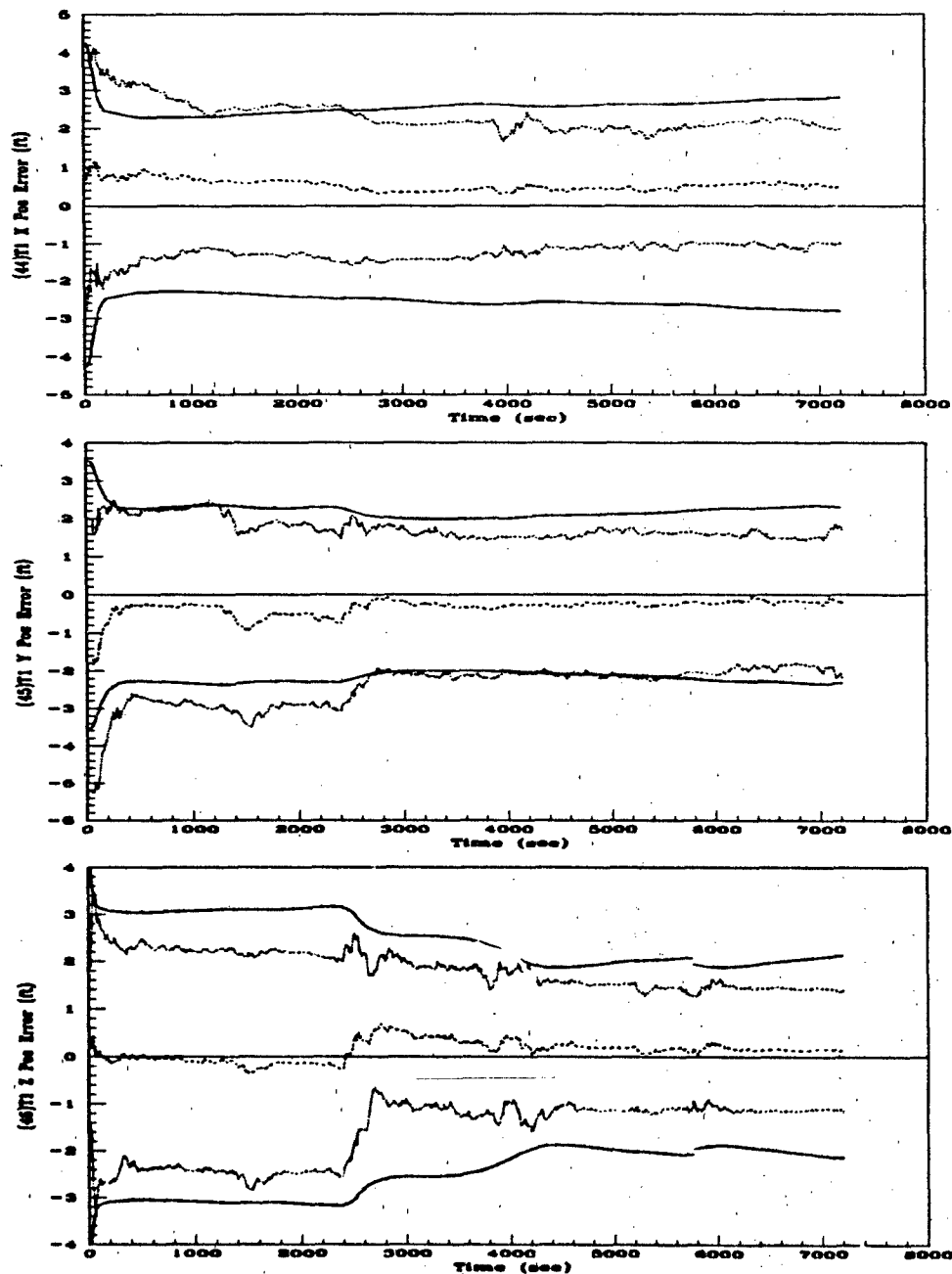


Figure E.7. 97-State NRS Filter (a) T1 X Position (b) T1 Y Position and (c) T1 Z Position Errors.

-----	$Mean\ Error = \bar{M}_x - (M_x)_{true}$
.....	$Mean\ Error \pm \sigma_{true}$
————	$0 \pm \sigma_{filter}$

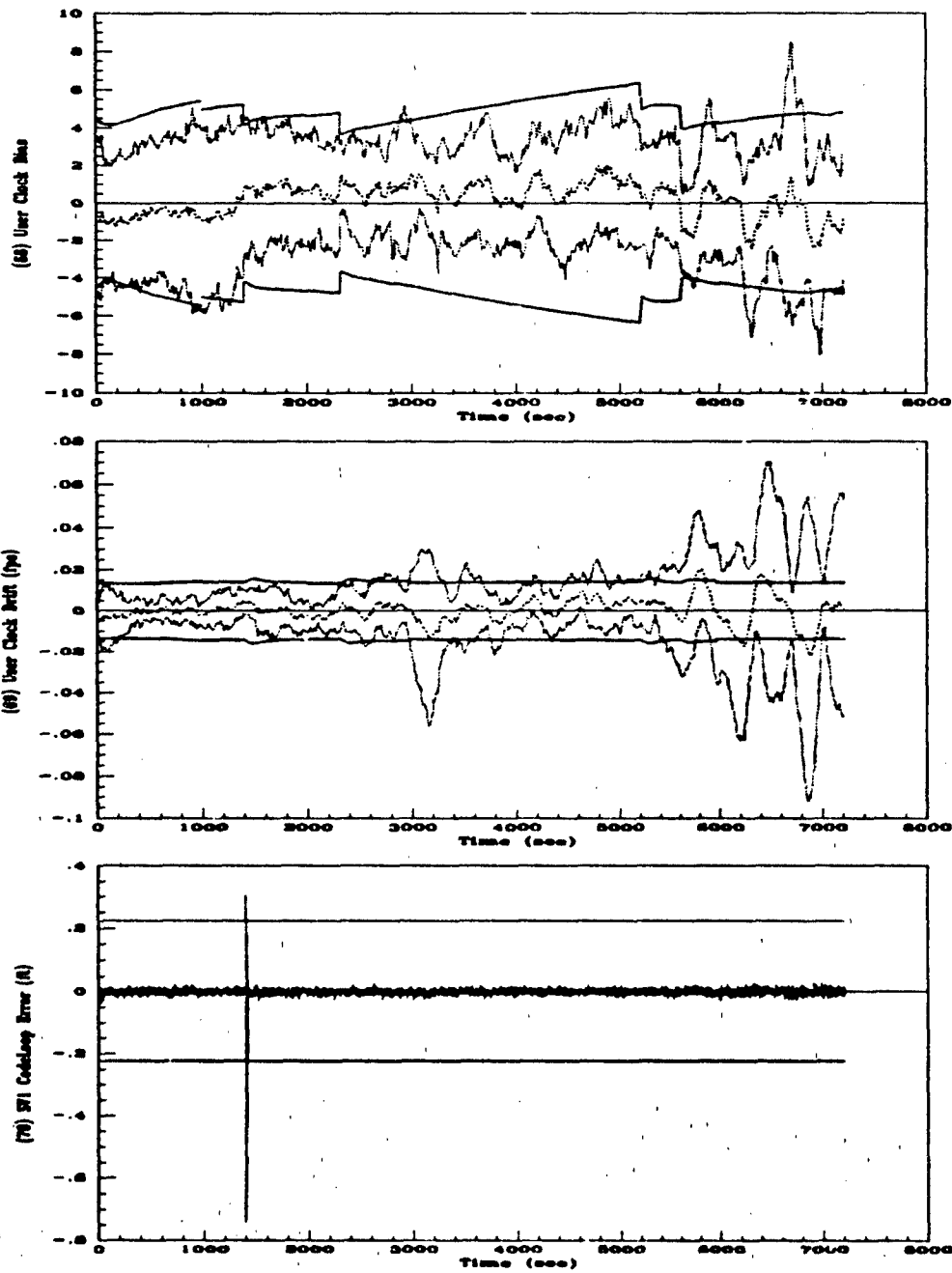


Figure E.8. 97-State NRS Filter (a) User Clock Bias (b) User Clock Drift and (c) SV1 Code Loop Errors.

----	Mean Error = $M_x - (M_x)_{true}$
.....	Mean Error $\pm \sigma_{true}$
—	$0 \pm \sigma_{filter}$

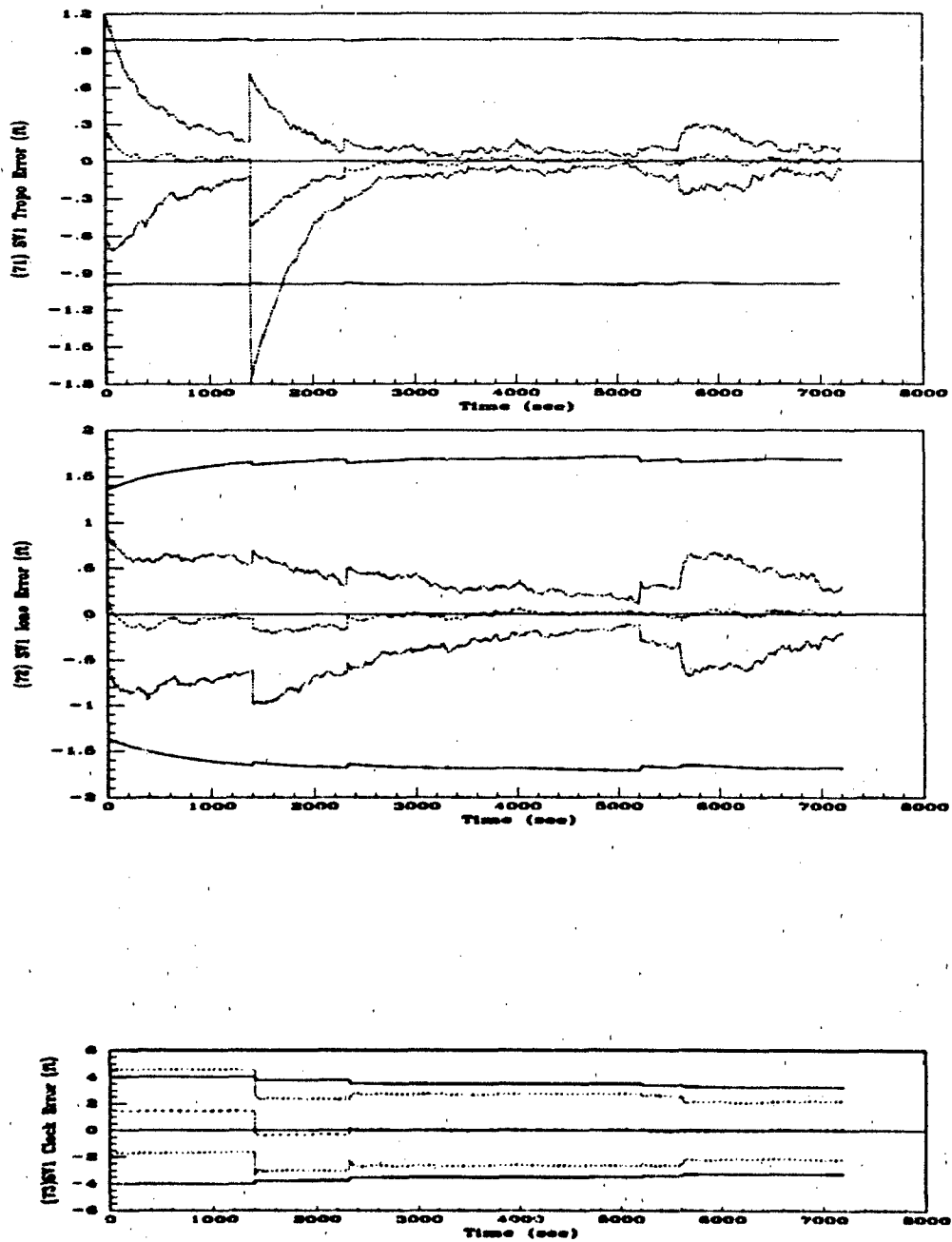


Figure E.9. 97-State NRS Filter (a) SV1 Troposphere (b) SV1 Ionosphere and (c) SV1 Clock Errors.

----	Mean Error = $\hat{M}_x - (M_x)_{true}$
.....	Mean Error $\pm \sigma_{true}$
—	$0 \pm \sigma_{filter}$

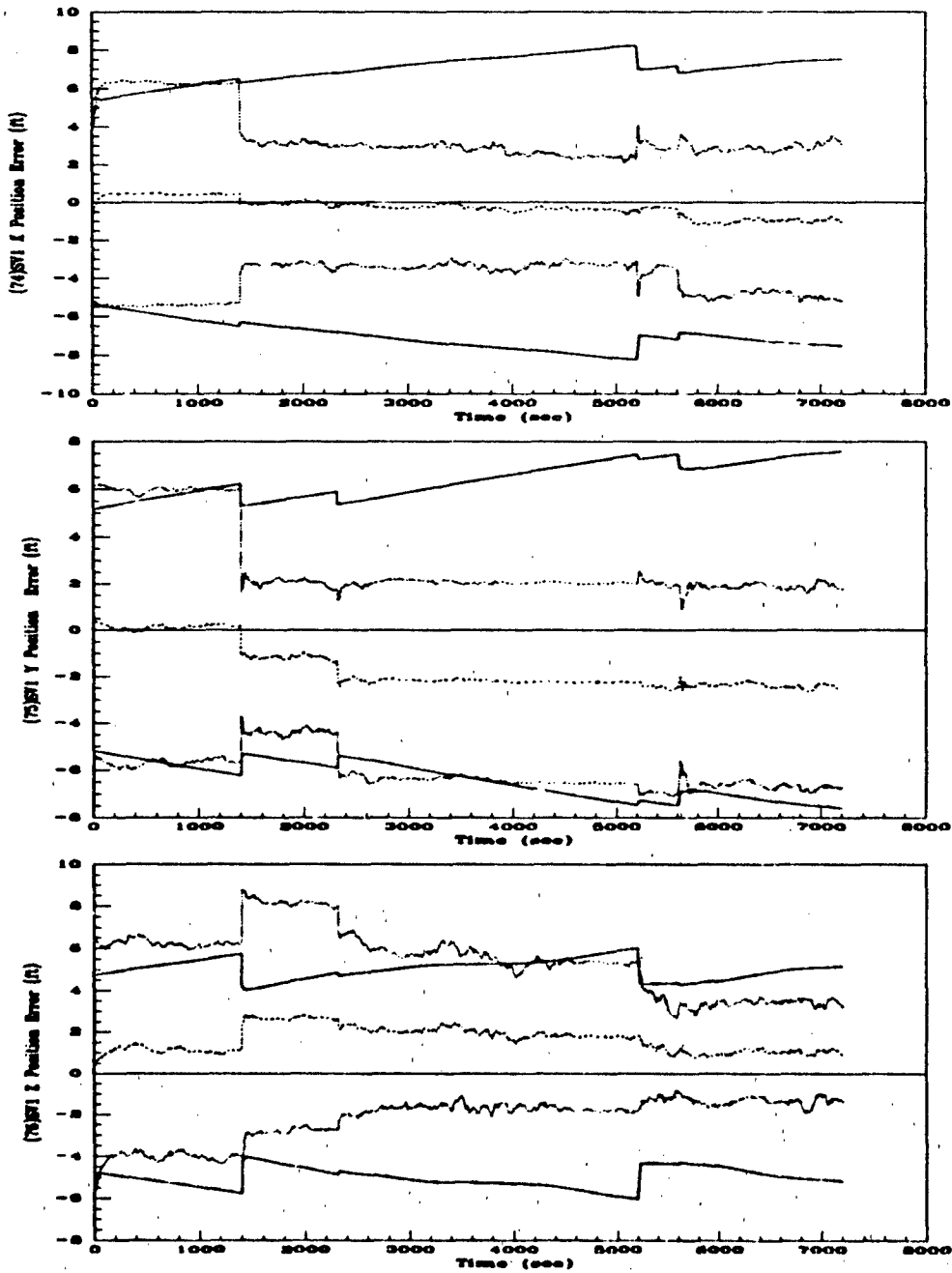


Figure E.10. 97-State NRS Filter (a) SV1 X Position (b) SV1 Y Position and (c) SV1 Z Position Errors.

----	Mean Error = $\bar{M}_x - (M_x)_{true}$
.....	Mean Error $\pm \sigma_{true}$
—	$0 \pm \sigma_{filter}$

Appendix F. *69-State NRS Filter Performance Plots*

The plots in this section represent results of a 10-run Monte Carlo 2-hour fighter flight profile simulation. This filter analysis was performed in double precision, so the GPS receiver clock errors are at their actual values. This reduced-order filter incorporates both RRS range and GPS pseudorange measurements.

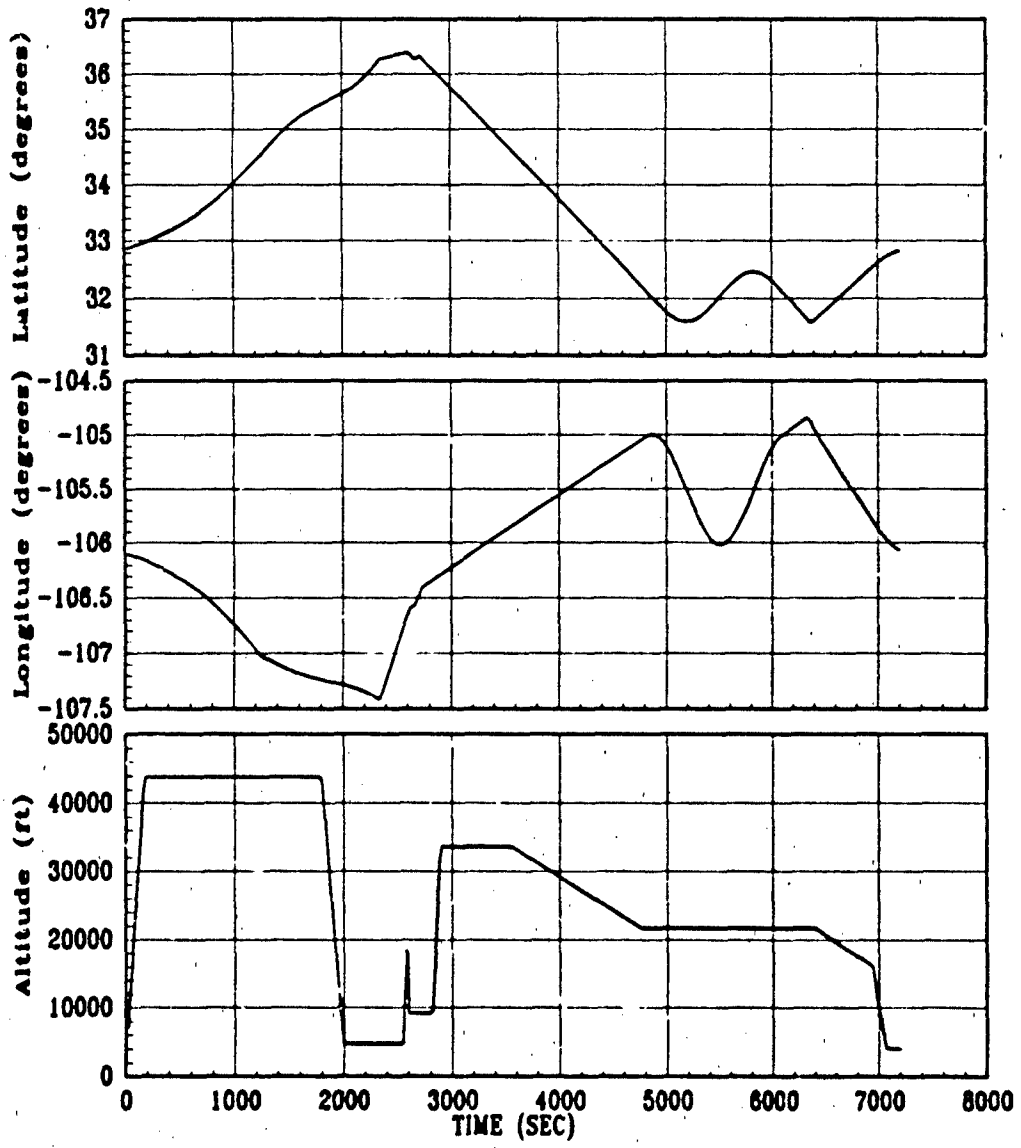


Figure F.1. 2-Hour Fighter Flight Profile (a) Latitude (b) Longitude and (c) Altitude

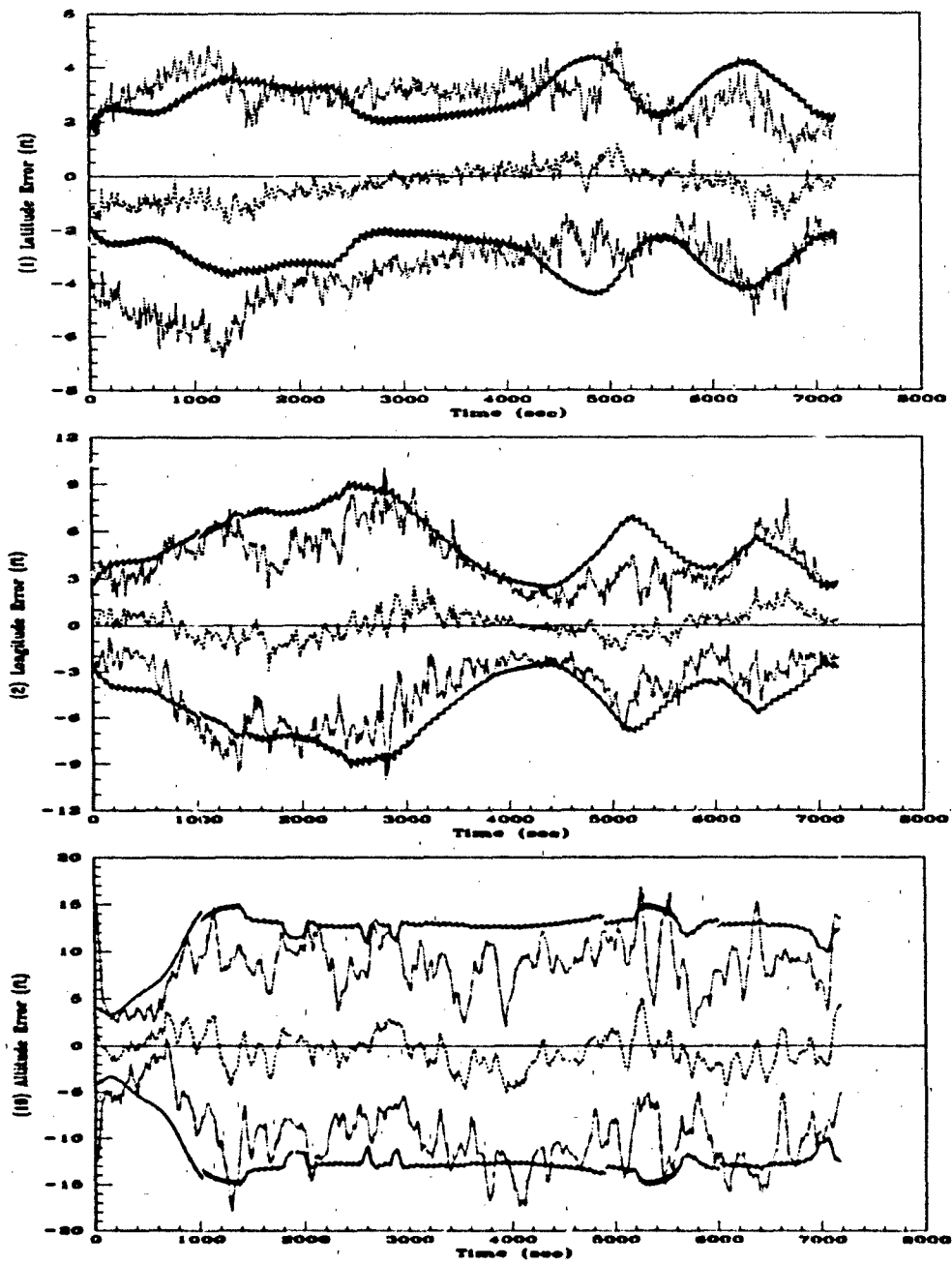


Figure F.2. 69-State NRS Filter (a) Latitude (b) Longitude and (c) Altitude Errors.

-----	Mean Error = $M_x - (M_x)_{true}$
.....	Mean Error $\pm \sigma_{true}$
————	$0 \pm \sigma_{filter}$

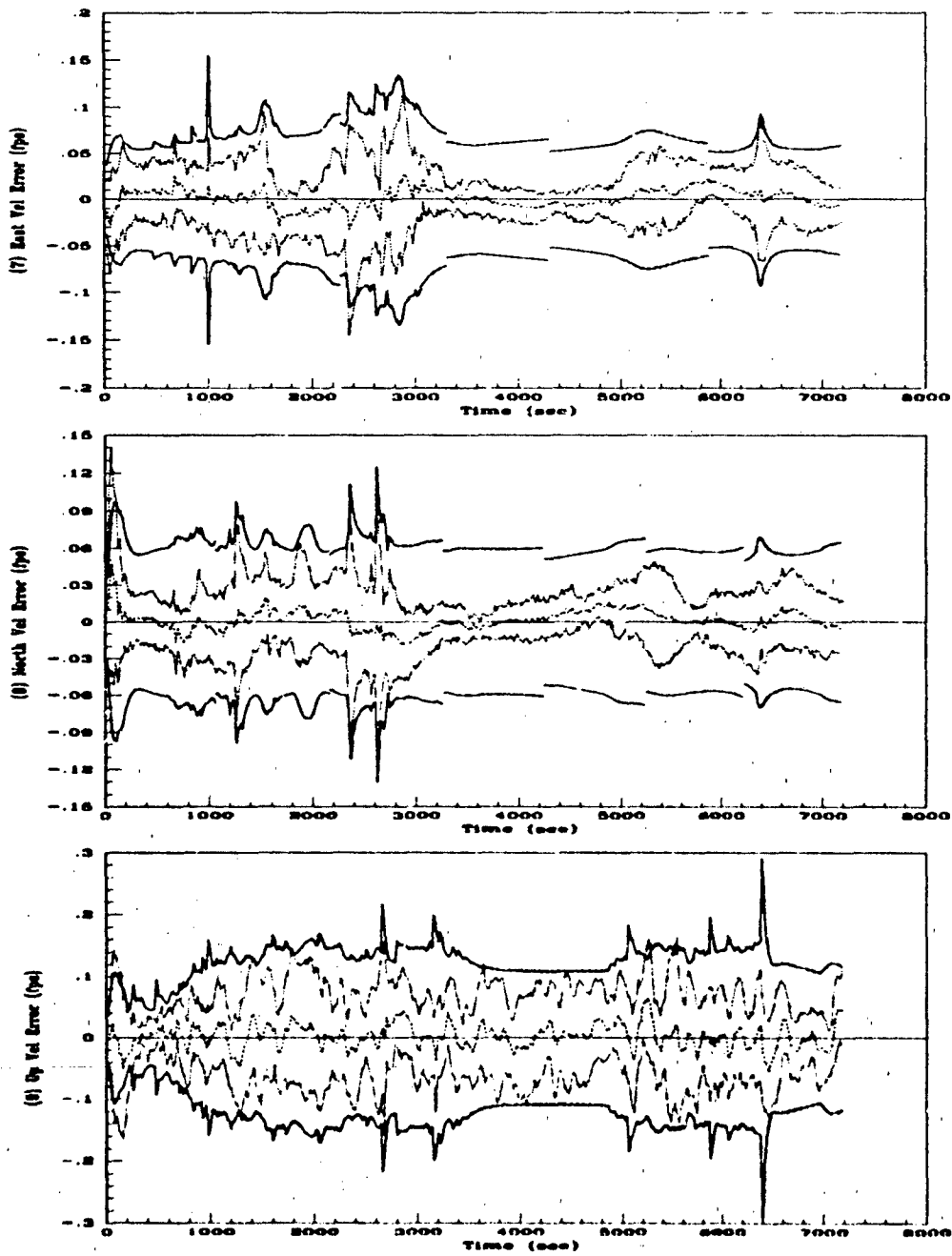


Figure F.3. 69-State NRS Filter (a) East Velocity (b) North Velocity and (c) Vertical Velocity Errors.

-----	Mean Error = $M_x - (M_x)_{true}$
.....	Mean Error $\pm \sigma_{true}$
—	$0 \pm \sigma_{filter}$

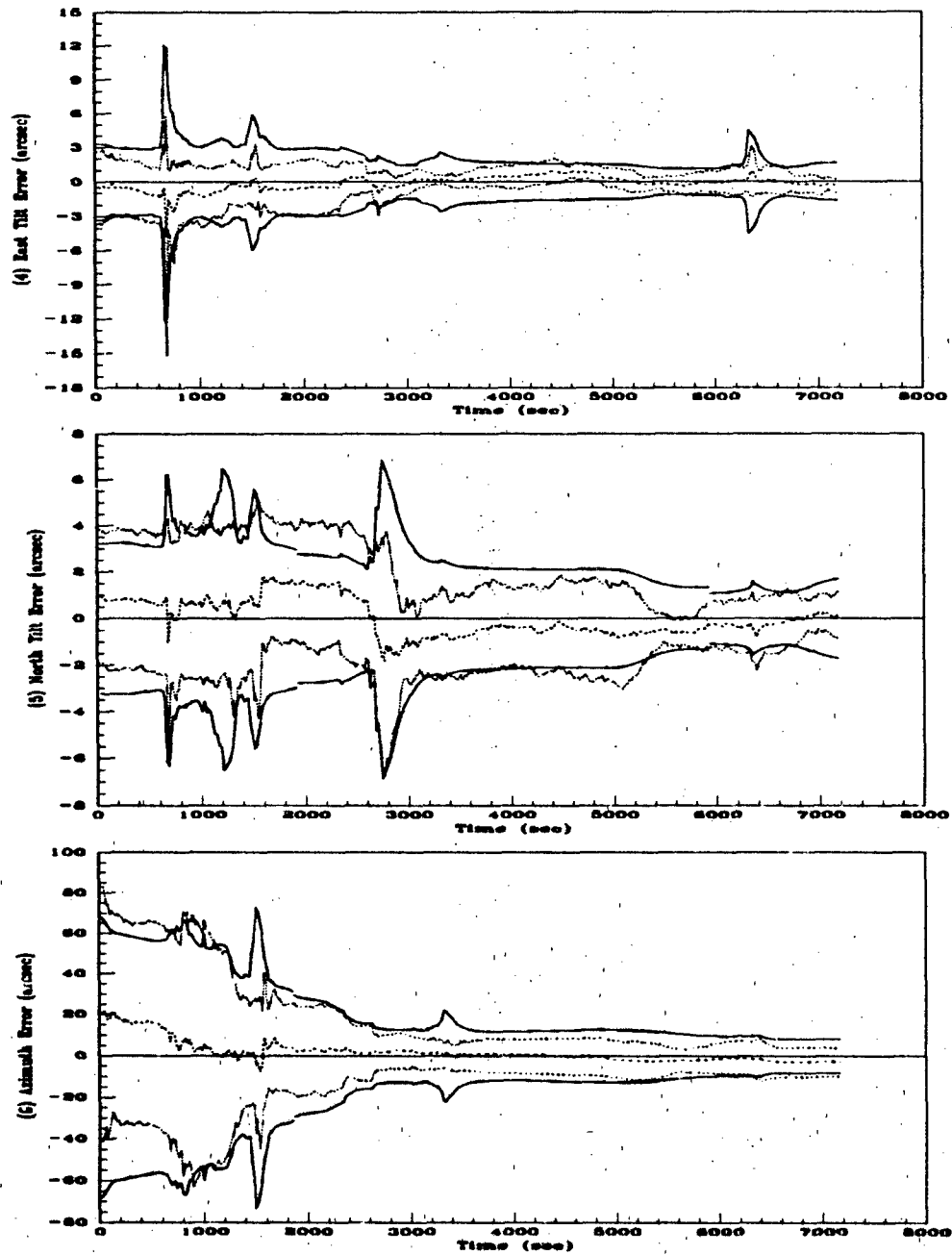


Figure F.4. 69-State NRS Filter (a) East Tilt (b) North Tilt and (c) Azimuth Errors.

----	Mean Error = $\bar{M}_x - (M_x)_{true}$
.....	Mean Error $\pm \sigma_{true}$
—	$0 \pm \sigma_{filter}$

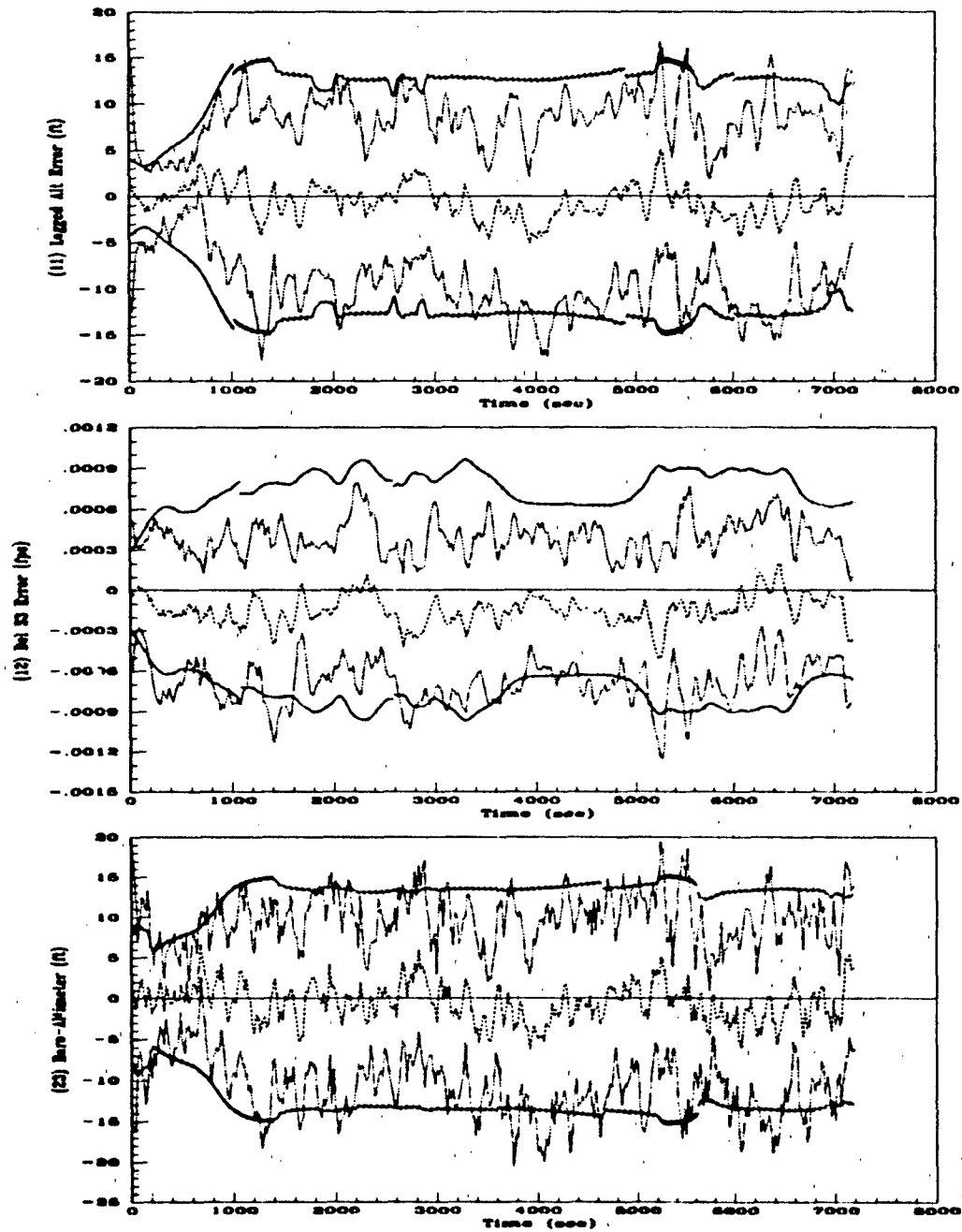


Figure F.5. 69-State NRS Filter (a) Lagged Altitude (b) Del S3 and (c) Baro-Altimeter Errors.

-----	Mean Error = $\bar{M}_z - (M_z)_{true}$
.....	Mean Error $\pm \sigma_{true}$
————	$0 \pm \sigma_{filter}$

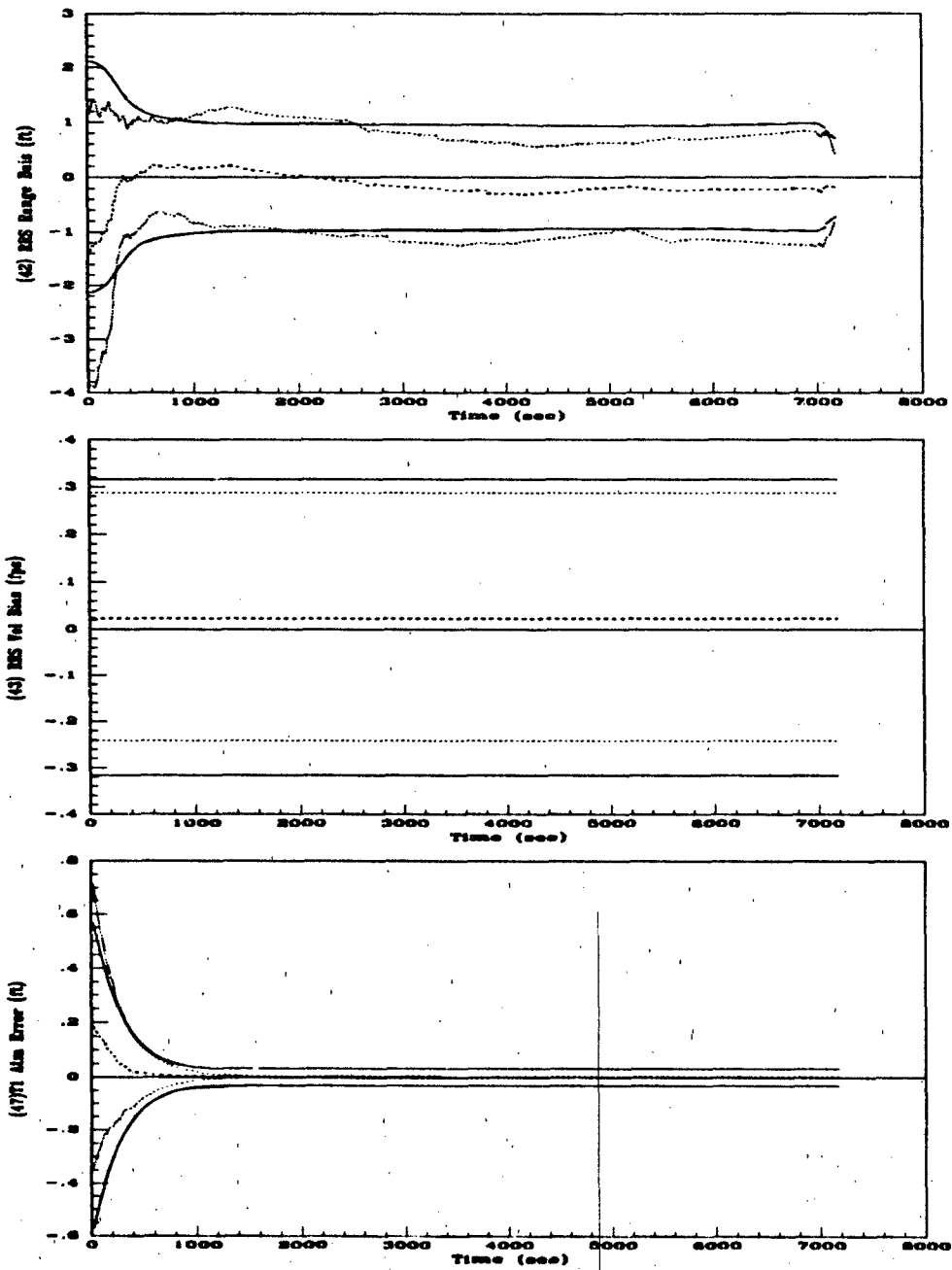


Figure F.6. 69-State NRS Filter (a) RRS Range Bias (b) RRS Vel Bias and (c) T1 Atmosphere Errors.

- - - -	Mean Error = $\bar{M}_z - (M_z)_{true}$
.....	Mean Error $\pm \sigma_{true}$
—	$0 \pm \sigma_{filter}$

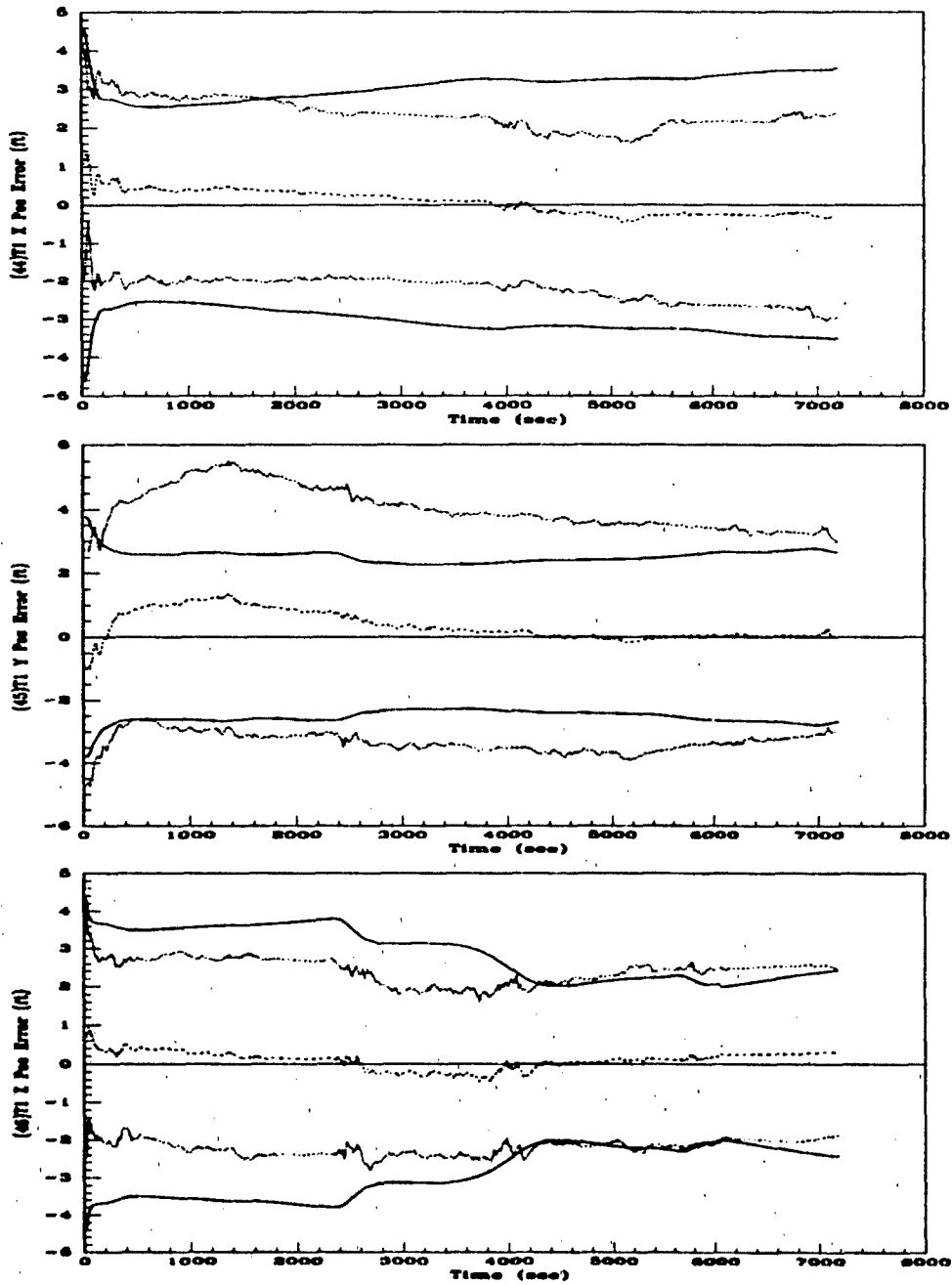


Figure F.7. 69-State NRS Filter (a) T1 X Position (b) T1 Y Position and (c) T1 Z Position Errors.

.....	Mean Error = $M_x - (M_x)_{true}$
.....	Mean Error $\pm \sigma_{true}$
—	$0 \pm \sigma_{filter}$

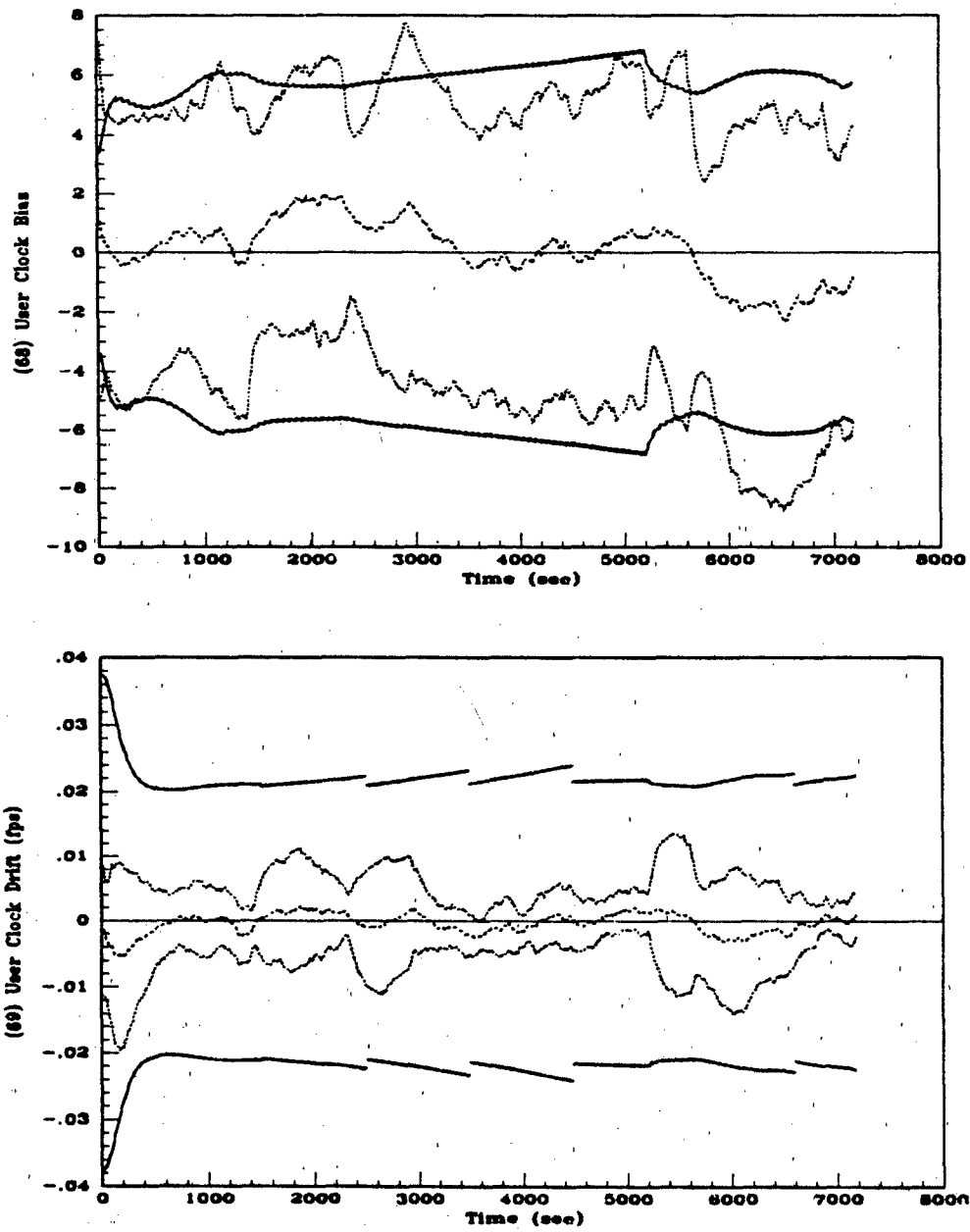


Figure F.8. 69-State NRS Filter (a) User Clock Bias and (b) User Clock Drift Errors.

---	Mean Error = $\bar{M}_x - (M_x)_{true}$
.....	Mean Error $\pm \sigma_{true}$
—	$0 \pm \sigma_{filter}$

Appendix G. *89-State ENRS Filter Performance Plots*

The plots in this section represent results of a 10-run Monte Carlo 2-hour fighter flight profile simulation. In these runs the GPS receiver clock states initial covariance values have been decreased 4 orders of magnitude, as discussed in Chapter V, so that single precision could be used in the MSOFE simulation. This filter incorporates both RRS range and DGPS pseudorange measurements.

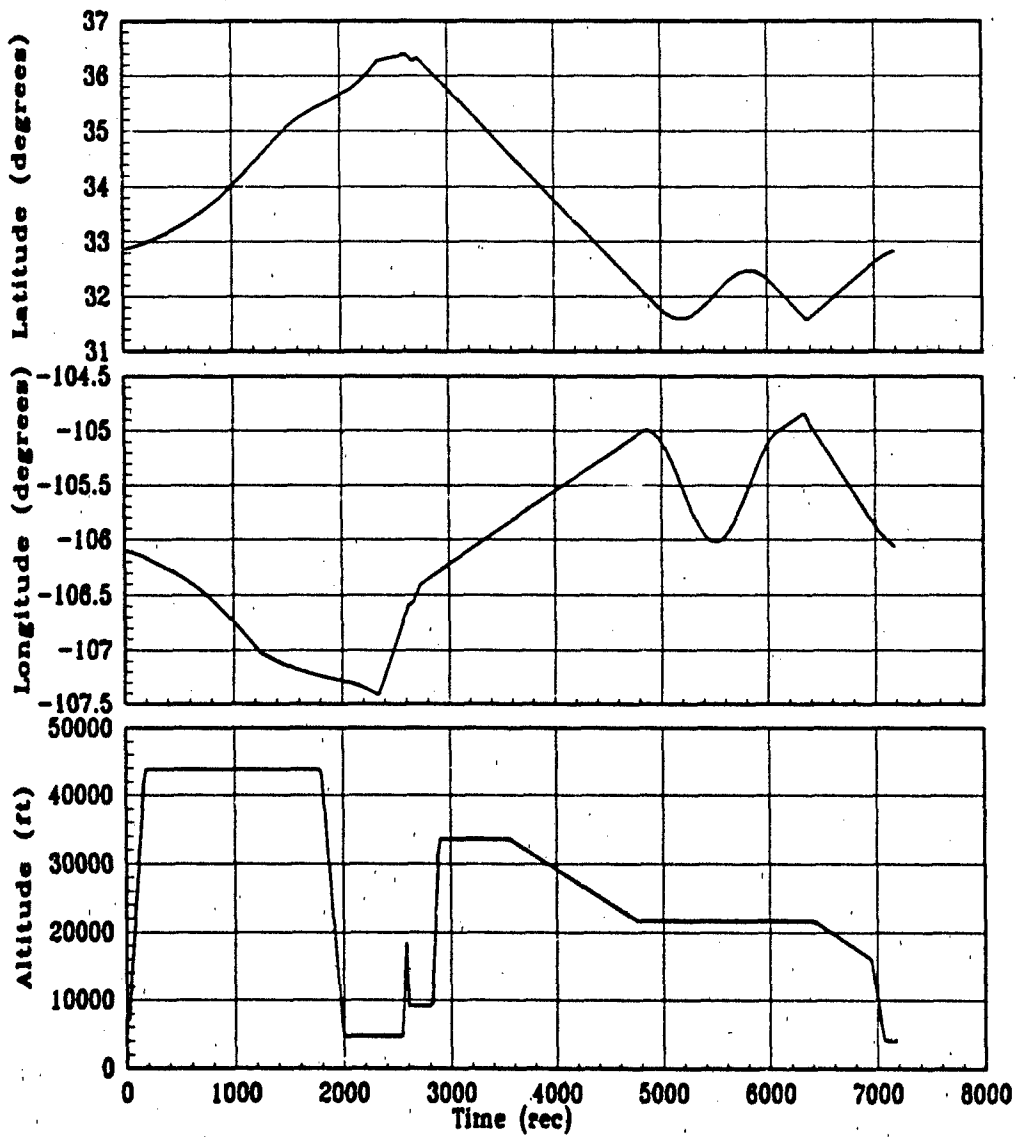


Figure G.1. 2-Hour Fighter Flight Profile (a) Latitude (b) Longitude and (c) Altitude

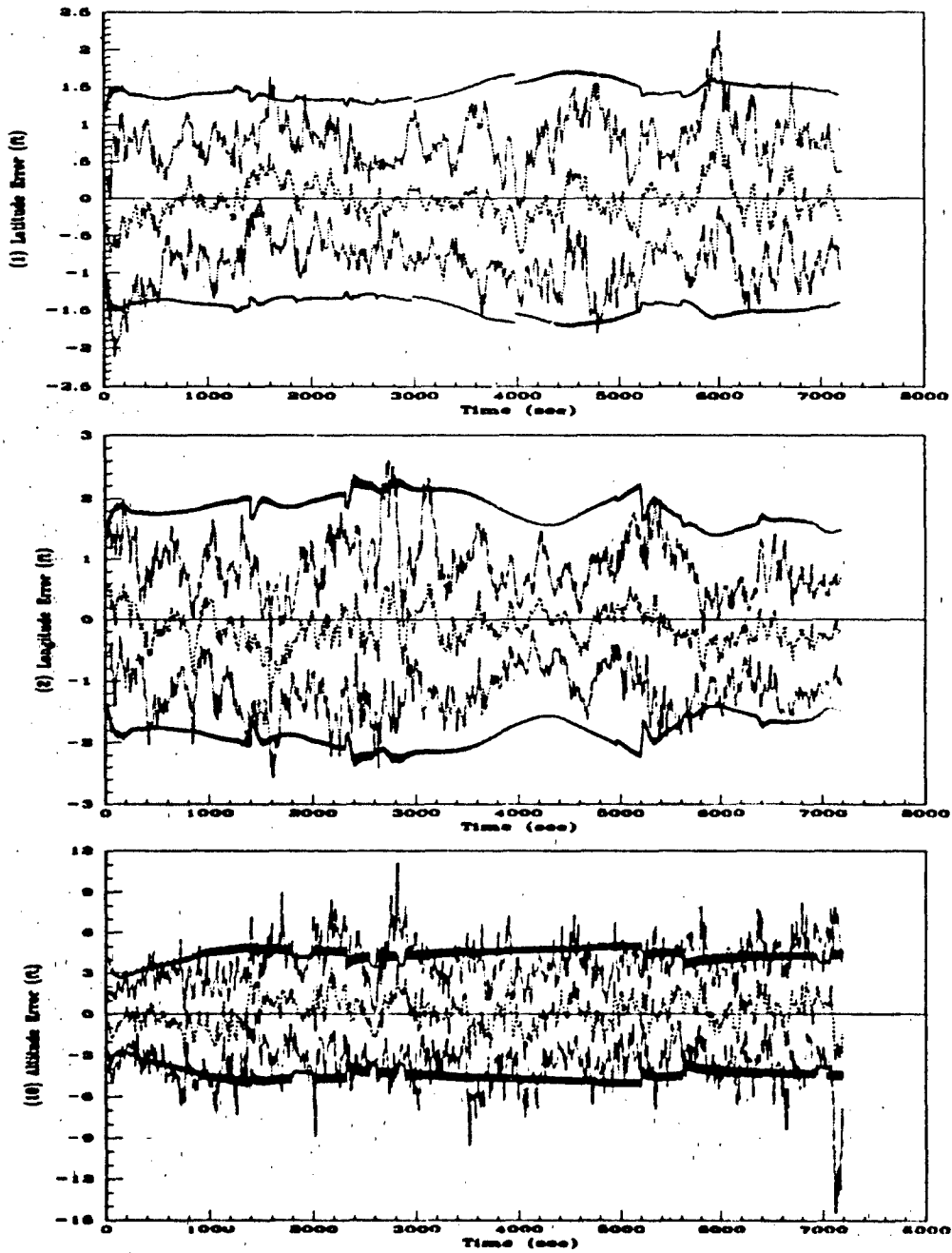


Figure G.2. 89-State ENRS Filter (a) Latitude (b) Longitude and (c) Altitude Errors.

-----	Mean Error = $\bar{M}_x - (M_x)_{true}$
.....	Mean Error $\pm \sigma_{true}$
————	$0 \pm \sigma_{filter}$

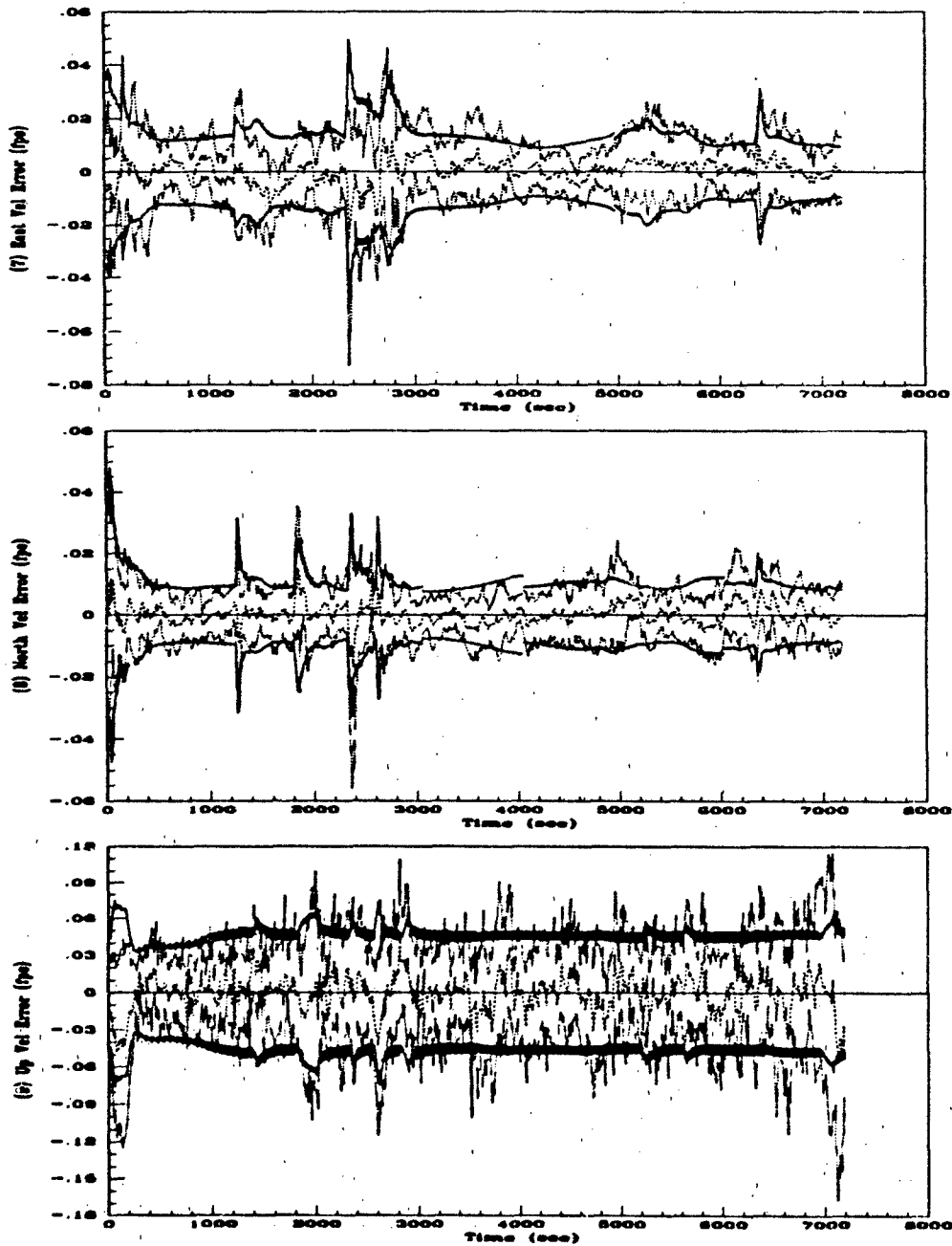


Figure G.3. 89-State ENRS Filter (a) East Velocity (b) North Velocity and (c) Vertical Velocity Errors.

-----	Mean Error = $M_x - (M_x)_{true}$
.....	Mean Error $\pm \sigma_{true}$
—	$0 \pm \sigma_{filter}$

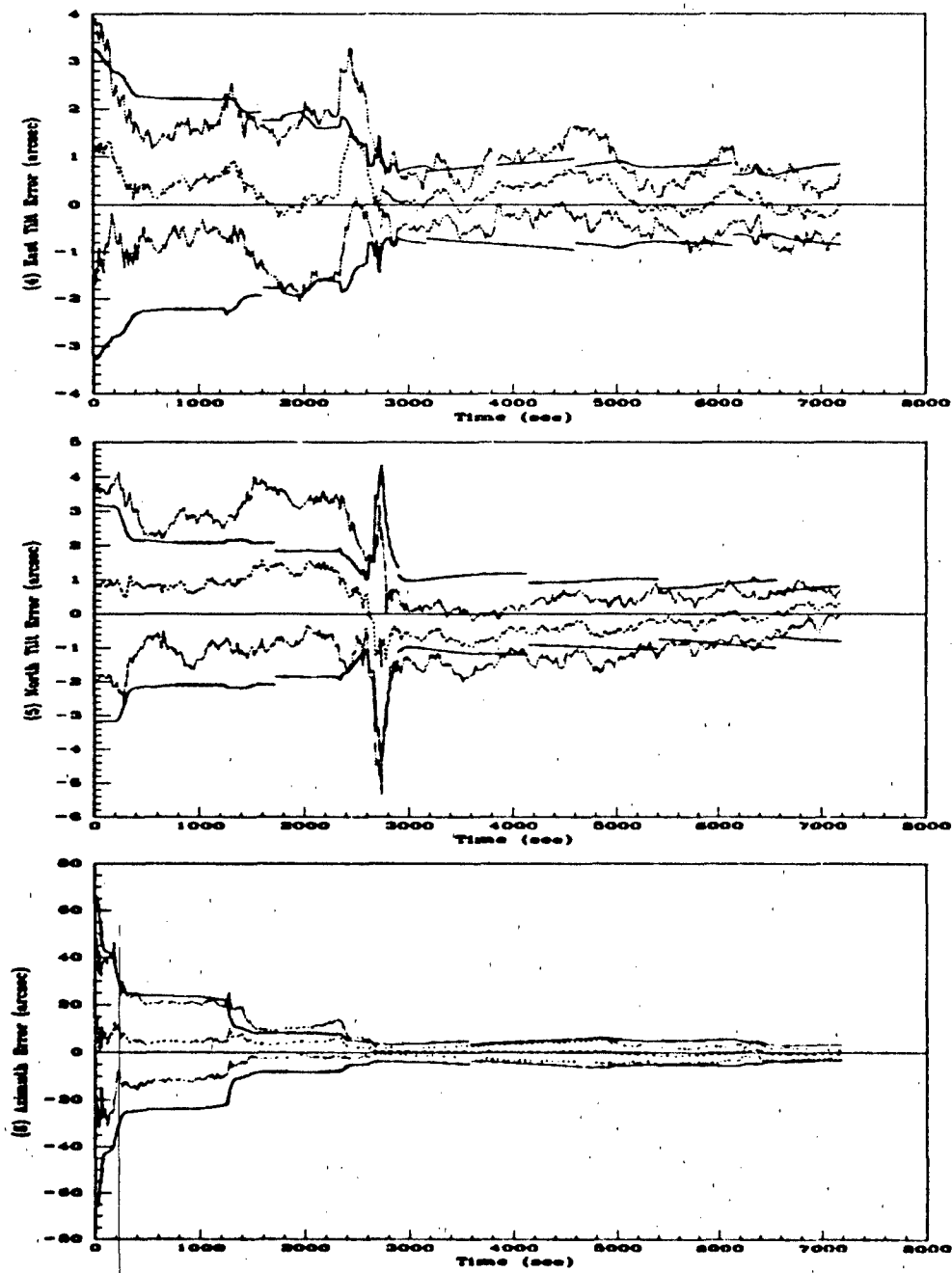


Figure G.4. 89-State ENRS Filter (a) East Tilt (b) North Tilt and (c) Azimuth Errors.

- - - -	Mean Error = $M_x - (M_x)_{true}$
.....	Mean Error $\pm \sigma_{true}$
—	$0 \pm \sigma_{filter}$

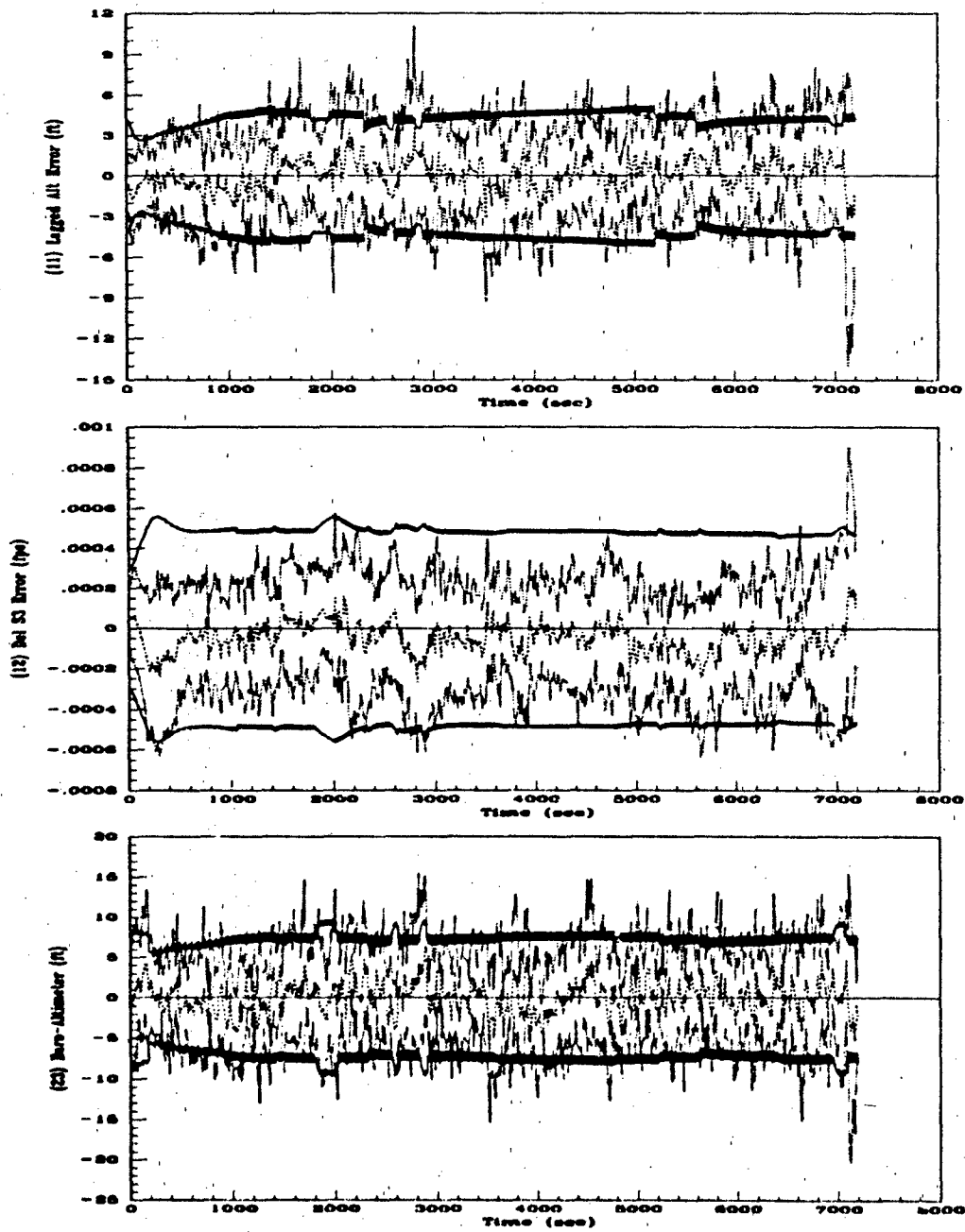


Figure G.5. 89-State ENRS Filter (a) Lagged Altitude (b) Del S3 and (c) Baro-Altimeter Errors.

- - - -	Mean Error = $\hat{M}_x - (M_x)_{true}$
.....	Mean Error $\pm \sigma_{true}$
————	$0 \pm \sigma_{filter}$

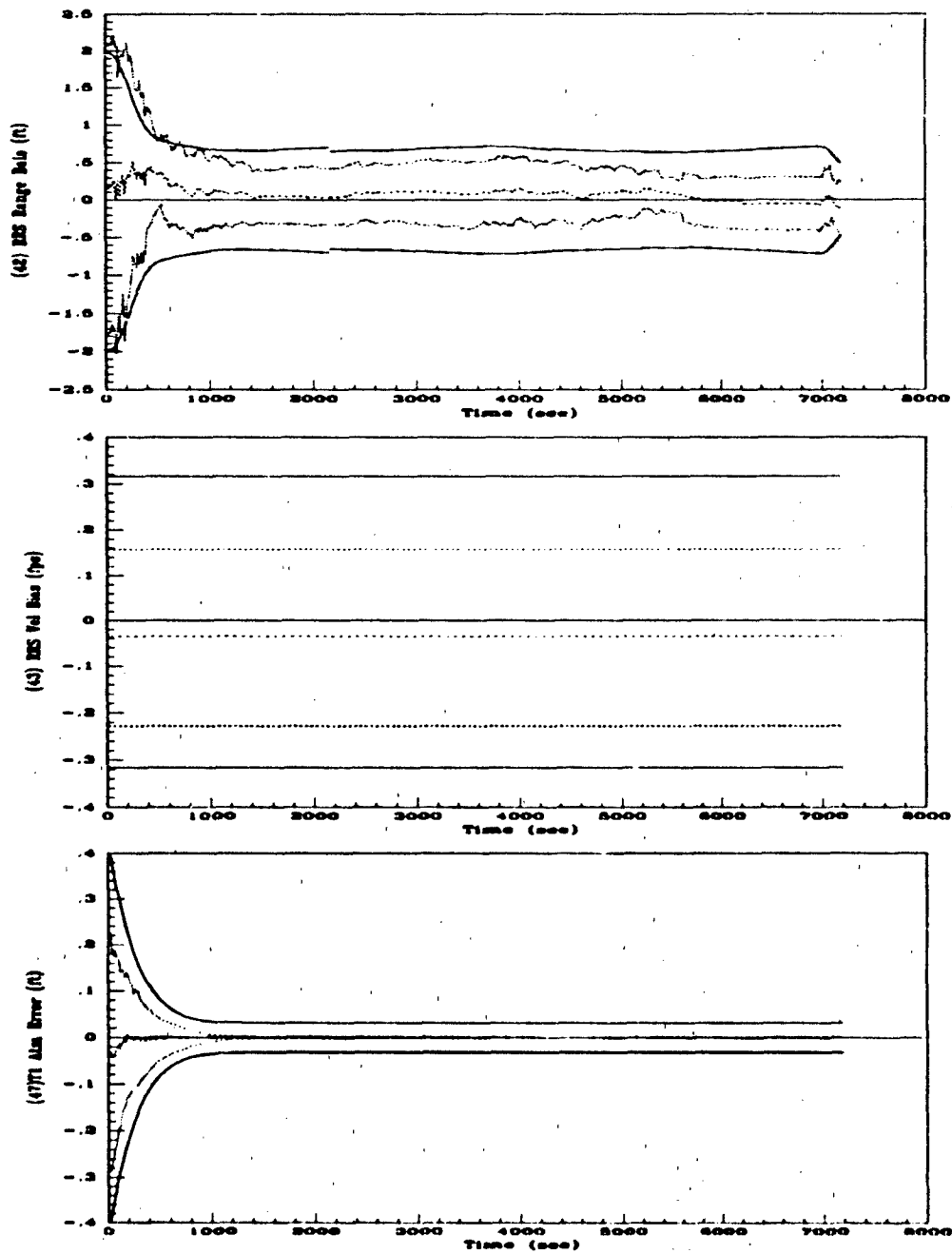


Figure G.6. 89-State ENRS Filter (a) RRS Range Bias (b) RRS Vel Bias and (c) T1 Atmosphere Errors.

.....	Mean Error = $M_x - (M_x)_{true}$
.....	Mean Error $\pm \sigma_{true}$
—	$0 \pm \sigma_{filter}$

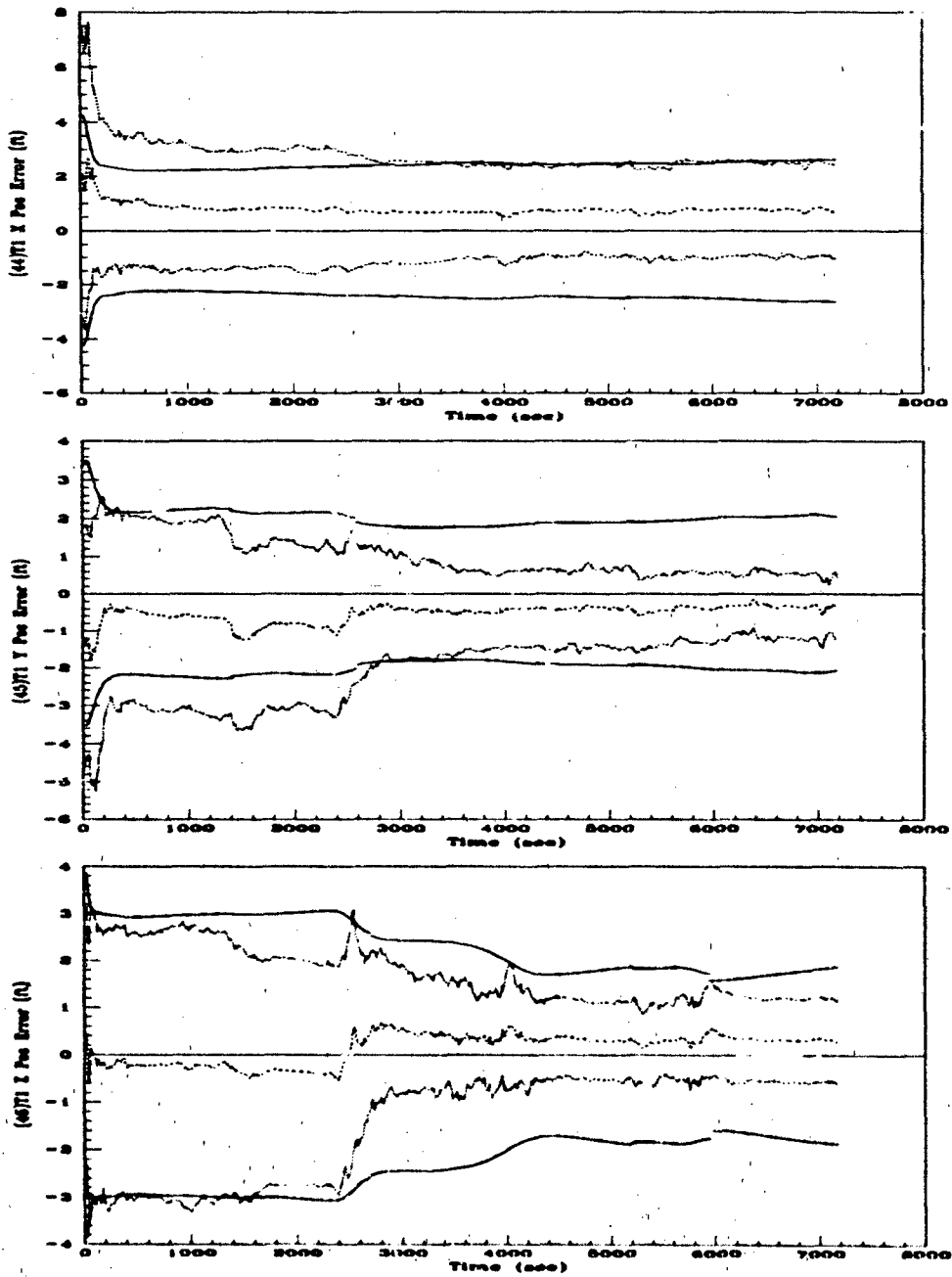


Figure G.7. 89-State ENRS Filter (a) T1 X Position (b) T1 Y Position and (c) T1 Z Position Errors.

-----	Mean Error = $M_x - (M_x)_{true}$
.....	Mean Error $\pm \sigma_{true}$
————	$0 \pm \sigma_{filter}$

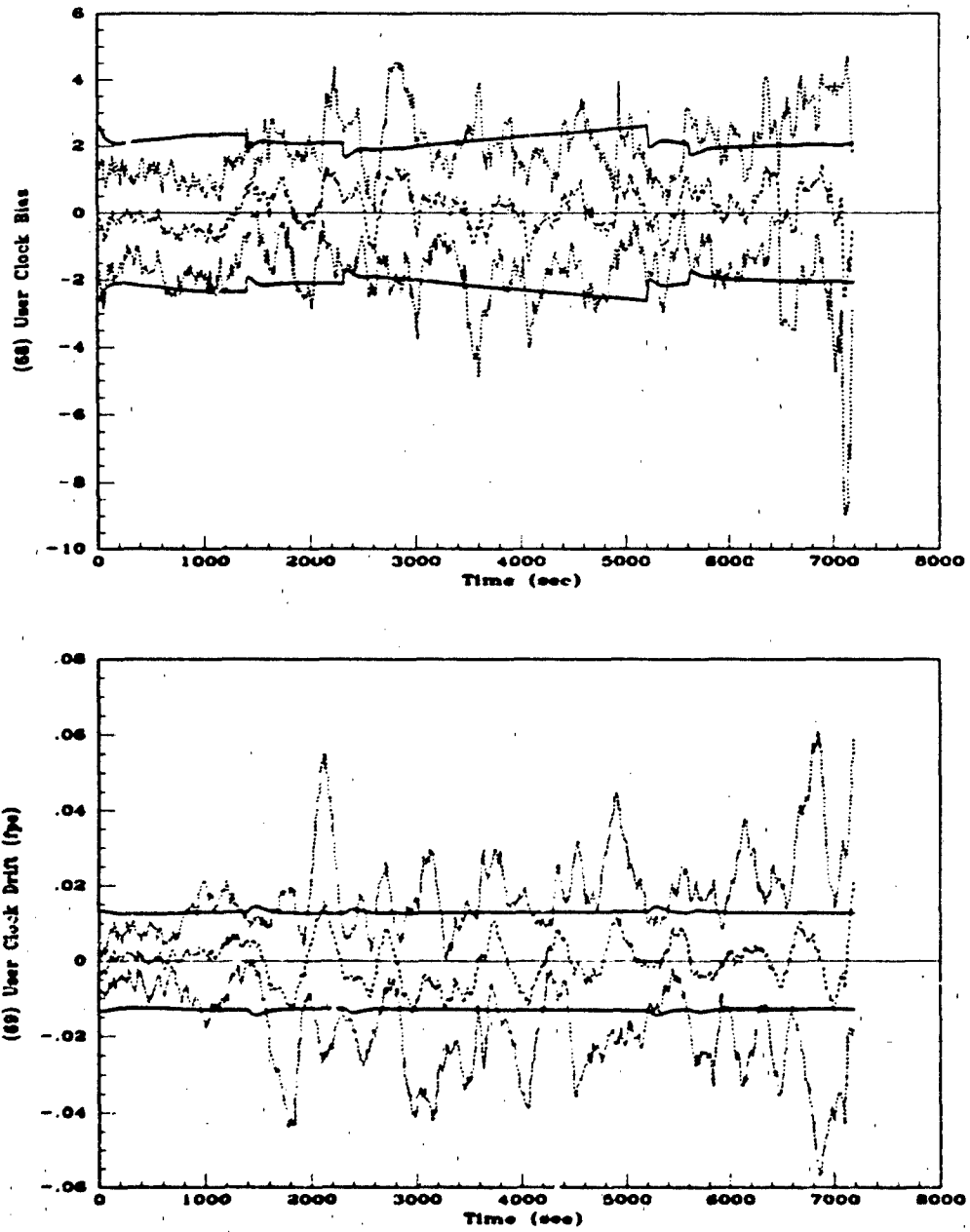


Figure G.8. 89-State ENRS Filter (a) User Clock Bias and (b) User Clock Drift Errors.

.....	Mean Error = $M_x - (M_x)_{true}$
.....	Mean Error $\pm \sigma_{true}$
—	$0 \pm \sigma_{filter}$

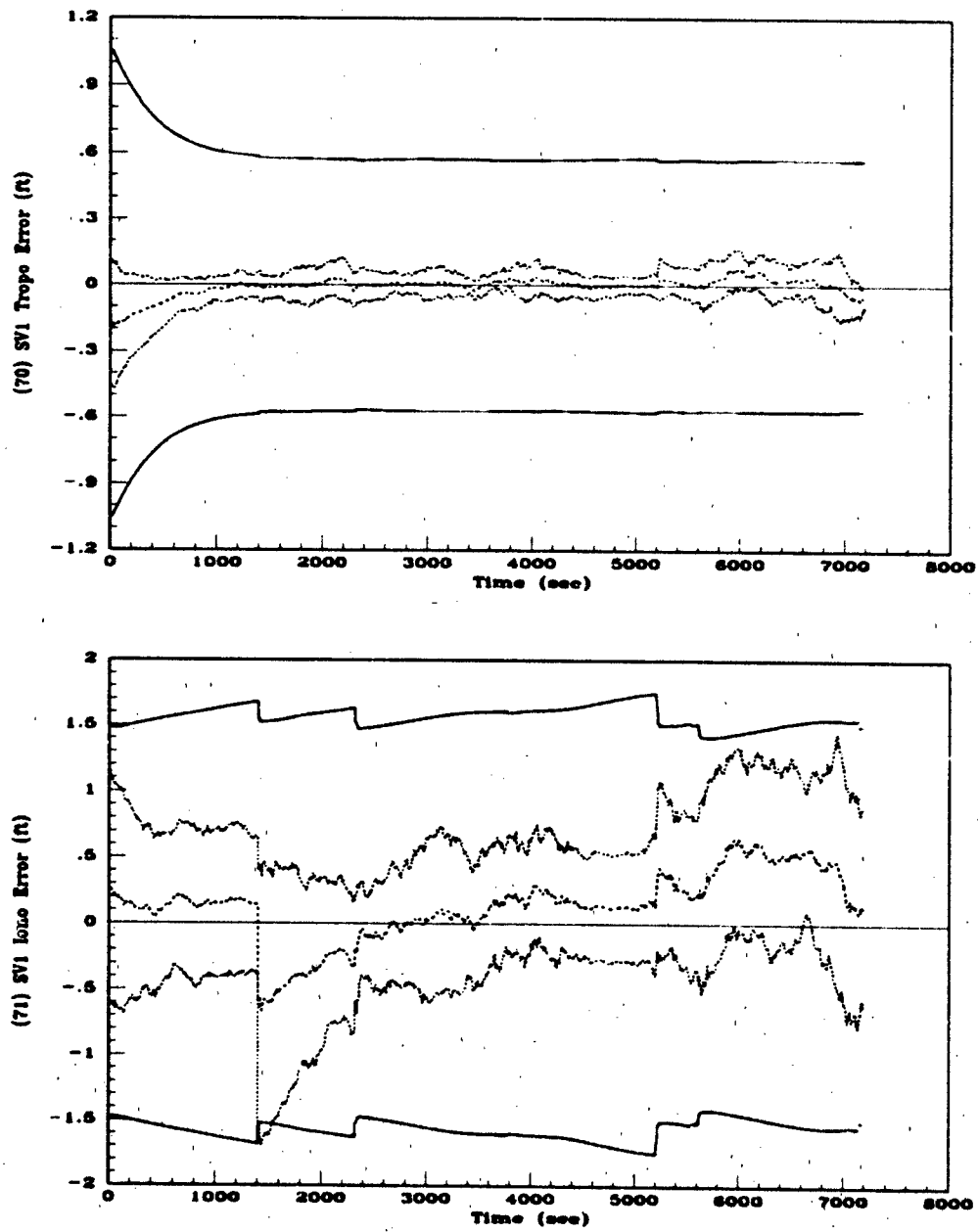


Figure G.9. 89-State ENRS Filter (a) SV1 Troposphere and (b) SV1 Ionosphere Errors.

-----	Mean Error $\equiv \bar{M}_x - (M_x)_{true}$
.....	Mean Error $\pm \sigma_{true}$
————	$0 \pm \sigma_{filter}$

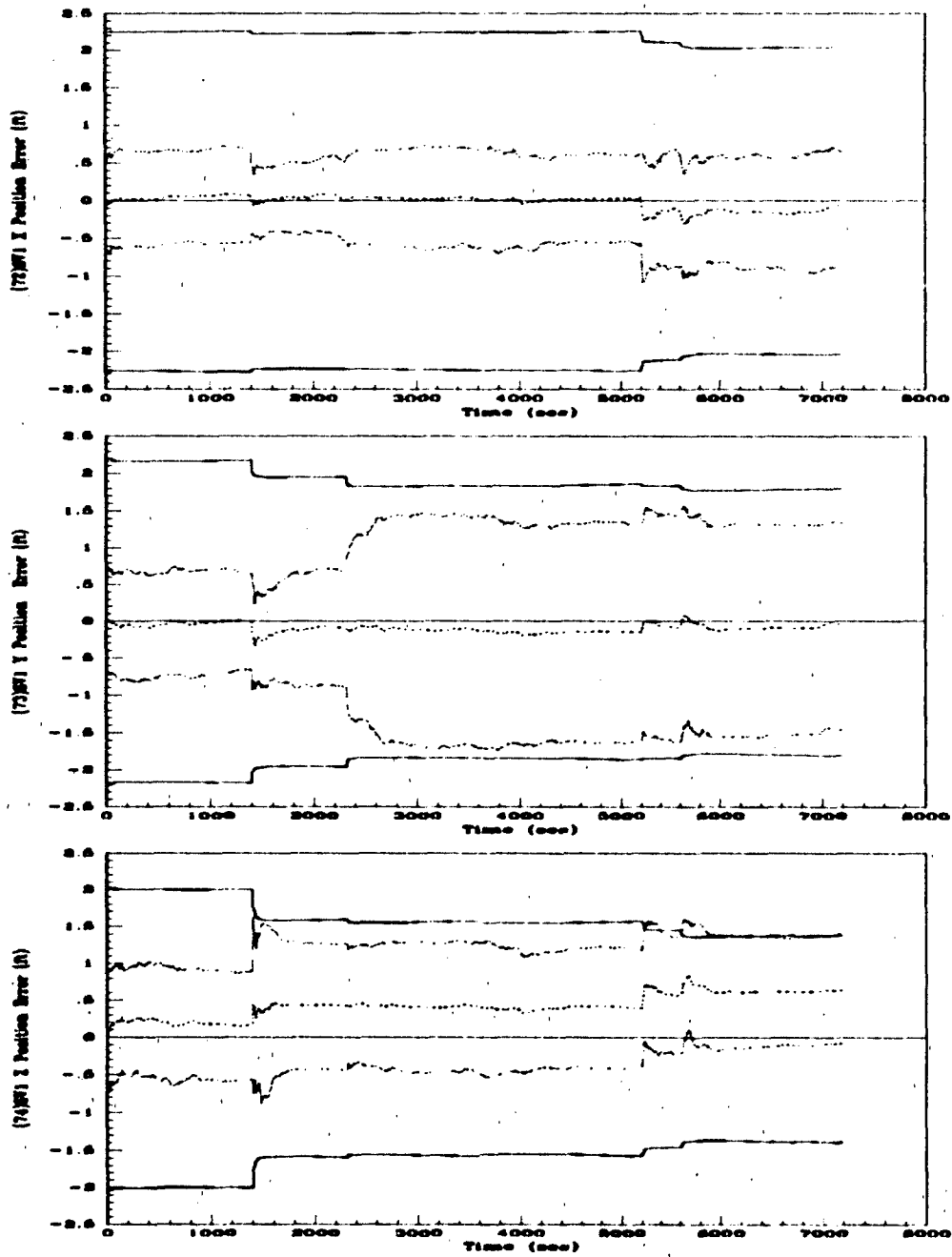


Figure G.10. 89-State ENRS Filter (a) SV1 X Position (b) SV1 Y Position and (c) SV1 Z Position Errors.

----	Mean Error = $M_x - (M_x)_{true}$
.....	Mean Error $\pm \sigma_{true}$
———	$0 \pm \sigma_{filter}$

Appendix H. *48-State ENRS Filter Performance Plots*

The plots in this section represent results of a 10-run Monte Carlo 2-hour fighter flight profile simulation. This filter analysis was performed in double precision, so the GPS receiver clock errors are at their actual values. This reduced-order filter incorporates both RRS range and DGPS pseudorange measurements.

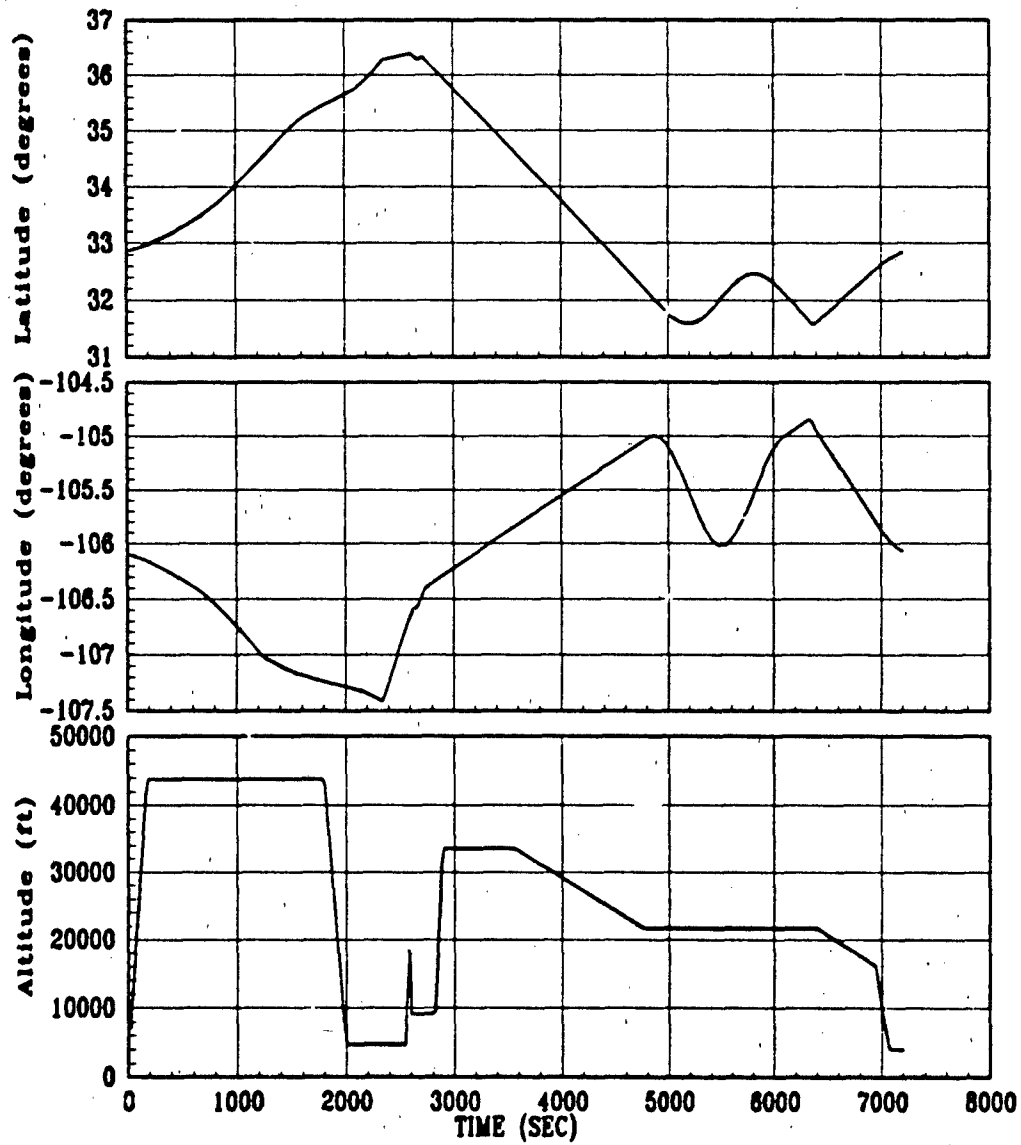


Figure H.1. 2-Hour Fighter Flight Profile (a) Latitude (b) Longitude and (c) Altitude

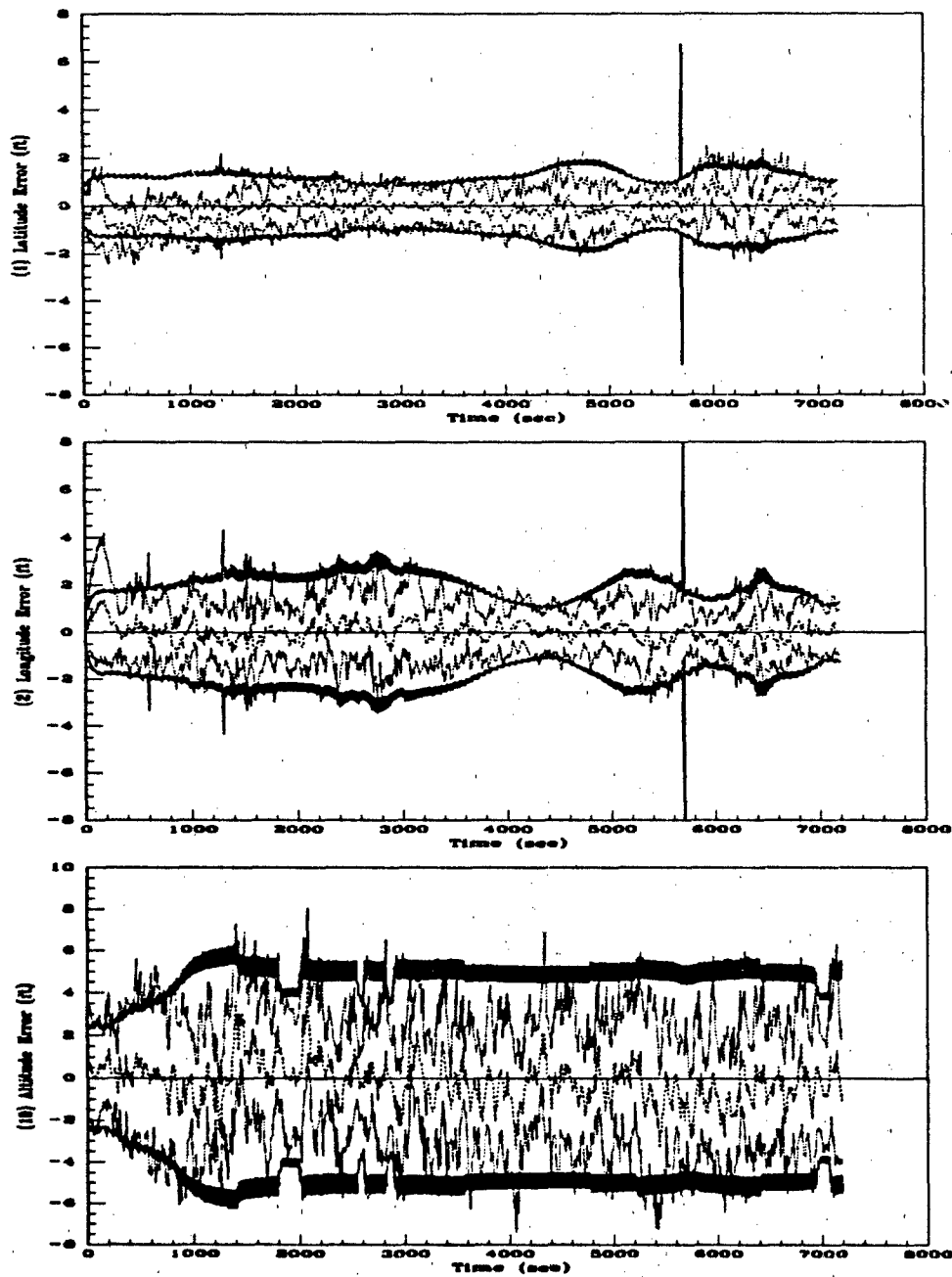


Figure H.2. 48-State ENRS Filter (a) Latitude (b) Longitude and (c) Altitude Errors.

-----	Mean Error = $\bar{M}_x - (M_x)_{true}$
.....	Mean Error $\pm \sigma_{true}$
—	$0 \pm \sigma_{filter}$

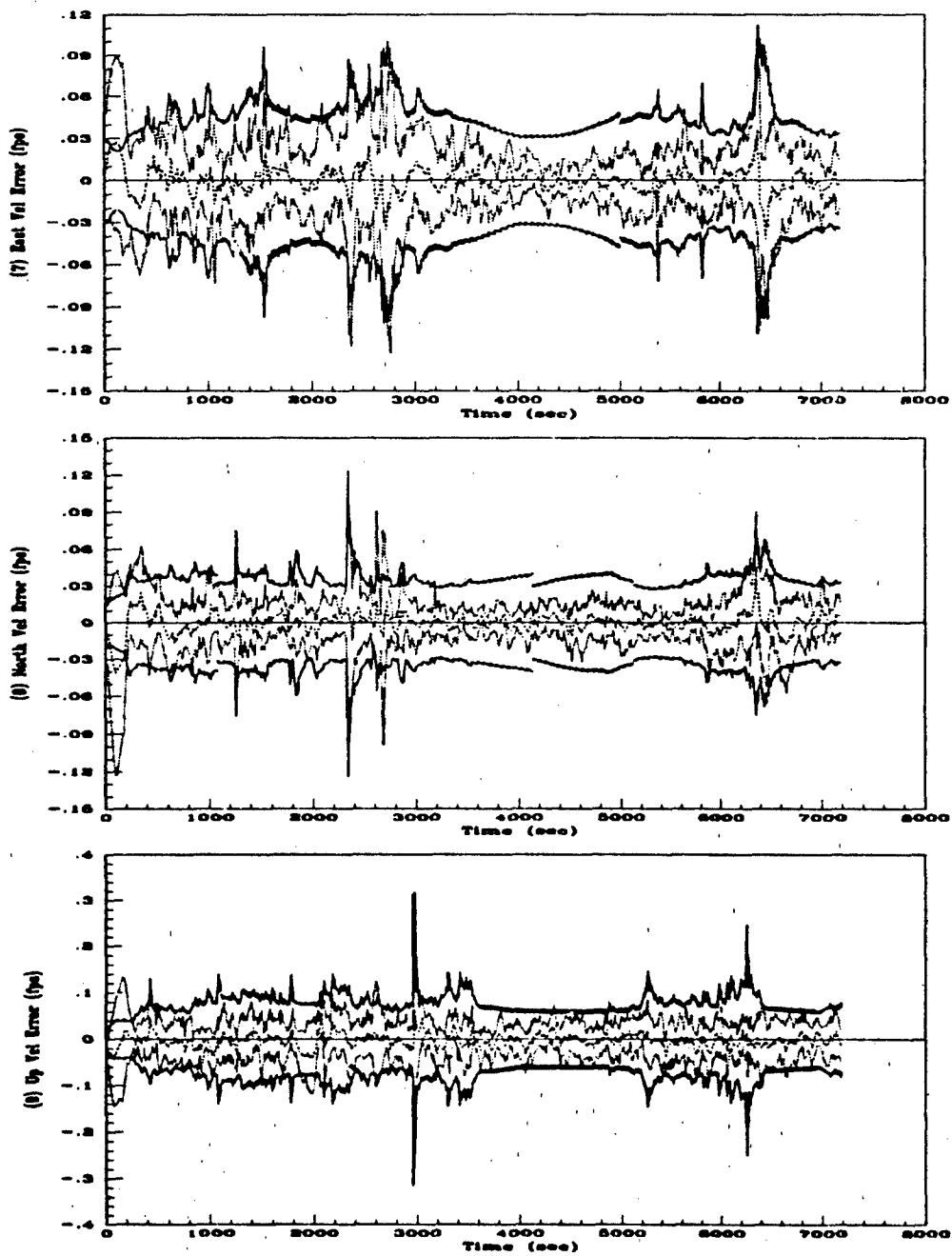


Figure H.3. 48-State ENRS Filter (a) East Velocity (b) North Velocity and (c) Vertical Velocity Errors.

---	Mean Error = $M_x - (M_x)_{true}$
.....	Mean Error $\pm \sigma_{true}$
—	$0 \pm \sigma_{filter}$

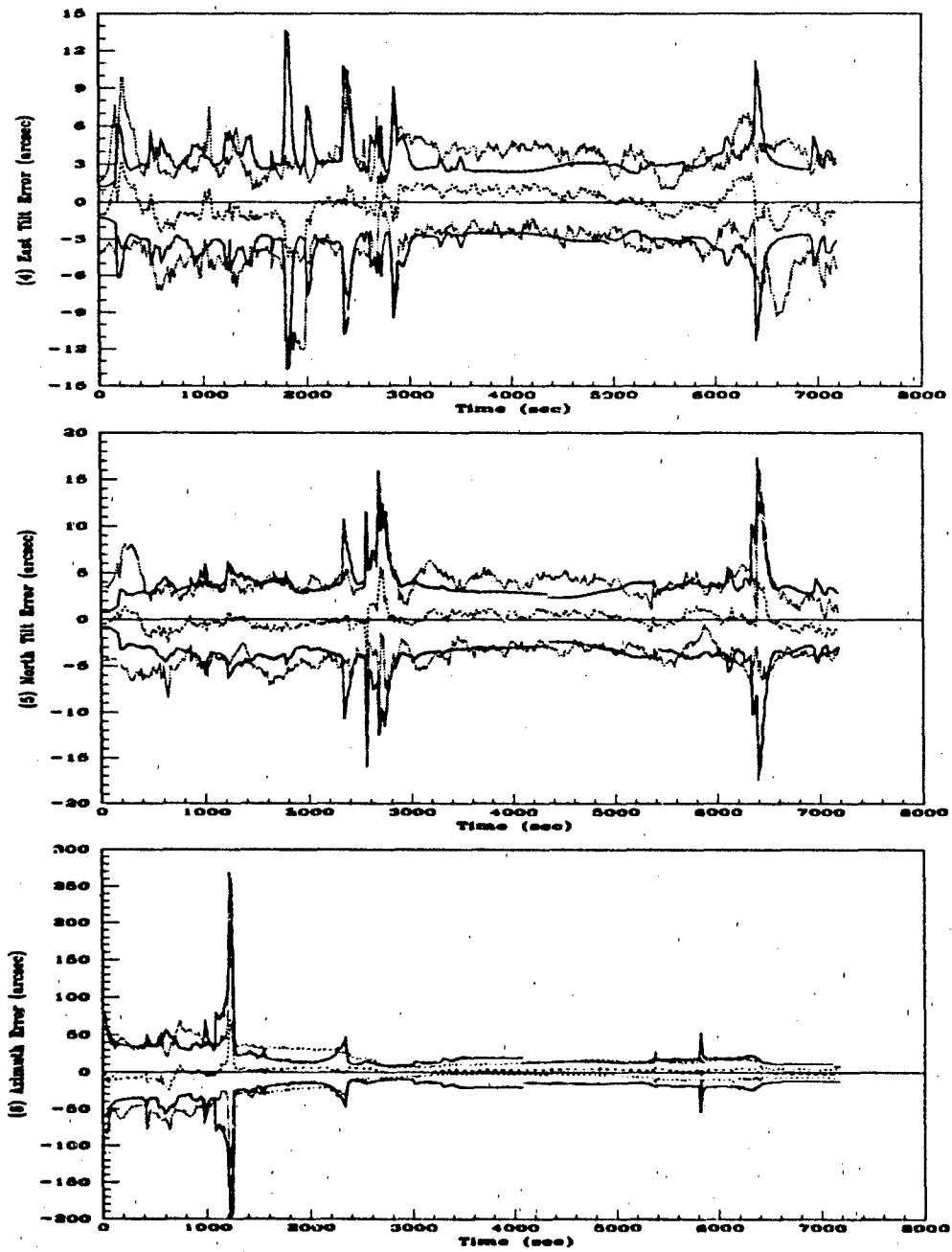


Figure H.4. 48-State ENRS Filter (a) East Tilt (b) North Tilt and (c) Azimuth Errors.

-----	Mean Error = $\bar{M}_x - (M_x)_{true}$
.....	Mean Error $\pm \sigma_{true}$
—	$0 \pm \sigma_{filter}$

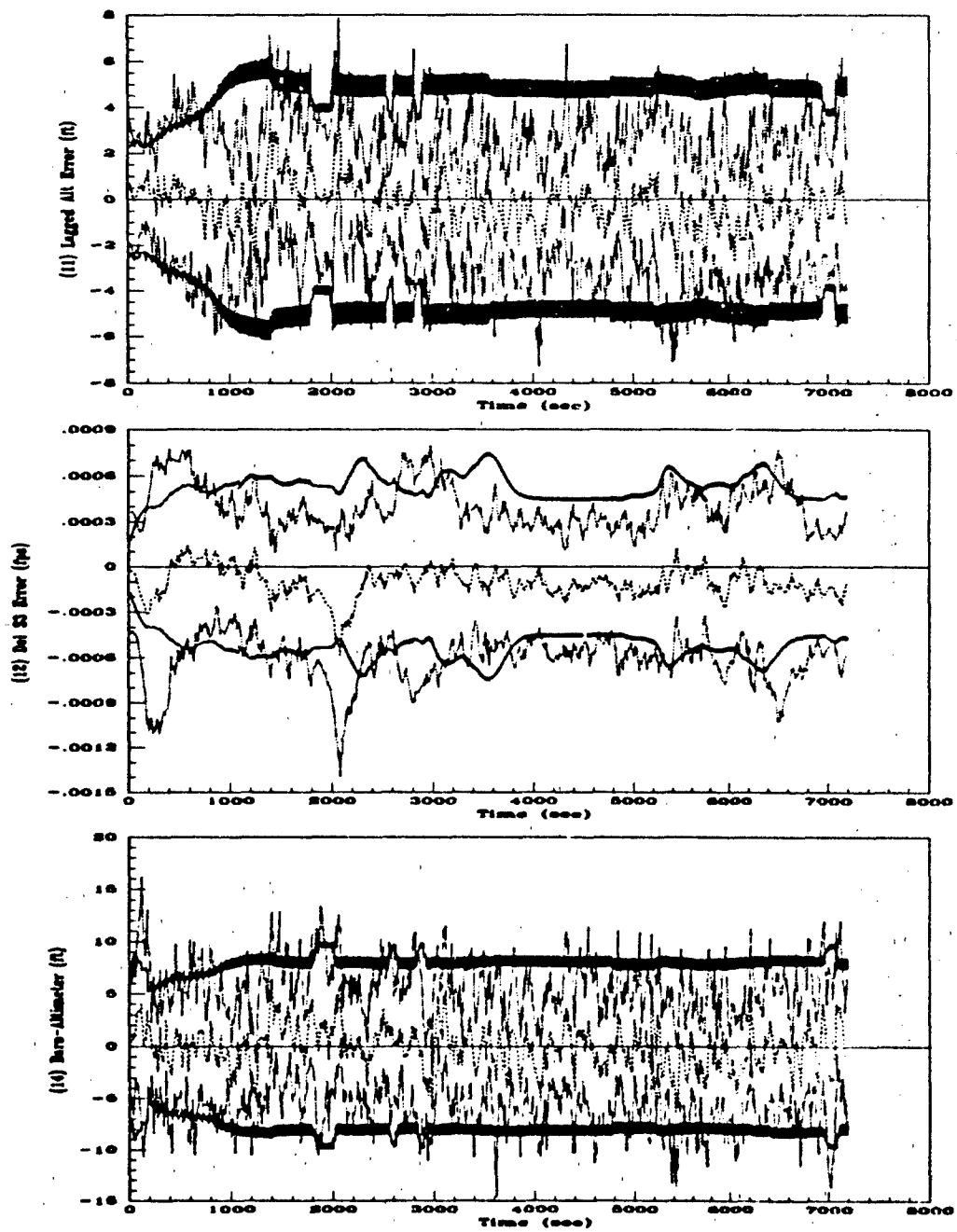


Figure H.5. 48-State ENRS Filter (a) Lagged Altitude (b) Del S3 and (c) Baro-Altimeter Errors.

----	Mean Error = $M_x - (M_x)_{true}$
.....	Mean Error $\pm \sigma_{true}$
—	$0 \pm \sigma_{filter}$

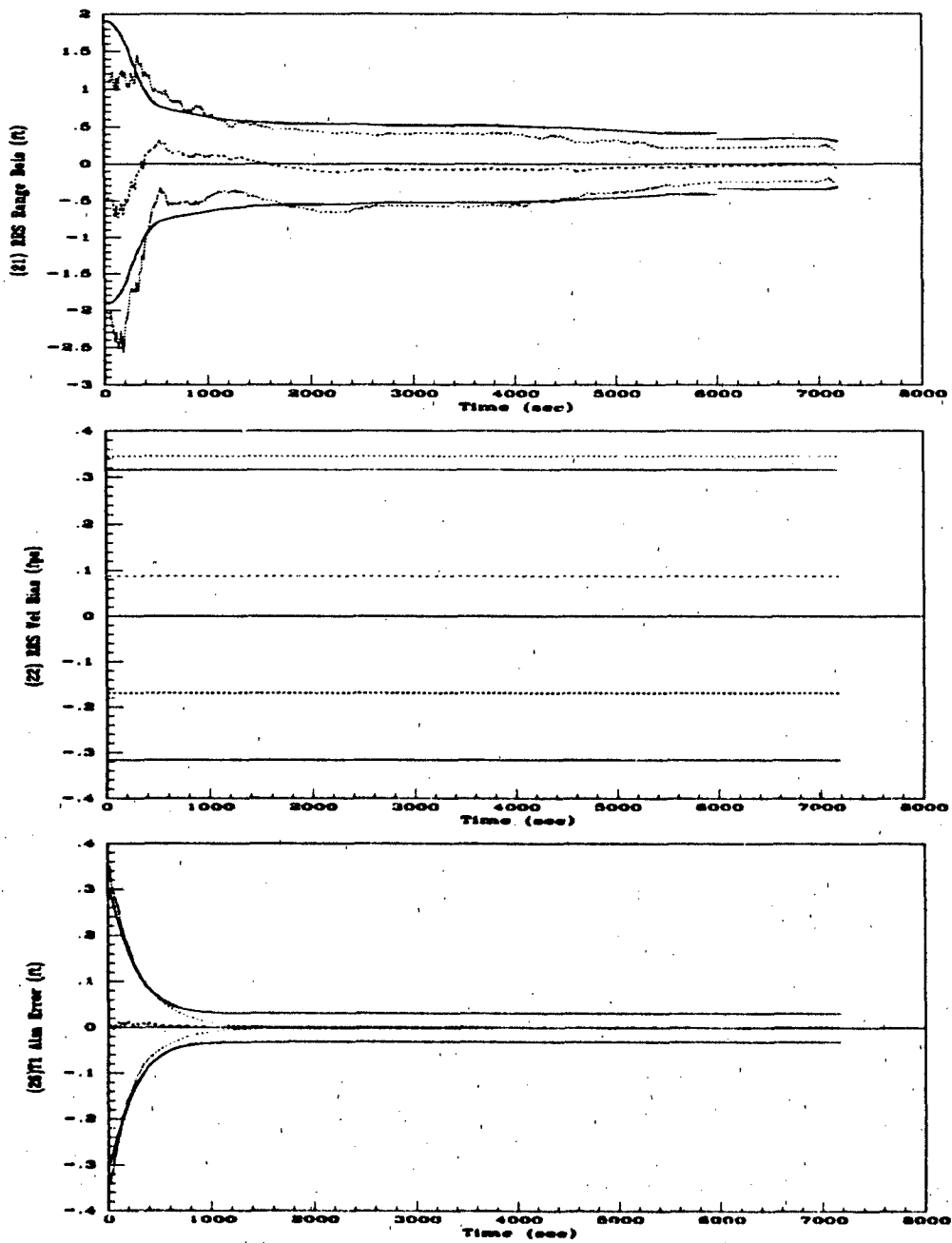


Figure H.6. 48-State ENRS Filter (a) RRS Range Bias (b) RRS Vel Bias and (c) T1 Atmosphere Errors.

----	Mean Error = $M_x - (M_x)_{true}$
.....	Mean Error $\pm \sigma_{true}$
—	$0 \pm \sigma_{filter}$

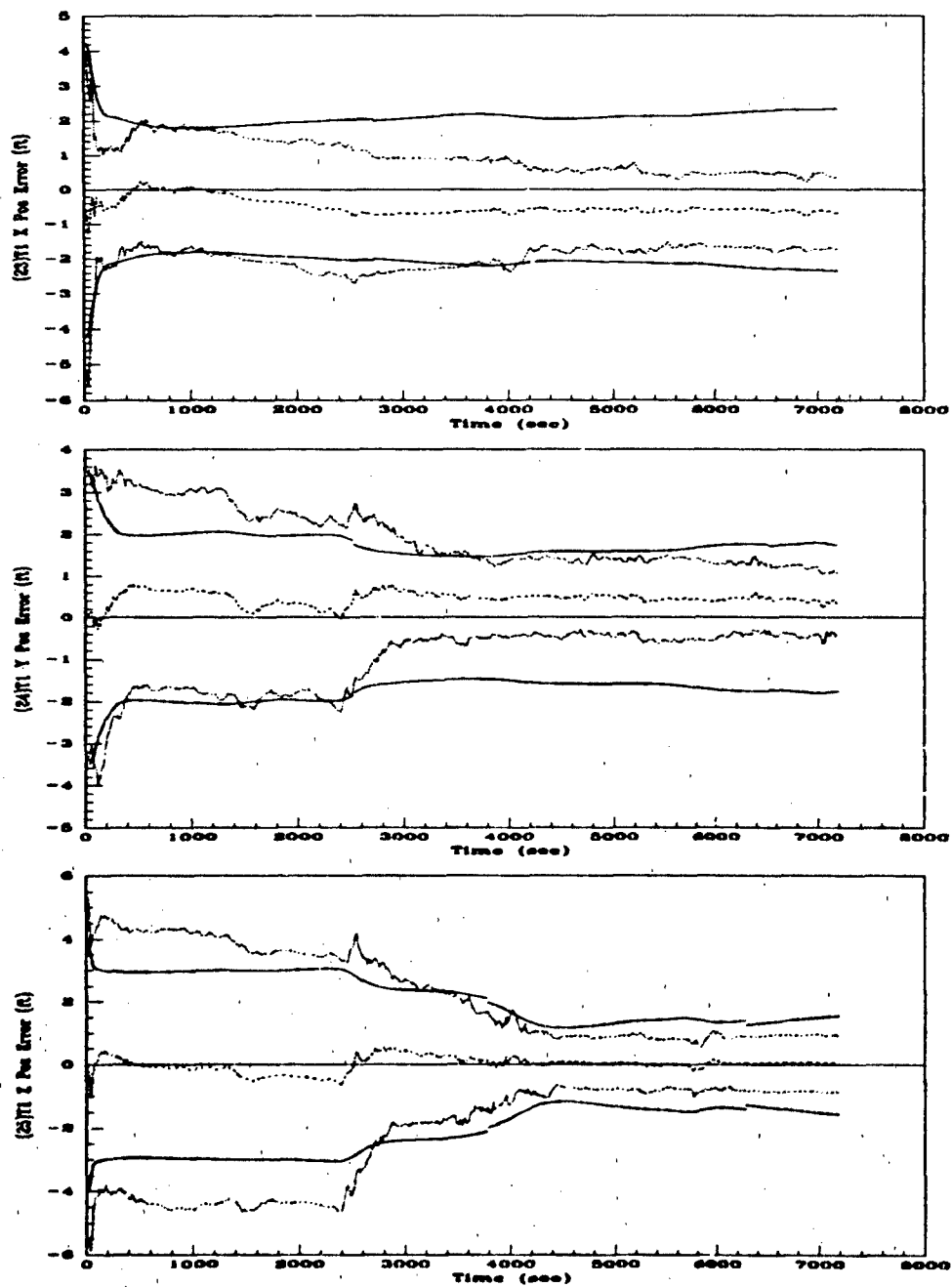


Figure H.7. 48-State ENRS Filter (a) T1 X Position (b) T1 Y Position and (c) T1 Z Position Errors.

----	$Mean\ Error = M_x - (M_x)_{true}$
.....	$Mean\ Error \pm \sigma_{true}$
—	$0 \pm \sigma_{filter}$

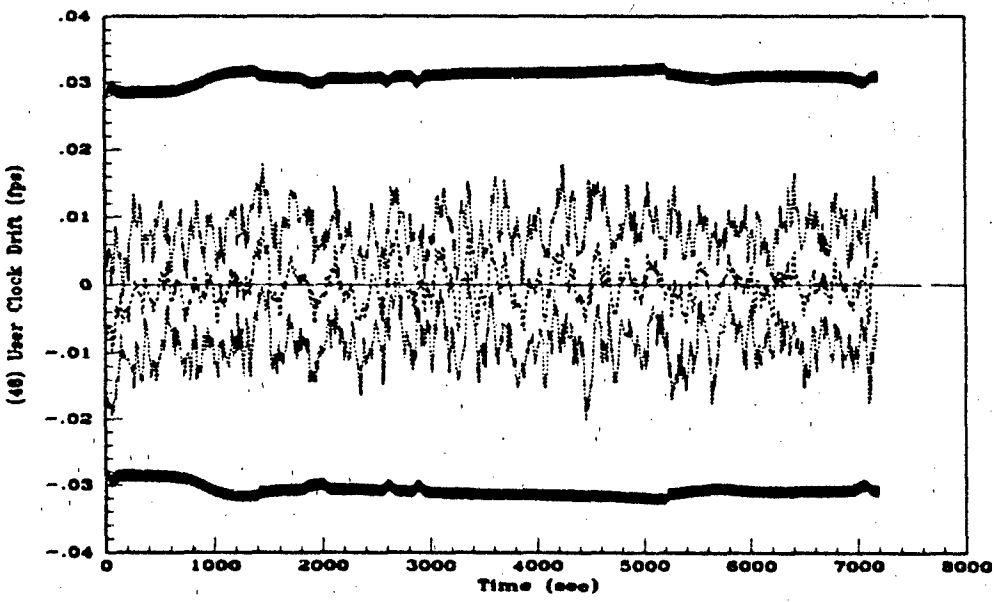
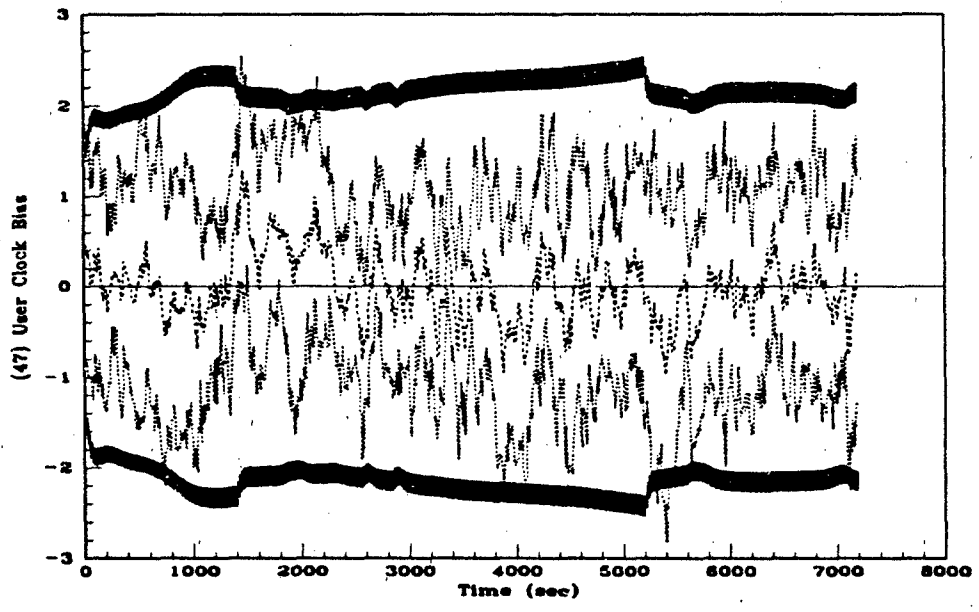


Figure H.8. 48-State ENRS Filter (a) User Clock Bias and (b) User Clock Drift Errors.

-----	Mean Error = $M_x - (M_x)_{true}$
.....	Mean Error $\pm \sigma_{true}$
————	$0 \pm \sigma_{filter}$

Appendix I. *22-State DGPS Filter Performance Plots*

The plots in this appendix present results of 10-run Monte Carlo simulations for a 22-state reduced-order filter used to implement delta-range measurements. The first section contains plots from the 2-hour fighter flight profile. The second section contains plots from a 2-hour straight trajectory. Both filter analyses were performed in double precision, so the DGPS receiver clock errors are at their actual values. These reduced-order filters incorporate both DGPS pseudorange and delta-range measurements.

I.1 2-Hour Fighter Flight Profile

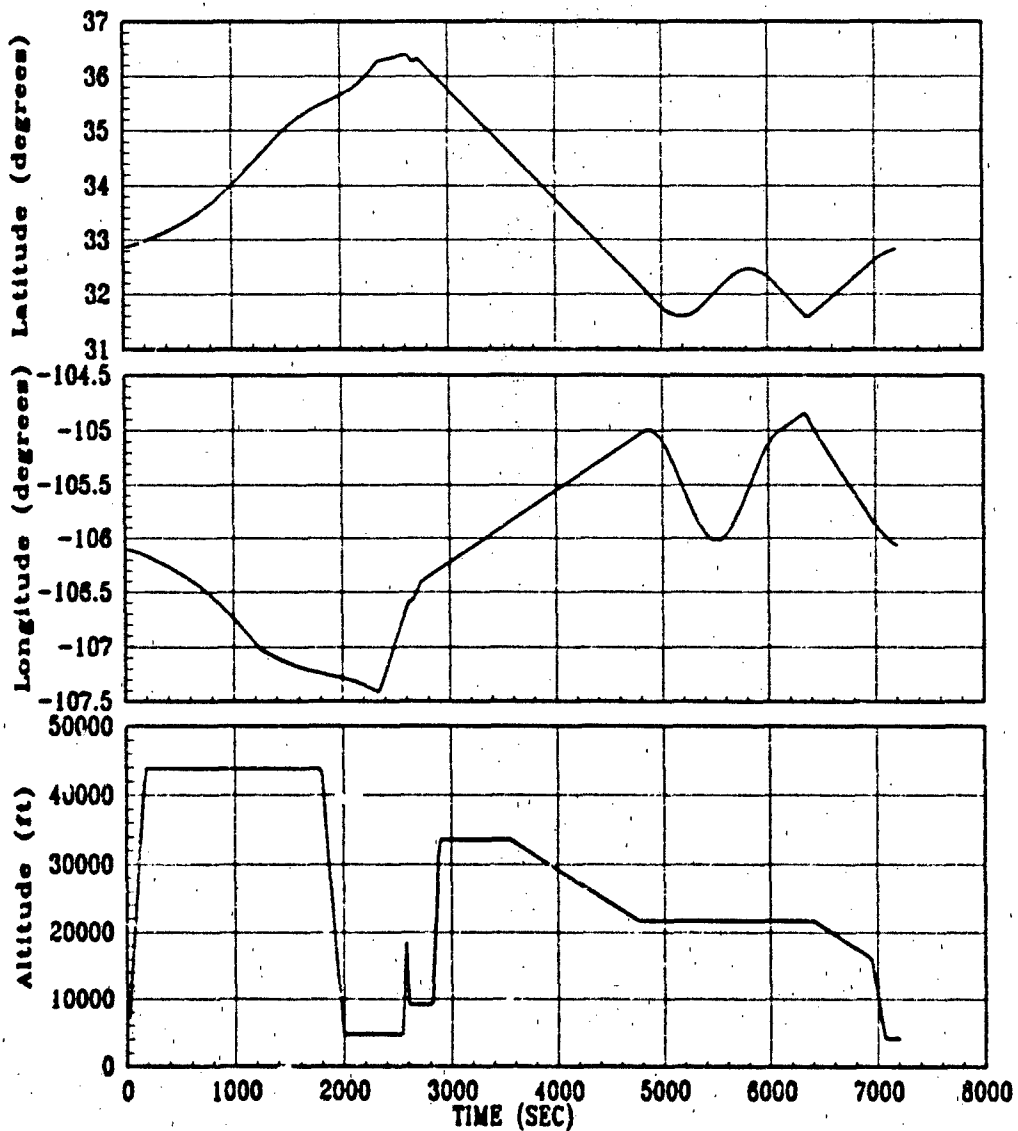


Figure I.1. 2-Hour Fighter Flight Profile (a) Latitude (b) Longitude and (c) Altitude

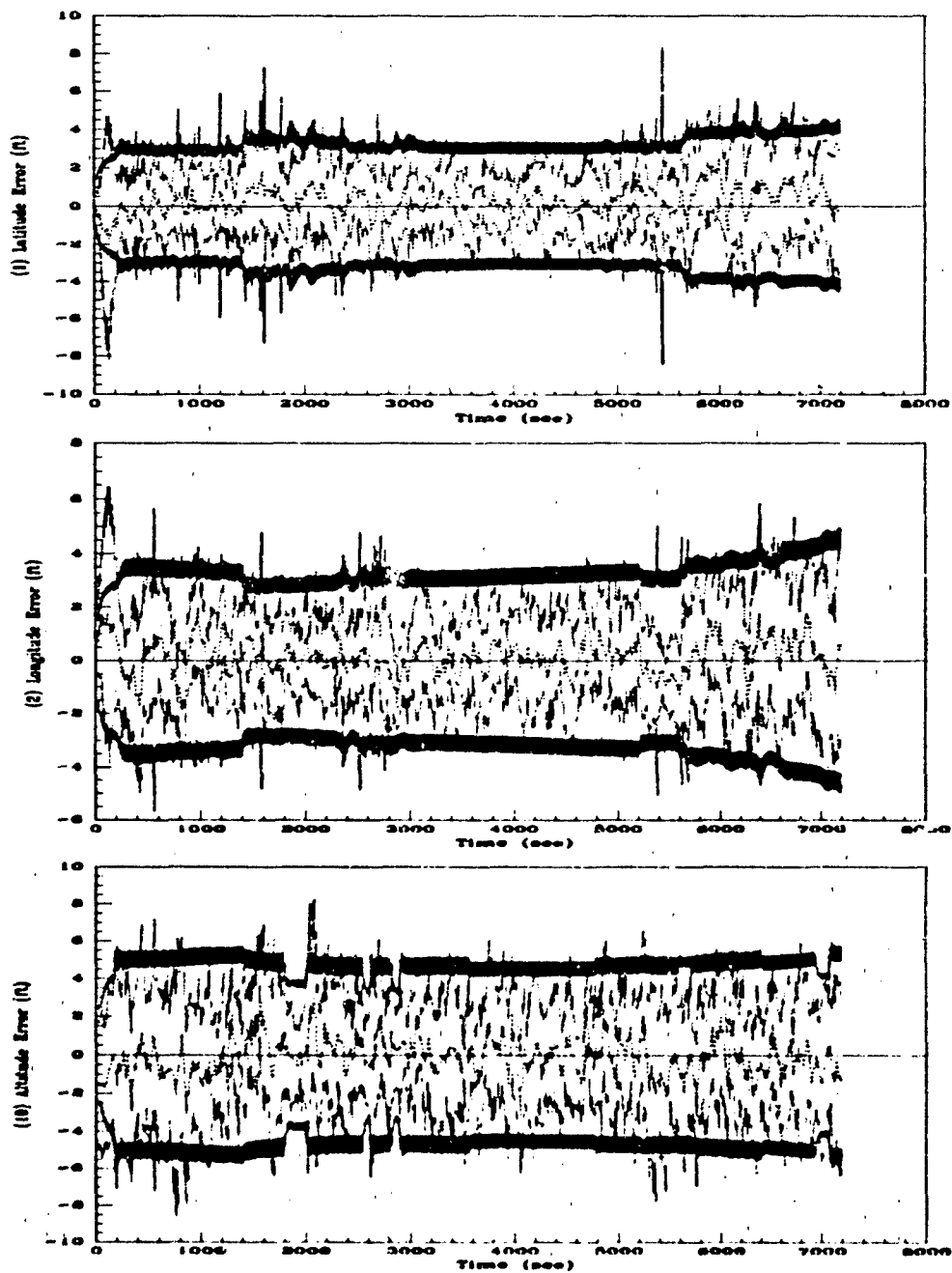


Figure 1.2. 22-State DGPS Filter, Fighter Flight Profile (a) Latitude (b) Longitude and (c) Altitude Errors.

.....	$Mean\ Error = M_r - (M_r)_{true}$
.....	$Mean\ Error \pm \sigma_{true}$
---	$0 \pm \sigma_{filter}$

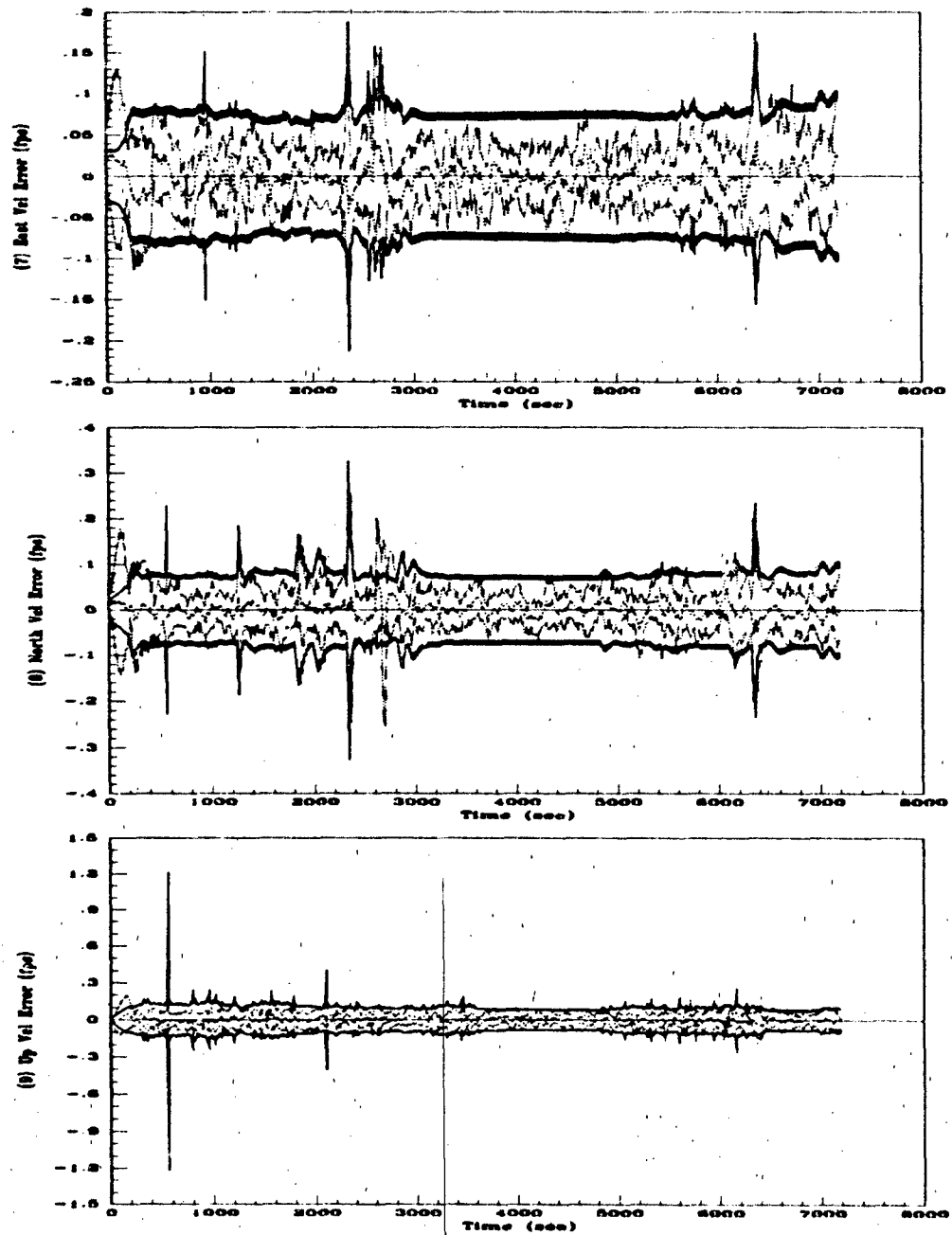


Figure I.3. 22-State DGPS Filter, Fighter Flight Profile (a) East Velocity (b) North Velocity and (c) Vertical Velocity Errors.

----	Mean Error = $\bar{M}_x - (M_x)_{true}$
.....	Mean Error $\pm \sigma_{true}$
—	$0 \pm \sigma_{filter}$

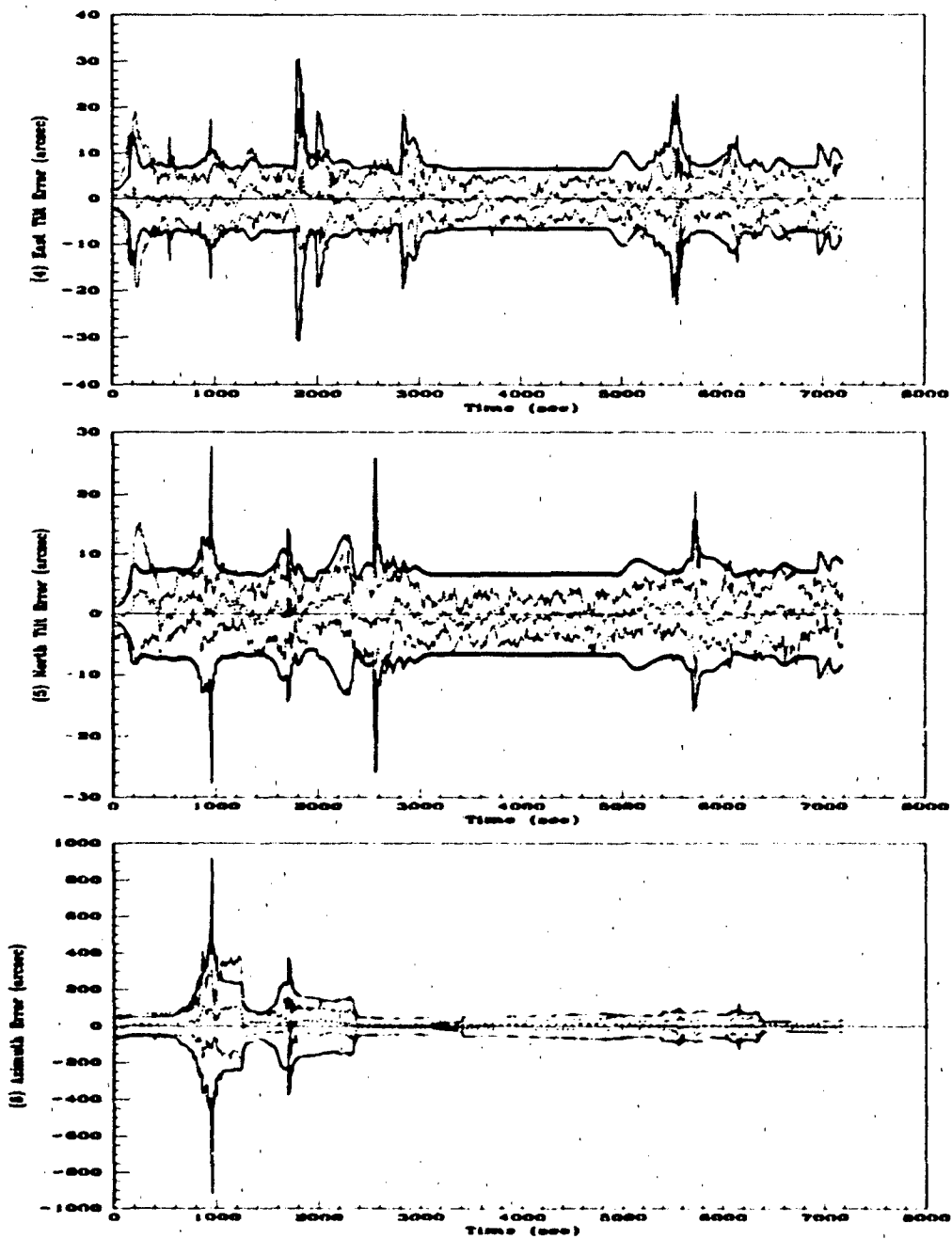


Figure 1.4. 22-State DGPS Filter. Fighter Flight Profile (a) East Tilt (b) North Tilt and (c) Azimuth Errors.

-----	Mean Error = $M_x - (M_x)_{true}$
.....	Mean Error $\pm \sigma_{true}$
————	$0 \pm \sigma_{filter}$

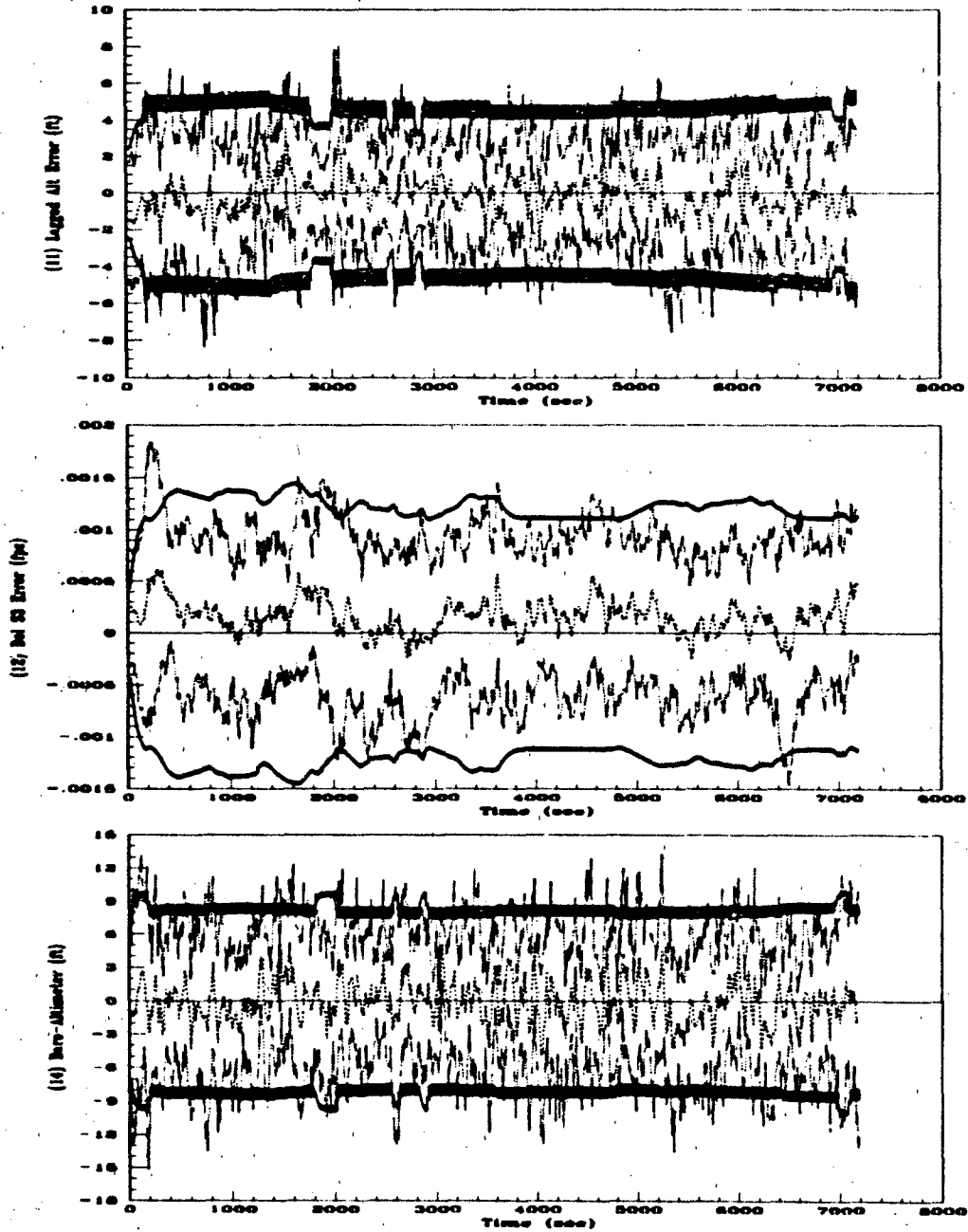


Figure I.5. 22-State DGPS Filter, Fighter Flight Profile (a) Lagged Altitude (b) Del S3 and (c) Baro-Altimeter Errors.

----	Mean Error = $\bar{M}_x - (M_x)_{true}$
.....	Mean Error $\pm \sigma_{true}$
—	$0 \pm \sigma_{filter}$

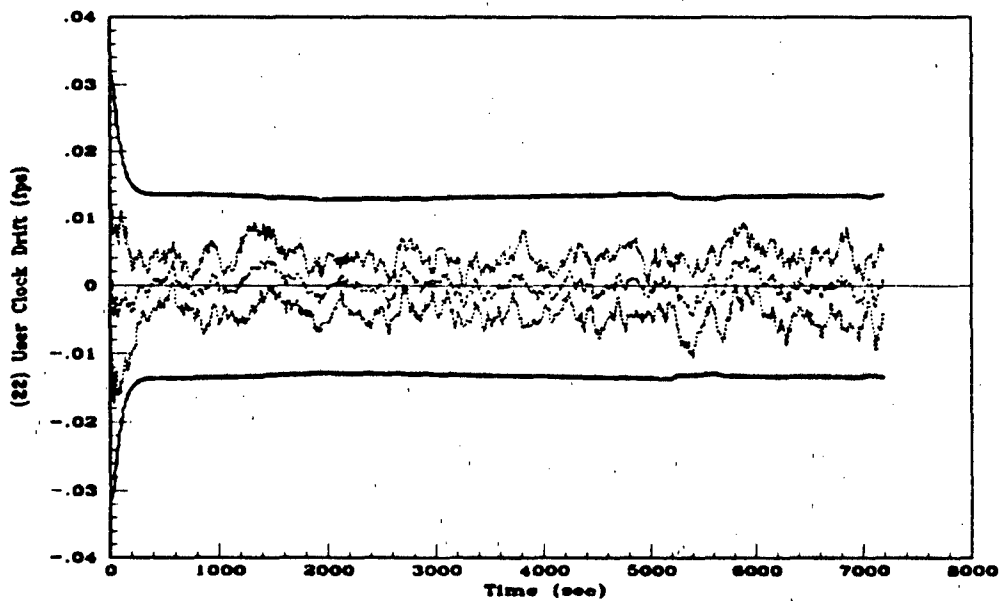
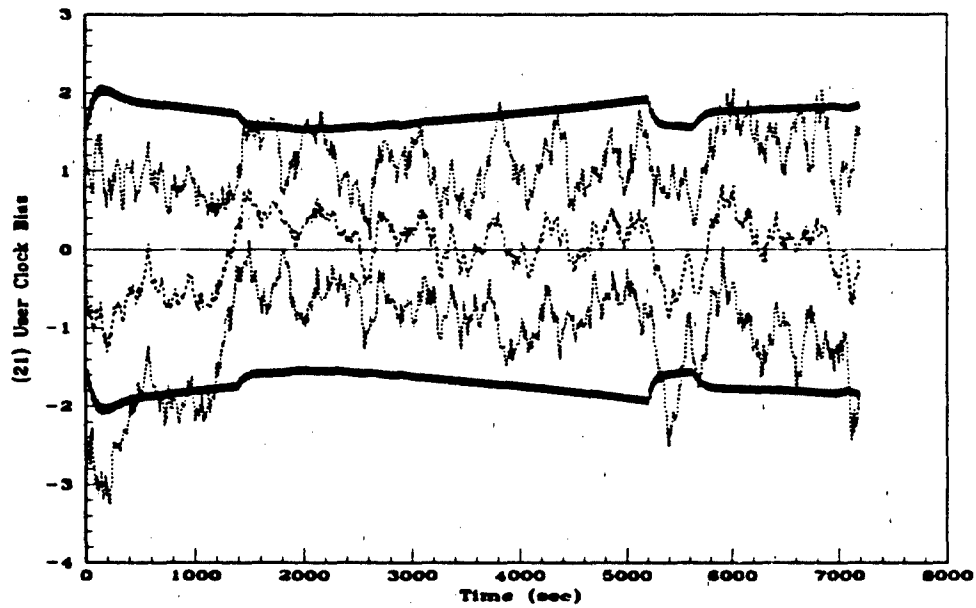


Figure I.6. 22-State DGPS Filter, Fighter Flight Profile (a) User Clock Bias and (b) User Clock Drift Errors.

-----	Mean Error = $\hat{M}_x - (M_x)_{true}$
.....	Mean Error $\pm \sigma_{true}$
—	$0 \pm \sigma_{filter}$

1.2 2-Hour Straight Flight Profile

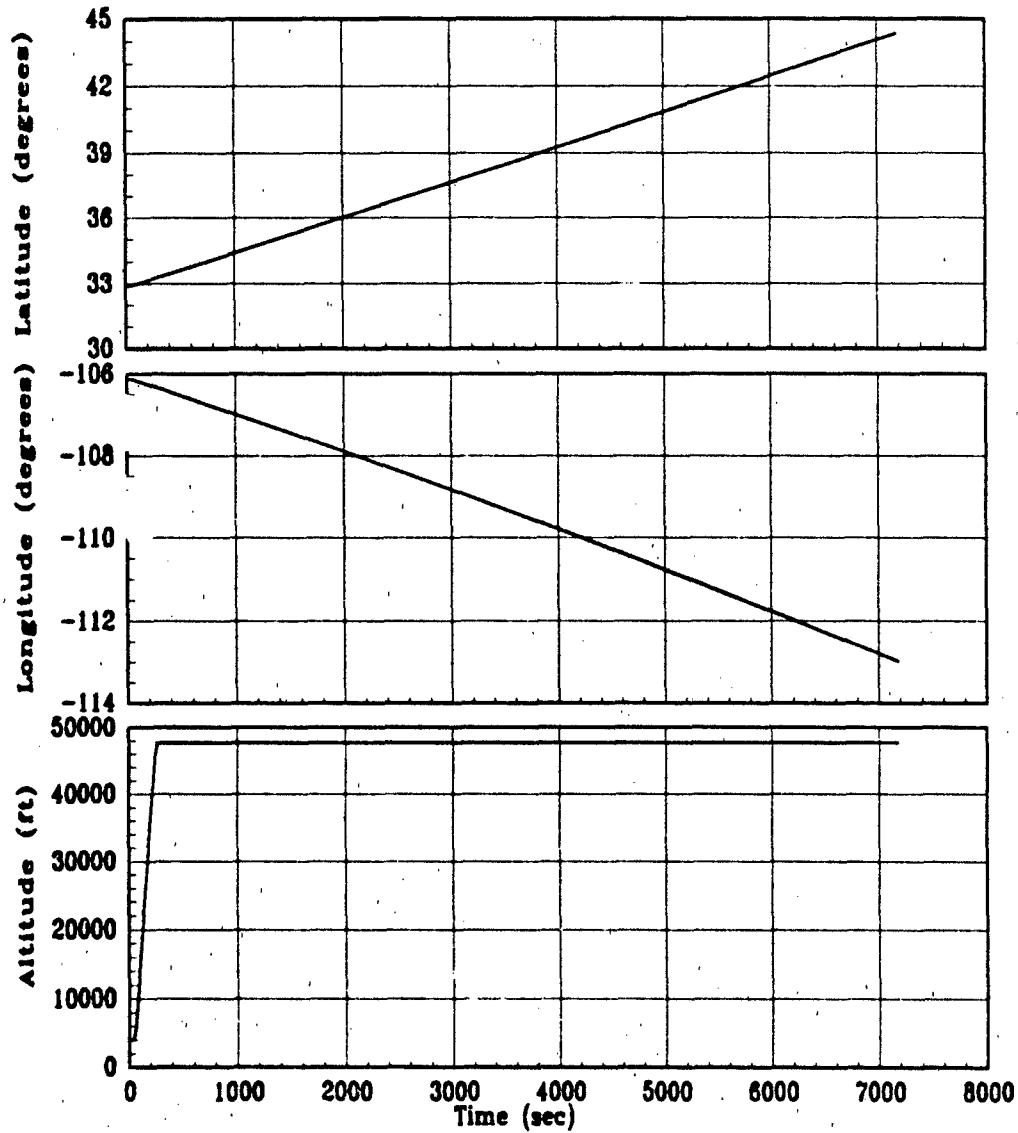


Figure I.7. 2-Hour Straight Flight Profile (a) Latitude (b) Longitude and (c) Altitude

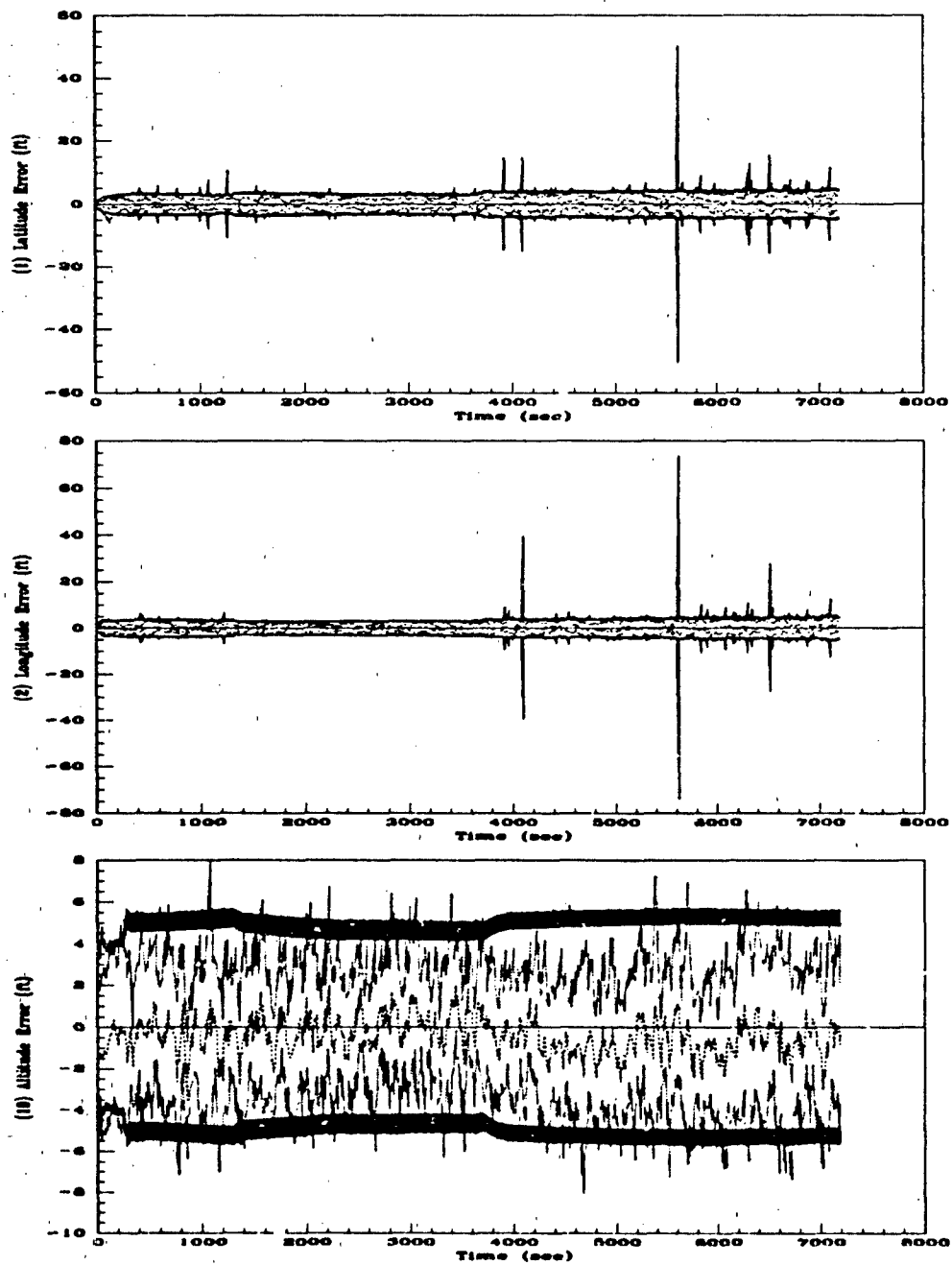


Figure I.8. 22-State DGPS Filter, Straight Flight Profile (a) Latitude (b) Longitude and (c) Altitude Errors.

----	$Mean\ Error = M_x - (M_x)_{true}$
.....	$Mean\ Error \pm \sigma_{true}$
—	$0 \pm \sigma_{filter}$

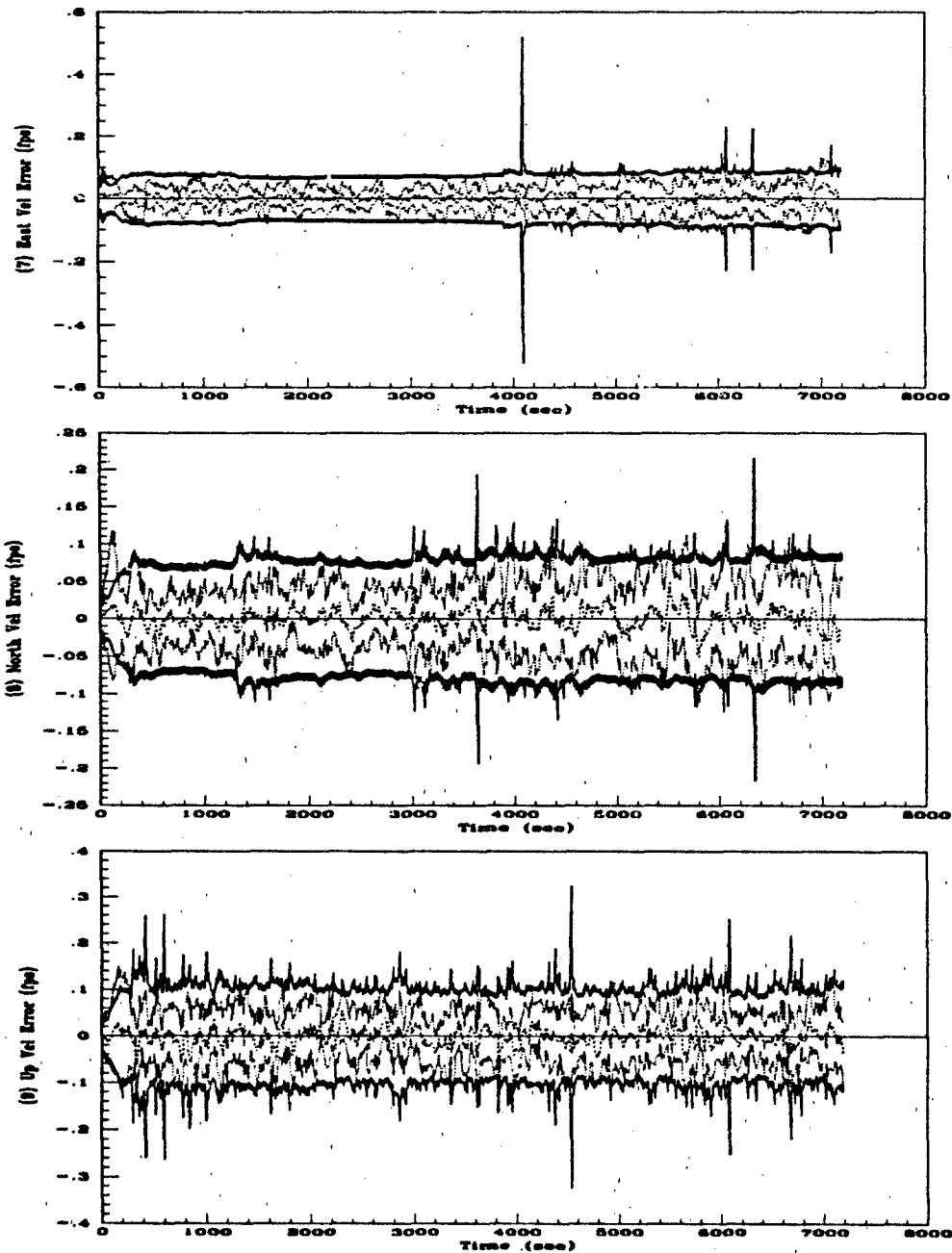


Figure I.9. 22-State DGPS Filter, Straight Flight Profile (a) East Velocity (b) North Velocity and (c) Vertical Velocity Errors.

----	Mean Error = $\bar{M}_x - (M_x)_{true}$
.....	Mean Error $\pm \sigma_{true}$
—	$0 \pm \sigma_{filter}$

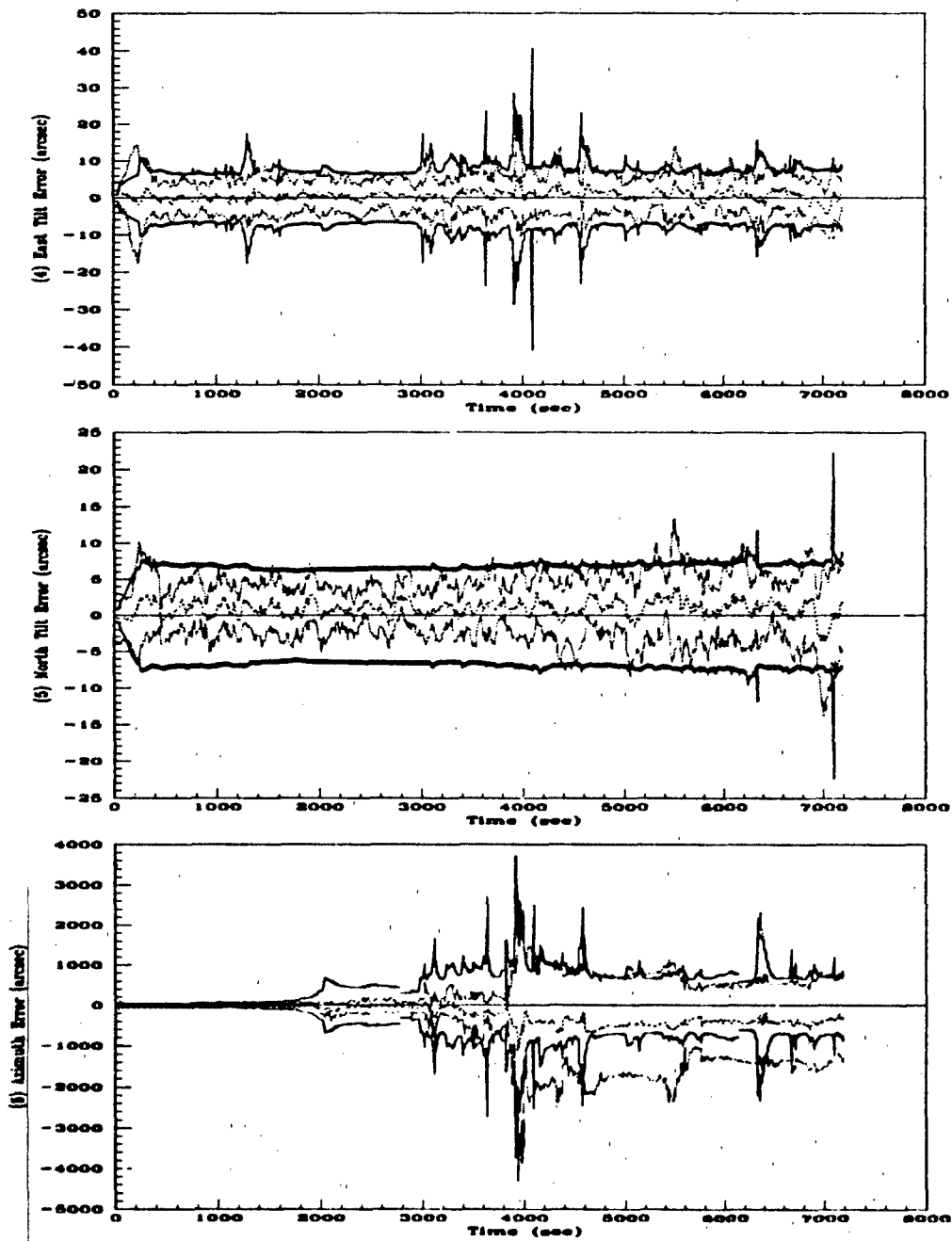


Figure I.10. 22-State DGPS Filter, Straight Flight Profile (a) East Tilt (b) North Tilt and (c) Azimuth Errors.

- - - -	Mean Error = $M_x - (M_x)_{true}$
.....	Mean Error $\pm \sigma_{true}$
————	$0 \pm \sigma_{filter}$

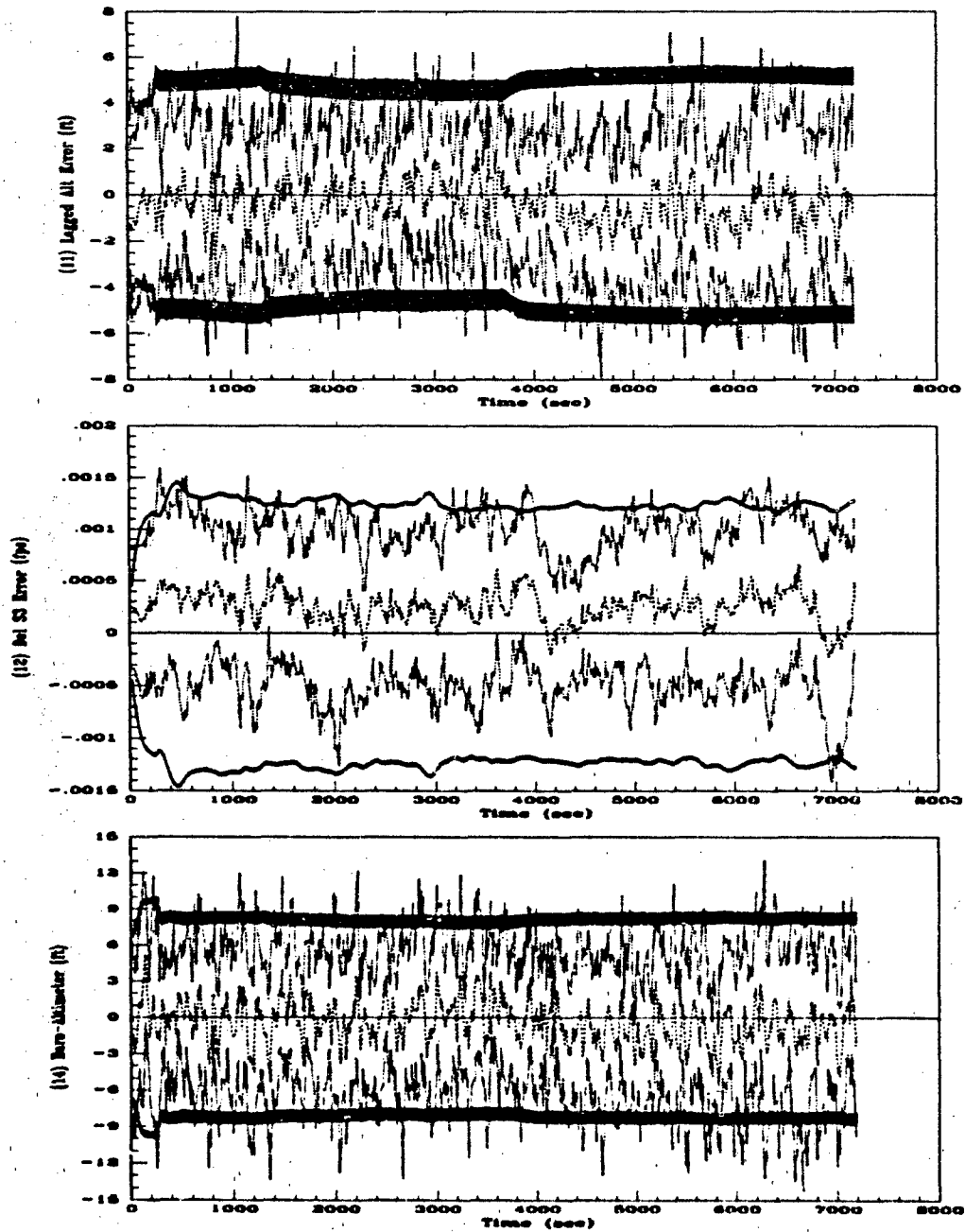


Figure I.11. 22-State DGPS Filter, Straight Flight Profile (a) Lagged Altitude (b) Del S3 and (c) Baro-Altimeter Errors.

----	Mean Error = $\bar{M}_z - (M_z)_{true}$
.....	Mean Error $\pm \sigma_{true}$
—	$0 \pm \sigma_{filter}$

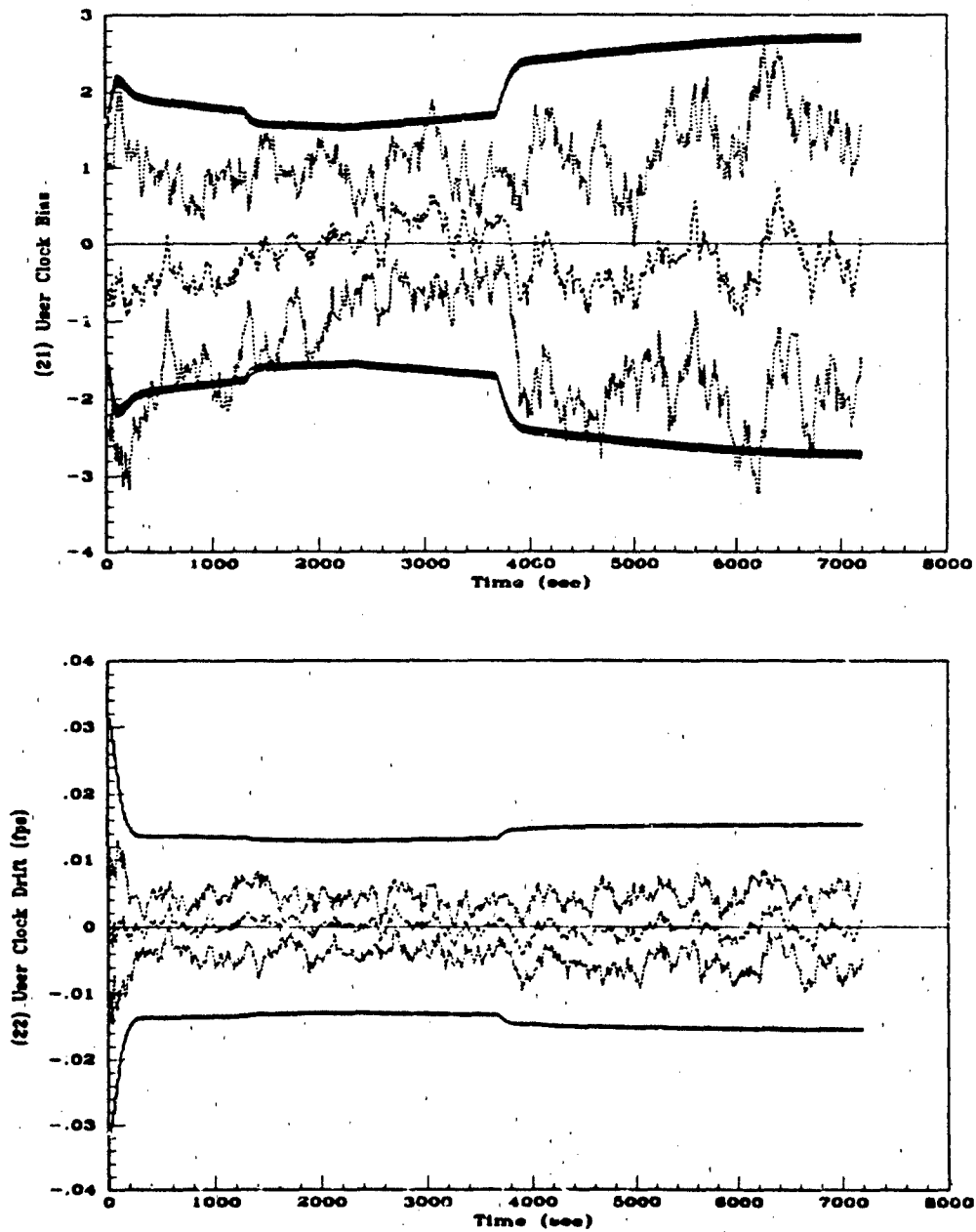


Figure I.12. 22-State DGPS Filter, Straight Flight Profile (a) User Clock Bias and (b) User Clock Drift Errors.

----	Mean Error = $M_x - (M_x)_{true}$
.....	Mean Error $\pm \sigma_{true}$
—	$0 \pm \sigma_{filter}$

Appendix J. *46-State CIRIS Filter Performance Plots*

The plots in this appendix present results of 10-run Monte Carlo simulations for a 46-state full-order filter used to implement range-range measurements. The first section contains plots from the 2-hour fighter flight profile. The second section contains plots from a 2-hour racetrack trajectory. Both filter analyses were performed in single precision since no DGPS states are modeled. These reduced-order filters incorporate both RRS range and range-rate measurements.

J.1 2-Hour Fighter Flight Profile

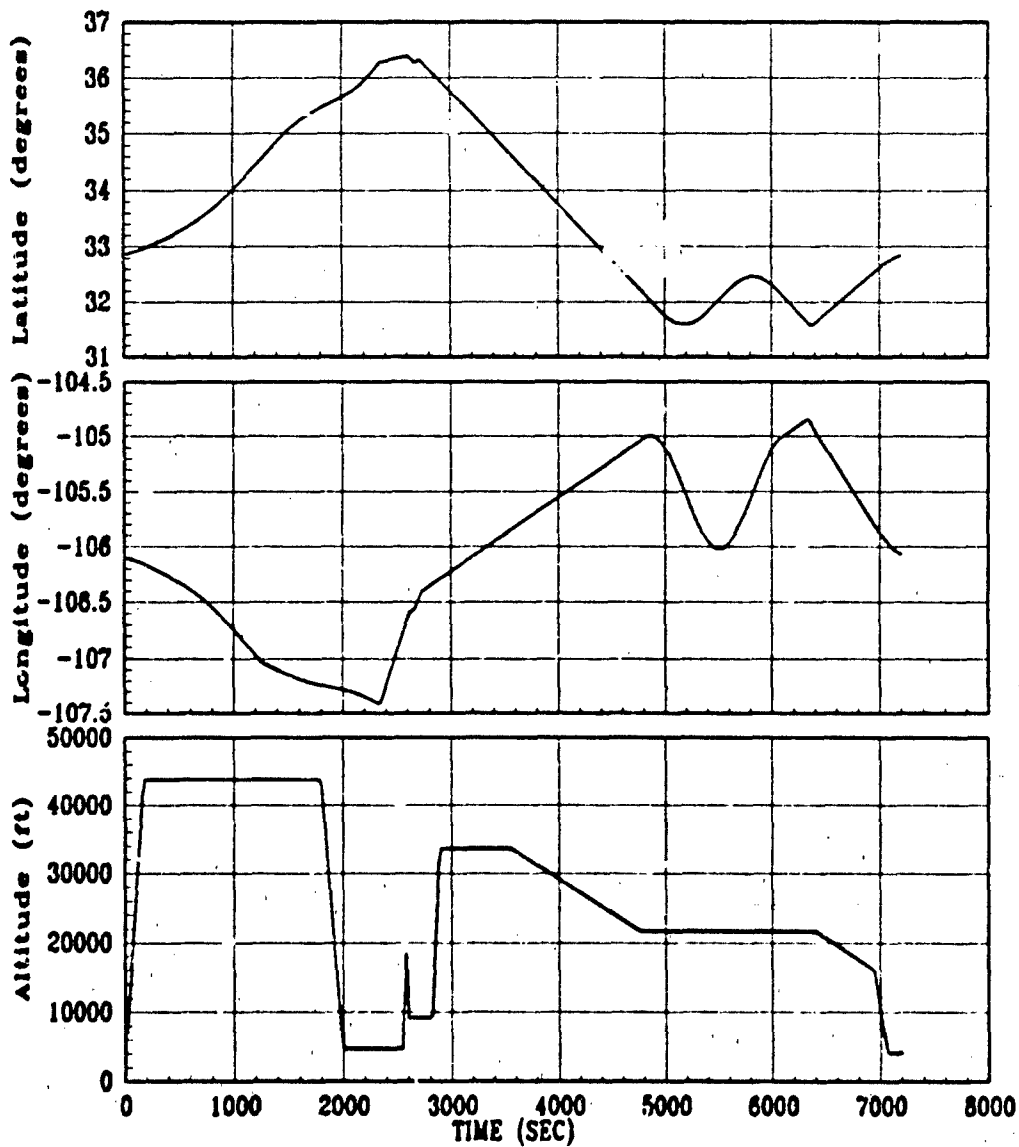


Figure J.1. 2-Hour Fighter Flight Profile (a) Latitude (b) Longitude and (c) Altitude

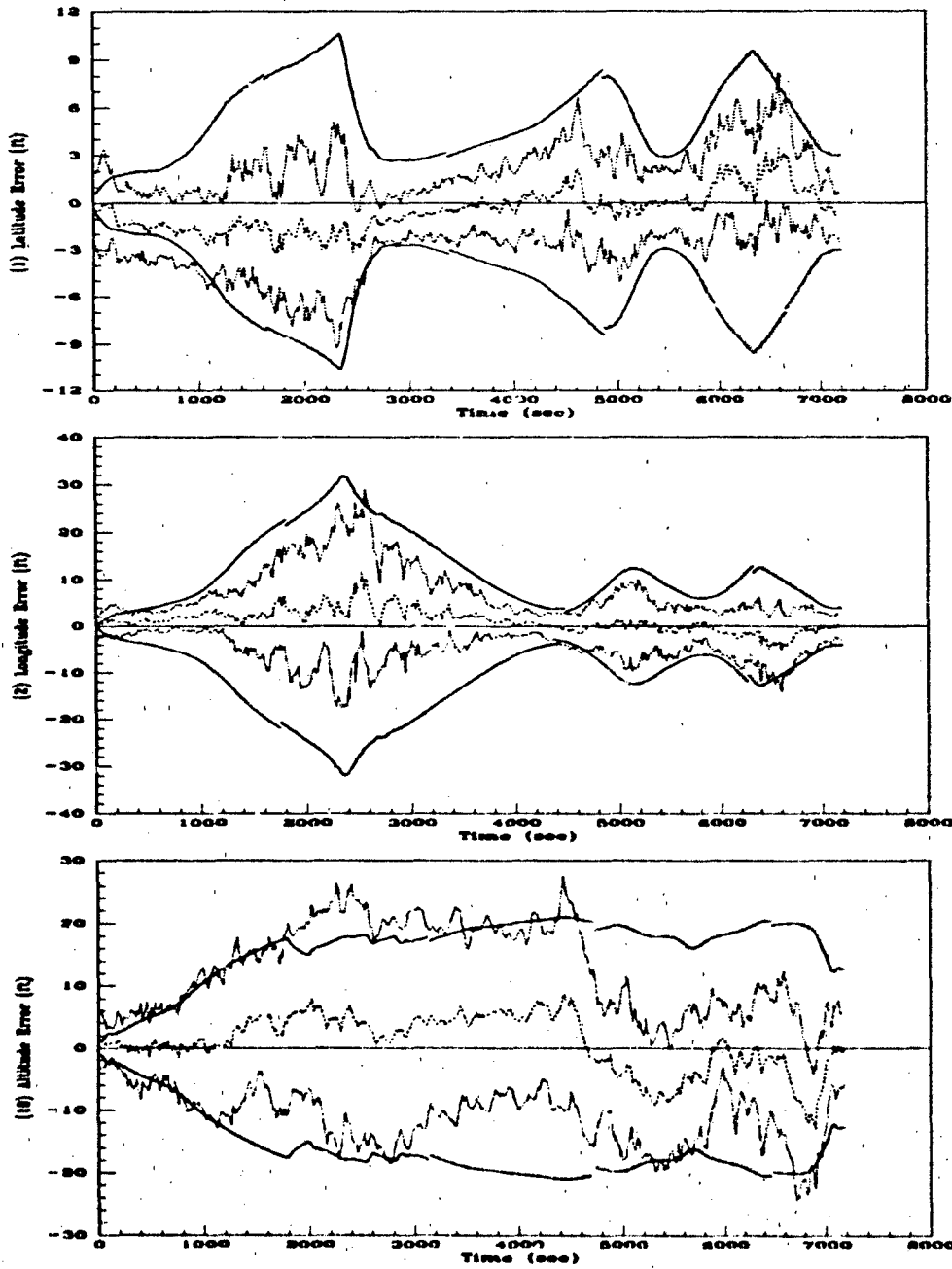


Figure J.2. 46-State CIRIS Filter, Fighter Flight Profile (a) Latitude (b) Longitude and (c) Altitude Errors.

- - - -	Mean Error = $\bar{M}_x - (M_x)_{true}$
.....	Mean Error $\pm \sigma_{true}$
————	$0 \pm \sigma_{filter}$

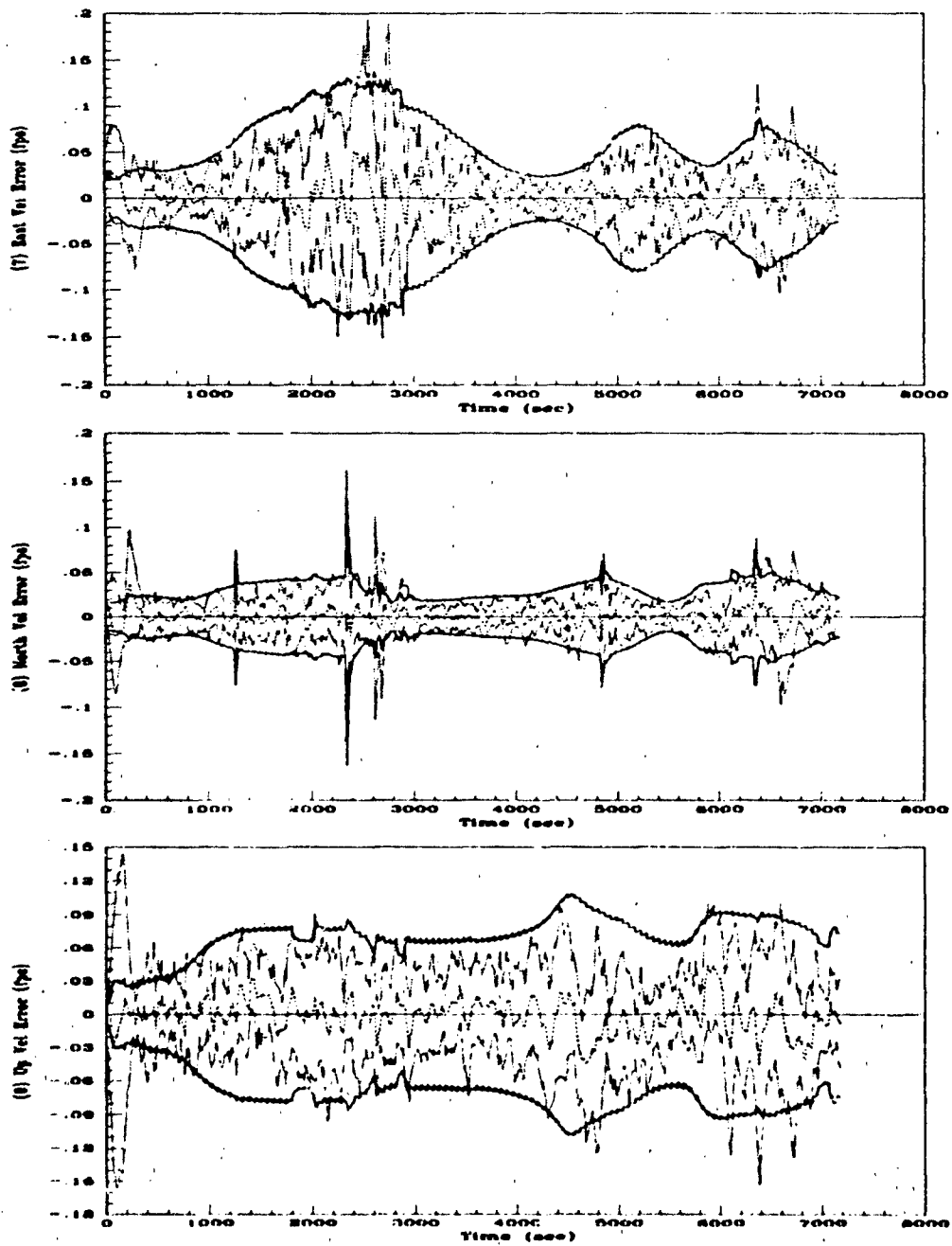


Figure J.3. 46-State CIRIS Filter, Fighter Flight Profile Filter (a) East Velocity (b) North Velocity and (c) Vertical Velocity Errors.

- - - -	Mean Error = $\bar{M}_r - (M_r)_{true}$
.....	Mean Error $\pm \sigma_{true}$
—	$0 \pm \sigma_{filter}$

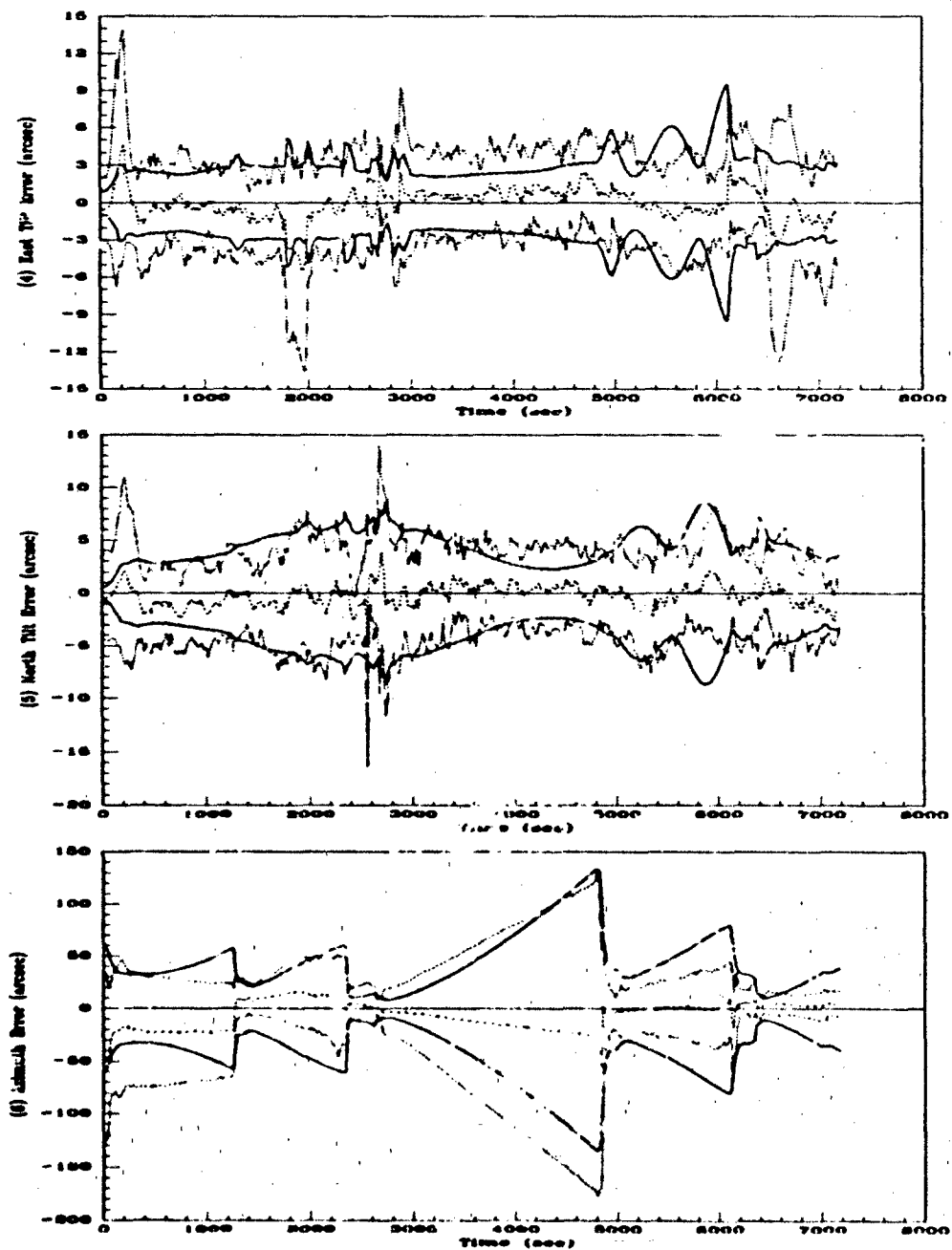


Figure J.4. 46-State CIRIS Filter, Fighter Flight Profile Filter (a) East Tilt (b) North Tilt and (c) Azimuth Errors.

- - - -	Mean Error = $M_x - (M_x)_{true}$
.....	Mean Error $\pm \sigma_{true}$
————	$0 \pm \sigma_{filter}$

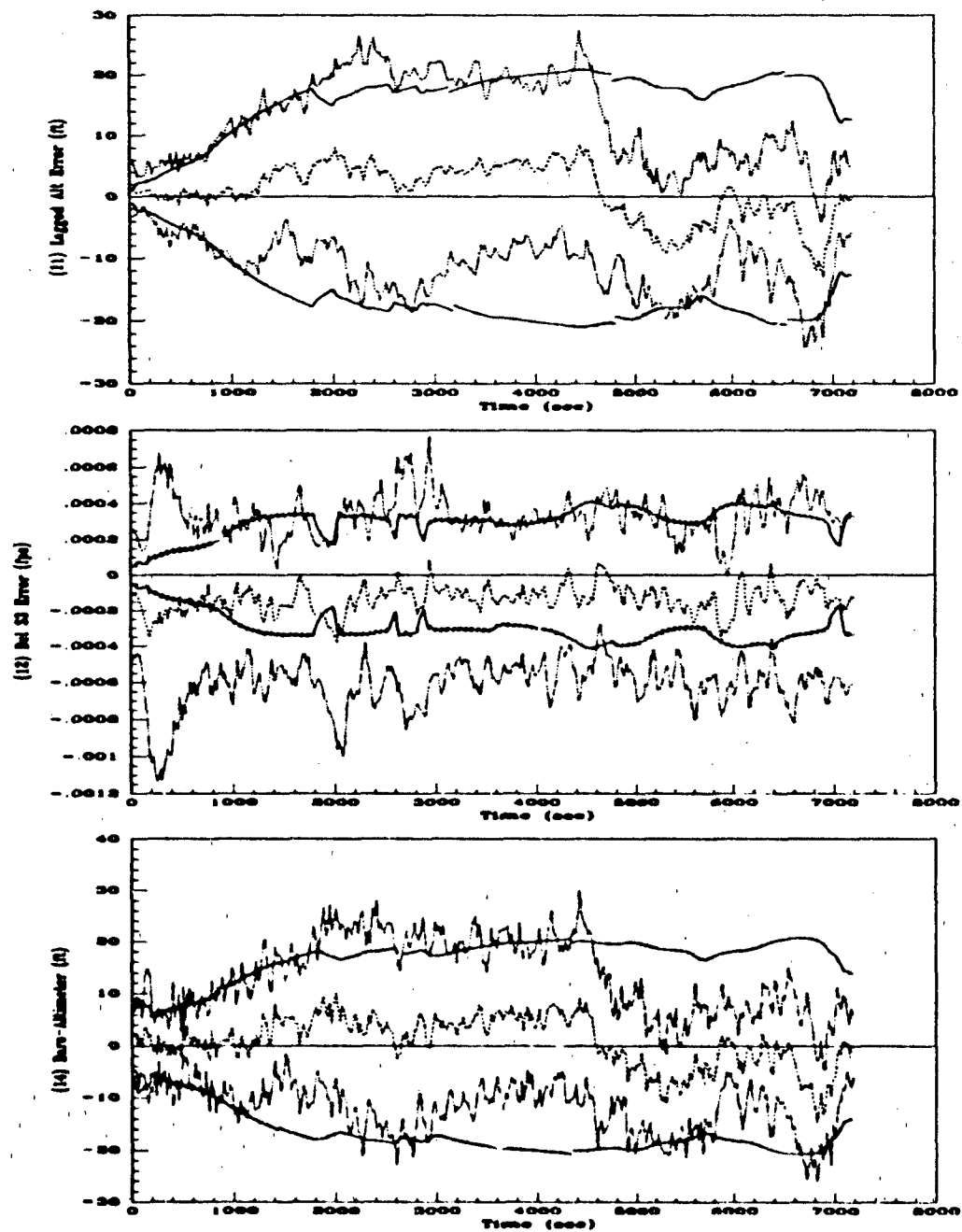


Figure J.5. 46-State CIRIS Filter, Fighter Flight Profile Filter (a) Lagged Altitude (b) Del S3 and (c) Baro-Altimeter Errors.

----	Mean Error = $\bar{M}_z - (M_z)_{true}$
.....	Mean Error $\pm \sigma_{true}$
—	$0 \pm \sigma_{filter}$

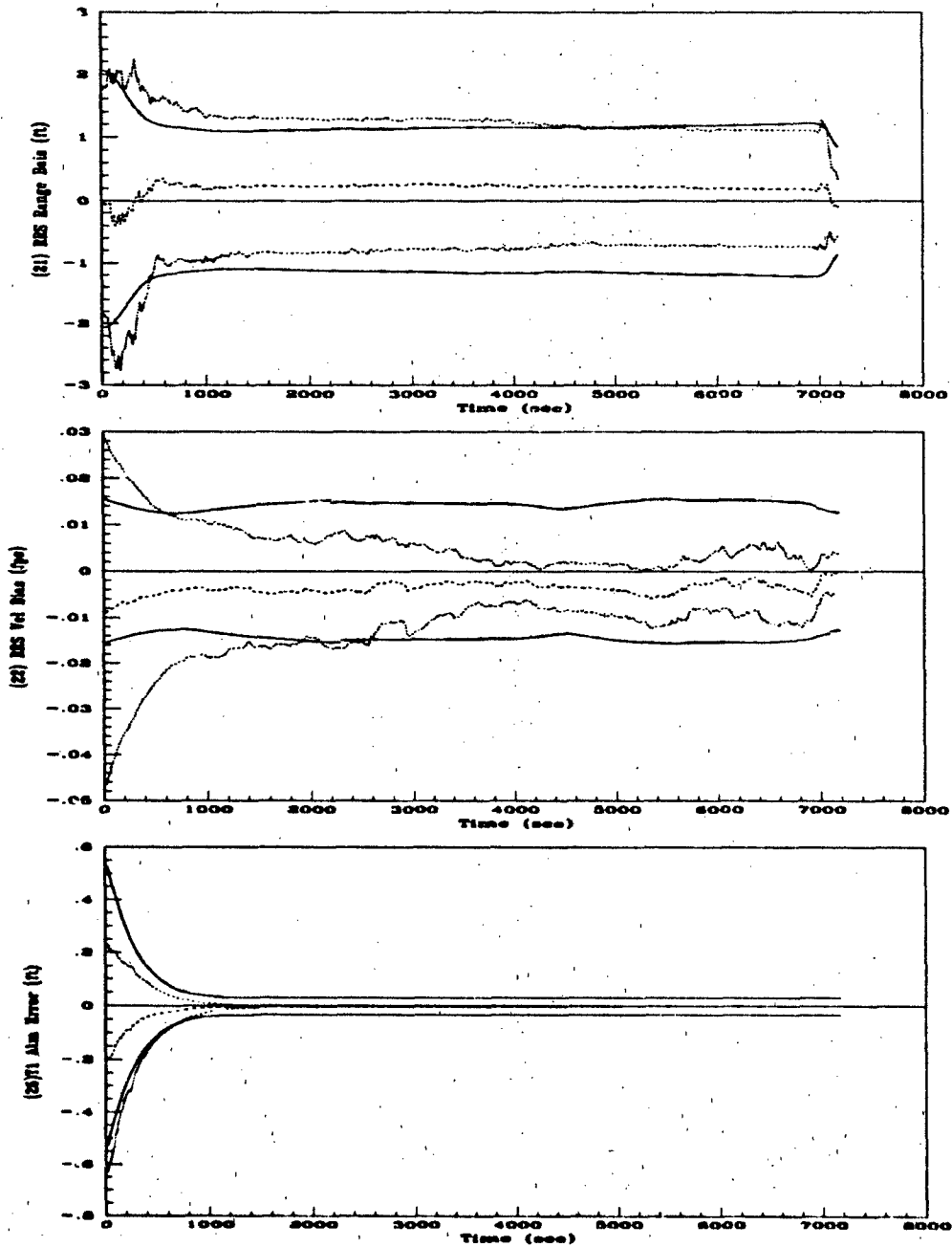


Figure J.6. 46-State CIRIS Filter, Fighter Flight Profile Filter (a) RRS Range Bias (b) RRS Vel Bias and (c) T1 Atmosphere Errors.

-----	Mean Error = $\bar{M}_z - (M_z)_{true}$
.....	Mean Error $\pm \sigma_{true}$
—	$0 \pm \sigma_{filter}$

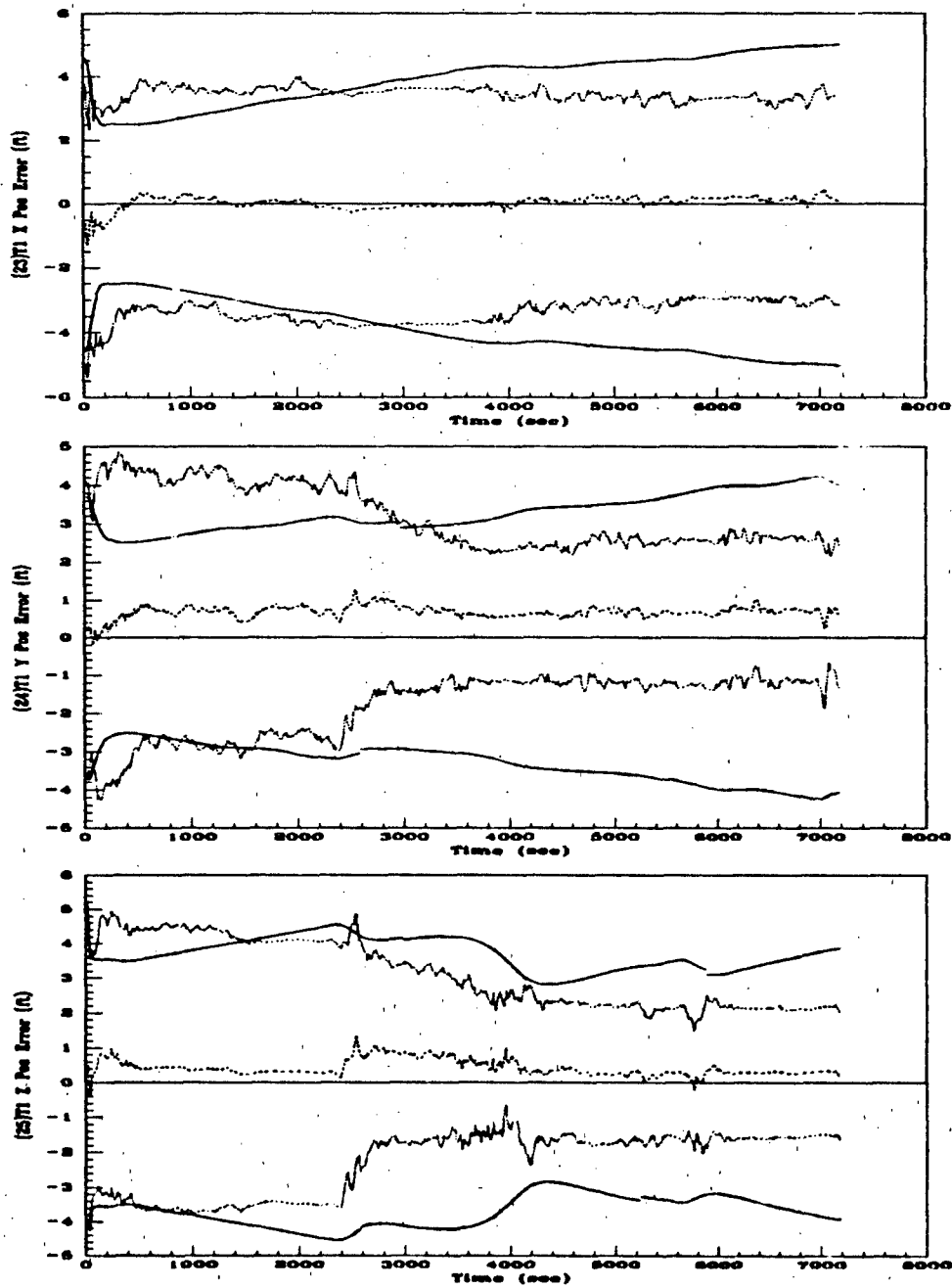


Figure J.7. 46-State CIRIS Filter, Fighter Flight Profile Filter (a) T1 X Position (b) T1 Y Position and (c) T1 Z Position Errors.

----	Mean Error = $\hat{M}_x - (M_x)_{true}$
.....	Mean Error $\pm \sigma_{true}$
—	$0 \pm \sigma_{filter}$

J.2 2-Hour Racetrack Flight Profile

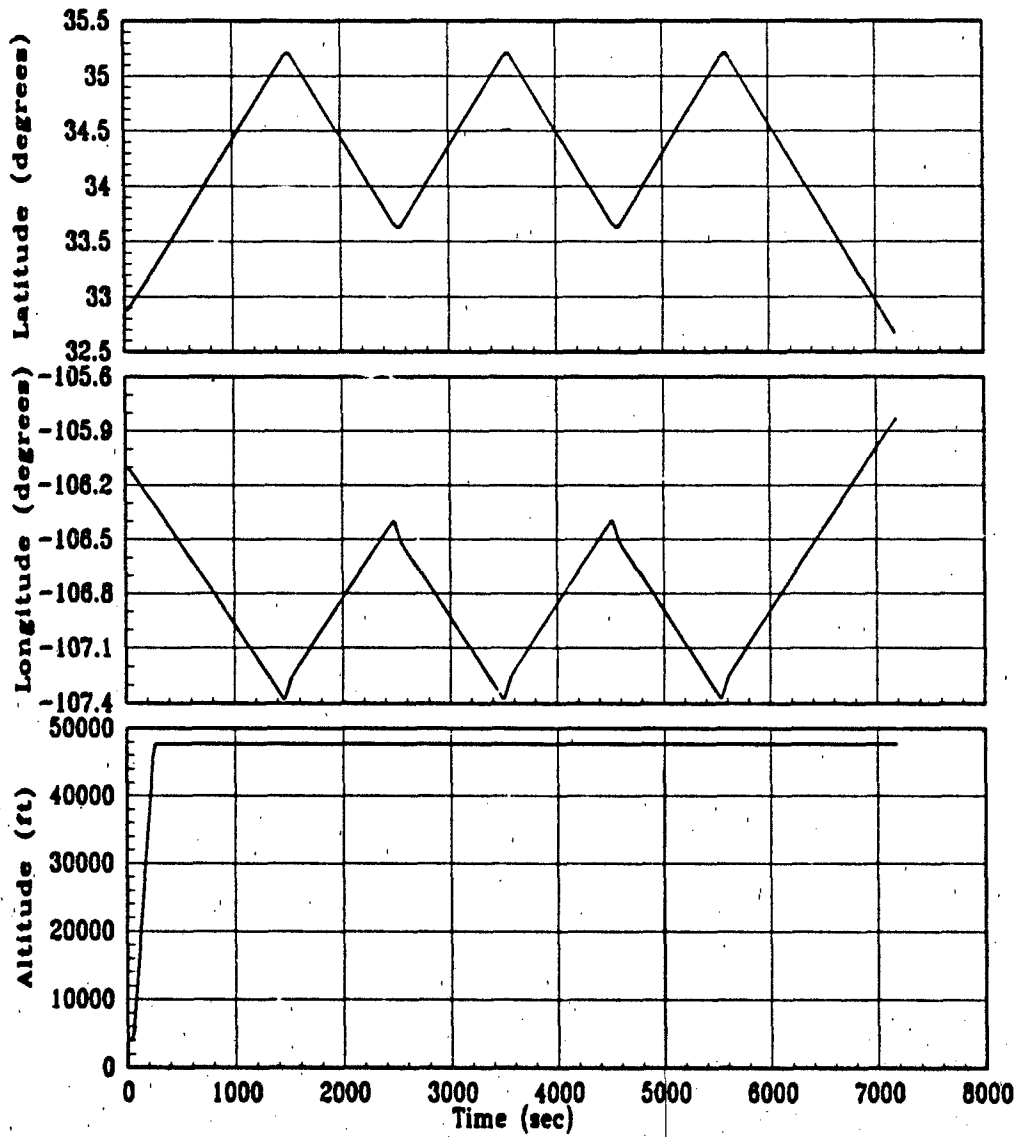


Figure J.8. 2-Hour Racetrack Flight Profile (a) Latitude (b) Longitude and (c) Altitude

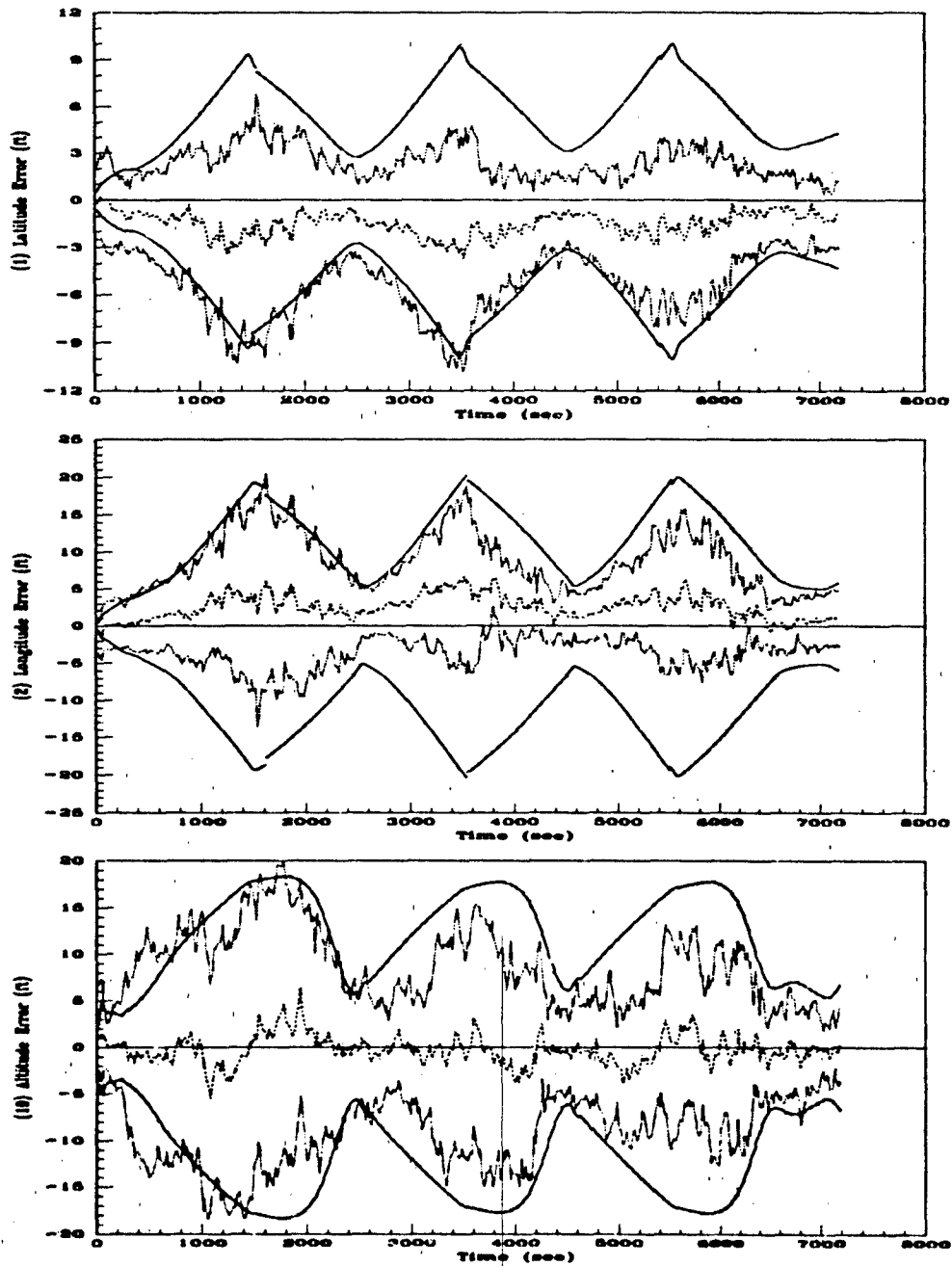


Figure J.9. 46-State CIRIS Filter, Racetrack Flight Profile (a) Latitude (b) Longitude and (c) Altitude Errors.

---	Mean Error = $\bar{M}_z - (M_z)_{true}$
.....	Mean Error $\pm \sigma_{true}$
—	$0 \pm \sigma_{filter}$

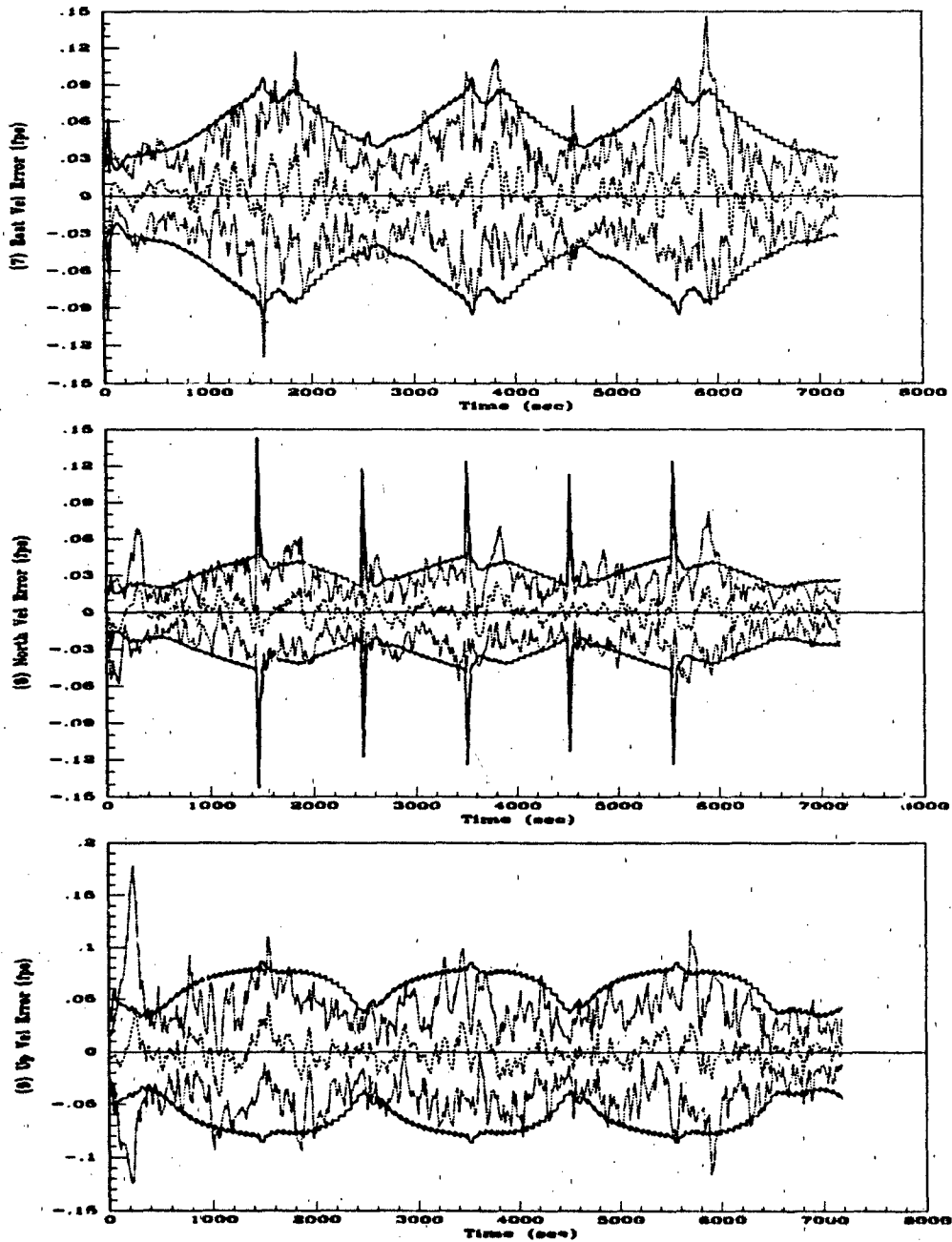


Figure J.10. 46-State CIRIS Filter, Racetrack Flight Profile Filter (a) East Velocity (b) North Velocity and (c) Vertical Velocity Errors.

----	Mean Error = $\bar{M}_z - (M_z)_{true}$
.....	Mean Error $\pm \sigma_{true}$
—	$0 \pm \sigma_{filter}$

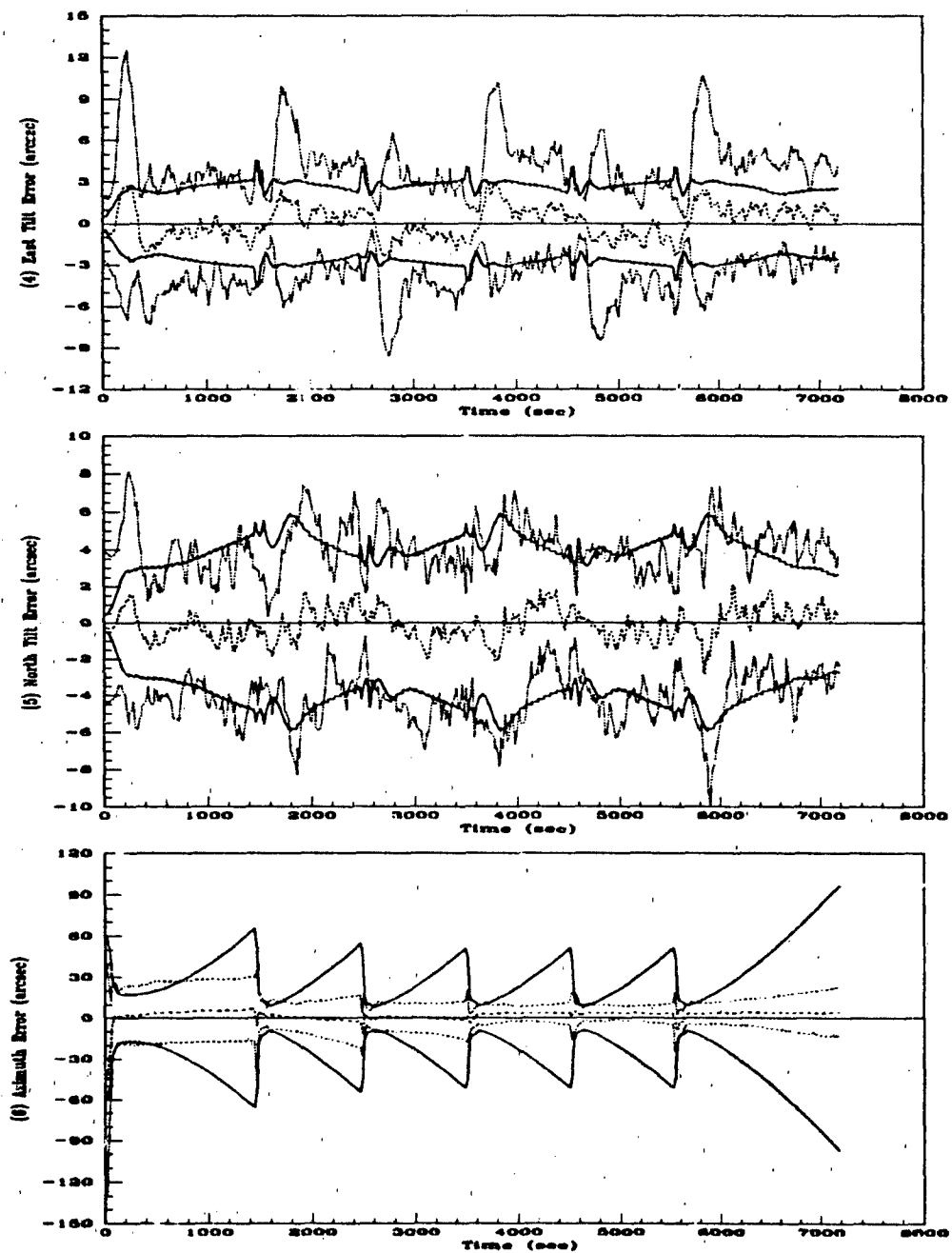


Figure J.11. 46-State CIRIS Filter, Racetrack Flight Profile Filter (a) East Tilt (b) North Tilt and (c) Azimuth Errors.

----	Mean Error = $\bar{M}_x - (M_x)_{true}$
.....	Mean Error $\pm \sigma_{true}$
—	$0 \pm \sigma_{filter}$

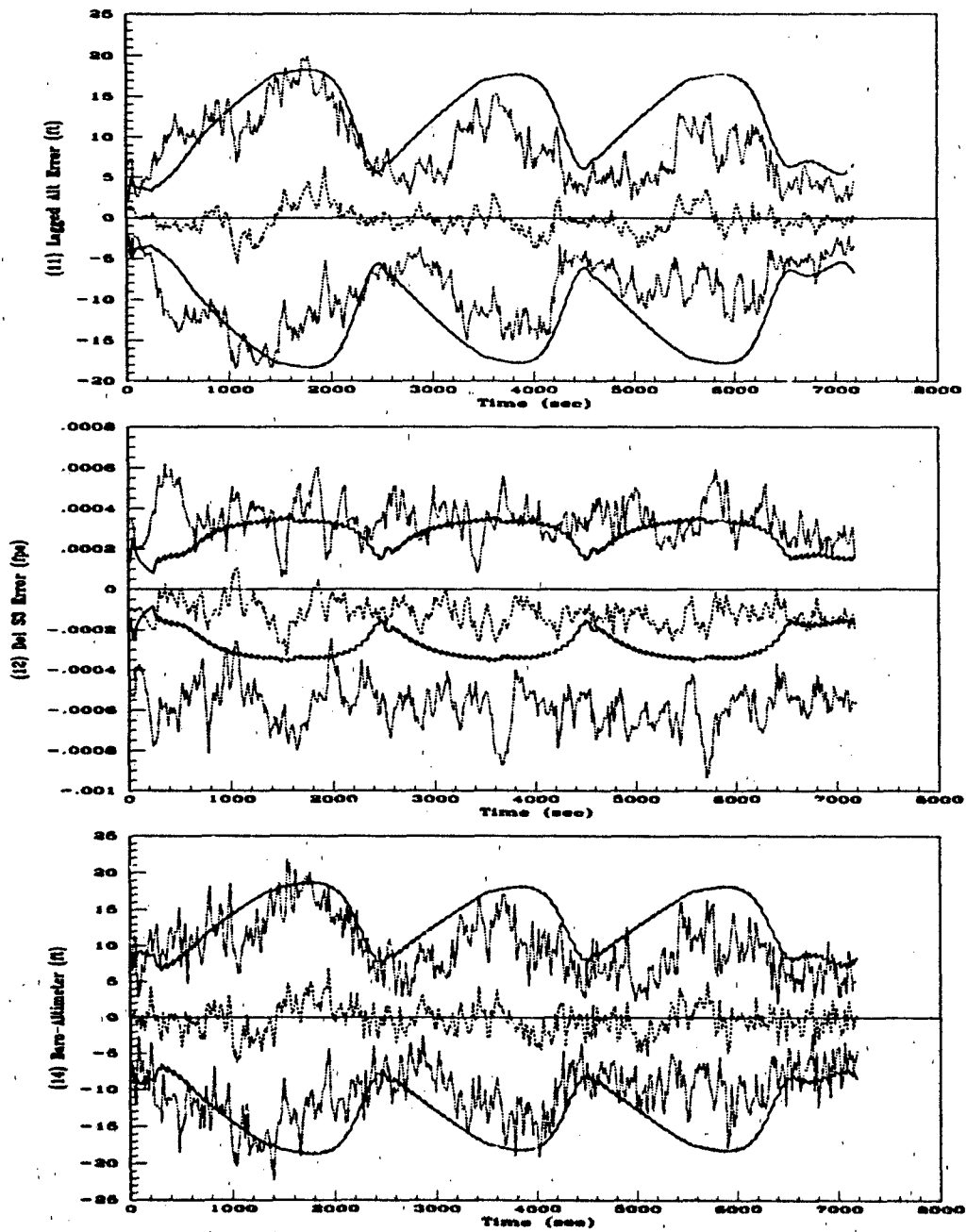


Figure J.12. 46-State CIRIS Filter, Racetrack Flight Profile Filter (a) Lagged Altitude (b) Del S3 and (c) Baro-Altimeter Errors.

----	Mean Error = $\bar{M}_z - (M_z)_{true}$
.....	Mean Error $\pm \sigma_{true}$
—	$0 \pm \sigma_{filter}$

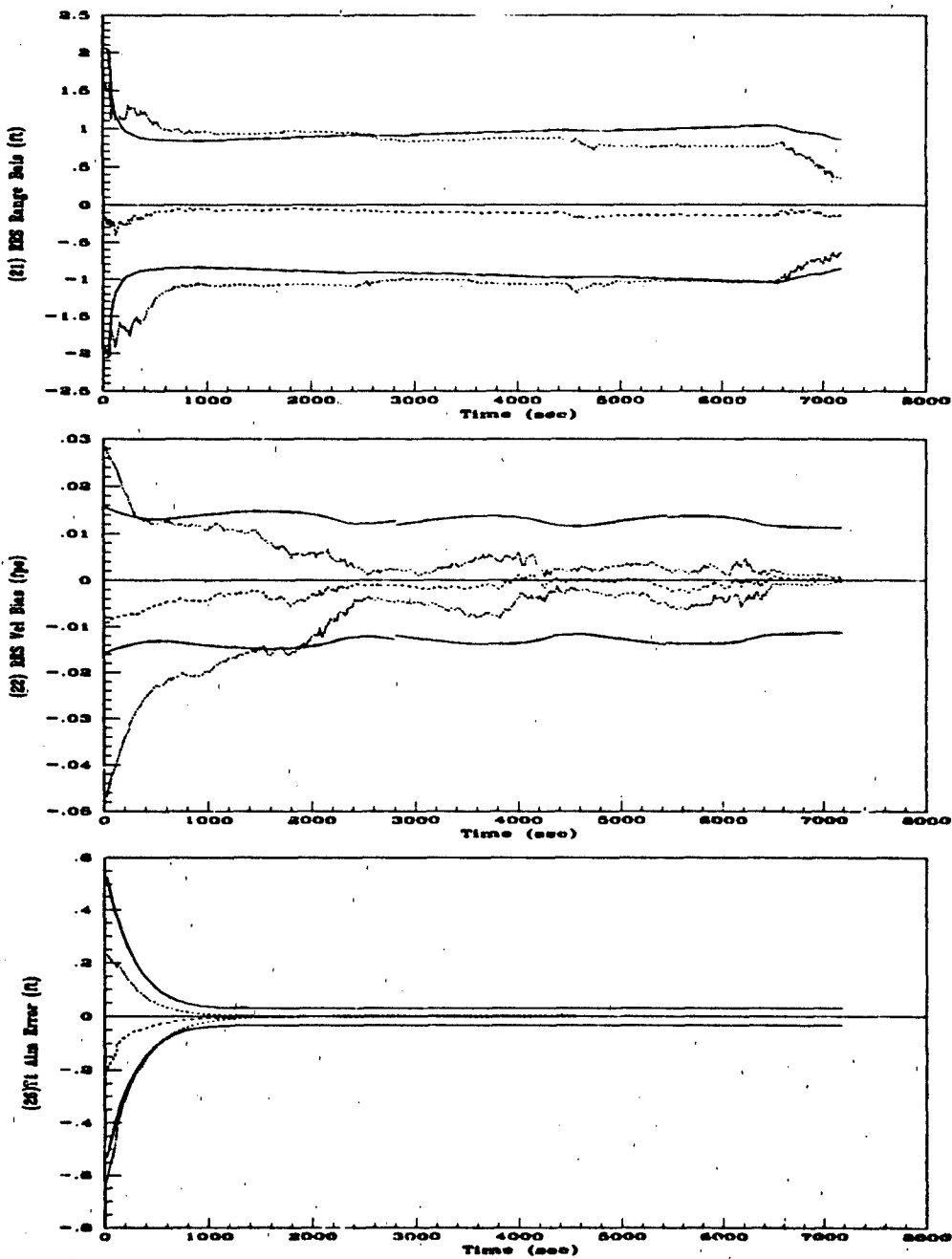


Figure J.13. 46-State CIRIS Filter, Racetrack Flight Profile Filter (a) RRS Range Bias (b) RRS Vel Bias and (c) T1 Atmosphere Errors.

-----	Mean Error = $\bar{M}_x - (M_x)_{true}$
.....	Mean Error $\pm \sigma_{true}$
—	$0 \pm \sigma_{filter}$

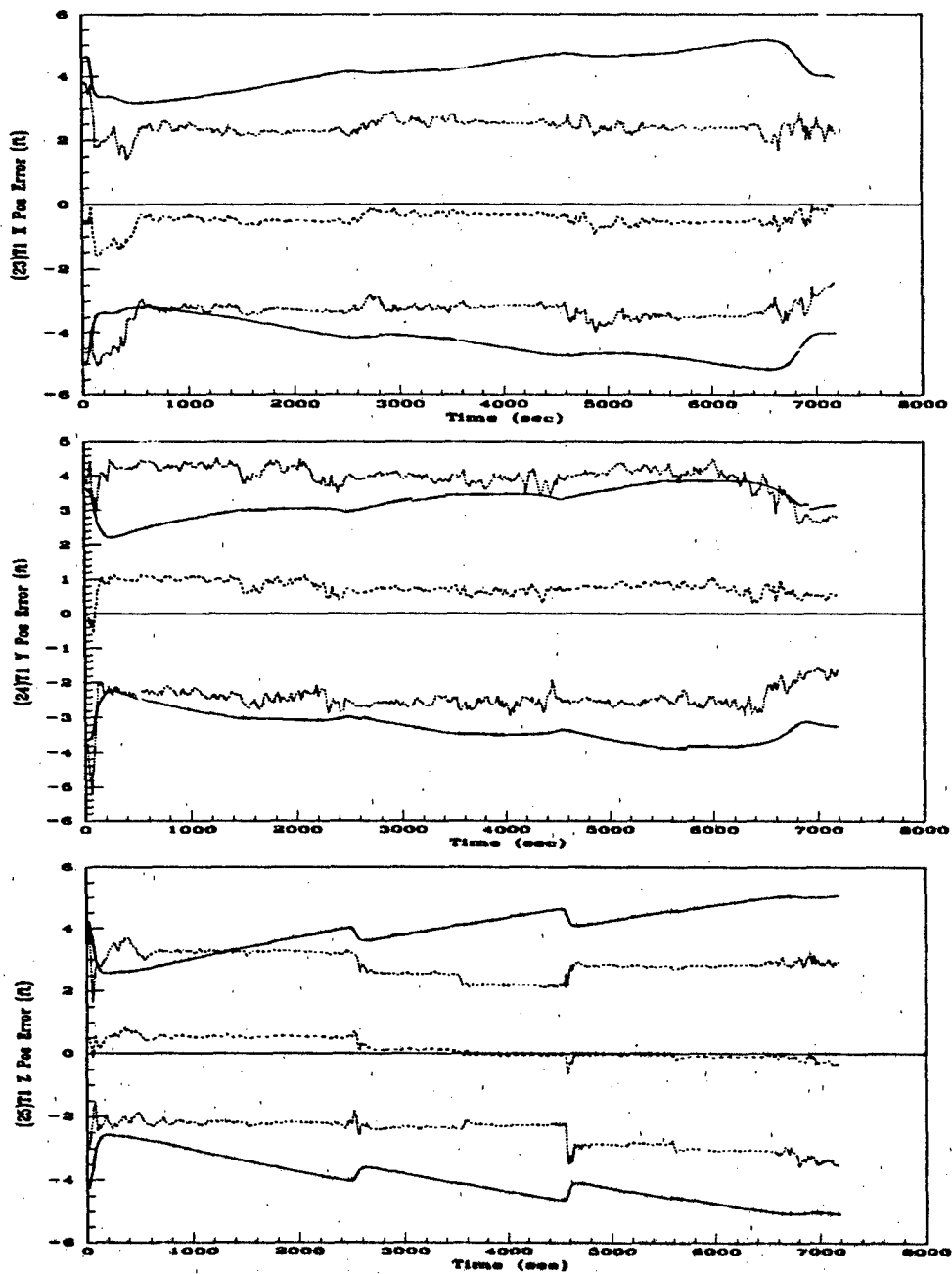


Figure J.14. 46-State CIRIS Filter, Racetrack Flight Profile Filter (a) T1 X Position (b) T1 Y Position and (c) T1 Z Position Errors.

.....	Mean Error = $M_x - (M_x)_{true}$
.....	Mean Error $\pm \sigma_{true}$
—	$0 \pm \sigma_{filter}$

Appendix K. *48-State ENRS Filter Performance Plots*

The plots in this section represent results of a 25-run Monte Carlo 2-hour fighter flight profile simulation. This filter analysis was performed in double precision, so the DGPS receiver clock errors are at their actual values. This reduced-order filter incorporates RRS range/range-rate and DGPS pseudorange/delta-range measurements.

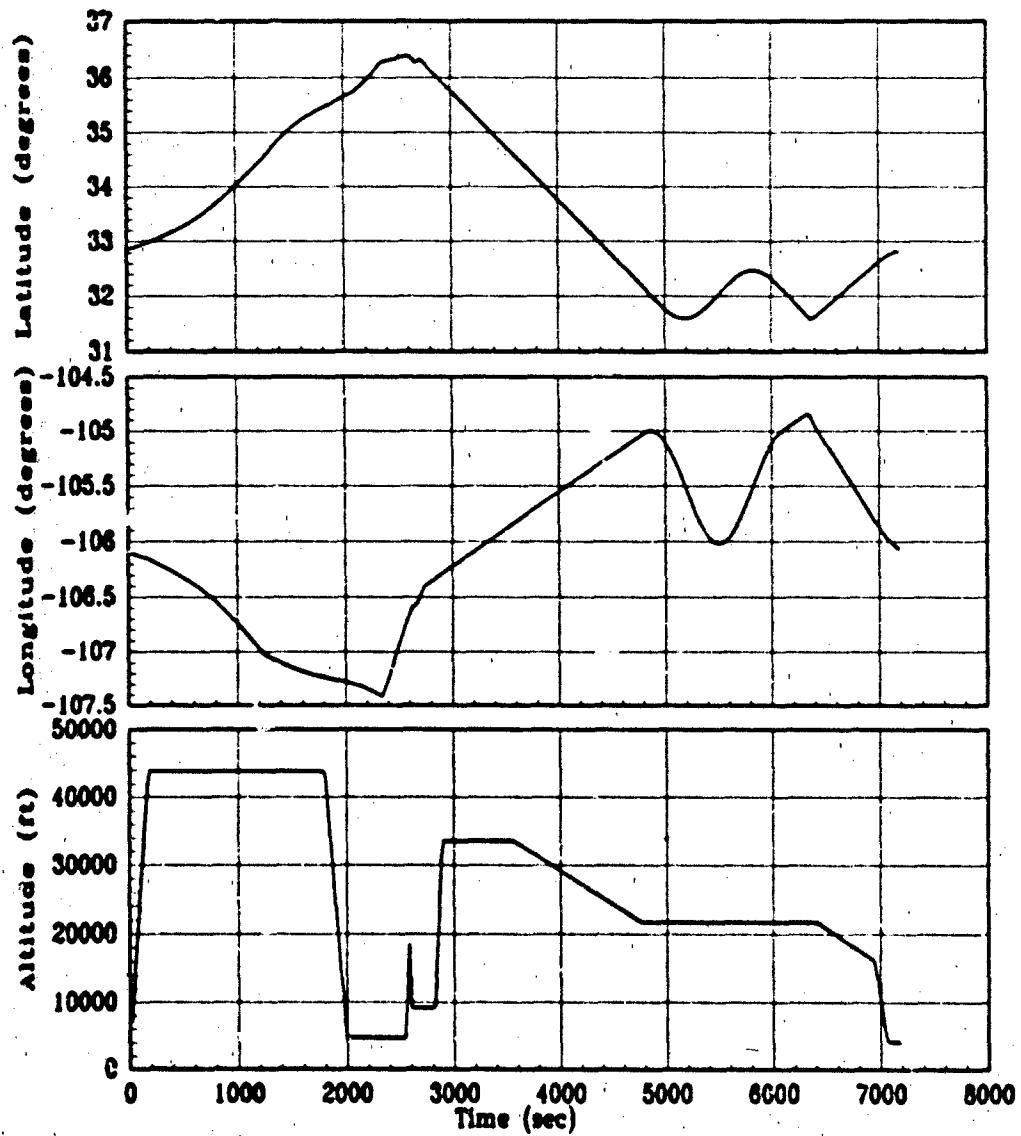


Figure K.1. 2-Hour Fighter Flight Profile (a) Latitude (b) Longitude and (c) Altitude

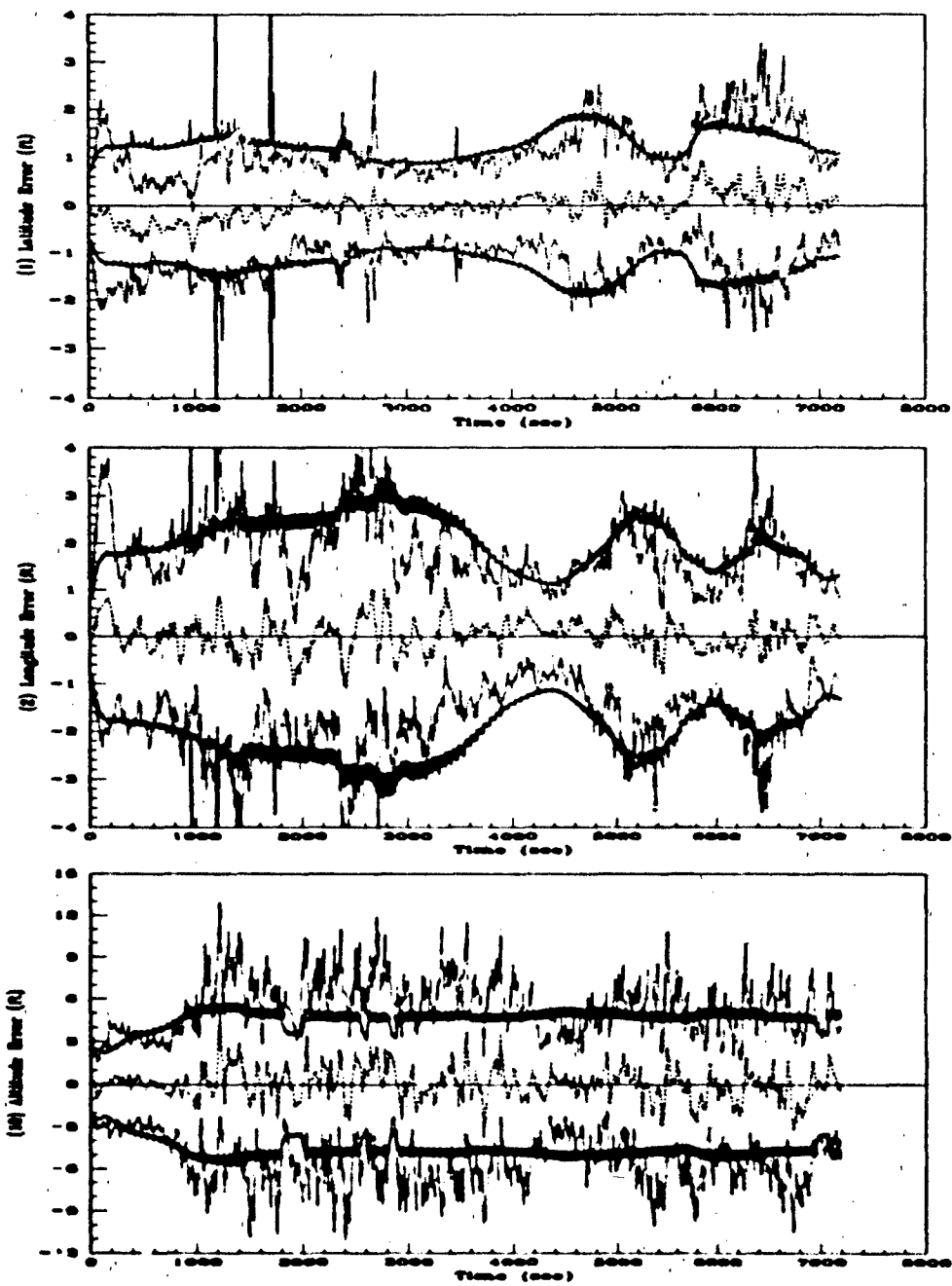


Figure K.2. 48-State ENRS Filter (a) Latitude (b) Longitude and (c) Altitude Errors.

- - - -	Mean Error = $M_x - (M_x)_{true}$
.....	Mean Error $\pm \sigma_{true}$
—	$0 \pm \sigma_{filter}$

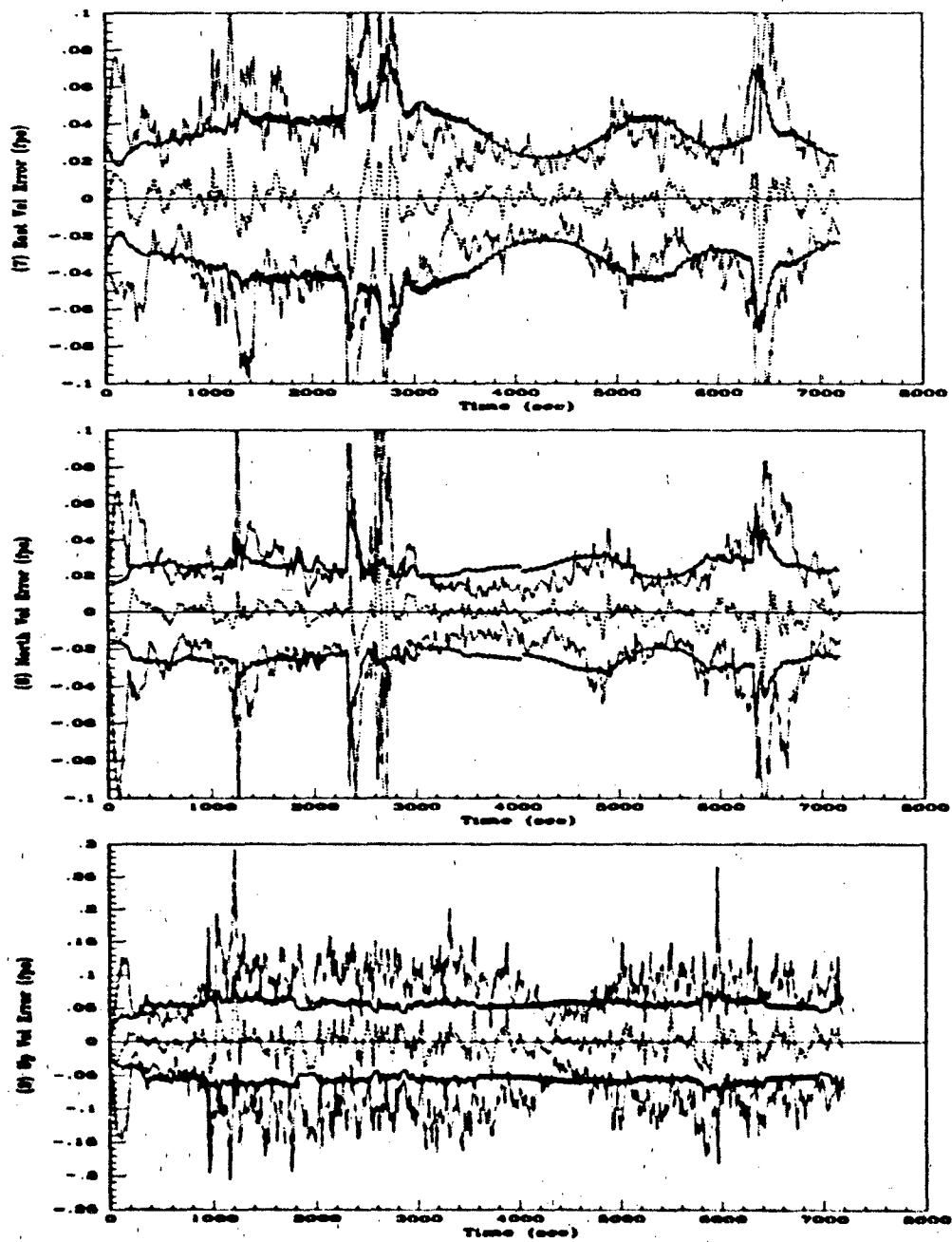


Figure K.3. 48-State ENRS Filter (a) East Velocity North Velocity and (c) Vertical Velocity Errors.

- . . .	Mean Error = $M_x - (M_x)_{true}$
-	Mean Error $\pm \sigma_{true}$
—	$0 \pm \sigma_{filter}$

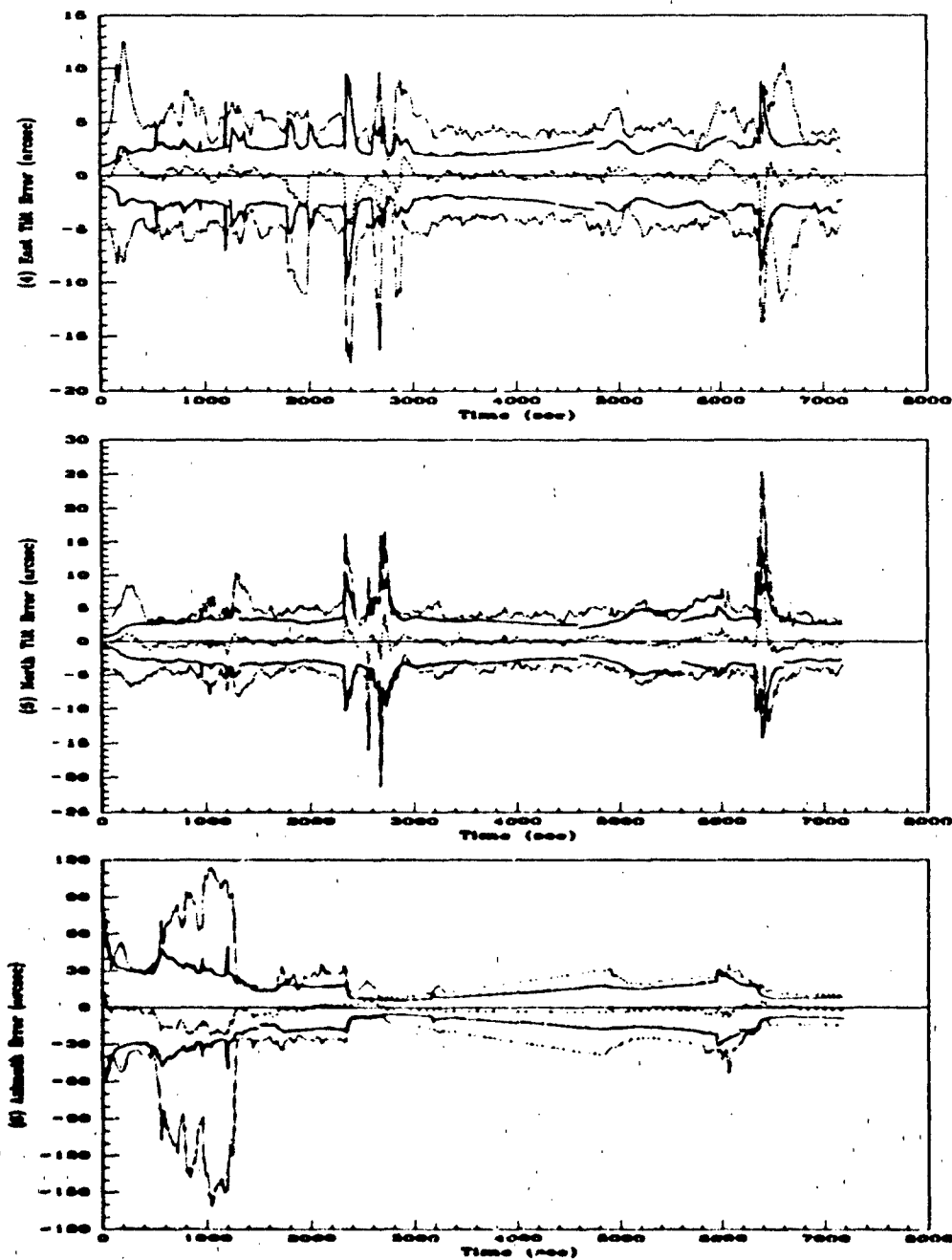


Figure K.4. 48-State ENRS Filter (a) East Tilt (b) North Tilt and (c) Azimuth Errors.

.....	Mean Error = $M_x - (M_x)_{true}$
.....	Mean Error $\pm \sigma_{true}$
—	$0 \pm \sigma_{filter}$

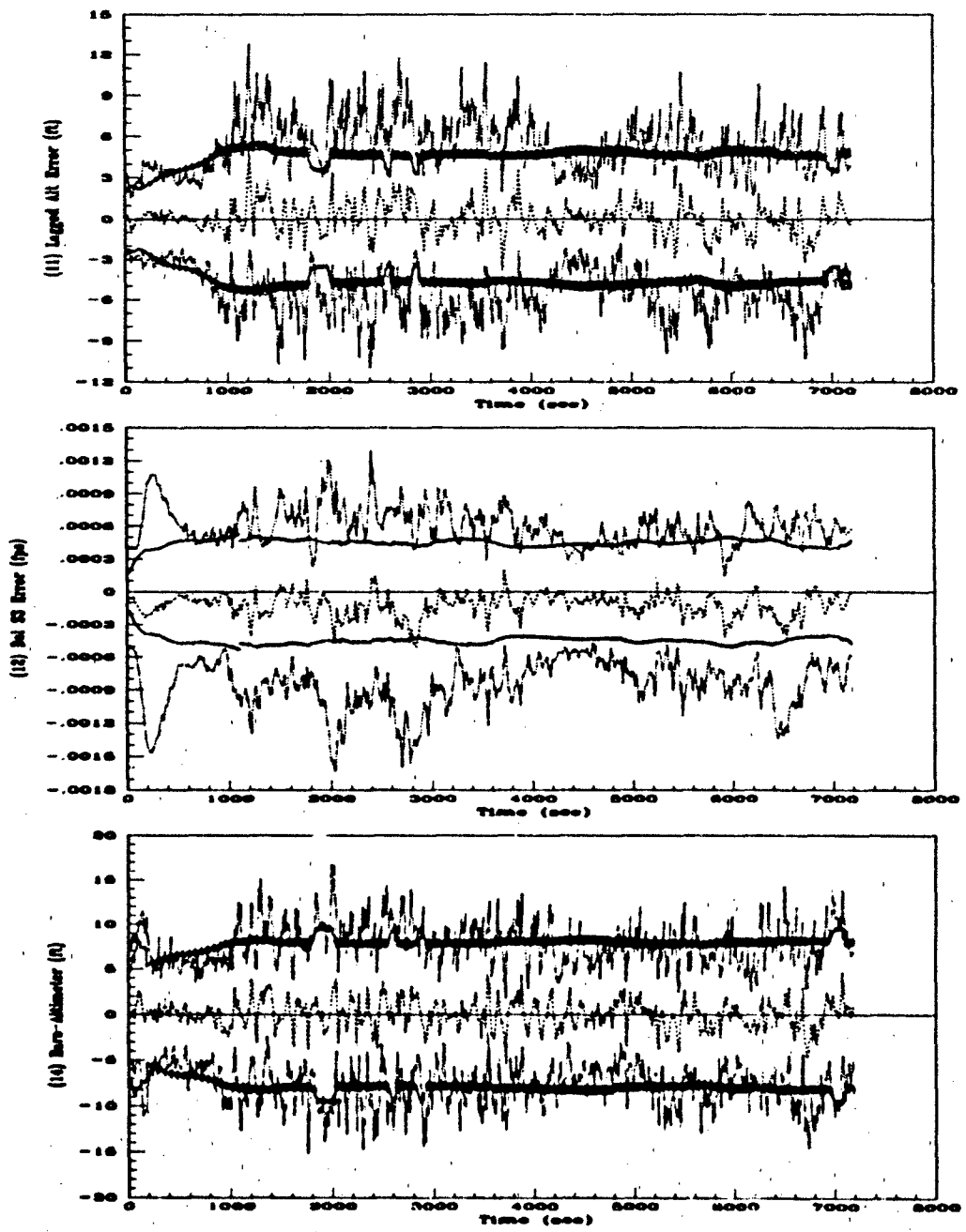


Figure K.5. 48-State ENRS Filter (a) Lagged Altitude (b) Del S3 and (c) Baro-Altimeter Errors.

---	Mean Error = $M_x - (M_x)_{true}$
.....	Mean Error $\pm \sigma_{true}$
—	$0 \pm \sigma_{filter}$

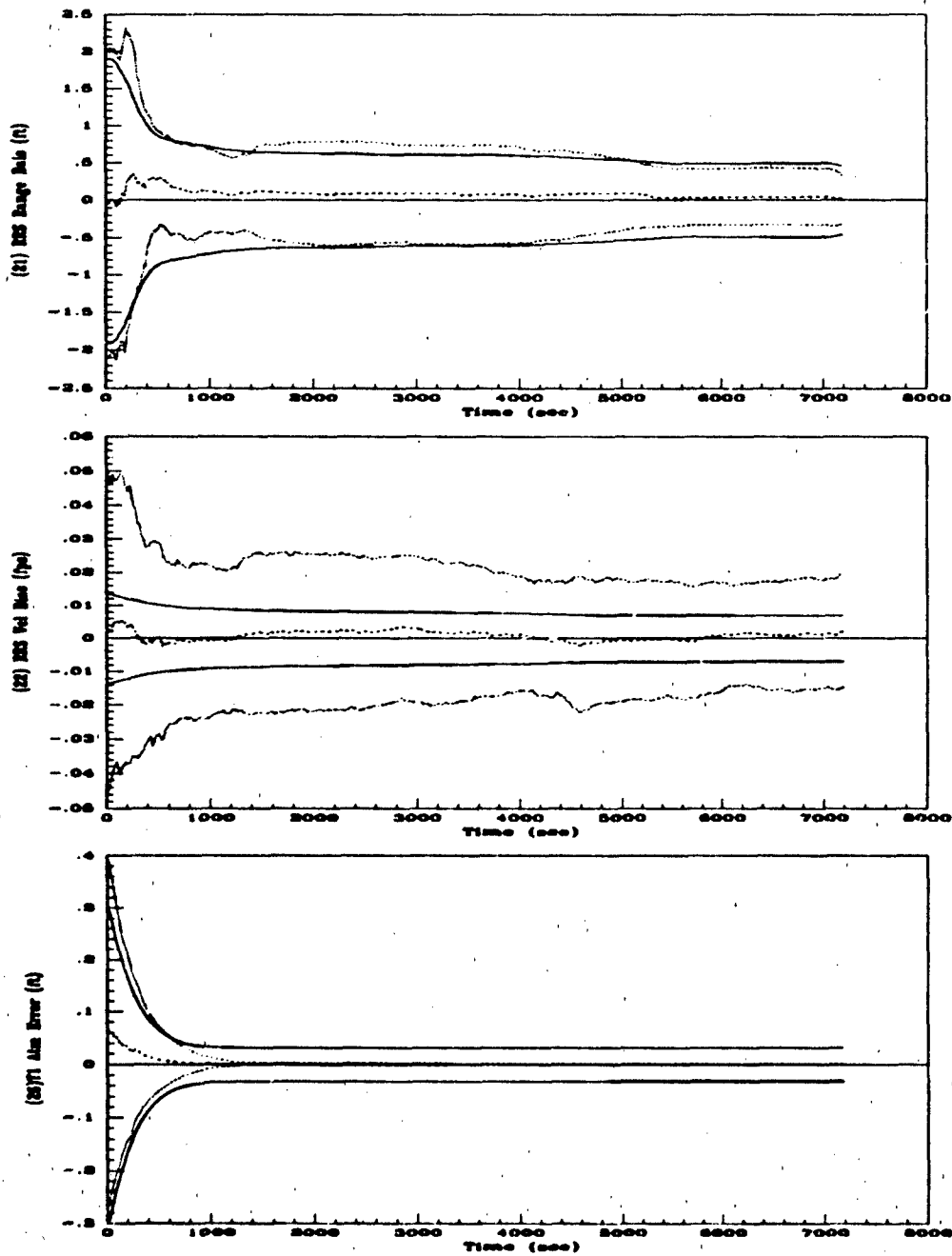


Figure K.6. 48-State ENPS Filter (a) RRS Range Bias (b) RRS Vel Bias and (c) T1 Atmosphere Errors.

- - - -	Mean Error = $\bar{M}_x - (M_x)_{true}$
.....	Mean Error $\pm \sigma_{true}$
—	$0 \pm \sigma_{filter}$

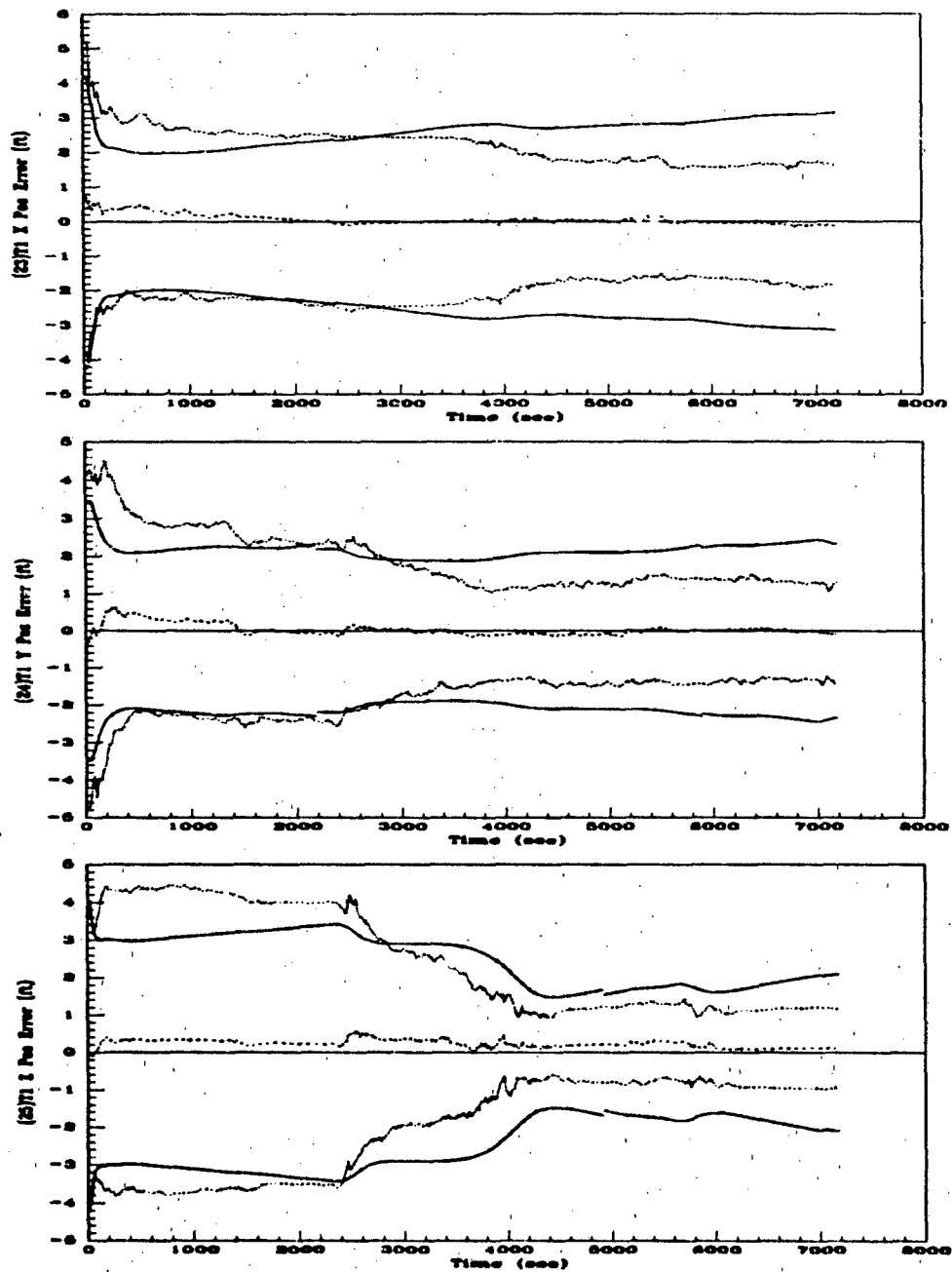


Figure K.7. 48-State ENRS Filter (a) T1 X Position (b) T1 Y Position and (c) T1 Z Position Errors.

.....	Mean Error = $\bar{M}_z - (M_z)_{true}$
.....	Mean Error $\pm \sigma_{true}$
———	$0 \pm \sigma_{filter}$

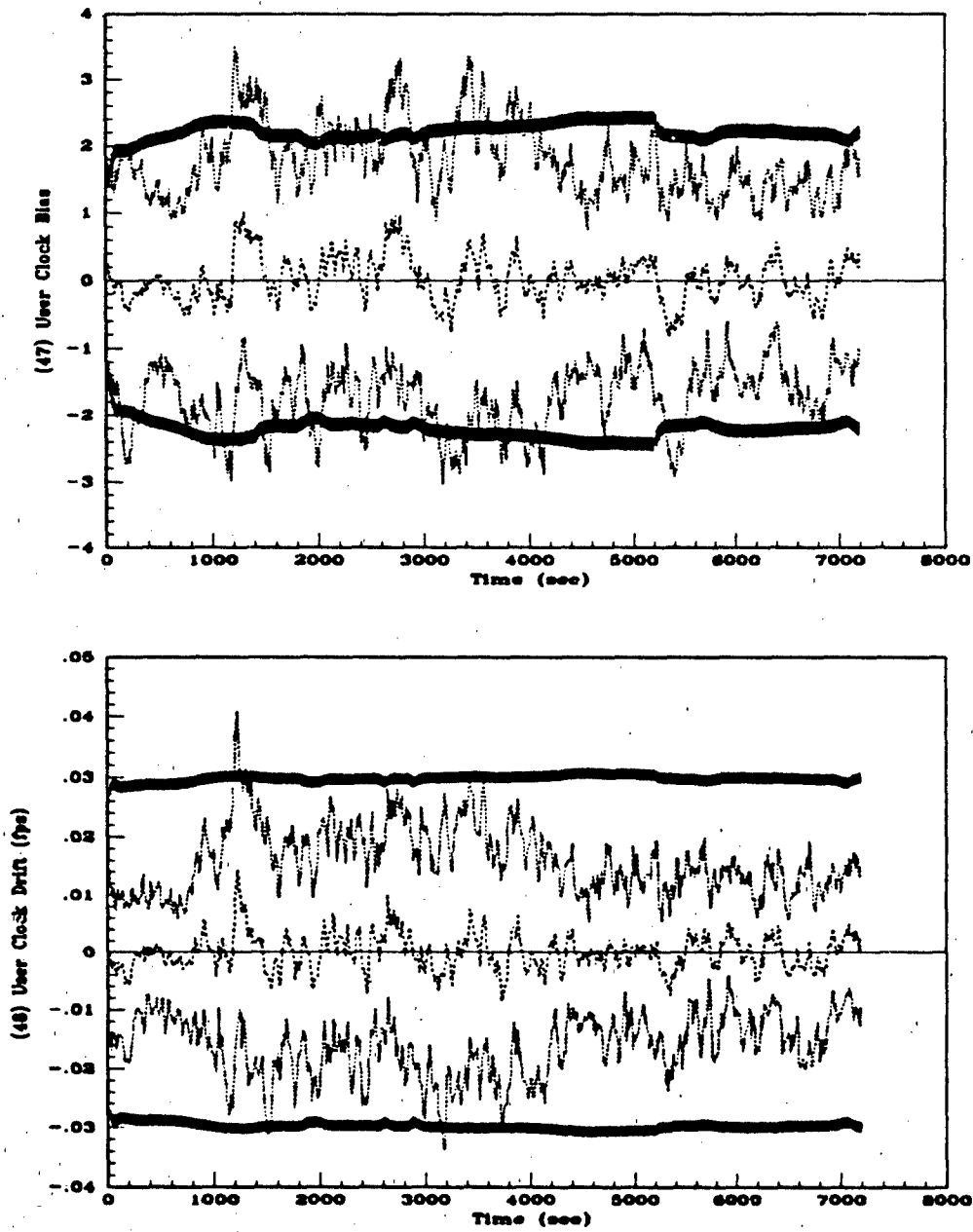


Figure K.8. 48-State ENRS Filter (a) User Clock Bias and (b) User Clock Drift Errors.

- - - -	Mean Error = $\bar{M}_x - (M_x)_{true}$
.....	Mean Error $\pm \sigma_{true}$
—	$0 \pm \sigma_{filter}$

Bibliography

1. Abbey, Darwin and Scott D. Dance of Intermetrics, Inc. *GPS Data Analysis Reference Station*, Briefing to AFIT Students, Holloman AFB, NM, June 1991.
2. Britting, Kenneth R. *Inertial Navigation Systems Analysis*. New York: Wiley-Interscience, 1971.
3. Carlson, Neal and Stanton Musik. *User's Manual for a Multimode Simulation for Optimal Filter Evaluation (MSOFE)*. AFWAL-TR-88-1138, Wright-Patterson AFB OH: Avionics Lab, AFWAL/AARN-2, Apr 1990.
4. Cox Jr., D. B. "Integration of GPS with Inertial Navigation Systems," *Global Positioning System, Papers Published in Navigation: Journal of the Institute of Navigation*, pages 144-153 (1980).
5. Dance, Scott D. Personal Interviews. Intermetrics, Inc., Holloman AFB, NM, June 1991.
6. GE-90D, EENG735 Class. *GPS Aided LN-93 INS*. EENG735 Class Project Final Report, Air Force Institute of Technology (AU), Wright-Patterson AFB OH, May 1990.
7. Green, G. B. and others. "The GPS 21 Primary Satellite Constellation," *Navigation: Journal of the Institute of Navigation*, 25:9-24 (Fall 1989).
8. Guidance Test Division. "CIRIS II Test Summary Report," In-House Report, CIGTF, 6585th Test Group, Holloman AFB, NM, May 1988.
9. Guidance Test Division. "The Completely Integrated Reference Instrumentation System (CIRIS)," Unpublished Contractor Informational Pamphlet, CIGTF, 6585th Test Group, Holloman AFB NM.
10. Lewantowicz, Zdzislaw H. and Danny W. Keen. "Graceful Degradation of GPS/INS Performance With Fewer Than Four Satellites," *The Institute of Navigation, National Technical Meeting* (Jan 1991).
11. Litton Guidance and Control Systems. *Performance Accuracy (Truth Model/Error Budget) Analysis for the LN-93 Inertial Navigation Unit*. DID No. DI-S-21433 B/T:CDRL No. 1002. Woodland Hills, CA, Jan 1985.
12. Martin, E. H. "GPS User Equipment Error Models." In Janiczek, P. M., editor, *Global Positioning System*, Washington, D.C.: The Institute of Navigation, 1980.

13. Maybeck, Peter S. Personal Interviews, Air Force Institute of Technology (AU), Wright-Patterson AFB, OH, June-November, 1991.
14. Maybeck, Peter S. *Stochastic Models, Estimation, and Control*, Volume 1. San Diego, CA: Academic Press, 1979.
15. Maybeck, Peter S. *Stochastic Models, Estimation, and Control*, Volume 2. San Diego, CA: Academic Press, 1982.
16. Maybeck, Peter S. *Stochastic Models, Estimation, and Control*, Volume 3. San Diego, CA: Academic Press, 1982.
17. Milliken, R. J. and C. J. Zoller. "Principles of Operation of NAVSTAR and System Characteristics," *Navigation, Journal of the Institute of Navigation*, 25:3-14 (Summer 1978).
18. Navtech Seminars, Inc. "Dynamic Differential GPS," Notebook from Course 311, Alexandria, VA, December, 1989.
19. Snodgrass, Faron Britt. *Continued Development and Analysis of a New Extended Kalman Filter for the Completely Integrated Reference Instrumentation System (CIRIS)*. MS Thesis, AFIT/GE/90M-5. School of Engineering, Air Force Institute of Technology (AU), Wright-Patterson AFB OH, March 1990.
20. Solomon, Joseph K. *Development of the Extended Kalman Filter for the Advanced Completely Integrated Reference Instrumentation System (CIRIS)*. MS Thesis, AFIT/GE/89M-8. School of Engineering, Air Force Institute of Technology (AU), Wright-Patterson AFB OH, March 1989.
21. Solomon, Joseph K. *CIRIS Special Study*, Final Report, EENG 699, Air Force Institute of Technology (AU), Wright-Patterson AFB OH, March 1989.
22. Stacey, Richard Darrell. *A Navigation Reference System (NRS) Using Global Positioning System (GPS) and Transponder Aiding*. MS Thesis, AFIT/GE/91M-04. School of Engineering, Air Force Institute of Technology (AU), Wright-Patterson AFB OH, March 1991.

Vita

Captain William Joseph Negast [REDACTED]

[REDACTED] After graduating from Bellevue West High School in Nebraska in 1979, he returned with his family to Texas where he first attended Baylor University and finally Southwest Texas State University graduating in 1984 with Bachelor of Science Degrees in Chemistry and Physics. He was then accepted into the Air Force Undergraduate Engineering Conversion Program and, after Officer Training School, was sent to Louisiana Tech University where he received a Bachelor of Science Degree in Electrical Engineering in August 1986. He was then assigned to Eglin AFB, Florida, where he worked as a simulation analyst, guidance and control engineer, and Executive Officer for the Deputy for Engineering, Munitions Systems Division, until May 1990. From June 1990 till March 1992 he attended the Air Force Institute of Technology receiving a Master of Science Degree in Electrical Engineering with emphasis in navigation and control. Following AFIT, he was assigned to the Central Inertial Guidance Test Facility, Holloman AFB, NM, where he is currently working.

[REDACTED]